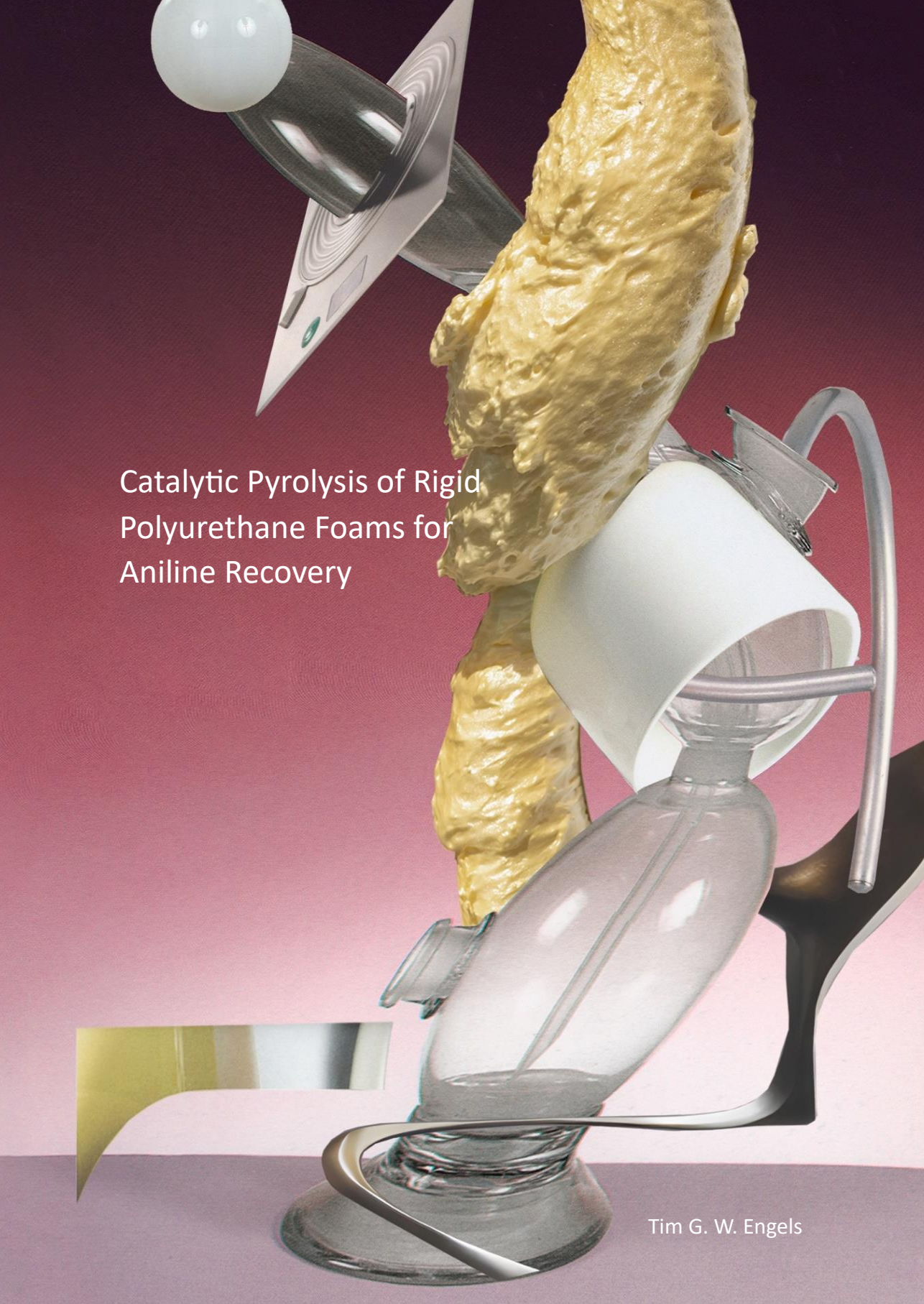

Catalytic Pyrolysis of Rigid Polyurethane Foams for Aniline Recovery

Tim G. W. Engels

Stellingen

Behorende bij het proefschrift:

Aniline recovery from pMDI-based rigid polyurethane foams via catalytic pyrolysis

Tim G. W. Engels

1. Availability of technology is clearly not the main bottleneck to implementing circular solutions for polyurethanes.

2. Calibrated aniline yields are rarely reported in the field of PUR pyrolysis, making cross-study comparison challenging.

3. The absence of Brønsted acid site formation (static vs dynamic) in ASA-type catalysts can lead to incorrect conclusions about its contribution to catalytic activity.
(Xu *et al.*, The Journal of Physical Chemistry C, 2007,*111*, 12075-12079, Bevilacqua *et al*., Catalysis Today, 2006, *116*, 132-142)

4. Although ethics is strongly emphasized during education, sadly, the reuse of previously published mechanisms or textual passages still appears in literature.
(Xu *et al.*, Polymer Testing, 2008, *67*, 159-168, Jiao *et al.*, Polymer Degradation and Stability, 2013, *98*(12), 2687-2696, Bao *et al.*, Microporous and Mesoporous Materials, 2022, *337*, 111897, Williams *et al.*, Journal of Catalysis, 2007 *251*(2), 485-496)

5. Proper sample preparation equipment is essential for obtaining reproducible data.

6. New materials produced with recovered chemicals should be designated with dedicated terminology to prevent confusion with second-hand products.

7. A fire-extinguishing course should be included in the PhD TSP to prevent fire tornadoes in fume hoods.

8. AI is a great tool to complete less important tasks faster, so there is more time for research.

9. Approachability is an essential attribute that every good manager should have.

10. Having a Brabants accent in the North is a unique characteristic that yields many friends, collaborations, and good memories.

Catalytic Pyrolysis of Rigid Polyurethane Foams for Aniline Recovery

Tim G. W. Engels

2026

The work described in this thesis was conducted at the Department of Chemical Engineering, Engineering and Technology Institute Groningen, University of Groningen, the Netherlands.
The work presented in this publication includes results developed within the Circular Foam project, which has received funding from the European Union's Horizon 2020 research and innovation programme under grant agreement No. 101036854.

Cover design: Fenna Schilling
Cover typography and layout: Roos Alberts
Printed by: Proefschrifmaken





university of groningen

Catalytic Pyrolysis of Rigid Polyurethane Foams for Aniline Recovery

PhD thesis

to obtain the degree of PhD at the
University of Groningen
on the authority of the
Rector Magnificus Prof. J.M.A. Scherpen
and in accordance with
the decision by the College of Deans.

This thesis will be defended in public on

Friday 20 November 2026 at 11.00 hours

by

Tim Gerardus Wilhelmus Engels

born on 19 March 1994

Supervisors
Prof. P.J. Deuss
Prof. H.J. Heeres

Assessment Committee
Prof. F. Picchioni
Prof. J. Xie
Prof. M. Carrier

This page has been left intentionally blank

Table of contents

Chapter 1.	**The Circular Foam Project**	
1.1	Introduction	2
1.2	Funding and project position within circularity	2
1.3	Project concept framework	5
1.4	Anticipated impact of the CF initiative	8
1.5	Outline of this dissertation	8
	References	9
Chapter 2.	**The current state of polyurethane waste management, recycling efforts, and research motivation**	
2.1	Annual plastic production	14
2.2	European legislation on waste management	15
2.3	Plastic waste treatment options	16
2.4	Polyurethane recycling	17
2.5	Current PUR waste management	18
2.6	Physical and chemical features of polyurethane foams	18
2.7	Polyurethane foam synthesis	20
2.8	Advances in Polyurethane recycling efforts	21
2.9	Thermal degradation pathways for polyurethanes	23
2.10	Catalytic pyrolysis of polyurethane	25
2.11	Reactor types	25
2.12	Operational modes (in- and ex-situ)	27
2.13	Catalyst types	28
2.14	Catalyst deactivation	32
2.15	Key developments in (catalytic) thermal degradation of rigid polyurethane foams	34
	References	35
Chapter 3.	**Chemical recycling of rigid polyurethane foam via thermocatalytic conversion to aniline**	
	Abstract with graphical abstract	46
3.1	Introduction	47
3.2	Results & discussion	49
3.3	Conclusions	60
	References	60
3.4	Supporting information	62
	References	88

Chapter 4.	**Insights into catalyst stability**	
	Abstract with graphical abstract	94
4.1	Introduction	95
4.2	Experimental section	96
4.3	Results & Discussion	100
4.4	Conclusions	109
	References	110
4.5	Supporting information	111
Chapter 5.	**Mechanistic insights using ^{13}C and deuterium model compounds**	
	Abstract with graphical abstract	126
5.1	Introduction	127
5.2	Experimental	128
5.3	Results & Discussion	133
5.4	Conclusions	148
	References	148
5.5	Supporting information	151
	References	182
Chapter 6.	**Catalyst-structure relations for the depolymerization of polyurethanes to aniline using amorphous silica alumina (ASA) catalysts**	
	Abstract with graphical abstract	186
6.1	Introduction	187
6.2	Experimental section	188
6.3	Results & Discussion	192
6.4	Conclusions	199
	References	200
6.5	Supporting information	202
	References	214
Chapter 7.	**Summary, perspective, and final remarks**	
7.1	Context and objectives	218
7.2	Summary	219
7.3	Perspective	220
	References	223
7.4	Supporting information	224
Appendix		
	Summary	244
	Samenvatting	246
	Academic output and conference contributions	248
	Acknowledgements	250



1

The Circular Foam Project

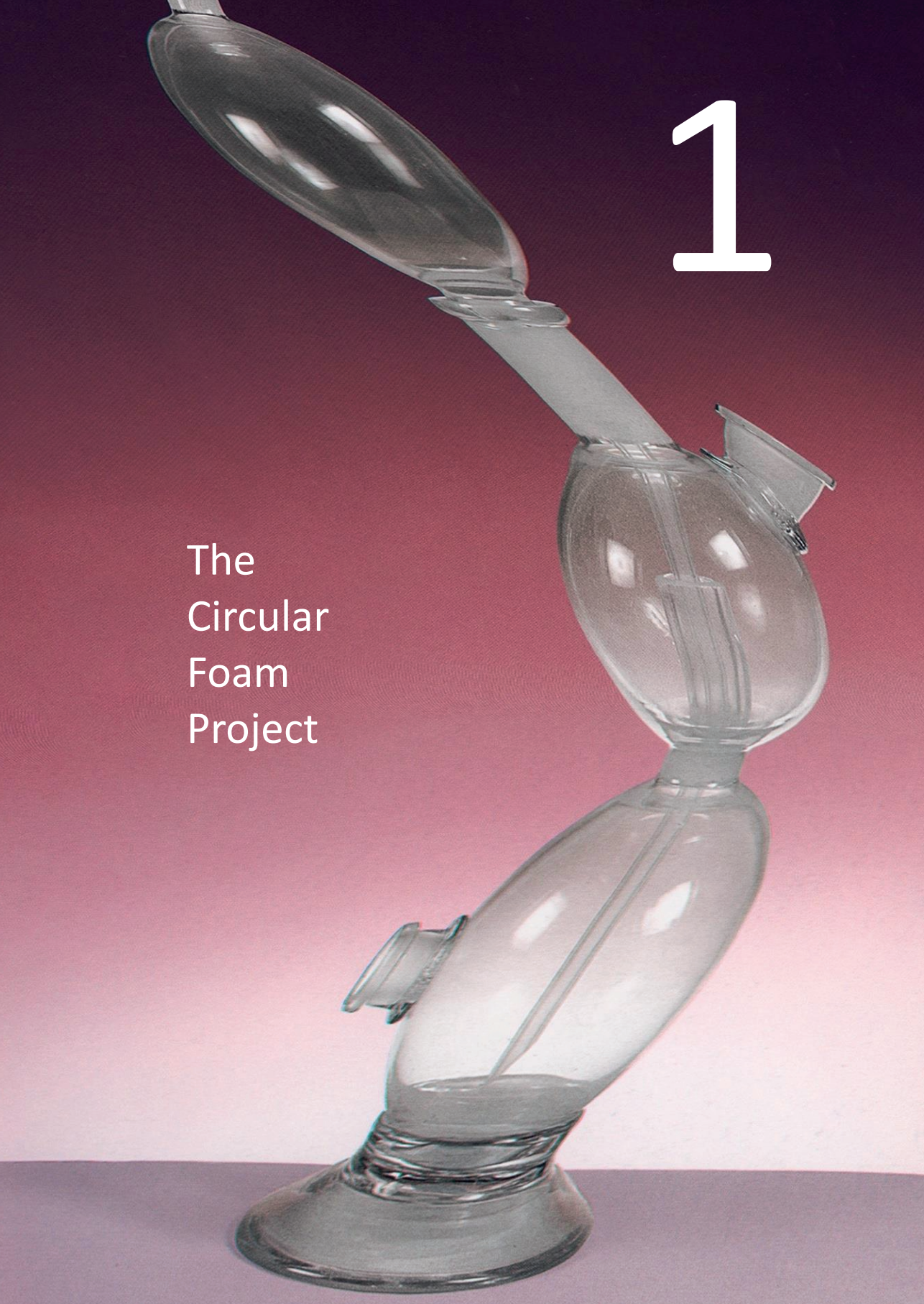

1.1. Introduction

European regulations governing plastic production have undergone a substantial transformation over the past decade, reflecting the commitment to achieve net-zero greenhouse gas emissions. Plastic products, while indispensable in modern society due to their versatility, durability, and cost-effectiveness, are intrinsically linked to fossil carbon feedstocks and energy-intensive production processes, contributing significantly to a chemically perturbed environment. A strategy to reduce plastic waste and dependence on fossil fuels is to advance plastic circularity through recycling.

The complex crosslinked thermoset architecture found in polyurethane products (e.g. refrigerators, roofing, floors, etc.) is a particularly challenging waste stream to recycle, preventing conventional reprocessing as production continues to increase worldwide.[1] Consequently, only approximately 25% of polyurethane waste is mechanically downcycled, with the remaining 75% left for incineration or landfill. Growing circular-economy demands have promoted efforts toward economically viable recycling strategies to recover both the polyol and isocyanate segments, potentially reducing emissions by up to 5.6 kg CO_2-eq per kg of polyurethane processed.[2]

The research described in this dissertation is part of the Circular Foam project (CF), an European Union Horizon 2020 project started in 2021 with a €19M budget, aimed at developing a thermochemical decomposition pathway for rigid polyurethane foams to recover chemical building block aniline for the production of new rigid polyurethane foam. This prelude serves as a conceptual link, positioning the research presented in this PhD thesis within the broader objective of achieving climate neutrality, which includes developing circular solutions for plastic products. A visual representation of the Circular Foam project vision is presented in Figure 1.1.

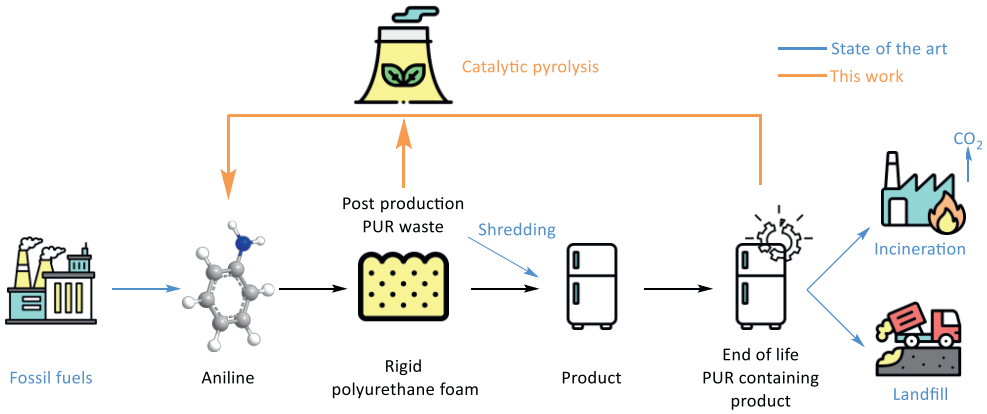

Figure 1.1. Current waste management (blue) compared to the approach proposed in this dissertation (orange)

1.2. Funding and project position within circularity

The European Green Deal (launched in 2019 by the European Commission)[3] aims to transform the current fossil-based economy into a resource-efficient, climate-neutral one by 2050, with emissions reduced by at least 55% by 2030, focusing on electronics, batteries, packaging, plastics, textiles,

construction, and food. Within this framework, achieving a plastic circular economy is embedded through the promotion of reusable/recycled-based packaging materials, waste minimization with a ban on single-use plastics, and advances in closed-loop recycling for high-performance plastics such as polyurethanes.[3–6] The latter implies scaling up mechanical and chemical recycling technologies, improving product design for future recyclability, and developing regional infrastructure capable of processing large volumes of plastic waste.

The Circular Cities and Regions Initiative (CCRI)[7] was launched by the Directorate-General for Research and Innovation from the European Commission as part of the EU Circular Economy Action Plan 2020 to support cities and regions in implementing circular systemic solutions under the European Green Deal. Complementary to the CCRI, an advisory panel was established in 2022 under the name Hubs for Circularity (H4C)[8] to bridge the gap between industrial actors, research institutions, public authorities, and civil society, thereby accelerating the European trajectory toward a climate-neutral, circular plastics system.

The CCRI and H4C started the LOOP cluster[9] in 2021 - 2022, funded under the same Horizon 2020 GD3.2 grant as the CCRI and H4C, to promote the development and implementation of specific plastic circular-economy solutions and value chains. It is a joint bottom-up initiative of four sister projects, including Agro2Circular,[10] CIRCULAR FOAM,[11] EcoeFISHent,[12] and FRONTSH1P.[13] Circular Foam fits within this cluster, as it focuses on producing circular polyurethane foams from end-of-life polyurethane waste, thereby directly addressing the scope of the CCRI. An overview of the CCRI, H4C, and LOOP cluster is outlined in Table 1.1.

Table 1.1.Overview of European initiatives launched to target climate neutrality in 2050

Initiative (Grant agreement)	Project timespan (budget)	Official project title	Main objective
Circular Cities and Regions Initiative [7] (Horizon)	6 years (€200M)	-	Support development of circular solutions across Europe
Hubs4Circularity [8] (01058416)[14]	Jun. 2022 – May 2026 (€2M)	Building a European Community of Practice of Hubs for Circularity	Facilitate the development of ecosystems across Europe
Hubs4Circularity [8] (101058656)[15]	Jun. 2022 – May 2026 (1.7M)	European Community of practice supporting Hubs for Circularity (H4C ECoP)	
Agro2Circular[10] (101036838)[16]	Oct. 2021 – Mar. 2025 (€ 17M)	Territorial circular systemic solution for the upcycling of residues from the agrifood sector	Post-industrial multilayer films recycling
Circular Foam[11] (101036854)[17]	Oct. 2021 – Sept. 2025 (€ 19M)	Systemic expansion of territorial circular ecosystems for end-of-life foam	Rigid polyurethane foam recycling
EcoeFISHent[12] (101036428)[18]	Sep. 2021 – Sep. 2026 (€19M)	Demonstrable and replicable cluster implementing systemic solutions through multilevel circular value chains for eco-efficient valorization of fishing and fish industries side-streams	Fishing industry side stream recycling
FRONTSH1P[13] (101037031)[19]	Nov. 2021 – Oct. 2025 (€ 19M)	FRONTrunner approach to a circular & resilient future: deployment of systemic solutions with the support of local clusters and the development of regional community-based innovation schemes	Plastic & rubber waste recycling or replacement for wood packaging

1.3. Project concept framework

Circular Foam is an European initiative comprising 26 industrial, research, and academic partners (Table 1.2)[20,21] with the goal to develop an economically and sustainably circular solution for the recycling of end-of-life rigid polyurethane refrigerator foam waste by producing a refrigerator unit based on 100% recycled insulation waste. The project was divided into eight work packages (Figure 1.2), each with its own specific deliverables to maximize output. (Table 1.3). Three strategically selected regions: **I**) North Rhine-Westphalia (Germany), **II**) Upper Silesia (Poland), and **III**) Greater Amsterdam (the Netherlands) were chosen based on their differences in industrial capacity, regional readiness for a circular transition, and the ability to generate region-specific recommendations to support a smooth circular transition elsewhere in Europe.[20–22]

A recent press release (1 October 2025)[23] stated that the Circular Foam project achieved a technically feasible closed-loop solution for the recovery of key components via the catalytic pyrolysis strategy described in this thesis. The recovered materials were successfully tested for reuse in refrigerators as an equivalent alternative to fossil fuels.

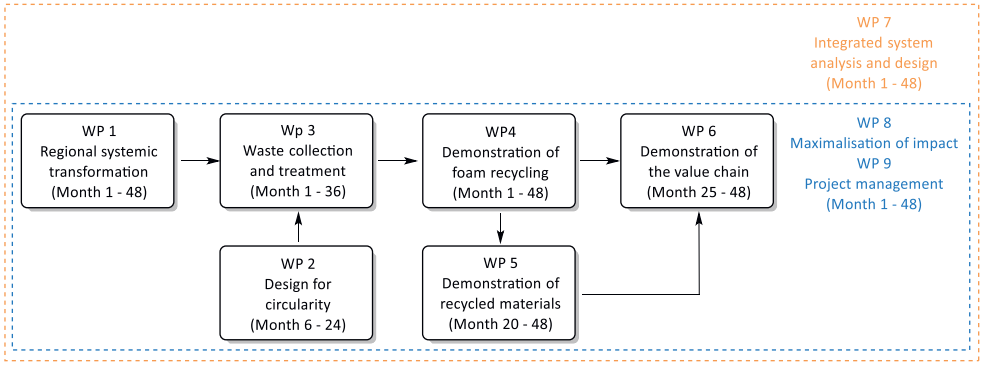

Figure 1.2. Work package hierarchy of the Circular Foam project. Based on: [24]

Table 1.2. Overview of all parties involved in the Circular Foam project [1]

Industrial partners	Abbreviation	Core business	Location
Alba	ALBA	municipal waste collection and treatment service	Poland
BioBTX	BioBTX	Renewable biobased aromatic company	Netherlands
Circularise	CIR	Provider of blockchain-based traceability	Netherlands
Covestro	COV	Polymer company	Germany
Electrolux	ELUX	appliance manufacturer	Italy
Kingspan Group	KING	Global supplier of high-performance insulation	Ireland
Interzero	INT	A waste and environmental services provider	Germany
IZNAB Sp	IZNAB	An engineering consultancy	Poland
REDWAVE	RED	A manufacturer of sensor-based sorting and recycling solutions	Austria
Sulzer	SUZ	A global leader in fluid engineering and chemical processing technologies.	Switzerland
Unilin Insulation	UNI	rigid PU insulation board manufacturer	Belgium

Academic partners		Core business	Location
University OF Amsterdam	HVA	Center of Expertise for Urban Technology	Netherlands
ETH Zurich	ETH	Energy and Process Systems Engineering	Switzerland
Ruhr-University Bochum	RUB	Environmental management, quantitative modeling, and qualitative socio-economic analysis	Germany
RWTH Aachen University	RWTH	CAT Catalytic Center & AVT Fluid Process Engineering	Germany
TU Dortmund	TUDO	Process Dynamics, Operations & Automation Systems	Germany
University of Groningen	RUG	Chemical Reaction Engineering Group	Netherlands
University of Wrocław	WUEB	Supply chain analysis, reverse logistics, risk assessment, and optimization	Poland

Research institutes	Abbreviation	Core business	Location
Centrum Wiskunde & Informatica	CWI	Quantitative modeling and data-driven methods	Netherlands
DECHEMA	DECHEMA	Process engineering and catalysis	Germany
Euro-Centrum Science and Technology Park	EUC	Stakeholder engagement, regional socio-economic research, and deployment frameworks	Poland
Forschungszentrum Jülich – IEK-STE	FZJ	Energy and Climate Research	Germany
Fraunhofer (IML)	FHG	material flow systems, reverse logistics, secondary resource supply chain design, and life cycle data provision	Germany
Fraunhofer (UMSICHT)	UNSICHT	Process engineering	Germany
Metropolis GZM	METR	socio-economic integration, stakeholder engagement, and municipal waste management planning	Poland
ZEDO e.V.	ZEDO	Integrated systems analysis and advisory system development	Germany

Table 1.3. Work package contribution overview

Work package (official title)	Contribution to the project
1 (Regional systemic transformation)	Established a hub for each region with digital traceability tools that include all relevant stakeholders in the polyurethane recycling chain and the recycling ecosystem
2 (Design for circularity)	Improved dismantling and thereby streamlined waste transport trough identification end-of-life polyurethane waste compositions. Transparency was improved by development of a digital waste traceability system
3 (Waste collection and treatment)	Improved the current waste collection, sorting, dismantling, and fine-sorting system by identification of bottlenecks in the polyurethane waste to product value chain via stakeholder interviews, workshops, legislation analysis
4 (Demonstration of foam recycling)	Developed a recycling pathway with according viability and environmental potential analysis and for end-of-life polyurethane waste. The chapters in this thesis contributed mainly to the catalytic pyrolysis approach described in this work package. More details on this work package are outlined in section 4.[1]
5 (Demonstration of recycled material usage)	Evaluated the quality of the recovered base chemicals of Work Package 4 by producing new polyurethane foam from the recycled material. The newly produced material compared to conventionally produced polyurethane foam
6 (Demonstration of the value chain)	Demonstrated the integration of the developed recycling process by combining data from all work packages into the current value chain with 50 refrigerators produced with recycled material as case study
7 (Integrated system analysis and design)	Analyzed an optimized the integration plan of work package 6 via techno-economic and life cycle assessment for incorporation into the current pMDI production chain to demonstrate the feasibility of the developed process
8 (Maximization of impact)	Maximized the project's impact through dissemination, stakeholder engagement, training, and policy recommendations, as evidenced by the number of stakeholders reached, publications, and uptake of project results
9 (Project management)	Covered the project management, coordinated all activities within the work packages, monitored milestones, and maintained compliance with EU reporting requirements, with clear timelines and deliverables to support project progress and alignment.

1.4. Anticipated impact of the CF initiative

Substantial economic and sustainability impacts were expected by demonstrating, for the first time, that high-performance rigid polyurethane waste can be chemically upcycled into virgin-equivalent polyols and isocyanates, thereby reducing dependence on fossil feedstocks and mitigating CO_2 emissions associated with incineration and primary production. By 2040, the approach could enable the recycling of approximately 600 kilotons of rigid polyurethane foam in Europe, avoiding 1.7 metric tons of CO_2 emissions per year. The project should strengthen European industrial competitiveness by creating regional industrial symbioses, fostering new markets for post-consumer polyurethane foams, and stimulating investment in advanced sorting and chemical recycling infrastructure, with significant job creation potential across the waste management, chemical production, and manufacturing sectors. Implementing regional Hubs4Circularity and a transferable governance blueprint enhances stakeholder coordination, enables regulatory alignment, and supports replication across heterogeneous European regions. Collectively, these outcomes contribute to decoupling economic growth from finite resource consumption, advance the objectives of the European Green Deal and the Circular Economy Action Plan, and position Europe as a technological leader in circular high-performance plastics systems.

1.5. Outline of this dissertation

Recycling plastic waste has become key to reducing reliance on fossil fuels and to mitigating CO_2 emissions, as reflected in the number of plastic circularity projects launched over the past 5 years. Most plastic producers have already taken steps to develop viable recycling pathways. Polyurethanes, however, are challenging to recycle, resulting in large volumes of end-of-life polyurethane at waste facilities. The Circular Foam project, as part of the European Green Deal, was launched to advance the circularity of rigid polyurethane foams. The research presented in this dissertation was conducted within work package 4 of the project and involved experimental and modeling studies at different scales for polyurethane recycling via catalytic pyrolysis to recover aniline. The main objectives for this work are: **I**) to develop a scalable process with a durable catalyst for the recovery of aniline from waste rigid polyurethane foams. **II**) To understand the reaction network of the catalytic rigid polyurethane conversion to aniline to aid catalyst research and serve as a basis for further process improvement.

Chapter 1 (prelude, this chapter) outlines the Circular Foam project and the role of the research described in this thesis in the project. In Chapter 2, the global plastic waste issue is outlined, and a literature survey of possible recycling solutions for polyurethanes is provided, including state-of-the-art work. It will be demonstrated that the development of aniline-focused chemical recycling pathways is in a state of infancy, highlighting the relevance of developing efficient processes for monomer recovery such as aniline. Chapter 3 describes a catalytic strategy for recovering aniline from end-of-life rigid polyurethane foam waste. Initial experimental work focused on batch milligram-scale catalyst screening employing post-production polyurethane foam as the feedstock. Key catalyst features were identified and quantified using a statistical model. The process's scalability was demonstrated using batch gram-scale, continuous gram-scale, and continuous kilogram-scale setups. The environmental impact was determined using a climate change impact analysis supported by a preliminary process design to assess the techno-economic viability. The stability of the best-performing catalyst (alumina-based SCCa 5/200) from the research outlined in Chapter 3 was evaluated in Chapter 4. Reversible and

irreversible catalyst deactivation pathways and associated changes in activity and chemoselectivity were investigated using various types of polyurethane foam at a batch gram scale. Catalytic pyrolysis of representative model compounds was conducted in Chapter 5 to elucidate the reaction network involved in catalytically converting rigid polyurethane foam into monomeric building blocks. Deuterated and carbon-13-labeled model compounds were synthesized and pyrolyzed in the presence of a catalyst to gain insights into the mechanisms of product and side-product formation. In Chapter 6, two commercial sets of amorphous silica-alumina-based catalysts (normal and high pore volume) containing both Brønsted and Lewis acidity were tested at batch milligram scale using post-production polyurethane foam. Structure-performance relationships were obtained by correlating product yields (specifically aniline and toluidine) with catalyst properties. Chapter 7 provides a brief overview of the achievements discussed in this dissertation and offers a perspective on future challenges for polyurethane recycling.

References

1. von der Leyen, U. The European green deal. (2019).
2. European Commission Directorate-General for Communication. The European Green Deal. https://commission.europa.eu/strategy-and-policy/priorities-2019-2024/european-green-deal_en.
3. European Parliament and the Council of the European Union. Directive (EU) 2025/1892 of the European Parliament and of the Council of 10 September 2025 Amending Directive 2008/98/EC on Waste. http://data.europa.eu/eli/dir/2009/ (2025).
4. European Parliament and the Council of the European Union. Regulation (EU) 2025/40 of the European Parliament and of the Council of 19 December 2024 on Packaging and Packaging Waste, Amending Regulation (EU) 2019/1020 and Directive (EU) 2019/904, and Repealing Directive 94/62/EC. http://data.europa.eu/eli/reg/2024/1781/oj (2025).
5. European Commission Directorate-General for Communication. Circular Cities and Regions Initiative – Supporting the implementation of circular economy across European cities and regions. https://circular-cities-and-regions.ec.europa.eu.
6. Hubs4Circularity Community of Practice. Hubs4Circularity - Accelerating the transition to industrial symbiosis and circular economy. https://www.h4c-community.eu.
7. ICONS Italy. The LOOP Cluster. https://circular-foam.eu/About+us/Related+Initiatives/_/FRONT1SHIP_Loop_Factsheet__20240404.pdf.
8. Agro2Circulair Consortium & Fuensanta, M. Agro2Circular - Territorial circular systemic solution for the upcycling of residues from the agri-food sector.
9. DECHEMA Gesellschaft für Chemische Technik und Biotechnologie e.V. CIRCULAR FOAM – Systemic expansion of territorial CIRCULAR Ecosystems for end-of-life FOAM. https://circular-foam.eu.
10. Finanziaria Ligure per lo Sviluppo Economico – FILSE S.p.A. EcoeFISHent. EcoeFISHent – Demonstrable and replicable cluster implementing systemic solutions through multilevel circular value chains for eco-efficient valorization of fishing and fish industries side streams. https://ecoefishent.eu.
11. European Association of Development Agencies (EURADA). FRONTSH1P: A FRONTrunner approach to Systemic circular, Holistic & Inclusive solutions for a new Paradigm of territorial circular economy. https://frontsh1p.eu.

12. European Commission (European Union). CORDIS – Community Research and Development Information Service, Publications Office of the European Union, Grant Agreement No. 101058416. https://cordis.europa.eu/project/id/101058416.
13. European Commission (European Union). CORDIS – Community Research and Development Information Service, Publications Office of the European Union, Grant Agreement No. 101058656. https://cordis.europa.eu/project/id/101058656/reporting.
14. European Commission (European Union). CORDIS – Community Research and Development Information Service, Publications Office of the European Union, Grant Agreement No. 101036838. Agro2Circular8 (101036838).
15. European Commission (European Union). CORDIS – Community Research and Development Information Service, Publications Office of the European Union, Grant Agreement No. 101036854. https://cordis.europa.eu/project/id/101036854/reporting.
16. European Commission (European Union). CORDIS – Community Research and Development Information Service, Publications Office of the European Union, Grant Agreement No. 101036428. https://cordis.europa.eu/project/id/101036428.
17. European Commission (European Union). CORDIS – Community Research and Development Information Service, Publications Office of the European Union, Grant Agreement No. 101037031. https://cordis.europa.eu/project/id/101037031.
18. DECHEMA Gesellschaft für Chemische Technik und Biotechnologie e.V. Deliverables; CIRCULAR FOAM Outcomes. https://circular-foam.eu/Outcomes/Deliverables.html.
19. DECHEMA Gesellschaft für Chemische Technik und Biotechnologie e.V. Partners; CIRCULAR FOAM About us. https://circular-foam.eu/About+us/Partners.html.
20. DECHEMA Gesellschaft für Chemische Technik und Biotechnologie e.V. Meet our regions; CIRCULAR FOAM project implementation. https://circular-foam.eu/Implementation/Meet+our+regions.html.
21. AIMPLAS – Plastics Technology Centre. URBANREC – New approaches for the valorisation of urban bulky waste into high added value recycled products. https://urbanrec-project.eu.
22. European Commission (European Union). CORDIS – Community Research and Development Information Service, Publications Office of the European Union, Grant Agreement No. 690103. https://cordis.europa.eu/project/id/690103/results.
23. Pittini Group. PolynSPIRE: Reusing plastics to produce steel. https://www.pittini.it/en/innovation/research-development/polynspire/.
24. European Commission (European Union). CORDIS – Community Research and Development Information Service, Publications Office of the European Union, Grant Agreement No. 820665. https://cordis.europa.eu/project/id/820665.
25. iCAREPLAST project consortium & Serra, J. M. iCAREPLAST: Integrated Catalytic Recycling of Plastic Residues Into Added-Value Chemicals. https://www.icareplast.eu/index.html.
26. European Commission (European Union). CORDIS – Community Research and Development Information Service, Publications Office of the European Union, Grant Agreement No. 820770. https://cordis.europa.eu/project/id/820770/de.
27. PUReSmart project consortium & Haelterman, B. PolyUrethane Recycling towards a Smart Circular Economy (PUReSmart). https://www.puresmart.eu/contact/.

28. European Commission (European Union). CORDIS – Community Research and Development Information Service, Publications Office of the European Union, Grant Agreement No. 814543. https://cordis.europa.eu/project/id/814543.

29. European Commission (European Union). CORDIS – Community Research and Development Information Service, Publications Office of the European Union, Grant Agreement No. 101057971. https://cordis.europa.eu/project/id/101057971.

30. DECHEMA Gesellschaft für Chemische Technik und Biotechnologie e.V. Work packages; CIRCULAR FOAM project implementation. https://circular-foam.eu/Implementation/Work+Packages.html.

31 Bart Pals. Covestro en Fraunhofer bouwen pilotinstallatie voor pyrolyse-recycling van PUR-schuim. https://www.industrielinqs.nl/chemie/2026/03/covestro-en-fraunhofer-bouwen-pilotinstallatie-voor-pyrolyse-recycling-van-pur-schuim/?gdpr=accept&gdpr=accept (2026).



2



The current state of Polyurethane waste management, recycling efforts, and research motivation

2.1. Annual plastic production

Plastics have become deeply integrated in modern society, with widespread applications across healthcare (17%)[1], automotive (8%)[2], packaging (44%)[3], and construction (18%)[4], among other sectors. This integration is driven by advances in polymer science and engineering that have enabled the development of a diverse range of materials with tailored mechanical, thermal, and chemical properties. Most synthetic plastics are derived from cracking fossil fuels into naphtha, followed by conversion into monoaromatics (benzene, toluene, and xylene) and light olefins (ethylene, propylene, etc.), which serve as building blocks for nearly all chemical products, including polymers. The monoaromatics and olefins listed above can be used in subsequent multistep synthesis to yield suitable starting materials for plastic manufacturing. A 2024 analysis on global plastic production[5] (Figure 2.1) provides quantitative data on a broad range of polymers, including polypropylene (PP), polyethylene (PE) variants (LD, LLD, MD, HD), polystyrene (PS), polyvinyl chloride (PVC), polyethylene terephthalate (PET), polyurethanes (PUR), other fossil-derived thermoplastics and thermosets as well as recycled polymers, and bio-based plastics sourced from renewable feedstocks such as starch or cellulose. In 2024, global plastic production reached 430.9 million metric tons, with Europe accounting for 12% of the total. The high demand for plastics has also created a major issue: plastic waste, with associated environmental and health issues.[6,7] Furthermore, while interest in developing more sustainable plastics has increased, only 10.1% of current production is based on circular processes, with the majority of recycled material being mechanically downcycled. These disparities highlight the pressing need for scalable, economically viable recycling technologies to transition toward a more sustainable plastics economy.

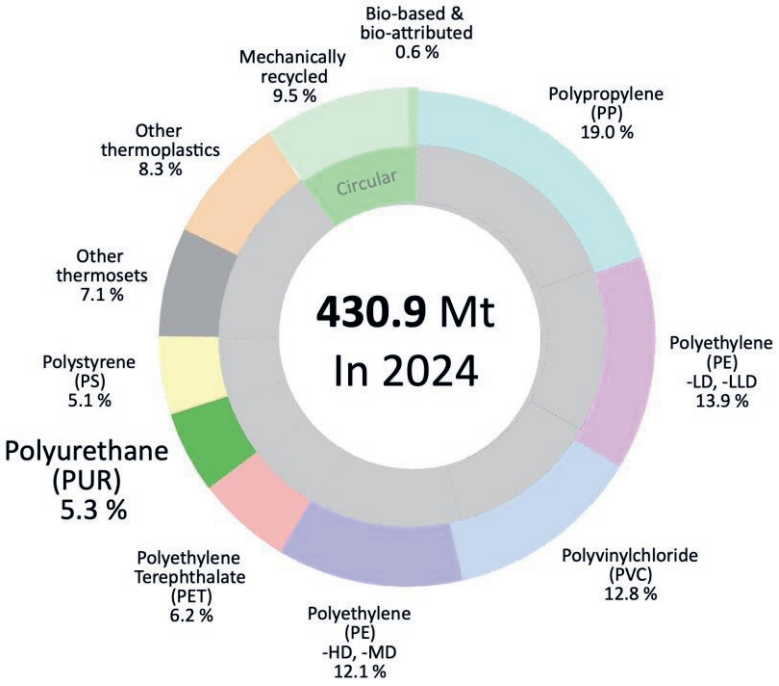

Figure 2.1. Distribution of the global plastics production by type. Adapted from: [5]

2.2. European legislation on waste management

As of June 2019, the European Union has issued a directive to reduce the environmental impact of certain plastic products through market restrictions and reduced consumption, contributing to the prevention of additional waste formation, as shown in Figure 2.2 (purple block).[8] Additionally, a zero-waste program was launched to reduce landfill (red block) to 35% by restricting the landfilling of recyclable waste.[9] A European Environment Agency landfill analysis showed that a select group of member states, including the Netherlands, already reached a target of <1% landfilling in 2023.[10]

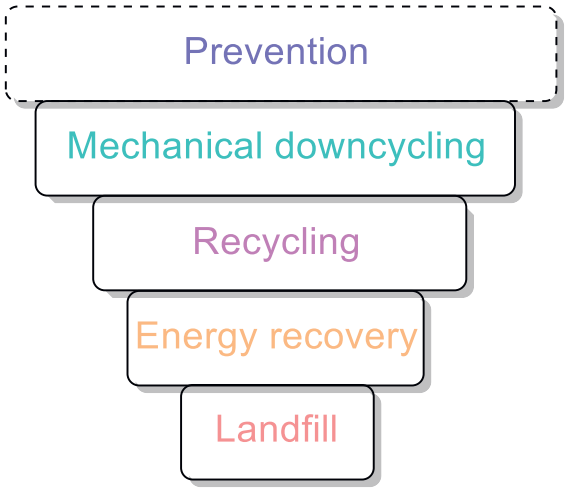

Figure 2.2. Waste management hierarchy. The dashed block has a non-waste status, and the non-dashed blocks have a waste status. Adapted from[8]

The remaining waste treatment options considered in the hierarchy are mechanical downcycling (blue block), recycling (pink block), and energy recovery (orange block). An important distinction made here is between downcycling and recycling.

Downcycling is considered the reprocessing of waste material to obtain a lower quality product that can be used for an application other than the original one. An advantage of this approach is that it is cost, energy, and resource efficient as the reintegration loop into new products is short. However, the resulting product is always lower quality than the original. For this reason, it cannot be used as a recycling option to produce the same quality original product again.

For recycling, waste needs to be treated using any technology that allows the recovered compounds to be used in the original product (closed loop) or other (higher value) products (open loop). A technology can only be considered closed-loop recycling if the recovered compounds are used to produce the original product with chemical and physical properties equal to those of the fossil-derived product. An overview of relevant technology examples, including their advantages and disadvantages, is presented in Table 2.1.[11–13] The remaining waste stream that is not suitable for mechanical downcycling or recycling, should be incinerated for energy recovery, thereby eliminating landfill as a waste management option.

The International Organization for Standardization (ISO) published guidelines to assist plastic industry stakeholders in the development of sustainable plastic solutions. Thereby promoting the recycling of plastic waste.[18] The waste management outcome (mechanical downcycling, recycling, incineration, and landfill) for each stream is determined by the plastic type, composition, and grade, which are directly correlated with contamination levels and the available recycling routes for that specific grade.

Table 2.1. Overview of currently investigated waste management methods, adapted from[11–13]

Waste management	Advantage	Disadvantage
Depolymerization	High recovery yield	Requires chemical reagents
Thermal Pyrolysis	Low quality mix waste as feedstock possible	The feedstock's quality controls process efficiency
Catalytic pyrolysis	Product selectivity	Efficient catalyst required
Gasification	Allows oxygen in feed	Energy intensive
Incineration	Energy recovery	CO_2 emissions

2.3. Plastic waste treatment options

For plastic recycling, two main waste streams can be distinguished: pre- and post-consumer waste. Pre-consumer waste is post-production[14] or closed-loop process waste[15] generated by a product's manufacturing process that does not end up in a consumer product (e.g., the excess of foam that is cut off when producing a car seat).[16] Post-consumer waste is end-of-life (EOL) contaminated material generated by consumers and must be sorted by quality before management (e.g., components of a discarded refrigerator).[17] It should be noted that post-production waste is typically easier to process because it is less contaminated and less complex than post-consumer waste

Plastic waste undergoes several key processing steps (collection, sorting, cleaning, size reduction, and separation) before its fate is determined.[19] Globally, five primary and cost-effective collection methods are commonly employed with variations in each country: (**I**) curbside collection via designated household bins, (**II**) vehicular collection of waste contained in trash bags, (**III**) drop-off recycling at centralized stations equipped with dedicated bins for source-separated plastics, (**IV**) buy-back centers that exchange plastic waste for goods or services, and (**V**) deposit refund systems, where plastic items are returned at collection points in exchange for monetary compensation or credits.[20] Collected plastics from these systems are subsequently transported to centralized facilities for further sorting and processing.

Most post-consumer collected plastic waste contains a complex mixture of contaminated and non-contaminated plastics with various non-plastic materials, such as food waste, paper, glass, and metals. Feed separation is automated in the EU[21] but still in most countries performed manually by operators, who extract bulky items such as plastic films and cardboard. Smaller materials, e.g., stones and glass, are subsequently removed using vibrating screens or rotary drums. The remaining stream, predominantly composed of plastic materials is classified as medium-sized plastic waste.[22] Advanced sorting technologies are employed to achieve efficient separation into homogeneous fractions to allow efficient downstream processing. Techniques adopted nowadays enable high-throughput, selective identification of polymers based on their molecular structure or elemental composition, thereby enhancing the efficiency and purity of subsequent recycling processes. Technologies of interest are:

laser-induced breakdown spectroscopy (LIBS)[23], triboelectric separation[24], X-ray fluorescence (XRF)[25], Fourier-transform infrared spectroscopy (FT-IR), froth flotation[26], magnetic density separation (MDS)[27], and hyperspectral imaging (HSI).[28] It should be noted that a large quantity still remains unsorted due to separation challenges and is discarded to incineration or landfill. An exact quantification of this stream is difficult to estimate, as it is typically discarded with other streams and treated as a single incineration or landfill stream in waste statistics.

The sorted homogeneous pre- and post-consumer waste suitable for downstream processing is rated for quality. Waste without significant loss of chemical and physical properties is reused into new products. An example is a transport crate that has been used but can be washed and used again without any treatment. The other fraction is graded according to available recycling pathways. Waste that is of poor quality for reuse but too high quality for recycling is mechanically downcycled through shredding or by melting the plastic and re-extruding it. An example of mechanically downcycled material is waste car tires that are shredded and extruded into lower quality rubber tiles.[14,17] The remaining fraction is assessed on its technical and economic viability. If the quality is high enough and there is a recycling technology available, it will be recycled. Otherwise, it will be disposed of in landfills or incinerated.

Current efforts to minimize incineration and landfill have shown promising results. Mechanical downcycling is a popular choice for polyethylene and polypropylene.[29,30] Advances in recycling have shown the possibility of blending recycled polyethylene terephthalate (rPET) with fossil-based PET.[31] A complete circular economy via depolymerization has been shown to be viable for polystyrene.[32] The two remaining major streams yet to be recycled due to processing limitations are polyvinyl chloride (PVC) and polyurethane (PUR).

Limitations of PVC include the formation of highly corrosive hydrochloric acid upon heating due to the presence of chlorine. The challenge with PUR is different. As it is a thermoset, PUR degrades upon heating instead of melting. Consequently, incineration and landfilling remain the primary waste management options for both streams.[33] These two example streams show that it is not possible to develop a single universal recycling method capable of processing all polymers. Instead, each type of plastic requires specific depolymerization pathways to be developed for efficient recycling. For this reason, the aim of this dissertation is to investigate a recycling technology for PUR as a challenging polymeric material to recycle.

2.4. Polyurethane recycling

Since their development in 1937, polyurethanes have progressively replaced traditional materials such as PVC, rubber, and PS due to the expansion of available feedstocks and the resulting tunability of their chemical structure, formulations, and properties.[34] Its unique molecular architecture is tailored using specific polyol and polyisocyanate starting materials, yielding linear, branched, or crosslinked structures that can exhibit a broad spectrum of mechanical and physicochemical properties.[35,36] Furthermore, performance enhancement has been introduced via the addition of biuret ($HN(CONH_2)_2$), allophanate ($H_2NCNHCO_2H$), or carbodiimide (HN=C=NH) functional groups.[37] Owing to its synthetic versatility and cost-effectiveness, polyurethanes have become integral to a wide range of industrial and consumer applications, including thermal insulation, surface coatings, lightweight

composites, and automotive components,[38] making it the sixth-most widely produced class of polymers globally, accounting for 5.3% of annual plastic production.[39]

The need for a circular economy has made the development of economically attractive recycling pathways urgent. Polyurethanes are a promising waste feedstock for circular technology, as they are abundantly available and are collected separately (e.g., refrigerators).[40] In the ideal case, recovering both the polyol and the isocyanate segments can reduce climate change impacts by 5.6 kg CO_2-eq per PUR kg treated when compared to incineration.[41]

2.5. Current PUR waste management

As polyurethane is a thermoset, it decomposes upon heating rather than melting, making reprocessing via re-extrusion impossible. The alternative option is mechanical shredding which requires a clean stream. For this reason, only 25% is mechanically downcycled via shredding.[39] The lack of suitable alternative recycling methods for polyurethanes has led to the largest stream (75%) currently being disposed of via incineration (35%) contributing to CO_2 emissions[42] and landfilling (40%).[43] The presence of trapped, volatile foaming agents and oxygen pockets within the polyurethane structure can cause spontaneous combustion, releasing toxic gases, including carbon monoxide, hydrogen cyanide, and ammonia, upon thermal degradation of waste polyurethane.[44] The severe harm of polyurethane smoke on health has been demonstrated by Moores *et al.*[45] Their research showed that the formation of radical isocyanates upon combustion of flexible foam resulted in rapid breakdown of macrophages (white blood cells of the immune system) in the lungs of mice after 30 minutes of exposure, demonstrating the damaging effects of polyurethane smoke and thus the need to prevent combustion. Despite the significant risks posed by fires and toxic fumes, landfill remains the predominant option for recycling polyurethane globally.[42]

2.6. Physical and chemical features of polyurethane foams

Polyurethanes are di-block polymers that are synthesized via the polyaddition of an isocyanate- (-NH(CO)O-) and an alcohol (-OH) based monomer. The monomer ratio as well as the choice of precursors are key determinants of the final material properties. The two main material types are flexible and rigid polyurethanes, which are directly correlated to their physical and chemical characteristics. Although both groups (flexible and rigid) are classified as polyurethanes, each requires a tailored waste management strategy because their molecular structures differ. Figure 2.3 shows a visual representation of both the physical appearances and the chemical structures. Differences in bonding interactions increase the interchain spacing between the two foams. Weak bonding interactions, as found in flexible foam, result in an open-cell structure with a sponge-like appearance. Strong bonding interactions lead to a closed-packing cell, producing a brittle appearance.[46,47]

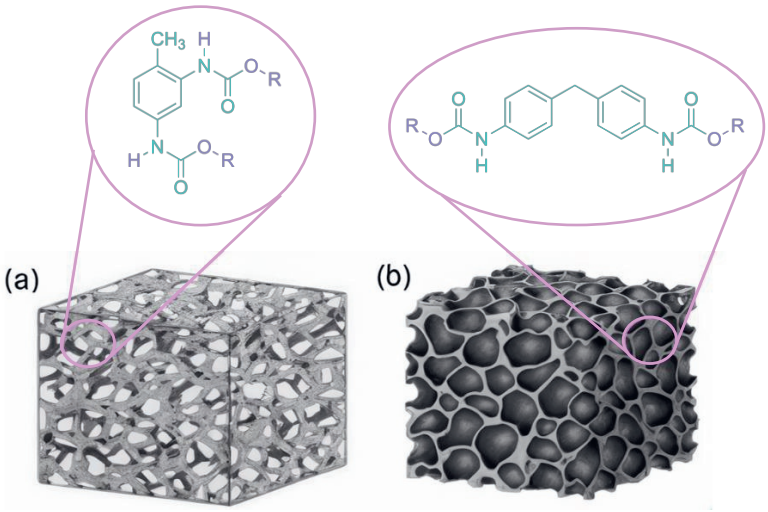

Figure 2.3. Open shell (a) and closed shell (b) polyurethane configurations. Open-shell is obtained from TDI-based, flexible polyurethane, and closed-shell from MDI-based, rigid polyurethane foam. The isocyanate (hard) segment is shown in blue, and the polyol (soft) segment in purple. Images adapted from[48]

Flexible polyurethanes are highly useful in shock-absorbent products such as mattresses or car seats. This type of foam is obtained by using toluene diisocyanate (TDI) as the isocyanate precursor during synthesis. The presence of a single aromatic ring provides an elastomer-like behavior, characterized by a low Young's modulus and high elongation at break, resulting in an easily bendable material that goes back into its original form after applying pressure.[49]

Rigid polyurethanes are used in insulation applications, including refrigerators, floors, and roofing. Rigid polyurethane foams are produced by using methylene diphenyl diisocyanate (MDI) as the isocyanate precursor. The presence of the extra aromatic ring in rigid PUR increases π-π interactions as well as π-stacking between monomers, giving rigid PUR a thermoset-like mechanical profile, with a high Young's modulus and lower elongation at break, consistent with a brittle behavior that does not go back into its original shape after applying force.[50]

Additive incorporation is a well-known approach in the polymer industry for enhancing the aesthetics or imparting specific properties to polymeric materials. In polyurethane formulations, key additives include blowing agents, crosslinkers, fillers, and whiteners. The latter two are relatively straightforward in application, owing to their long-standing and well-characterized roles. Fillers are conventionally added to improve the mechanical performance of the polymer matrix, such as tensile strength and stiffness, while reducing production costs via volume expansion. Typical examples of fillers include calcium carbonate and silica. Whiteners and pigments are typically used to modulate the visual appearance of polymers. Common pigmentary additives are titanium dioxide, iron oxide, and carbon black. These pigments are widely used for their high tinting strength, opacity, and ultraviolet (UV) stability, which collectively enable precise control over the final polymeric material's visual characteristics.[51]

Blowing agents are low-vapor-pressure compounds that evaporate rapidly during foaming, driven by the exothermic reaction between the isocyanate and polyol components. The transition from the liquid to the gas phase in the polyurethane mixture generates gas bubbles that expand the polyurethane, increasing its volume and lowering its thermal conductivity, thereby improving its insulating performance.[52]

The type of blowing agent is a critical parameter for closed-cell structures, as rigid polyurethane foams (closed-cell) require a thermal conductivity of 0.0085 - 0.012 W/m·K to achieve efficient insulation. Trapping the gas from a blowing agent in the pockets reduces thermal conductivity, thereby increasing the polyurethane's insulation properties. Historically, chlorofluorocarbons were employed as blowing agents. Environmental challenges and regulatory restrictions have led to a shift toward more sustainable alternatives. Air and CO_2 have been considered green alternatives. However, the higher thermal conductivities of air (0.026 W/m·K) and CO_2 (0.016 W/m·K) prevent these compounds from being used as effective insulating materials.[53] More recently, hydrocarbons such as cyclopentane have been a popular choice as blowing agents as they combine improved environmental profiles with adequate foaming efficiency and insulating performance.[54]

The presence of various additives together with the PUR formulation determines the recycling strategy, as no PUR type decomposes in a similar pathway. In the next section, brief overview of synthesis strategies in TDI- and MDI-based PUR is provided to provide an in-depth view of the molecular structures and clarify why the development of a universal method to recycle PUR remains challenging.

2.7. Polyurethane foam synthesis

Flexible polyurethane (Figure 2.4*a*) is produced via the nitration of toluene (**1**) followed by a reduction of the nitro functional groups to form toluene diamine (**2** TDA). Addition of phosgene in the presence of hydrochloric acid produces the isocyanate adduct (**3** TDI). Finally, the introduction of a polyol to TDI results in formation of flexible polyurethane foam (**4**).[55]

The production of rigid polyurethane foam (Figure 2.4*b*) involves reacting aniline (**5**) with formaldehyde in the presence of hydrochloric acid to form methylenedianiline (**6** MDA). Treatment of MDA with phosgene in the presence of hydrochloric acid produces methylenediphenyl diisocyanate (**7** MDI). Finally, the addition of a polyol to MDI produces rigid polyurethane foam (**8**).[56]

The synthetic pathways outlined in Figure 2.4*a,b* represent the first developed strategies for preparing flexible and rigid polyurethane foams, respectively. However, PUR formulations have evolved over the years in response to the demand for specific chemical and physical characteristics in products. This has led to variations in the isocyanate and polyol precursors used to synthesize flexible and rigid polyurethane foams. This variability has led to substantial year-to-year differences in polyurethane production and, consequently, differences in polymer composition across formulations. The need for higher crosslinked PUR led to the formation of structurally more complex polyurethane networks, as illustrated in Figure 2.4*c*. A typical synthetic method starts with the formation of a polymeric methylene dianiline (**9** pMDA) distribution through the reaction of formaldehyde with aniline (**5**) in the presence of hydrochloric acid. Treatment of pMDA (**9**) with phosgene produces a polymeric

methylene diphenyl diisocyanate (**10** pMDI) distribution. Finally, the addition of a polyol mixture to the pMDI distribution produces a more complex rigid polyurethane foam (**11**).[56]

2.8. Advances in Polyurethane recycling efforts

As can be seen in Figure 2.4, closed-loop recycling of flexible and rigid polyurethane foams can be achieved by recovering both the isocyanate segment (TDI, MDI, pMDI) and the polyol segment. For flexible polyurethane foams, closed-loop recycling has shown promising results[55,57,58] as both TDI and polyol have been recovered via various approaches such as glycolysis.[62] For rigid polyurethane foams, polyol recovery has been well established through various approaches.[59–65] Examples of rigid MDI-based polyurethane recycling pathways are shown in Table 2.2, with each limitation marked in red.

Recovering the isocyanate segment has proven challenging as reflected by the limited available literature. In 2025, for the first time, 87% pure pMDA was recovered from end-of-life refrigerator foam via ammonolysis.[59] However, highly pure pMDA (>99%) is required to achieve equal chemical and physical properties to those of fossil-based PUR. Additionally, the demand for specific characteristics in PUR-based products requires specific pMDA formulations. This highlights the difficulties and strict limitations in recycling pMDI-based PUR.

An alternative approach is to go a step further back by recovering base chemical aniline. From here, specific pMDA formulations with high purities can be produced to meet industry standards. Formation of aniline from waste PUR has been shown to be viable via thermal degradation processes such as pyrolysis.[64,66]

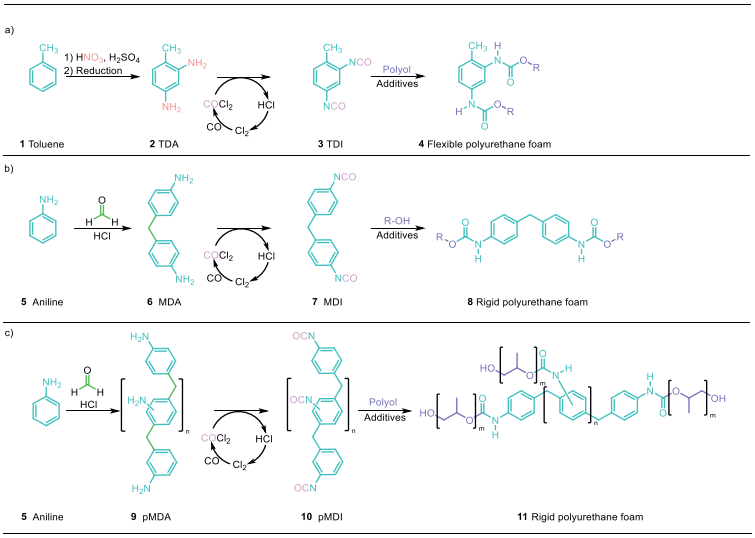

Figure 2.4. Synthesis of various polyurethane foams focusing on variations in the isocyanate fragment. Flexible polyurethane foam from toluene (a), rigid polyurethane foam from aniline (b), and rigid polyurethane foam from aniline via polymeric intermediates (c).[56] Please note that the for rigid foams typically polymeric MDA (pMDA) and polyol chemicals used as shown in c, which are oligomer mixtures isocyanide and polyol to increase the overall crosslinking

Table 2.2. Reported methods for recycling of rigid polyurethane foams, the main disadvantages are highlighted in red

Method	Rigid PUR Feed	Chemical input	Reaction conditions	Scale	Output	Limitations
Hydrolysis[60]	Waste[d]	NaOH, EtOH:H_2O[h]	80 °C, 2 h	20 mL	Polyol, isocyanate	Lab scale
Acidolysis[61]	Model[e]	Succinic acid, N_2	205 °C, 5 h	1 kg	Polyol	Long reaction time
Glycolysis[62]	Waste[d]	DEG, NaAc[a]	225 °C, 20 min	600 g	Polyol	Low conversion (40%)
Alcoholysis[63]	Waste[f]	MOF, EtOH	195 °C, 4h	50 g	Polyol	Expensive MOF required
Ammonolysis[59]	Model[e]	NH_3	150 °C, 2h	60 mL	Polyol, pMDA	Only partial depolymerization (pMDA)
Pyrolysis[64]	Model[e]	γ-Al_2O_3	550 °C,	1 g	Aniline	(unusable) solid, gas products (50%)
Gasification[66]	Waste[g]	CaO	1100 °C	2 g	Synthesis gas	Extreme conditions/ high energy input
Hydrogenolysis[65]	Waste[f]	Mn-4[c], KO^{t}Bu, H_2	60 bar, 200 °C, 65 h	1 g	MDA	Use of hydrogen gas at high pressure requires extensive safety measurements

[a]Diethylene glycol and sodium acetate
[b]Metal organic framework as catalyst
[c]Pincer complex as catalyst
[d]Post-production waste
[e]Synthesized foam
[f]Waste refrigerator foam
[g]Unspecified waste rigid polyurethane foam
[h]Ratio's used (EtOH:H_2O): 8:2, 6:4, 4:6, 2:8, and 0:10

2.9. Thermal degradation pathways for polyurethanes

The pyrolysis and gasification methods introduced as thermal degradation options in Table 2.2 offer approaches for base chemical recovery from rigid polyurethane foams, from which in principle, new foam can be produced. Thermal degradation is a broad term that includes many types (Table 2.3). It is important to clearly differentiate between pyrolysis (including torrefaction, carbonization, intermediate pyrolysis, and fast pyrolysis) and gasification. Both techniques produce gas, liquid, and solids, but the reaction conditions differ greatly. During pyrolysis, polyurethane is thermally decomposed into oil, char, and gas in an inert atmosphere at elevated temperatures between 400 and 700 °C, with the liquid product usually as the main target.[67] The liquid phase is typically a combination of oil and water. In addition to external water release upon heating, dehydration reactions produce water. Gaining insights into water formation is an important aspect as specific catalysts are susceptible to degradation upon interaction with water (e.g zeolites). The absence of oxygen with these technologies prevents the feed from combusting. Instead, the feedstock is cracked into smaller segments via catalytic and radical reactions. In gasification, polyurethane is decomposed further into syngas as the target gaseous product by carefully controlling the oxygen-to-carrier gas ratio.[68]

As shown in Table 2.3, the reaction conditions determine the gas, liquid, and solid ratios, which are tuned via reactor design and catalyst choice (*vide infra*).[69] Lower temperatures with a long residence time (torrefaction) favor char formation, high temperatures with a short residence time (fast pyrolysis) favor liquid formation, and very high temperatures with a short residence time (gasification) predominantly yield highly volatile products. Examples of possible reactor designs are shown in the table for illustration purposes. Please note that each technology is currently operating at industry scale. However, the specific scales corresponding to the shown yields have not been published. For this reason, it is not added to the table.

Most PUR foam is typically synthesized from a pMDA and polyol mixture. Recovered pMDA requires high purity (>99%), providing a significant challenge for effective recovery. As such, recovering starting material aniline via (catalytic) pyrolysis can be of great interest, as this allows for a short route towards the synthesis of pMDA with equal properties. Fast pyrolysis is here the technology of choice over other (slower) thermal degradations as it typically yields the largest liquid fraction (75% for biomass that also contains a high amount of heteroatoms next to hydrocarbon constituents).

Table 2.3. Product distribution based on pyrolysis reaction conditions data obtained from: [68,70]

Technique	Timescale	Temperature (°C)	Heating rate (°C s^{-1})	Example reactor design	Solid (%)	Liquid/H_2O (%)	Gas (%)
Torrefaction	Slow 10 – 60 min	200 - 300	0.2 - 0.8	Rotary drum	80	0/ND	20
Carbonization	Slow Hours – days	300 - 500	0.1 - 1	Rotary kiln	35	30	35
Pyrolysis	Intermediate 10 – 30 s	500 – 700	0.4 - 10	Fixed bed	25	50/50	25
Pyrolysis	Fast Seconds	400 - 600	10 – 200	Fluidized bed	12	75/25	13
Gasification	Fast Seconds	750 - 900	1000	Gasifier	10	5/ND	85

2.10. Catalytic pyrolysis of polyurethane

From the data in Table 2.3, it became clear that the pyrolysis heating rate (slow, intermediate, fast) dictates the liquid (oil and water), and gas yields. However, the amounts of aniline with non-catalytic pyrolysis are low.[71] For this reason, introducing a catalyst into thermal pyrolysis may increase aniline yields by lowering the activation barrier and thereby promoting new bond-breaking/recombination events such as hydrogenation, deoxygenation, aromatization, ketonization, aldol condensation, hydrotreating, and reforming. However, it further complicates the pyrolysis process.[72,73]

Although many types of catalysis are employed in chemical synthesis (e.g. homogeneous transition metal-ligand complexes, or enzymes), catalysts used in pyrolysis are exclusively heterogeneous due to the need for thermal stability. Additionally, using a heterogeneous catalyst for pyrolysis offers advantages such as robustness under harsh conditions, ease of product separation, and scalability for large-scale applications. A brief introduction to heterogeneous catalytic pyrolysis, with a focus on rigid polyurethane foams, is provided below, highlighting key considerations for successful results. Moreover, the section includes a highly condensed state-of-the-art summary of non-catalytic and catalytic pyrolysis of rigid polyurethanes, with a more in-depth overview in Chapter 3.

Four key considerations for catalytic pyrolysis are: **I**) reactor type, **II**) operational mode, **III**) catalyst properties, and **IV**) catalyst deactivation. These four considerations form the foundation of the research presented in this thesis and are discussed in detail below.

2.11. Reactor types

Since pyrolysis gained prominence in 1970, significant attention has been devoted to reactor design. Currently, there are over 100 different pyrolysis reactor types, each customized for specific feeds and products.[68,70,74–76] However, no reactor is universal. The most common reactor types reported in literature for the decomposition of polyurethanes are provided in Figure 2.5, with advantages and disadvantages shown in Table 2.4.

Fixed-, and fluidized bed reactors (**a** – **e)** have been used in literature to recycle rigid polyurethane foams. Ablative and rotating cone designs (**f** and **g**) have not yet been used for PUR recycling but are popular choices in the fast pyrolysis regime.[89] Ablative pyrolysis has been shown to be a suitable technique for kilogram-scale operations with large-particle-size biomass, producing predominantly liquid (60%).[90,91] Rotating cone reactors have been used in tandem reactions, in which high gas fractions were obtained in the first step, followed by aromatization in the second step to recycle polyethylene and polypropylene.[92]

Typical preliminary screening work on the pyrolysis of rigid polyurethane is conducted at milligram scale on a two-staged tandem microreactor (pyroprobe, **a** and TMR, **b**)[77–79] or a tubular furnace (**c**).[80–82] These reactors are used primarily in literature for product identification rather than quantification. However, yields can be obtained from these setups with appropriate calibration. For example, Font *et al*. reported 0.6% aniline formation from synthesized model PUR compounds with non-catalytic pyrolysis using a pyroprobe at 600 °C.[83]

Suitable upscaling work is conducted at gram and kilogram scale using batch fixed bed (**d**)[84–86], and continuous fluidized (**e**) reactors.[87,88] The highest reported aniline yield (19%) was obtained on a batch fixed bed setup at 1.0 g scale using an alumina-based catalyst at 500 °C.[64]

Table 2.4. Brief overview of fast pyrolysis reactor designs with their respective advantages and disadvantages. Data obtained from:[70,74,76,89,91,93–95]

Reactor type [scale]	Advantage	Disadvantage
Small scale fixed bed[a] [miligram]	Fast reaction screening	Idealizing physical limitations
Large scale fixed bed [gram/kilogram]	Simplistic design	Slow heating rates
Fluidized [gram/kilogram]	Accurate temp. control	2 mm largest particle feed
Ablative [gram/kilogram]	Large particle size feed	High maintenance (moving objects)
Rotating cone [gram/kilogram]	No carrier gas needed	Scale up issues (complex design)

[a]Including: pyroprobe, tandem micro reactor, tubular furnace, and larger scale

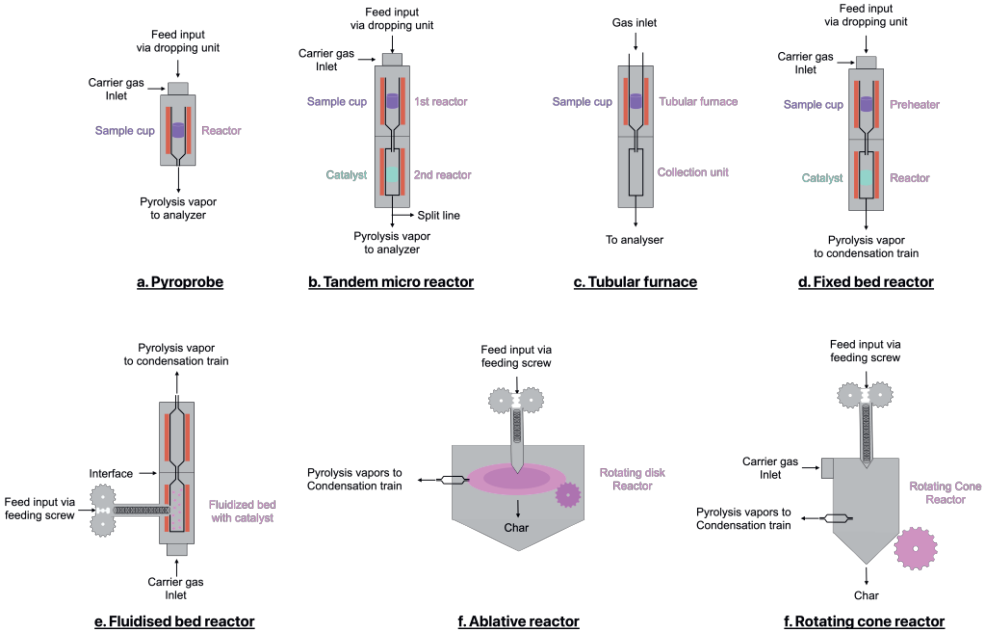

Figure 2.5. Common reactor designs used in polyurethane pyrolysis. Pyroprobe (a), small fixed bed, tandem micro reactor (b), Tubular furnace (c), Large fixed bed reactor (d), Fluidized bed reactor (e), Ablative reactor (f), Rotating cone reactor (g). Images inspired by[70,89,94,95]

2.12. Operational modes (in- and ex-situ)

Depending on the desired contact pattern, catalytic pyrolysis can be performed in two ways: in-situ or ex-situ.[96] In an in-situ configuration, the catalyst is mixed with the feedstock, leading to solid-solid, liquid-solid, and/or gas-solid interactions. Operating in in-situ mode with metal chlorides (manganese, cobalt, and iron) in a thermogravimetric analyzer resulted in lower initial degradation temperatures (from 225 to 200 °C) compared to thermal pyrolysis for a model MDI-based PUR, as reported by Moroi *et al*.[97] A disadvantage of this operation is that impurities in the feedstock accumulate on the catalyst, potentially leading to deactivation (see section 3.4 for details on catalyst deactivation). With an ex-situ configuration, thermal pyrolysis and catalytic pyrolysis are performed in separate units. Thermal cracking of the feedstock into smaller fragments occurs in the first reactor, followed by the vapor-phase containing small feedstock fragments flowing through a catalytic bed in the second reactor. Here, the contact is a gas-solid interaction.[98–100] Compared to non-catalytic pyrolysis, ex-situ pyrolysis of post-production MDI-based PUR in an activated carbon fixed bed at 550 °C showed a decrease in high-viscosity compounds in the condensates, according to Takamoto *et al*.[101] The advantage of this operation is that contaminants do not accumulate on the catalyst. However, non-catalytic cracking is required in the first reactor to allow small gas fractions to enter the second reactor.

An alternative ex-situ operation includes catalytic cracking in the first reactor, which is preferably loaded with a cheap sacrificial catalyst that adsorbs potential feedstock impurities, followed by catalytic upgrading of the small fragments in the gas phase that flow through a catalytic bed in the second reactor. An advantage of this configuration is that the upgrading catalyst in the second bed receives only “clean” gas fragments, making it less prone to deactivation, contributing positively to the techno-economics. This configuration also allows both reactors to operate under different conditions (temperature, gas mixtures, separation steps, etc.).

The limited available literature on optimal operational modes for catalytic pyrolysis demonstrates that substantial understanding of these modes remains to be discovered. From a theoretical perspective, addition of a catalyst lowers the activation energy which should lower the operational temperature to achieve cracking, thereby contributing to economic viability. For this reason, all milligram scale work throughout the chapters were performed via in-situ mode. Furthermore, continuous operation at scale showed that it was more successful using a combined in- and ex-situ operational configuration. Ideal case scenario operations of in-situ and in-situ + ex-situ are shown in Figure 2.6. Details on this matter can be found in Chapter 3.

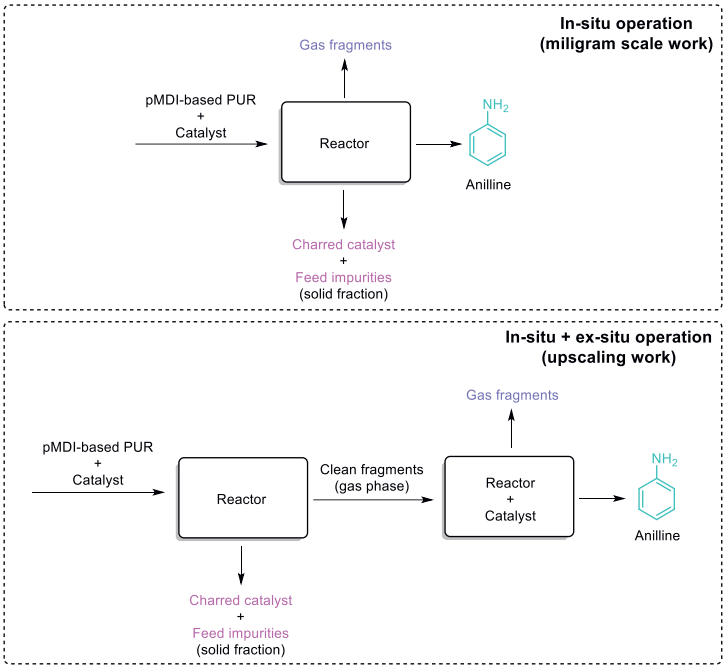

Figure 2.6. Representative Illustration of catalytic pyrolysis strategies for PUR in this thesis at milligram scale (top), and catalytic pyrolysis at upscaling setups (bottom)

2.13. Catalyst types

Adding a heterogeneous catalyst to thermal pyrolysis is a highly complex process that requires careful tuning of specific parameters that depend on the nature of the stream. For rigid polyurethanes, 2 important parameters that are inherently correlated are: **I**) Catalyst surface interactions and **II**) interaction strengths between the catalyst and the feed. Catalyst surface interactions with the feed are typically influenced by tuning pore size, pore width, pore volume, and surface area. The interaction strengths include substrate binding, reaction, and desorption interactions, which can be tuned by adjusting the catalyst's acidity.

Solid acid catalysts contain solely Lewis acid sites (e.g. alumina oxides) or both Brønsted and Lewis acid sites (e.g zeolites) based on their configuration. Stronger acid sites yield higher binding energies, whereas weaker acid sites yield lower binding energies.[102] An example of an intermediate-bond-strength reaction is the chemisorption of an amine on alumina. Alumina (Al^{3+}) has an electron-deficient shell, giving it a Lewis acid character. The amine's nitrogen lone pairs coordinate to alumina in order to allow catalytic pathways to occur.[103,104]

Alumina-based catalysts have been shown to be highly effective in pyrolysis processes in industry[112,113] and also specifically in the depolymerization of rigid polyurethanes.[64] For this reason, zeolites, alumina oxides, and amorphous silica aluminas were selected as catalysts of interest. Each type is discussed in detail below to clarify why these catalysts were selected for this work.

Zeolites

Zeolites are porous, highly crystalline materials composed of silicon and aluminum that excel at cracking and shaping reactions and also serve as adsorbents due to their crystalline structure. [114–118] The well-defined rigid 3D structure consists of tetrahedral microstructural channels described by their ring size (e.g., 8- 14 rings) that interconnect cavities with dimensions approaching those of molecules (2–20 Å). The acid sites that catalyze hydrocarbon conversion reactions process only molecules that fit inside. This results in the pore size and shape adding selectivity to the reaction. For this reason, zeolites are often shown in shape examples in Figure 2.7.

An on-topic example of using a zeolite in the depolymerization of MDI-based rigid polyurethane foam via catalytic pyrolysis has been demonstrated by Bozi *et al.*[119] The group reported non-quantified data showing a wide range of N-containing aromatic compounds upon using zeolite HY at 500 °C. However, limited amounts of aniline and toluidine were observed as Zeolites typically contain high amounts of Brønsted acidity. This result demonstrates the large effect of acid types on the pyrolysis process.

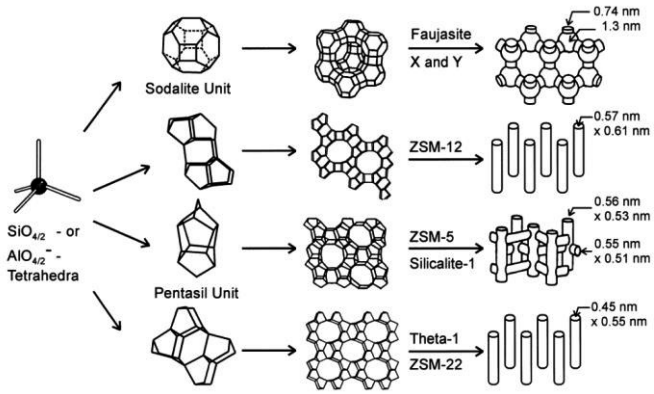

Figure 2.7. Structures of four selected zeolites (from top to bottom: faujasite or zeolites X, Y; zeolite ZSM-12; zeolite ZSM-5 or silicalite-1; zeolite Theta-1 or ZSM-22) and their microscopic pore systems and dimensions. Image copied from:[116]

Zeolites have Brønsted acid sites in addition to the existing aluminum Lewis acid sites. Substitution of a tetra-valent silica (Si^{4+}) for a tri-valent aluminum (Al^{3+}), generates a negative charge in the silica matrix that is compensated by a proton, giving rise to a bridging Si-OH-Al species. The proton-donating ability renders this active site a highly acidic Brønsted acid site. (Figure 2.8). The Brønsted acid strength is mainly dictated by the silica-to-alumina ratio. At high aluminum loading (e.g., Si/Al 5/95), the OH bond energy is higher compared to lower aluminum loading (e.g., Si/Al 80/20). The higher bond energy arises from an excess of effective negative charge, resulting in a weaker acid site. At lower aluminum loading, the proton interaction energy and intrinsic acidity of the proton are constant. When a proton-catalyzed reaction is carried out at a high Si loading (e.g., Si/Al 80/20), the rate, when normalized on the proton content, will therefore be constant. However, at high Al loading (e.g., Si/Al 5/95), aluminum atoms occupy tetrahedral sites with silicon (Si^{4+}), thereby decreasing the intrinsic acidity per proton. This phenomenon is reflected in total acidity; a volcano-shaped optimum in acidity would be observed as the silica-to-alumina ratio changes.[120]

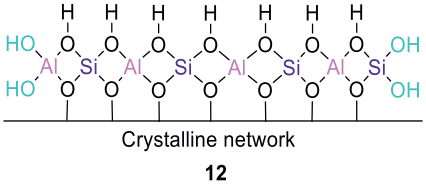

Figure 2.8. Typical Al-OH-Si crystalline framework found in zeolites

Aluminum oxides

Alumina oxides are aluminum-based solid-acid catalysts widely used in industry. Popular reactions include oxidation, dehydration, and hydrocracking.[121–123] Alumina oxide has been reported as a catalyst for the depolymerization of rigid polyurethane foam by Eiden *et al.*[64] The group showed the formation of aniline, toluidine, and MDA by using alumina oxide as a catalyst at 550 °C. An extended investigation on tuning alumina oxide based catalyst to obtain higher aniline yields is described in Chapter 3.

The main type of acidity in this catalyst is Lewis acidity. The acid site forms via a 4-fold (Al_{IV}) Al-O-Al framework, with the aluminum atoms acting as Lewis acid sites as highlighted in pink in Figure 2.9, **13**. The balanced charge distribution between aluminum and oxygen atoms causes no protons to be bound to the oxygen atom, and for this reason, no bridging hydroxyl-based Brønsted acid sites are present in aluminum oxides. The endcap consists of a terminal Al-OH group (highlighted in blue), which accounts for weak Brønsted acid sites that are typically not observed by suitable analyses such as ammonia desorption or pyridine infrared analysis. The presence of only weaker Lewis acid sites results in alumina oxides having a mildly acidic character.

The Lewis acid structural morphology has been identified by solid-state ^{27}Al NMR as a 4-, 5-, or 6-fold-coordinated species (Figure 2.9 **13 – 15**, respectively).[124] Typical framework aluminum is characterized by a 4-oxygen-bound species. Non-framework (NF-Al) alumina is a cationic and neutral cluster forming within catalyst pores at high calcination temperatures (300 – 800 °C). [125–127] These species have been identified as 5-fold penta-covalent (Al_V), 6-fold octahedral Al_{VI}, and Al_xOH_y species. The structural features of alumina, including specific surface area, phase composition, pore size, total acidity, and acid site density, dictate its activity and reactivity.[128] Additionally, the simplicity and mesoporosity of this catalyst make it an ideal support for metal loading, enabling changes in selectivity and acidity.

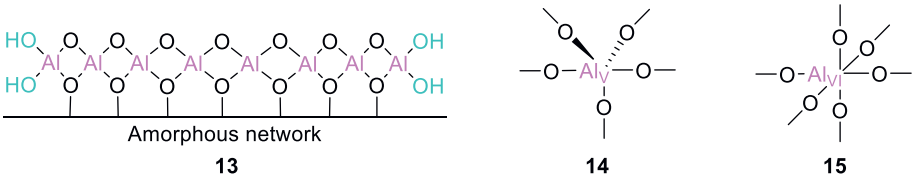

Figure 2.9. Various alumina species that are found in an alumina oxide based Lewis acid framework: 4-fold framework Al_{IV}-O-Al_{IV} (**13**), Penta coordinated non-framework 5-fold aluminum Al_V (**14**), Octahedral non-framework 6- fold aluminum Al_{VI} (**15**)

Amorphous silica alumina's

Amorphous silica-alumina (ASA) catalysts are between alumina oxides and zeolites. The presence of both Brønsted and Lewis acidity originates from silicon and aluminum atoms in the catalyst framework. The amorphous nature yields a mesoporous network rather than a well-defined microporous network, as in zeolites. As a result, flexible bonding around bridging hydroxyl groups in ASAs creates a broader range of acid sites with varying strengths, resulting in lower overall acidity compared to zeolites.[129,130] The reasons outlined here lead to reactions such as hydrocracking, hydrotreating, dehydrogenation, isomerization, and alkylation, rather than aromatization.[131] Research on tuning the Brønsted to Lewis ratio with ASA catalyst to obtain the highest aniline yield with the catalytic pyrolysis of PUR is described in Chapter 6.

The structural flexibility of ASA has sparked extensive debate in the scientific community.[125,132–134] It is widely accepted that Lewis acid sites (LAS) in ASAs occur in three forms: a weak tetrahedral framework (Al_{IV}), a strong non-framework 5-fold species (Al_V), and a strong non-framework 6-fold octahedral species (Al_{VI}).[126,135,136] The amorphous structure of ASAs likely facilitates a shift from octahedral to tetrahedral coordination through partial hydrolysis by water. The incorporation of octahedral alumina into silica matrices lacks experimental confirmation, so it is presumed that all incorporated alumina are 4-fold tetrahedral (Al_{IV}) species.[126] Non-framework aluminum atoms (NF-Al) originate via dihydroxylation, steaming, and dealumination. The NF-Al_V species alters active-site strength by coordinating to the hydroxyl group, thereby changing the charge distribution and influencing the electronegativity of the oxygen atom.[137] [132,138]

Variations in the presence and interactions between alumina species have recently been debated. Examples are: an Al_{IV} species distorted by NF-Al Figure 2.10 **16**)[139], a pseudo bridging hydrogen-bonded silanol (Figure 2.10 **17**)[140]**,** pseudo bridging coordinated silanol (Figure 2.10 **18**)[141], and a silanol bound to three aluminum atoms of which two Al_{VI} and one Al_v (Figure 2.10 Figure 2.10 **19**).[130,140] It should be noted that these structures are not possible in zeolites due to their crystallinity, demonstrating the complexity and possibly the milder acidity of ASAs.

For Brønsted acid sites (BAS), weak BAS mainly consist of terminal and geminal silanols (Figure 2.10 **20 – 22**)[142], associated with high silica zones.[130] Al_{IV}, Al_V, and Al_{VI} can also coordinate with weak silanol groups, enhancing Brønsted acidity (Figure 2.10 **23**).[143,144] Strong BAS formation is thought to occur via a similar pathway as zeolites, resulting in the structure shown in Figure 2.10 **12**)[142,145,146] However, evidence for such species is inconclusive.[130,147–149] A dynamic "drawbridge" process has been proposed instead.[148] Weak BAS silanols can coordinate with NF-Al during adsorption, forming pseudo-bridging hydroxyl groups that act as strong BAS (Figure 2.10 **24**).[142] Excess NF-Al promotes more coordination and bridging, increasing Brønsted acidity.[143] In contrast, in zeolites, excess NF-Al tends to reduce acidity by altering electronegativity at Si-O-Al bridges.[133,150] Therefore, high levels of silanol and NF-Al benefit ASAs, whereas low levels are preferable in zeolites to maintain stable bridging hydroxyls. These properties are controlled during synthesis: homogeneous, high-silanol matrices are produced by regulating pH and temperature. Inhomogeneous, low-silanol matrices are created through co-gelation, grafting, co-precipitation, or hydrolysis.[143]

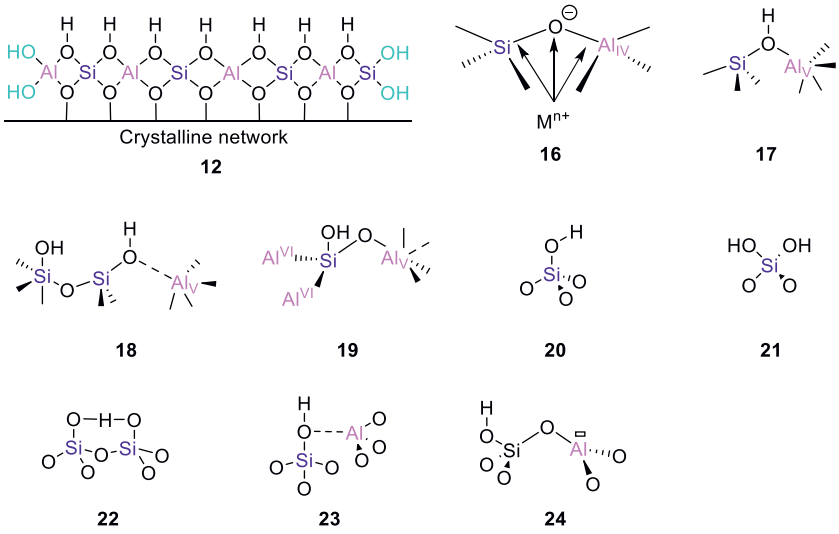

Figure 2.10. Various ASA frameworks that are reported in literature: Typical Al-OH-Si crystalline framework found in zeolites (**12**), distorted Al_{IV} species (**16**), Al_V pseudo bridging hydrogen bonded silanol (**17**), Al_V pseudo bridging silanol (**18**), tri-coordinated silanol (**19**), terminal silanol (**20**), geminal silanol (**21**), vicinal silanol (**22**), enhanced silanol group (**23**), and pseudo bridging ("drawbridge") hydroxyl group (**24**)

The catalysts described above highlight the complexity of incorporating a catalyst into the already intricate pyrolysis process. Successful catalyst implementation requires a good understanding of the thermal degradation pathways as well as the catalyst's role in the process. A detailed mechanistic investigation on the thermal degradation of PUR via catalytic pyrolysis using deuterium and ^{13}C labelled model compounds is outlined in Chapter 5.

2.14. Catalyst deactivation

Insights into catalyst deactivation are essential to assess the techno-economic viability of a catalytic pyrolysis process. In this respect, the turnover number (TON) is a key indicator and is used as input for such analyses. Catalyst stability is critical in this context and must be assessed to gain insight into the viability of the developed process. However, limited work has been devoted on catalyst stability regarding recycling of rigid polyurethanes as reflected by the absence of published work on this matter. Therefore, this section provides general considerations on catalyst deactivation on catalytic pyrolysis processes. An extensive investigation of the catalytic stability of an alumina-based catalyst used for the catalytic pyrolysis of PUR to yield aniline is presented in Chapter 4.

Catalyst deactivation occurs through physical, chemical, or mechanical phenomena. A simplified schematic overview of possible deactivation pathways is given in Figure 2.11. Four main deactivation pathways can be distinguished, each with its own subdivision: **I**) coking (pink), **II**) thermal degradation (purple), **III**) poisoning (green), and **IV**) catalyst deformation (blue). [151] All phenomena may contribute to the catalytic recycling of PU to aniline, especially given the complex feed, which includes a wide range of additives.

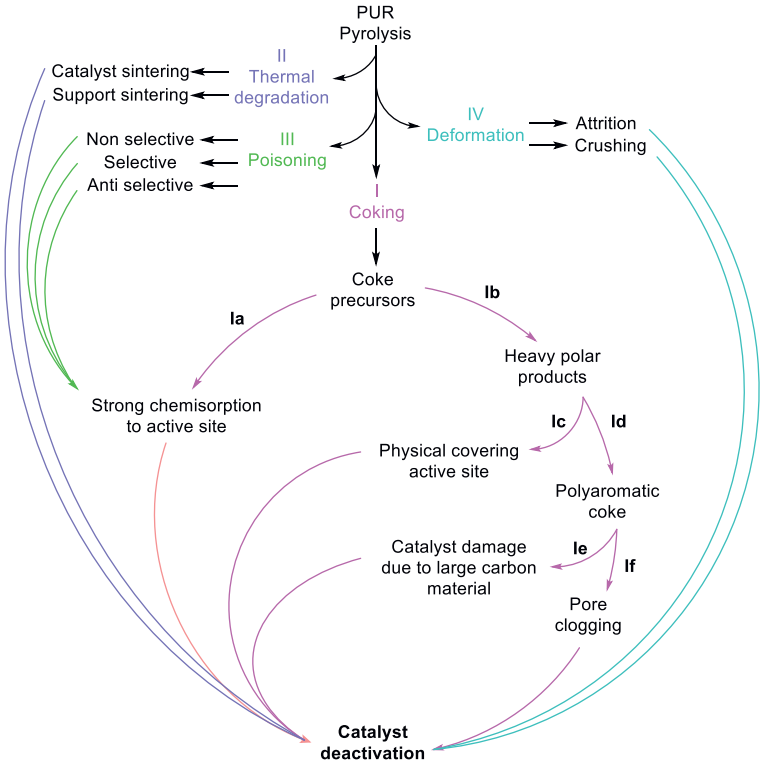

Figure 2.11. Possible Catalyst deactivation pathways through catalytic pyrolysis. Irreversible binding of coke precursors to the active site (**Ia**), precursor condensation into heavy polar products (**Ib**), physical covering of the catalyst active site by heavy polar coke (**Ic**), cyclization of heavy polar products into polyaromatic coke (**Id**), physical damage to the morphology of the catalyst due to large coke fragments (**Ie**), and catalyst deactivation due to pore clogging by polyaromatic coke (**If**)

Coking is a term that is used to indicate the deposition and stacking of unwanted carbonaceous material on the catalyst. In short, hydrocarbons undergo rapid dehydration to form stable carbon-rich compounds that are difficult to remove. The formation of these stable carbon compounds proceeds through three main steps. First, cracking of the feed results in Short-chain, carbon heavy, carbon-heavy alkenes and dienes (soft coke) that can proceed via 2 routes: **Ia,** irreversible binding of coke precursors to the active sites (metal, metal oxides, acidic, basic sites), leading to deactivation, or **Ib,** rapid condensation of coke precursors into heavy polar products. The formed heavy products proceed via 2 pathways: **Ic** encapsulation of the active sites, which causes reduction of the activity, or **Id** formation of large stable (poly)aromatics (hard coke) via cyclization. These large polyaromatics are less reactive due to their bulkiness and lack of polarization. The bulkiness causes irreversible physical damage to the catalyst's morphology (**Ie**) or traps it in the catalyst's pores, blocking the active sites (**If**). At high temperatures, longer stacking of these polyaromatic chains ultimately forms graphite, a highly crystalline, inert carbon sheet that is difficult to remove from the catalyst.[152] Depending on the type of coke (soft, hard, graphite, or soot), the catalyst can be regenerated by thermal reactivation through combustion or by chemical reactivation methods.[153,154]

Thermal degradation of a catalyst refers to changes in its structure caused by process temperature. Agglomeration of small metal crystallites into larger ones is called sintering. Sintering decreases activity by reducing the surface-to-volume ratio. It can occur in both supported and unsupported catalysts, as both types can contain metals. Various mechanisms drive crystallite agglomeration, making it difficult to identify which mechanism is at work at any given time. The type and rate of sintering depend on many factors, including temperature, atmosphere, metal type, metal dispersion, support type, presence of promoters, contaminants, surface area, morphology, and porosity. The three main pathways are: **I**) migration of small crystallites, which occurs with weak metal-support interactions and poor dispersion; **II**) migration of metal atoms from catalyst crystallites to support crystallites, typically observed in highly dispersed catalysts; and **III**) at temperatures over 500 °C, redispersion occurs, reversing crystallite growth. This process takes place in the presence of oxygen or chlorine and involves the formation of volatile metal oxides or chlorides, which decompose into smaller crystallites upon reduction.[155]

Poisoning is the loss of catalytic activity due to strong chemisorption of impurities on the active sites of the catalyst. These contaminants originate from additives or residual materials used in the disassembly process to separate the end-of-life feed and are identified as metal contaminants or well-known poisons such as sulfur, chlorine, and others. The type of poison varies with the catalyst and reaction. For example, the active species in zeolites are acidic sites. Neutralization of acidity by basic molecular impurities results in catalyst degradation, whereas the active sites in transition metals are the metal itself. Adding basic molecules does not deactivate the metal site, so such molecules are not considered poisons for transition metals. Some poisons are considered general poisons because they deactivate nearly all catalysts. Examples include alkali metals, sulfur, chlorine, phosphorus, and iron. The effectiveness of a poison is measured by the correlation between the poison's concentration and catalytic activity. Poison efficiency can be categorized into three regions: selective, nonselective, and anti-selective. If the catalyst is deactivated at low poison concentrations, it binds selectively to the most active sites. If moderate deactivation occurs, the poison initially binds to less active sites. If the activity loss is proportional to the amount of poison absorbed, it is considered an anti-selective poison.[156]

Structural changes due to mechanical issues are often overlooked in catalyst deactivation. The key mechanical parameters are the bed type (fluidized or packed), flow rate, and loading. In a packed bed, particle crushing can occur when a heavy reactor load combines with high flow. Unlike in a fluidized bed, where a circulating catalytic bed causes constant collisions that lead to particle breakage (attrition). Adjusting the flow and loading in a fluidized bed reduces attrition.[157]

2.15. Key developments in (catalytic) thermal degradation of rigid polyurethane foams

The chapters in this dissertation each contain extensive reviews of the relevant state of the art specific to their respective topics. The section below presents key findings from the literature that motivated further investigations described in the following four chapters.

An initial literature study on rigid polyurethane recycling revealed predominantly studies on the recovery of the polyol segment rather than the isocyanate.[158] Recent work on isocyanate valorization has shown successful pMDA recovery with 87% purity via ammonolysis at a 300 g h^{-1} scale.[59] Literature focusing on aniline formation reported 0.9% aniline at scale (1.6 kg) via non-catalytic pyrolysis.[71] Very

recently, Covestro obtained 19 wt% aniline from MDI-based PUR in a 25 mL fixed bed reactor using catalytic pyrolysis.[64] This result formed the basis for the investigation of this strategy as a PUR recycling concept as studied in this thesis. A detailed overview of state-of-the-art work on recovery of aniline via (non)-catalytic pyrolysis is outlined in Chapter 3, showing how immature this field is and how revolutionary the aniline recovery via thermocatalytic conversion is. As a consequence of the novel approach, no complementary studies on catalyst stability have been reported yet. For this reason, an investigation into catalyst deactivation is described in Chapter 4.

A literature study on mechanistic insights into the thermal degradation pathway of rigid polyurethane foams crystallized into two main degradation pathways: **I**) Non-catalytic thermal degradation starts with volatilization of small molecules (H_2O, blowing agents), followed by formation of isocyanate- and polyol segments in a chain scission fashion. The polyol fragment decomposes into aliphatic alcohols, ethers, alkanes, and alkenes, and the isocyanate segment into primary amines and CO_2[159], and **II**) Catalytic thermal degradation using a Zeolite showed MDA formation via β-H transfer which releases polyol fragments (CO_2, alkenes). In the second step, aniline and toluidine form via fragmentation and hydrogen atom donation. However, the origin of the hydrogen atoms were not explained.[119] This observation led us to start an in-depth investigation on the thermal degradation pathway of PUR using deuterium and ^{13}C synthesized model compounds. A comprehensive overview of (non)-catalytic thermal degradation of rigid polyurethane foam is presented in Chapter 5.

The results in Chapter 3 showed the highest aniline yields using an alumina-oxide based catalyst. For this reason, alumina oxide-based catalysts, zeolites, clays, and ASA's catalyst were considered as catalyst types of interest for our catalyst tuning study. Literature showed minimal amount of aniline formation with using zeolites and clays.[119,159,160] For this reason, ASA's were investigated to a further extent as these type of catalyst are mildly acidic thereby possibly promoting aniline formation. An extensive state-of-the-art overview of zeolites, clays, and ASA's is described in Chapter 6.

Based on the literature review, 2 main questions arose, which are addressed in this dissertation. **I**) What is the best catalyst to obtain the highest aniline yield with catalytic pyrolysis of rigid polyurethane foams and how stable is it? **II**) How does the catalytic thermal degradation pathway of rigid polyurethane foam proceed?

References

1. Rizan, C., Mortimer, F., Stancliffe, R. & Bhutta, M. F. Plastics in healthcare: time for a re-evaluation. *J. R. Soc. Med.* **113**, 49–53 (2020).
2. Katarína Szeteiová, I. *Automotive Materials Plastics in Automotive Markets Today*. *Machine technologies and materials* (2010).
3. Sundqvist-Andberg, H. & Åkerman, M. Sustainability governance and contested plastic food packaging – An integrative review. *J. Clean. Prod.* **306**, (2021).
4. Limantara, A. D. *et al.* Comparative Study of Bio-Asphalt, Coconut Shell Distillation TAR, and Plastic Road in Terms of Construction, Economical, and Regulatory Aspects. in *Journal of Physics: Conference Series* vol. 1364 (Institute of Physics Publishing, 2019).
5. Plastics Europe AISBL. *Plastics the Facts 2025*. (2025).
6. Padervand, M., Lichtfouse, E., Robert, D. & Wang, C. Removal of microplastics from the environment. A review. *Environ. Chem. Lett.* **18**, 807–828 (2020).

7. Andrady, A. L. The plastic in microplastics: A review. *Mar. Pollut. Bull.* **119**, 12–22 (2017).
8. Directive 2008/98/EC of the European Parliament and of the Council of 19 November 2008 on waste and repealing certain Directives (Text with EEA relevance). https://eur-lex.europa.eu/eli/dir/2008/98/oj/eng.
9. Deselnicu, D. C., Militaru, G., Deselnicu, V., Săinescu, G. & Albu, L. Towards a circular economy– a zero waste programme for europe. *ICAMS Proceedings of the International Conference on Advanced Materials and Systems* 563–568 (2018) doi:10.24264/icams-2018.XI.4.
10. European Environment Agency. Diversion of Waste from Landfill in Europe. https://www.eea.europa.eu/en/analysis/indicators/diversion-of-waste-from-landfill?activeAccordion=ecdb3bcf-bbe9-4978-b5cf-0b136399d9f8 (2025).
11. Pandey, P., Dhiman, M., Kansal, A. & Subudhi, S. P. Plastic waste management for sustainable environment: techniques and approaches. *Waste Dispos. Sustain. Energy* **5**, 205–222 (2023).
12. Maris, J. *et al.* Mechanical recycling: Compatibilization of mixed thermoplastic wastes. *Polym. Degrad. Stab.* **147**, 245–266 (2018).
13. Clark, R. A. & Shaver, M. P. Depolymerization within a Circular Plastics System. *Chem. Rev.* **124**, 2617–2650 (2024).
14. Al-Salem, S. M., Lettieri, P. & Baeyens, J. Recycling and recovery routes of plastic solid waste (PSW): A review. *Waste Management* **29**, 2625–2643 (2009).
15. Sadat-Shojai, M. & Bakhshandeh, G. R. Recycling of PVC wastes. *Polym. Degrad. Stab.* **96**, 404–415 (2011).
16. Kumar, S., Panda, A. K. & Singh, R. K. A review on tertiary recycling of high-density polyethylene to fuel. *Resour. Conserv. Recycl.* **55**, 893–910 (2011).
17. Singh, N. *et al.* Recycling of plastic solid waste: A state of art review and future applications. *Compos. B Eng.* **115**, 409–422 (2017).
18. ISO 15270:2008 Plastics Guidelines for the recovery and recycling of plastics waste. https://www.iso.org/standard/45089.html.
19. Hopewell, J., Dvorak, R. & Kosior, E. Plastics recycling: Challenges and opportunities. *Philosophical Transactions of the Royal Society B: Biological Sciences* **364**, 2115–2126 (2009).
20. Balwada, J., Samaiya, S. & Mishra, R. P. Packaging Plastic Waste Management for a Circular Economy and Identifying a better Waste Collection System using Analytical Hierarchy Process (AHP). in *Procedia CIRP* vol. 98 270–275 (Elsevier B.V., 2021).
21. Wilts, H., Garcia, B. R., Garlito, R. G., Gómez, L. S. & Prieto, E. G. Artificial intelligence in the sorting of municipalwaste as an enabler of the circular economy. *Resources* **10**, 28 (2021).
22. Serranti, S. & Bonifazi, G. Techniques for separation of plastic wastes. in *Use of Recycled Plastics in Eco-efficient Concrete* 9–37 (Elsevier, 2018). doi:10.1016/B978-0-08-102676-2.00002-5.
23. Anabitarte, F., Cobo, A. & Lopez-Higuera, J. M. Laser-Induced Breakdown Spectroscopy: Fundamentals, Applications, and Challenges. *ISRN Spectroscopy* **2012**, 1–12 (2012).
24. Tilmatine, A., Medles, K., Bendimerad, S. E., Boukholda, F. & Dascalescu, L. Electrostatic separators of particles: Application to plastic/metal, metal/metal and plastic/plastic mixtures. *Waste Management* **29**, 228–232 (2009).

25. Bezati, F., Froelich, D., Massardier, V. & Maris, E. Addition of X-ray fluorescent tracers into polymers, new technology for automatic sorting of plastics: Proposal for selecting some relevant tracers. *Resour. Conserv. Recycl.* **55**, 1214–1221 (2011).
26. Carvalho, T., Durão, F. & Ferreira, C. Separation of packaging plastics by froth flotation in a continuous pilot plant. *Waste Management* **30**, 2209–2215 (2010).
27. Maio, F. Di, Rem, P., Hu, B., Serranti, S. & Bonifazi, G. The W2Plastics Project: Exploring the Limits of Polymer Separation. *The Open Waste Management Journal* **3**, 90–98 (2010).
28. Henriksen, M. L., Karlsen, C. B., Klarskov, P. & Hinge, M. Plastic classification via in-line hyperspectral camera analysis and unsupervised machine learning. *Vib. Spectrosc.* **118**, (2022).
29. Xanthos, M. Recycling of the #5 polymer. *Science (1979).* **337**, 700–702 (2012).
30. Ma, Y., Jiang, X., Xiang, X., Qu, P. & Zhu, M. Recent developments in recycling of post-consumer polyethylene waste. *Green Chemistry* **27**, 4040–4093 (2025).
31. Suhaimi, N. A. S., Muhamad, F., Abd Razak, N. A. & Zeimaran, E. Recycling of polyethylene terephthalate wastes: A review of technologies, routes, and applications. *Polym. Eng. Sci.* **62**, 2355–2375 (2022).
32. Kim, J. S., Lee, W. Y., Lee, S. B., Kim, S. B. & Choi, M. J. Degradation of polystyrene waste over base promoted Fe catalysts. *Catal. Today* **87**, 59–68 (2003).
33. Ait-Touchente, Z., Khellaf, M., Raffin, G., Lebaz, N. & Elaissari, A. Recent advances in polyvinyl chloride (PVC) recycling. *Polym. Adv. Technol.* **35**, (2024).
34. Akindoyo, J. O. *et al.* Polyurethane types, synthesis and applications-a review. *RSC Adv.* **6**, 114453–114482 (2016).
35. Chattopadhyay, D. K. & Raju, K. V. S. N. Structural engineering of polyurethane coatings for high performance applications. *Progress in Polymer Science (Oxford)* **32**, 352–418 (2007).
36. Narayan, R. *et al.* Synthesis and characterization of crosslinked polyurethane dispersions based on hydroxylated polyesters. *J. Appl. Polym. Sci.* **99**, 368–380 (2006).
37. Zia, K. M., Bhatti, H. N. & Ahmad Bhatti, I. Methods for polyurethane and polyurethane composites, recycling and recovery: A review. *React. Funct. Polym.* **67**, 675–692 (2007).
38. Król, P. Synthesis methods, chemical structures and phase structures of linear polyurethanes. Properties and applications of linear polyurethanes in polyurethane elastomers, copolymers and ionomers. *Prog. Mater. Sci.* **52**, 915–1015 (2007).
39. Ragaert, K., Delva, L. & Van Geem, K. Mechanical and chemical recycling of solid plastic waste. *Waste Management* **69**, 24–58 (2017).
40. Banik, J., Chakraborty, D., Rizwan, M., Shaik, A. H. & Chandan, M. R. Review on disposal, recycling and management of waste polyurethane foams: A way ahead. *Waste Management and Research* **41**, 1063–1080 (2023).
41. Pillich, M., Schilling, J., Bosetti, L. & Bardow, A. What to do with polyurethane waste? The environmental potential of chemically recycling polyurethane rigid foam. *Green Chemistry* **26**, 10893–10906 (2024).
42. Datta, J., Kopczyńska, P., Simón, D. & Rodríguez, J. F. Thermo-Chemical Decomposition Study of Polyurethane Elastomer Through Glycerolysis Route with Using Crude and Refined Glycerine as a Transesterification Agent. *J. Polym. Environ.* **26**, 166–174 (2018).
43. Kemona, A. & Piotrowska, M. Polyurethane recycling and disposal: Methods and prospects. *Polymers (Basel).* **12**, (2020).

44. BOTT B, FIRTH JG & JONES TA. Evolution of toxic gases from heated plastics. *Brit Polymer J* **1**, 203–204 (1969).
45. Moores, H. K., Janigan, D. T. & Hajela, R. P. Lung Injury after Experiniental Smoke Inhalation: Particle-Associated Changes in Alveolar Macrophages*. *Toxicol. Pathol.* **21**, 521–527 (1993).
46. Sáenz-Pérez, M. *et al.* Methylene diphenyl diisocyanate (MDI) and toluene diisocyanate (TDI) based polyurethanes: Thermal, shape-memory and mechanical behavior. *RSC Adv.* **6**, 69094–69102 (2016).
47. Sook, C., Sungla, P. & Schneider, N. S. Infrared Studies of Hydrogen Bonding in Toluene Diisocyanate Based Polyurethanes. *Macromolecules* **8**, 68–73 (1975).
48. Chen, Y., Wang, N., Ola, O., Xia, Y. & Zhu, Y. Porous ceramics: Light in weight but heavy in energy and environment technologies. *Materials Science and Engineering R: Reports* **143**, (2021).
49. Krupers, M. J., Bartelink, C. F., Gr, H. J. M. & M611er, M. Formation of rigid polyurethane foams with semi-fluorinated diblock copolymeric surfactants. **39**, 2049–2053 (1998).
50. Simón, D., Borreguero, A. M., de Lucas, A. & Rodríguez, J. F. Recycling of polyurethanes from laboratory to industry, a journey towards the sustainability. *Waste Management* **76**, 147–171 (2018).
51. Alshammari, B. A. *et al.* Impact of Hybrid Fillers on the Properties of High Density Polyethylene Based Composites. *Polymers (Basel).* **14**, (2022).
52. Al-Moameri, H., Zhao, Y., Ghoreishi, R. & Suppes, G. J. Simulation Blowing Agent Performance, Cell Morphology, and Cell Pressure in Rigid Polyurethane Foams. *Ind. Eng. Chem. Res.* **55**, 2336–2344 (2016).
53. Perkins, R. *et al.* Thermal conductivities of alternatives to CFC-11 for foam insulation. *J. Chem. Eng. Data* **46**, 428–432 (2001).
54. Berardi, U. The impact of temperature dependency of the building insulation thermal conductivity in the Canadian climate. in *Energy Procedia* vol. 132 237–242 (Elsevier Ltd, 2017).
55. Maamoun, A. A., Arafa, M. & Esawi, A. M. K. Flexible polyurethane foam: materials, synthesis, recycling, and applications in energy harvesting - a review. *Materials Advances* vol. 6 1842–1858 Preprint at https://doi.org/10.1039/d4ma01026d (2025).
56. Bulan, A. *et al.* Process for producing isocyanates. (2012).
57. Bharti, K. & Kaur, R. A Review Of Chemical Recycling Pathways For Waste Polyurethane. *Metallurgical and Materials Engineering* **5**, 1781–1803 (2025).
58. Kemona, A. & Piotrowska, M. Polyurethane recycling and disposal: Methods and prospects. *Polymers (Basel).* **12**, (2020).
59. Van Belleghem, L. *et al.* Recovery of Polyol and Aromatic Amines from Rigid Polyurethane Foams via Ammonolysis. *JACS Au* **5**, 3444–3452 (2025).
60. Liu, L. J., Wang, X. L., Gu, Z. Y., Ren, X. L. & Chang, T. Rapid hydrolysis of waste polyurethane and facile system separation. *Sep. Purif. Technol.* **354**, (2025).
61. Agnoletto, A. *et al.* Recycling of rigid polyurethane foams via acidolysis. *Progress in Rubber, Plastics and Recycling Technology* https://doi.org/10.1177/14777606241308651 (2024) doi:10.1177/14777606241308651.
62. Ivashchuk, O. S. *et al.* Depolymerization of rigid polyurethane waste by catalytic glycolysis with diethylene glycol. *S. Afr. J. Chem. Eng.* **52**, 61–67 (2025).

63. Xu, L. *et al.* Efficient alcoholysis of waste rigid polyurethane foam using MIL-101(Fe) catalyst. *Sep. Purif. Technol.* **366**, (2025).
64. Eiden, S. *et al.* Pyrolysis of polyurethane compound-containing material in order to recover raw materials. Patent US 2024/0254395 A1 (2024).
65. Zubar, V., Haedler, A. T., Schütte, M., Hashmi, A. S. K. & Schaub, T. Hydrogenative Depolymerization of Polyurethanes Catalyzed by a Manganese Pincer Complex. *ChemSusChem* **15**, (2022).
66. Guo, X., Wang, L., Zhang, L., Li, S. & Hao, J. Nitrogenous emissions from the catalytic pyrolysis of waste rigid polyurethane foam. *J. Anal. Appl. Pyrolysis* **108**, 143–150 (2014).
67. Dickerson, T. & Soria, J. Catalytic fast pyrolysis: A review. *Energies (Basel).* **6**, 514–538 (2013).
68. Mohan, D., Pittman, C. U. & Steele, P. H. Pyrolysis of wood/biomass for bio-oil: A critical review. *Energy and Fuels* **20**, 848–889 (2006).
69. Zhang, M. *et al.* Numerical investigation on the heat transfer of plastic waste pyrolysis in a rotary furnace. *Chemical Engineering Journal* **445**, (2022).
70. Bridgwater, A. V. Review of fast pyrolysis of biomass and product upgrading. *Biomass Bioenergy* **38**, 68–94 (2012).
71. Grittner, N., Kaminsky, W. & Obst, G. Fluid bed pyrolysis of anhydride-hardened epoxy resins and polyether-polyurethane by the Hamburg process. *J. Anal. Appl. Pyrolysis* **25**, 293–299 (1993).
72. Guo, Z. *et al.* Separation characteristics of biomass pyrolysis oil in molecular distillation. *Sep. Purif. Technol.* **76**, 52–57 (2010).
73. Wang, S. *et al.* Separation of bio-oil by molecular distillation. *Fuel Processing Technology* **90**, 738–745 (2009).
74. Bridgwater, A. V & Bridge, S. A. *A Review of Biomass Pyrolysis and Pyrolysis Technologies*. (1991). doi:10.1007/978-94-011-3844-4_2.
75. Meier, D. & Faix, O. tate of the art of applied fast pyrolysis of lignocellulosic materials — a review. *Bioresour. Technol.* **68**, 71–77 (1999).
76. Czernik, S. & Bridgwater, A. V. Overview of applications of biomass fast pyrolysis oil. *Energy and Fuels* **18**, 590–598 (2004).
77. Bozi, J. & Blazsó, M. Catalytic thermal decomposition of polyamides and polyurethanes mixed with acidic zeolites. *J. Anal. Appl. Pyrolysis* **97**, 189–197 (2012).
78. Bozi, J., Mihályi, M. R. & Blazsó, M. Study on temperature dependence of catalytic thermal decomposition of polyamides and polyurethanes mixed with acidic zeolites. *J. Anal. Appl. Pyrolysis* **101**, 103–110 (2013).
79. Eschenbacher, A., Varghese, R. J., Weng, J. & Van Geem, K. M. Fast pyrolysis of polyurethanes and polyisocyanurate with and without flame retardant: Compounds of interest for chemical recycling. *J. Anal. Appl. Pyrolysis* **160**, 105374 (2021).
80. Terakado, O., Yanase, H. & Hirasawa, M. Pyrolysis treatment of waste polyurethane foam in the presence of metallic compounds. *J. Anal. Appl. Pyrolysis* **108**, 130–135 (2014).
81. Xu, S. *et al.* Insight into waste polyurethane pyrolysis pathways: Mechanism functions analysis and in-situ coupling online monitoring. *J. Anal. Appl. Pyrolysis* **177**, 106301 (2024).
82. Yuan, Y. *et al.* Highly efficient catalysts for reducing toxic gases generation change with temperature of rigid polyurethane foam nanocomposites: A comparative investigation. *Compos. Part A Appl. Sci. Manuf.* **112**, 142–154 (2018).

83. Font, R., Fullana, A., Caballero, J. A., Candela, J. & García, A. Pyrolysis study of polyurethane. *J. Anal. Appl. Pyrolysis* **58–59**, 63–77 (2001).
84. Guo, X., Wang, L., Li, S., Tang, X. & Hao, J. Gasification of waste rigid polyurethane foam: optimizing operational conditions. *J. Mater. Cycles Waste Manag.* **17**, 560–565 (2015).
85. Kumagai, S., Yabuki, R., Kameda, T., Saito, Y. & Yoshioka, T. Simultaneous recovery of H2-rich syngas and removal of HCN during pyrolytic recycling of polyurethane by Ni/Mg/Al catalysts. *Chemical Engineering Journal* **361**, 408–415 (2019).
86. Zeller, M. *et al.* Characteristics of Polyurethane Pyrolysis—Experimental Investigations and Product Analyses for the Assessment of Chemical Recycling Potentials. *J. Appl. Polym. Sci.* **143**, (2025).
87. Grittner, N., Kaminsky, W. & Obst, G. Fluid bed pyrolysis of anhydride-hardened epoxy resins and polyether-polyurethane by the Hamburg process. *J. Anal. Appl. Pyrolysis* **25**, 293–299 (1993).
88. Kaminsky, W. Chemical recycling of plastics by fluidized bed pyrolysis. *Fuel Communications* **8**, 100023 (2021).
89. Garcia-Nunez, J. A. *et al.* Historical Developments of Pyrolysis Reactors: A Review. *Energy fuels* **31**, (2017).
90. Luo, G. *et al.* Pyrolysis of whole wood chips and rods in a novel ablative reactor. *Fuel* **194**, 229–238 (2017).
91. Peacocke, G. V. C. & Bridgwater, A. V. ABLATIVE PLATE PYROLYSIS OF BIOMASS FOR LIQUIDS. **7**, 147–154 (1994).
92. Westerhout, R. W. J., Waanders, J., Kuipers, J. A. M. & Van Swaaij, W. P. M. Development of a Continuous Rotating Cone Reactor Pilot Plant for the Pyrolysis of Polyethene and Polypropene. *Ind. Eng. Chem. Res* **37**, 2316–2322 (1998).
93. Bridgwater, T. Challenges and opportunities in fast pyrolysis of biomass: Part I. *Johnson Matthey Technology Review* **62**, 118–130 (2018).
94. Han, Z. *et al.* Micro reactors for measurement and analysis of thermochemical gas-solid reactions. *Resources Chemicals and Materials* **1**, 152–166 (2022).
95. Eigenberger, G. Fixed-Bed Reactors. in *Ullmann's Encyclopedia of Industrial Chemistry* (Wiley-VCH Verlag GmbH & Co. KGaA, 2000). doi:10.1002/14356007.b04_199.
96. Li, N. *et al.* Ex-situ catalytic pyrolysis of paper sludge over a Pt/Al2O3 catalyst. (2026).
97. Moroi, G. Influence of ion species on the thermal degradation of polyurethane interaction products with transition metal ions. *J. Anal. Appl. Pyrolysis* **71**, 485–500 (2004).
98. Priharto, N. *et al.* Ex Situ Catalytic Fast Pyrolysis of Lignin-Rich Digested Stillage over Na/ZSM-5, H/ZSM-5, and Fe/ZSM-5. *Energy and Fuels* **34**, 12710–12723 (2020).
99. Wan, S. & Wang, Y. A review on ex situ catalytic fast pyrolysis of biomass. *Front. Chem. Sci. Eng.* **8**, 280–294 (2014).
100. Galadima, A. & Muraza, O. In situ fast pyrolysis of biomass with zeolite catalysts for bioaromatics/gasoline production: A review. *Energy Convers. Manag.* **105**, 338–354 (2015).
101. Takamoto, D. Y. & Petrich, M. A. Effect of Heterogeneous Secondary Pyrolysis Reactions on the Thermal Decomposition of Polyurethane Scrap. *Ind. Eng. Chem. Res* **33**, 3004–3009 (1994).
102. Ertl, G. ., Knözinger, Helmut., Schüth, Ferdi. & Weitkamp, J. . *Handbook of Heterogeneous Catalysis*. (Wiley-VCH Verlag GmbH & Co. KGaA, 2008).

103. Liu, C. *et al.* Frontier Molecular Orbital Based Analysis of Solid-Adsorbate Interactions over Group 13 Metal Oxide Surfaces. *Journal of Physical Chemistry C* **124**, 15355–15365 (2020).
104. Bag, P., Weetman, C. & Inoue, S. Experimental Realisation of Elusive Multiple-Bonded Aluminium Compounds: A New Horizon in Aluminium Chemistry. *Angew. Chem. Int. Ed.* **57**, 14394–14413 (2018).
105. Boudart, M. Heterogeneous catalysis by metals. *Journal of Molecular Catalysis* **30**, 27–38 (1985).
106. Chen, J. *et al.* Metal-support interactions for heterogeneous catalysis: mechanisms, characterization techniques and applications. *J. Mater. Chem. A Mater.* **11**, 8540–8572 (2023).
107. Védrine, J. C. Heterogeneous catalysis on metal oxides. *Catalysts* **7**, (2017).
108. Startsev, A. N. Concerted mechanisms in heterogeneous catalysis by sulfides q. *J. Mol. Catal. A Chem.* **152**, 1–13 (2000).
109. Védrine, J. C. Metal Oxides in Heterogeneous Oxidation Catalysis: State of the Art and Challenges for a More Sustainable World. *ChemSusChem* **12**, 577–588 (2019).
110. White, J. L. & Truitt, M. J. Heterogeneous catalysis in solid acids. *Prog. Nucl. Magn. Reson. Spectrosc.* **51**, 139–154 (2007).
111. Su, F. & Guo, Y. Advancements in solid acid catalysts for biodiesel production. *Green Chemistry* **16**, 2934–2957 (2014).
112. Palanivelrajan, A. R. & Feroskhan, M. Comparison of various catalysts in pyrolysis process: A review. *Mater. Today Proc.* **84**, 47–56 (2023).
113. Cai, R. *et al.* Biomass Catalytic Pyrolysis over Zeolite Catalysts with an Emphasis on Porosity and Acidity: A State-of-the-Art Review. *Energy and Fuels* **34**, 11771–11790 (2020).
114. Wei, L., Wang, H., Dong, Q., Li, Y. & Xiang, H. A Review on the Research Progress of Zeolite Catalysts for Heavy Oil Cracking. *Catalysts* **15**, 401 (2025).
115. Pérez-Botella, E., Valencia, S. & Rey, F. Zeolites in Adsorption Processes: State of the Art and Future Prospects. *Chem. Rev.* **122**, 17647–17695 (2022).
116. Weitkamp, J. Zeolites and catalysis. *Solid State Ion.* **131**, 175–188 (2000).
117. Taarning, E. *et al.* Zeolite-catalyzed biomass conversion to fuels and chemicals. *Energy Environ. Sci.* **4**, 793–804 (2011).
118. Zheng, S. *et al.* Benzenoid Aromatics from Renewable Resources. *Chem. Rev.* **124**, 10701–10876 (2024).
119. Bozi, J. & Blazsó, M. Catalytic thermal decomposition of polyamides and polyurethanes mixed with acidic zeolites. *J. Anal. Appl. Pyrolysis* **97**, 189–197 (2012).
120. Hanefeld, Ulf. & Lefferts, Leon. *Catalysis : An Integrated Textbook for Students*. (Wiley-VCH, 2018).
121. Husein, M. M. & Alkhaldi, S. J. In situ preparation of alumina nanoparticles in heavy oil and their thermal cracking performance. *Energy and Fuels* **28**, 6563–6569 (2014).
122. Knözinger, H. Dehydration of Alcohols on Aluminum Oxide. *Angewandte Chemie International Edition in English* **7**, 791–805 (1968).
123. Assebban, M., Kasmi, A. El, Harti, S. & Chafik, T. Intrinsic catalytic properties of extruded clay honeycomb monolith toward complete oxidation of air pollutants. *J. Hazard. Mater.* **300**, 590–597 (2015).

124. González-Peña, V., Díaz, I., Márquez-Alvarez, C., Sastre, E. & Pérez-Pariente, J. Thermally stable mesoporous alumina synthesized with non-ionic surfactants in the presence of amines. *Microporous and Mesoporous Materials* **44–45**, 203–210 (2001).
125. Ma, D. *et al.* An Investigation of the Roles of Surface Aluminum and Acid Sites in the Zeolite MCM-22. *Chemistry–A European Journal* **8**, 162–170 (2002).
126. Thomas, C. L. Chemistry of Cracking Catalysts. *Ind. Eng. Chem.* **41**, 2564–2573 (1949).
127. Irwin, A. D., Holmgren, J. S. & Jonas, J. 27AI and 29Si N MR study of sol-gel derived aluminosilicates and sodium aluminosilicates. *Journal of material sciences* **23**, 2908–2912 (1988).
128. Čejka, J. Organized mesoporous alumina: Synthesis, structure and potential in catalysis. *Appl. Catal. A Gen.* **254**, 327–338 (2003).
129. Hensen, E. J. M., Poduval, D. G., Magusin, P. C. M. M., Coumans, A. E. & Veen, J. A. R. van. Formation of acid sites in amorphous silica-alumina. *J. Catal.* **269**, 201–218 (2010).
130. Crépeau, G. *et al.* Nature, structure and strength of the acidic sites of amorphous silica alumina: An IR and NMR study. *Journal of Physical Chemistry B* **110**, 15172–15185 (2006).
131. Ali, M. A., Tatsumi, T. & Masuda, T. Development of heavy oil hydrocracking catalysts using amorphous silica-alumina and zeolites as catalyst supports. *Appl. Catal. A Gen.* **233**, 77–90 (2002).
132. Coster, D., Blumenfeld, A. L. & Fripiat, J. J. Lewis Acid Sites and Surface Aluminum in Aluminas and Zeolites: A High-Resolution NMR Study. *J. Phys. Chem.* **24**, 6201–6211 (1994).
133. H. Douglas Morris & Paul D. Ellis. Aluminum-27 cross polarization of aluminas. The NMR spectroscopy of surface aluminum atoms. *J. Am. Chem. Soc.* **111**, 6045–6049 (1989).
134. Omegna, A., Van Bokhoven, J. A. & Prins, R. Flexible Aluminum Coordination in Alumino-Silicates. Structure of Zeolite H-USY and Amorphous Silica-Alumina. *J. Phys. Chem. B* **107**, 8854–8860 (2003).
135. Hansford, R. C. A Mechanism of Catalytic Cracking. *Ind. Eng. Chem.* **7**, 849–852 (1947).
136. Peeters, M. P. J. & Kentgens, A. P. M. A 27A1 MAS, MQMAS and off-resonance nutation NMR study of aluminium containing silica-based sol-gel materials. *Solid State Nucl. Magn. Reson.* **9**, 203–217 (1997).
137. Chen, F. R., Davis, J. G. & Fripiat, J. J. Aluminum Coordination and Lewis Acidity in Transition Aluminas. *J. Catal.* **133**, 263–278 (1992).
138. Chen, F. R. & Fripiat, J. J. Formation of radical ion pairs in aniline adsorption on zeolites. *J. Phys. Chem.* **96**, 819–823 (1992).
139. Van Bokhoven, J. A. *et al.* Changes in structural and electronic properties of the zeolite framework induced by extraframework Al and la in H-USY and La(x)NaY: A29Si and27AI MAS NMR and27A1 MQ MAS NMR study. *Journal of Physical Chemistry B* **104**, 6743–6754 (2000).
140. Chizallet, C. & Raybaud, P. Acidity of amorphous silica-alumina: From coordination promotion of lewis sites to proton transfer. *ChemPhysChem* **11**, 105–108 (2010).
141. Chizallet, C. & Raybaud, P. Pseudo-bridging silanols as versatile brønsted acid sites of amorphous aluminosilicate surfaces. *Angew. Chem. Int. Ed.* **48**, 2891–2893 (2009).
142. Trombetta, M. *et al.* FT-IR Studies on Light Olefin Skeletal Isomerization Catalysis III. Surface Acidity and Activity of Amorphous and Crystalline Catalysts Belonging to the SiO2-Al2O3 System. *J. Catal.* **179**, 581–596 (1998).

143. Huang, J., Van Vegten, N., Jiang, Y., Hunger, M. & Baiker, A. Increasing the Brønsted acidity of flame-derived silica/alumina up to zeolitic strength. *Angew. Chem. Int. Ed.* **49**, 7776–7781 (2010).
144. Wang, Z. *et al.* Brønsted acid sites based on penta-coordinated aluminum species. *Nat. Commun.* **7**, 13820 (2016).
145. Xu, B. *et al.* Strong Brønsted acidity in amorphous silica - aluminas. *Journal of Physical Chemistry C* **111**, 12075–12079 (2007).
146. Góra-Marek, K. & Datka, J. IR studies of OH groups in mesoporous aluminosilicates. *Appl. Catal. A Gen.* **302**, 104–109 (2006).
147. Daniell, W. *et al.* Enhanced surface acidity in mixed alumina-silicas: a low-temperature FTIR study. *Appl. Catal. A Gen.* **196**, 247–260 (2000).
148. Bevilacqua, M., Montanari, T., Finocchio, E. & Busca, G. Are the active sites of protonic zeolites generated by the cavities? *Catal. Today* **116**, 132–142 (2006).
149. Williams, M. F. *et al.* Hydrogenation of tetralin on silica-alumina-supported Pt catalysts I. Physicochemical characterization of the catalytic materials. *J. Catal.* **251**, 485–496 (2007).
150. Jacobs, P. A., Mortier, W. J. & Uytterhoeven, J. B. Properties of zeolites in relation to their electronegativity: Acidity, carboniogenic activity and strength of interaction in transition metal complexes. *Journal of Inorganic and Nuclear Chemistry* **40**, 1919–192 (1978).
151. Grams, J. & Ruppert, A. M. Catalyst stability—bottleneck of efficient catalytic pyrolysis. *Catalysts* **11**, 1–24 (2021).
152. Bartholomew, C. H. Carbon Deposition in Steam Reforming and Methanation. *Catalysis Reviews* **24**, 67–112 (1982).
153. Anekwe, I. M. S. & Isa, Y. M. Unlocking catalytic longevity: a critical review of catalyst deactivation pathways and regeneration technologies. *Energy Advances* **4**, 1075–1113 (2025).
154. Du, S., Valla, J. & Bollas, G. M. Characteristics and origin of char and coke from fast and slow, catalytic and thermal pyrolysis of biomass and relevant model compounds. *Green Chemistry* **11**, 3214–3229 (2013).
155. Bartholomew, C. H. Mechanisms of catalyst deactivation. *Appl. Catal. A Gen.* **212**, 17–60 (2001).
156. Hegedus, L. L. & McCabe, R. W. Catalyst poisoning. *Stud. Surf. Sci. Catal.* **6**, 471–505 (1980).
157. Werther, J. & Reppenhagen, J. Catalyst Attrition in Fluidized-Bed Systems. *Reactors, Kinetics, and Catalysis* **45**, 2001–2010 (1999).
158. Liu, B. *et al.* Opportunities in Closed-Loop Molecular Recycling of End-of-Life Polyurethane. *ACS Sustain. Chem. Eng.* **11**, 6114–6128 (2023).
159. Jiao, L., Xiao, H., Wang, Q. & Sun, J. Thermal degradation characteristics of rigid polyurethane foam and the volatile products analysis with TG-FTIR-MS. *Polym. Degrad. Stab.* **98**, 2687–2696 (2013).
160. Chen, H. *et al.* Clay mineral as catalysis for controlling the nitrogen containing pollutants during sewage sludge pyrolysis. *Science of the Total Environment* **913**, 169535 (2024).



Chemical recycling of rigid polyurethane foam via thermocatalytic conversion to aniline



3

This chapter is based on published work:

Engels, T. G. W., Stevelink, R., Vaze S., van der Zijpp, M., Pillich, M., Eiden, S., Schenk, N., Bardow, A., Heeres, H. J. & Deuss, P. J. Chemical recycling of rigid polyurethane foam via thermocatalytic conversion to aniline. ChemRevxiv (2026)

Abstract

Polyurethanes possess unique properties that find many applications and are produced globally at around 22 million tons per year. Current recycling pathways primarily focus on recovering polyol rather than nitrogen-rich components. Here, we report on the thermocatalytic conversion of poly-methylenedianiline (pMDA) carbamate-based rigid polyurethane foams back to their platform chemical, aniline. A two-stage tandem microreactor recovered >50% of the original aniline input in the feed under optimized conditions (550 ˚C and specific alumina catalysts), with an additional 15% as toluidine, a major secondary product. The catalytic process was upscaled in multiple stages, from mg to continuous operation at >100 $g_{feedstock}$ h^{-1} and 5 $kg_{feedstock}$ $h^{-1,}$ where over 25% aniline and toluidine recovery was achieved. Although non-optimized, preliminary assessments of these upscaled runs show the potential to reduce climate change impacts by 0.6 $kg_{CO2\text{-}eq}$ per $kg_{treatedPUR}$ compared to incineration and to offer economic benefits even for a catalyst lifetime of 44 hours.

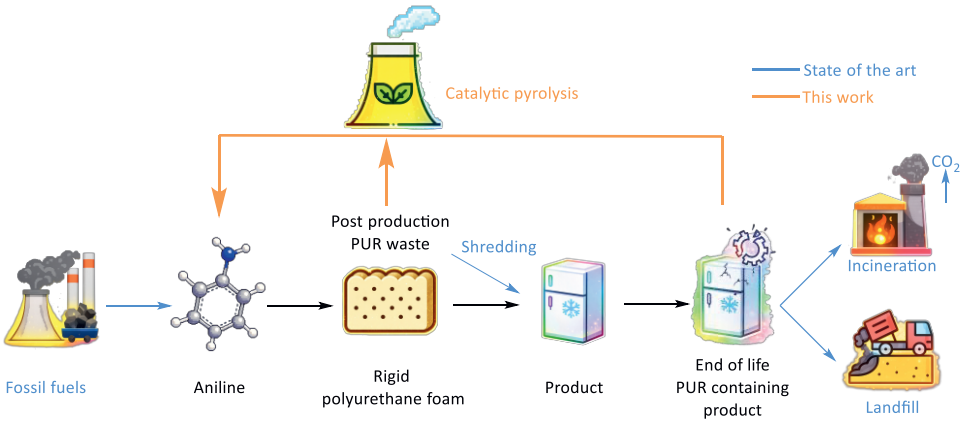

3.1. Introduction

In 1937, Otto Bayer discovered polyurethane (PUR), a new material synthesized via polyaddition of isocyanates and polyols. Over the years, PUR has established a dominant position in many sectors including: construction materials, mattresses, insulation, refrigerators, coatings, and paints.[1–5] PUR production levels have increased tremendously in the past 30 years due to the high versatility of properties arising from different chemical formulations[6], thereby replacing polymers such as PVC, rubber, and polystyrene in applications. For example, the rigidity of PUR foams can be controlled by the type and amounts of isocyanate and polyol components used in the formulation. Nowadays, polyurethanes are the sixth most widely used thermoset, accounting for 8% of the polymer materials produced annually worldwide.[7] Currently, three main waste management strategies are in place for end-of-life polyurethane (EOL PUR) (*see state-of-the-art in* Figure 3.1): Globally, the largest portion of EOL PUR (40%) is disposed of in landfills[8], while 25% is processed via downcycling[8], which involves shredding non-contaminated, post-production PUR typically into small flakes for reuse. The remaining 35% is incinerated to recover energy[8]. Therefore, improved recycling options, such as chemical recycling to starting materials, are needed for PUR products to support circular value chains.

PUR can be classified into two main types: flexible and rigid. Flexible PUR is commonly used in shock-absorbing materials such as mattresses or car seats, while rigid PUR foams are suitable for thermal insulation, e.g. in refrigerators, buildings, and roofs. The type of foam depends on the carbamate moiety used in the synthesis. Toluene diisocyanate (TDI) is mainly used as an isocyanate source to obtain flexible PUR, whereas poly methylene diphenyl diisocyanate (pMDI) is used for rigid PUR. Refrigerator isolation foam (rigid PUR), in particular, is an interesting recycling target as it is abundantly collected at waste facilities. A representative case is Germany where 16.9 kt of refrigerator foam was collected in 2021.[9] Additionally, rigid PUR foams are typically synthesized with a high content of aniline-derived polymeric methylene diphenyl diisocyanate (pMDI) (Figure 3.1).[10] The production steps involve the formation of polymeric methylene dianiline (pMDA) via the reaction of formaldehyde with aniline in the presence of hydrochloric acid (**1**); a subsequent reaction of pMDA with phosgene produces polymeric methylene diphenyl diisocyanate (pMDI, **2**). The addition of an additive formulated polyol to pMDI produces a polyurethane (**3**).[11]

Available chemical recycling pathways include hydrolysis, acidolysis, glycolysis, and aminolysis. These closed-loop recycling strategies have shown that the recovered polyol can replace fossil-based chemicals in PUR production.[10] However, for the reduction of environmental impacts, recovering the isocyanide side is more promising.[13,14] Most reported chemical recycling methods focus on TDI-based PUR (flexible)[15] rather than MDI-based PUR (rigid). MDI-based PUR is typically synthesized from a mixture of oligomeric MDA (pMDA), making the recovery and reuse of the isocyanate more challenging. Recent work on the recycling of pMDI-based PUR reported the recovery of 87% pMDA from EOL pMDI-based refrigerator PUR via ammonolysis.[16] However, when such a recovered pMDA is used without carefully controlled oligomeric distributions and purity, the phosgenation of pMDA to pMDI yields a product with different specifications compared to those of the pMDI used in the original material. This illustrates the narrow margins and challenges of recycling pMDI-based PUR. Due to these purification challenges, it can be of notable interest to develop a method for recovering aniline, which is the precursor to pMDI. This compound presents the most valuable base chemical component

and allows to facilitates purification for reintegration into the pMDI-based production chain to yield the same quality product (Figure 3.1, orange pathway).

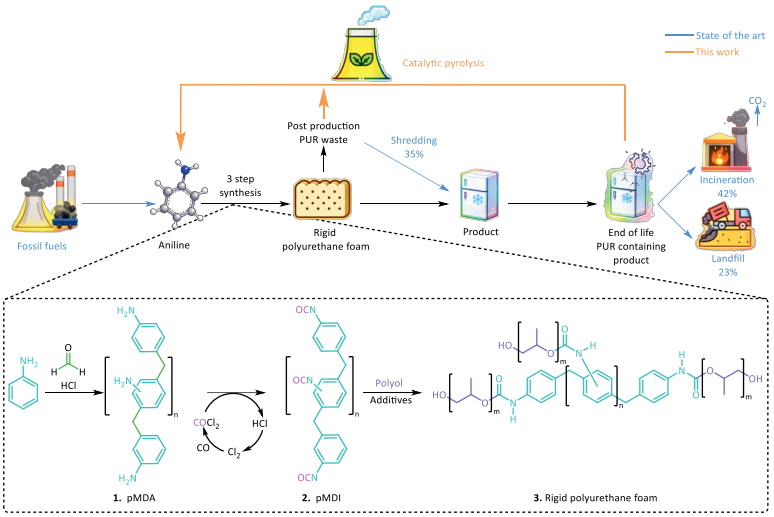

Figure 3.1. Polyurethane production and current waste management.[12] Quantitative data are taken from: [8]

Catalytic pyrolysis is a promising approach for converting plastics into low-molecular-weight building blocks via thermal decomposition in an oxygen-free environment at elevated temperatures (300 – 700 °C), using a catalyst to further crack and convert these into desired products.[17] As introduced here, thermocatalytic pyrolysis enables the conversion of rigid PUR into nitrogen-containing compounds, including aniline. The addition of suitable catalysts enables higher liquid yields and can tune the product selectivity towards increased amounts of target base-chemicals[18], in this instance, aniline.

The latest mechanistic work on the thermochemical decomposition of waste polyurethane refrigerator foam revealed that PUR degradation can be explained in a simplified manner through a two-stage degradation process. **I**) The evolution of volatile C1 - C4 fragments originating from polyol decomposition (>310 °C), followed by **II**) the formation of N-containing compounds, including aniline, toluidine, and MDA (>480 °C).[19] A comprehensive collection of all reported work on the thermal and thermal degradation (with and without catalysts) of polyurethane is provided in the supplementary information, revealing that the selective production of nitrogen-containing compounds has been barely explored (Supporting, Tables S3.4.1 & S3.4.2).

Existing studies on (catalytic) thermal degradation of PUR provide detailed identification and, especially, rigorous quantification of the product composition, but typically report no reliable aniline yields. An overview of literature works in which aniline is quantified reveals yields below 5%, with the majority calculated on unreliable area percentage approaches rather than on calibration of the corresponding compound (Table S3.4.1). The only exception is a recent Covestro patent involving one of the coauthors on the catalytic pyrolysis of post-production MDI-based PUR, which reaches an

aniline yield of 19 wt% in a fixed-bed reactor at 500 °C using an alumina-magnesium-based catalyst, and serves as the starting point for the current study.[12]

This work presents the development of a thermocatalytic conversion technology for the recovery of aniline from EOL MDI-based PUR. The approach enables, for the first time, partial closed-loop recycling of this thermoset, as the recovered aniline can be used to produce new PUR with properties equal to those of fossil-based PUR. A proof of concept was established at the milligram scale in a tandem microreactor through comprehensive catalyst screening and reaction-condition optimization. First steps towards scaling this technology are demonstrated by transitioning from milligram-scale conditions to kilogram-per-hour pilot production, using new and end-of-life PUR feedstocks. The potential of the developed process to reduce climate change impacts of current PUR waste treatment practice is assessed through an environmental potential analysis and expressed as kilogram CO_2-eq reduced per kilogram PUR waste treated. Additionally, the targets for catalyst performance were calculated to allow economic feasibility.

3.2. Results & discussion

Feedstock characterization

Three rigid polyurethane (PUR) feeds were used in this study. For initial experiments in developing a thermocatalytic conversion method, newly produced rigid PUR foam (nPUR) was used. Foam details are described in the patented work of Covestro.[12] Subsequent studies included end-of-life PUR insulation foam polyurethanes (EOL_1 & EOL_2) obtained from waste facilities, which were further processed into condensed pellets suitable for reactor feeding. The bulk densities were determined to be 530 and 460 kg/L for EOL_1 and EOL_2, respectively. FTIR spectroscopy confirmed that all three feeds were MDI-based, as evidenced by the distinct signal at 1500 cm^{-1} (S2.1.4) for MDI-based PUR. Elemental analysis showed nitrogen contents of 7.5 wt%, 6.6 wt%, and 7.1 wt% for the nPUR, EOL_1, and EOL_2 feeds, respectively. X-ray fluorescence (XRF) after aerobic combustion allowed identification and quantification of ash contaminants. A total ash content of 0.8 wt%, 5.7 wt%, and 2.7 wt% was found for nPUR, EOL_1, and EOL_2, respectively. The metal impurities mainly consisted of silicate (stabilizer) and calcium/titanium dioxide (whiteners) for nPUR. EOL_1 and EOL_2 exhibited more complex compositions, containing iron and, in the case of EOL_1, also zinc oxide, which are likely contaminants introduced during waste processing as the whole refrigerator is shredded. Other relevant PUR components were determined via thermal decomposition coupled to mass spectroscopy. The presence of cyclopentane was detected in nPUR, originating from a blowing agent. In the EOL feeds, 12% (EOL_1) and 5% (EOL_2) polystyrene were found, originating from the refrigerator liner that mixes during processing. Based on the nitrogen content from the elemental analysis, the aniline unit content was calculated to be 50%, 44%, and 47%, respectively. The experimental aniline recovery yield upon pyrolysis was calculated as fraction of this theoretical maximum recovery value. (See calculation 3.4.2 for the details).

Exploratory catalyst screening studies

The potential of thermocatalytic chemical recycling of rigid PUR to recover aniline was tested using a small-scale tandem microreactor (TMR, Frontier lab model Rx-3050TR) coupled to a GC-FID by screening 21 catalysts from four catalyst families Figure 3.2. Catalysts were selected based on previous

work by Guo *et al.* (alkaline earth catalysts)[20,21] Eiden *et al*. (alumina /post transition metals)[12], and Terakado *et al*. (transition metal-based catalysts).[22] Additionally, clays such as bentonite and sepiolite were tested.[23] Experiments were conducted by mixing nPUR feed with the catalyst in an in-situ mode of pyrolysis at 550 °C. The latter temperature was selected based on preliminary temperature-screening work by Eiden et al.[12] Unlike literature that often reports area% yields that are deceptive, the yields reported in this work are based on a quantification using an internal standard calibration and expressed relative to the theoretical aniline recovery yield based on the calculated aniline content in the feed (see above). This also allows for a better comparison of catalytic systems with vastly different product pyrolysis gas yields and composition and also between different feeds with different aniline contents (See calculation 3.3.2 for N-based yield). It should be noted that yields were also calculated on a different basis (e.g. based on area % (3.4.3), total feed weight input (3.4.5), and per amount of catalyst (3.4.6) for comparisons between systems and with literature data (Table S3.4.1).

Thermal pyrolysis (without catalyst) of PUR under the selected conditions resulted in low yields of the desired N-containing monomers (5.5% MDA, with no aniline or toluidine; Figure 3.2). The presence of most catalysts significantly increased the formation of aniline, toluidine, and MDA. For example, hafnium oxide showed an N-based yield of 33% aniline, 7.0% toluidine, and 6.7% MDA. The range of aniline yields for the four investigated catalyst families: alkaline (1.5 – 4.3%) < clays (8.6 – 20%) < transition metals (0.0 – 33%) < post-transition metals (3.7 – 40%). The highest yield for the desired nitrogen-containing products was observed with γ-alumina as a catalyst. The latter yielded 40% aniline, 12% toluidine, and 6.7% MDA. These yields exceed values reported in the scientific literature by an order of magnitude (Table S3.4.2). Using γ-alumina as catalyst, the yield of aniline on total PUR input is 20 wt%, which is in line with the reported aniline yield of 19 wt% in the initial patent by Covestro, which was carried out in a 25 mL fixed bed reactor at 500 °C and a reaction time of 30 minutes.[12]

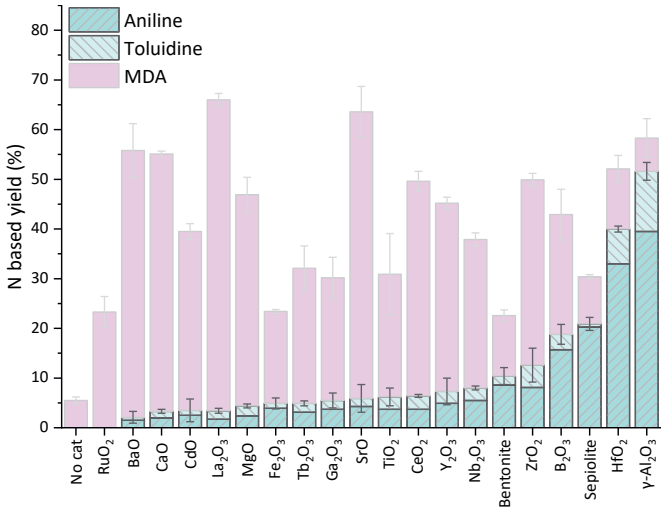

Figure 3.2. Overview of catalyst performance for PUR pyrolysis in the tandem microreactor. Reaction conditions: 0.5 mg nPUR, catalyst-to-feed ratio of 5 to 1, 550 °C with a helium flow of 205 mL/min and a pyrolysis time of 10 seconds. A comprehensive yield overview of the data also expressed based on area% can be found in the section S4.2. Note that γ-alumina (γ-Al_2O_3) used here corresponds to Alumina 4 in the γ-alumina series used below

Product selectivity is strongly dependent on the catalyst used. For most catalysts tested, MDA (including the 4,2-minor isomer) is the major product (Figure 3.3). MDA is considered an intermediate product that can be further cracked to aniline and toluidine. However, MDA is not a desired product due to the cumbersome downstream processing hindered by its high boiling point, nor is it a suitable starting material for current pMDI production. The selectivity shifts from MDA-dominant to aniline/toluidine as the major product when using sepiolite, HfO_2, and alumina as catalysts. Toluidine is considered a valuable product as it can be readily purified and sold separately or dealkylated to aniline.

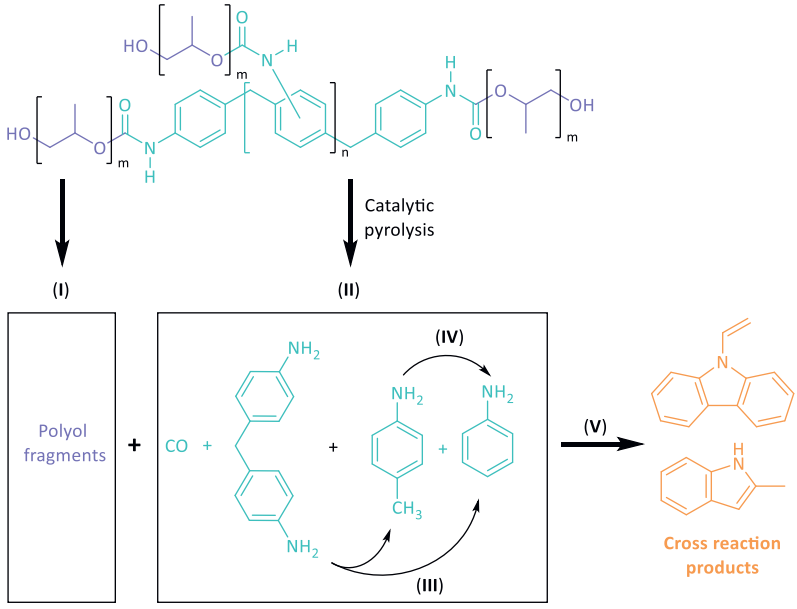

Figure 3.3. Simplified overview of the main pathways for the thermocatalytic pyrolysis of nPUR

Catalysts that provide high yields of aniline and toluidine are those that break down pMDA-derived fragments like MDA into aniline and toluidine. If pMDA is represented as a trimer (Figure 3.3, Purple), it is theoretically expected to depolymerize into at least a 1:2 aniline-to-toluidine ratio. For higher oligomers, this ratio would change further towards toluidine. However, catalytic pyrolysis with alumina yields a 3:1 aniline-to-toluidine ratio, indicating significant dealkylation of toluidine into aniline. Dealkylation is not expected to occur on larger oligomeric fragments, as these would not readily enter the catalyst pores. So, the reaction is expected to take place either on the surface of the particle or on the released toluidine. Anand *et al.* [24] investigated the alkylation of *o*-toluidine with methanol over acidic zeolites. The group observed the disproportionation of toluidine into aniline at 400 °C in the presence of zeolite H-beta, a reaction that could also be occurring here.[24]The possibility of toluidine dealkylation has been supported by patented work on toluidine dealkylation into aniline at 350 °C in the presence of carbon-supported transition metals such as Pt, Pd, Ni, Co,.[25] Thus, by appropriately selecting the catalyst, the product slate can be tuned towards aniline.

Looking more deeply into the product portfolio beyond pMDA-derived fragments (aniline, toluidine, and MDA) of the best-performing catalyst (γ-Al_2O_3), several other compound classes can be observed

upon GCMS analysis (Table S3.4.10).[26] Firstly, cyclopentane is detected, which is a blowing agent in nPUR. Secondly, CO_2 and acetone are observed to be assigned to the fragmentation of the polypropylene oxide-derived polyol. Finally, several other nitrogen-containing compounds are observed, likely arising from secondary reactions between the released polyol and pMDA fragments (e.g., alkylated anilines, quinolines, indoles, and acridines).[26] The total area% is in the order of 10 wt%. Although not the primary target of this study, these compounds have been utilized in the pharmaceutical industry as antibacterial agents and thus have potential value.[27,28] Overall, this allows us to simplify the catalytic breakdown pathways to those shown in Figure 3.3.

Alumina catalyst optimization and structure-performance relationships

Based on the finding that the tested γ-alumina catalyst (amorphous) showed high aniline yields, an additional catalytic pyrolysis experiment using a highly crystalline α-alumina (as shown by XRD analysis in Figure S3.4.5) was subjected to equal pyrolysis conditions to investigate the effect of crystallinity on the formation of aniline and toluidine. Please note that the γ-alumina catalyst in the general screening set described above corresponds to alumina 4 in the following alumina screening set. Results are shown in Figure 3.4. The significantly lower aniline and toluidine yields were observed, confirming that the α-alumina's highly crystalline nature leaves it unreactive compared to amorphous γ-alumina. For this reason, the research was continued using nine commercially available γ-alumina-based catalysts with different physicochemical properties (also shown in Figure 3.4). Significant differences in the yields of the desired N-containing compounds were observed for different γ-alumina's. For instance, the N-based aniline yield ranges from 9.7% using Alumina 0 to 51% with Alumina 8. The highest observed N-based aniline yield of 51%, corresponding to 26 wt% of the total PUR feed, is a significant increase over the other tested catalysts.

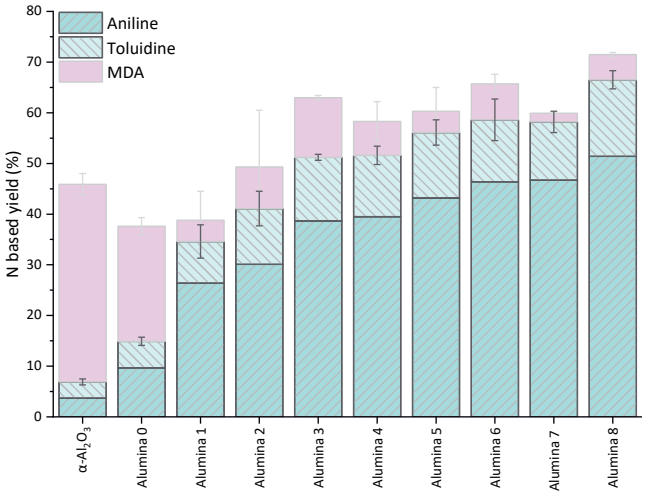

Figure 3.4. Overview of catalyst performance for PUR pyrolysis using a range of γ-alumina catalysts compared to α-alumina (GC-MS/FID). Reaction conditions: 0.5 mg nPUR, catalyst-to-feed ratio of 5 to 1, 550 °C with a helium flow of 205 mL/min., and a pyrolysis time of 10 s. A detailed overview of the product distribution for all alumina-based catalysts is provided in pyrolysis results section. An example of formed products can be found in Table S3.4.10)

The product distribution varies significantly among the nine alumina-based catalysts, with MDA being the main component for Alumina 0 and aniline for Alumina 8. Focusing on the two extremes depicted in Figure. 3.5 as composition reveals a noticeable shift in product distribution from MDA and volatiles (36% and 39%, respectively, from Alumina 0) to aniline and other N-containing products (41% and 18%, respectively, for Alumina 8). Increased formation of both aniline and toluidine, together with other N-containing side products, is in line with their formation through cross-reactions between released MDA, aniline, and toluidine with polyol fragments. These findings show that the catalyst's properties significantly influence the product distribution, and that the effective secondary cracking of MDA improves the yields of aniline and toluidine but also increases the formation of products from cross-reactions between these products and polyol fragments.

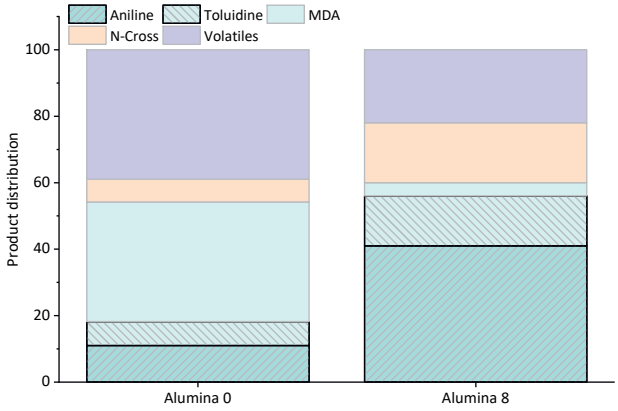

Figure 3.5. Product distribution upon catalytic pyrolysis of PUR using alumina 0 and alumina 8. Distribution is based on area% according to calculation (S3.4.3) in the supplementary information. Reaction conditions: 0.5 mg nPUR, catalyst-to-feed ratio of 5 to 1, reaction time 10 s. Volatiles are typically identified as small fragments derived from the polyol segment of polyurethane. The colors match the fragment colors shown in Figure 3.3

A catalyst structure-performance relationship was obtained by characterizing all catalysts in detail using various techniques, including temperature-programmed desorption of ammonia and carbon dioxide (NH_3 and CO_2 TPD), scanning and transmission electron microscopy (SEM & TEM) with energy-dispersive X-ray (EDX) analysis, Brunauer–Emmett–Teller nitrogen physisorption (BET), pyridine-IR spectroscopy (Py-IR), and X-ray diffraction (See Table 3.1 for results and section S3.4 for experimental details). The surface area ranged between 98 - 242 m^2/g, aligning with published values of 147 - 232 m^2/g for other γ-alumina catalysts.[29] Acidities varied between 204 - 488 µmol/g (NH_3-TPD) and were identified to be dominated by Lewis acid sites via Py-IR. The reported Lewis acidity of 360 µmol/g for γ-alumina is within this range.[30] The basicity ranged between 79 - 391 µmol/g (CO_2-TPD) and was in accordance to a literature value of 84 µmol/g for a similar catalyst.[31] SEM showed an average particle size of 3 - 144 µm, with smaller particles observed by TEM in the 11.5 - 39.0 nm range which are either in the smaller fraction of the particle-size distribution or formed by attrition. Comparison with literature is challenging because a clear distinction between SEM and TEM particle sizes is not consistently drawn. For example, Wang *et al*. reported a particle size of 5 - 9 nm for γ-alumina[32] whereas Chauruka et al. reported a particle size of 3.9 - 37 µm.[33]

Table 3.1. Aniline Yield data upon use in catalytic pyrolysis using the tandem microreactor and relevant properties of the γ-alumina catalyst family. Note that γ-alumina (γ-Al_2O_3) used here corresponds to Alumina 4 in the γ-alumina series used below

Catalyst	Aniline yield[a] (%)	Surface area[b] (m^2/g)	Total acidity[c] (µmol/g)	Acid site density[d] (µmol/m^2)	Brønsted/ Lewis ratio[e]	Crystallinity[f] (%)	Total Basicity[g] (µmol/g)	Basic site density[h] (µmol/m^2)	Agglomerate size[i] (µm)	Particle size[j] (nm)
Alumina 0	9.7	98.0	350	3.57	ND	ND	239	2.44	3.00	39.0
Alumina 1	26.4	147	329	2.24	0/100	56	151	1.03	10.2	16.3
Alumina 2	30.1	141	337	2.39	0/100	59	154	1.09	12.3	22.6
Alumina 3	38.7	147	204	1.39	0/100	ND	79.0	0.54	93.0	12.4
Alumina 4	39.5	179	330	1.84	ND	53	386	2.15	3.3	16.0
Alumina 5	43.2	197	221	1.12	0/100	59	161	0.82	121	11.5
Alumina 6	46.4	208	488	2.35	0/100	33	201	0.97	21.0	12.3
Alumina 7	46.7	242	412	1.70	0/100	55	391	1.61	144	13.1
Alumina 8	51.4	218	406	1.86	0/100	55	187	0.86	84.1	15.0

[a]Reaction conditions: 0.5 mg nPUR, catalyst-to-feed ratio of 5 to 1, 550 °C with a helium flow of 205 mL/min and a pyrolysis time of 10 seconds. A comprehensive yield overview based on area%, input, and N-based for all catalysts can be found in the section S4, Tables S10 – S16

[b]Determined via value at $P/P_0 = 0.99$

[c]Obtained via ammonia Thermal programmed desorption (NH_3-TPD)

[d]Calculated via $\frac{Total\ acidity}{Surface\ area}$

[e]Calculated via peak integration of Py-IR results

[f]Obtained via x-ray diffraction (XRD)

[g]Obtained via carbondioxide Thermal programmed desorption (CO_2-TPD)

[h]Calculated via $\frac{Total\ basicity}{Surface\ area}$

[i]Obtained via SEM imaging, average of minimal 50 agglomerates

[j]Obtained via TEM imaging, average of 200 measurements

A quadratic fit was obtained using acidity and surface area as input parameters and aniline yield as the response (Figure. 3.6). The results showed that a higher surface area is the most important catalyst parameter for achieving high aniline yields. The effect of Lewis acidity is more complicated, as this parameter was found to depend on surface area. A possible explanation is that a high surface area is preferred to facilitate the initial bond-breaking event in polyurethane, yielding polyol and carbamate fragments. The formed smaller fragments are easier to diffuse into the catalyst pore, which contains almost exclusively Lewis acidic catalytic sites that facilitate cracking of larger pieces into smaller products. Based on the investigation, the best catalyst is a Lewis acidic alumina with a high surface area.

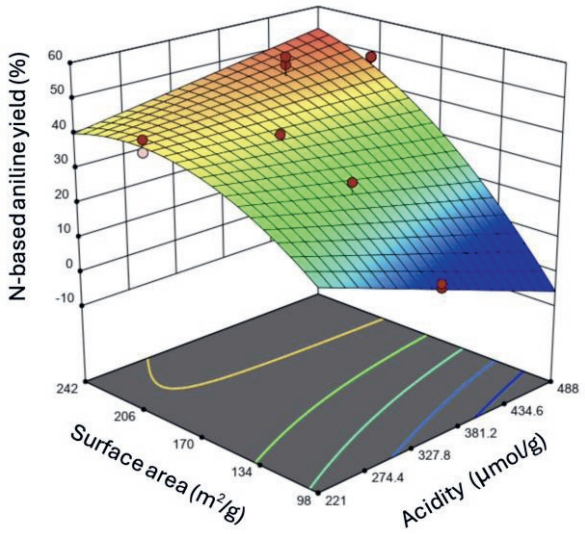

Figure 3.6. 3D response surface of total Lewis acidity and catalyst surface area concerning aniline yield

Mass balances and steps towards scale-up

To obtain a better overview of the mass balance and provide a first step in upscaling, thermocatalytic conversion of nPUR with the optimal catalyst (alumina 8) was performed at the batch gram scale using a staged free-fall catalytic pyrolysis reactor setup described in earlier work by our group.[34] 3.0 g of sample and 3.0 g of catalyst were placed in a steel tube and loaded into the reactor's preheat chamber for 40 min at 200 °C. After 40 min, the sample was transferred to the first reactor and held at 550 °C for 30 min with an experimentally determined heating rate of 3 °C/min. After 30 minutes, the steel tube was transferred to a cooling zone, and the tube containing residue was collected for analysis. Operating details are available in the supplementary section.

The results showed 14 wt% solid residue in the tube, and 32 wt% collected liquid, of which 2% water. The gas yield was 54% and calculated on difference to obtain a closed mass balance. The liquid yielded on intake (wt%)/N-based yield (%): 5.2/10, 2.5/4.4, and 1.4/2.7 for aniline, toluidine, and MDA, respectively. The suboptimal results indicate that operational conditions are a vital consideration, as

the reactor's slow heat-transfer rates were not suitable for this process. For this reason, we were interested in using specifically fast catalytic pyrolysis setups, which are included in this work as continuous double-fluidized reactors (gram- and kilogram-scale).

Continuous catalytic pyrolysis of EOL PUR was performed in two setups consisting of a feeding system, two separate fluidized bed reactors operated in series, and a condensation system (Table 3.2). End-of-life rigid PUR feeds EOL_1 and EOL_2 were used for the gram-scale and kilogram-scale work, respectively. Feed preparations are described in the materials and methods supporting section. The compositions of the two feedstocks differ. For this reason, these were compared at milligram scale (TMR) to assess any compositional differences. The results showed about half the yields of aniline and toluidine for the EOL feeds compared to the nPUR (40.7 - 42.2 % for the EOL PURs vs 56.4 % for nPUR based on N-content in the feed, respectively, Table S3.4.17). As discussed above, the EOL feedstocks contain several elemental impurities, and the presence of other polymers, such as polystyrene, can potential, negatively affect the catalyst's performance. Thus, lower yields were expected upon scale-up experiments with the EOL feeds. Further investigations will be required to substantiate the precise causes for the decreased yields. Please note that all upscaling experimental work was performed under non-optimized conditions, as the recovery of aniline from rigid polyurethane had not been performed at this scale and setup before. Moreover, continuous operation introduced additional major challenges compared to batch operation. Examples of issues encountered included reactor blockages due to cold spots, mixing of the high-density catalyst with the low-density feed, collapse of the catalytic bed, poor condensation conditions due to the required high flow throughput resulting in failure to completely condense aniline into the liquid phase, and feeding low-density PUR into the system.

Table 3.2. Overview of results for the catalytic pyrolysis of PUR in the various setups

Set-up[a] (Mode/feed)	Temp. R1/R2 (°C)	Feedrate (g/h)	Total PUR fed (g)	Catalyst loading (g)	Yields An/Tol (N%)	Yield MDA (N%)
Mini plant[b] (ex-situ/ EOL_1)	500/ 550	139	556	450	17/10	0.0
Pilot plant[c] (In/ex-situ/EOL_2)	612/ 531	5000	15000	25000	14/12	0.0

[a]Alumina 8 and Alumina 5 were used as catalyst for the miniplant and the pilot plant, respectively
[b]Operating conditions: 139 g PUR per hour, R1 loaded with 400 g sand, and R2 loaded with 450 g catalyst, R1 500 °C, R2 550 °C, with a weight hourly space velocity (WHSV) of 0.31 h^{-1}, and a total operation time of 4 h
[c]Operating conditions: 5 kg PUR per hour, R1 loaded with 10 kg catalyst, and R2 loaded with 15 kg catalyst, R1 612 °C, R2 531 °C, with a weight hourly space velocity (WHSV) of 0.33 h^{-1}, and a total operation time of 3 h

The miniplant (continuous gram scale) was operated at a feedstock rate of 139 g h^{-1} (EOL_1) for a time on stream of 4 h. Products were collected and quantified, and the overall mass balance was determined Figure 3.7. The liquid yield calculated on input (according to calculation 3.4.6) was 36 wt%, comprising 30 wt% organics and 6.1 wt% water. The aniline yield on input (wt%)/ N-based (%) was: 9.8/17, and the toluidine yield was 6.4/10. Other products included N-containing compounds from cross-reactions and aromatics (e.g., styrene, which originates from the observed polystyrene

contamination). A significant amount of gas phase components was formed (19 wt%) with, among others, CO, CO_2, and small hydrocarbons (e.g., CH_4 and C_3H_6). The solid yield was 20 wt%, of which 14 wt% was coke and 5.7 wt% was determined to be minerals. The latter were mainly composed of Fe_2O_3 (2.1 wt%) and ZnO (1.6 wt%) in alignment with the ash composition discussed earlier.

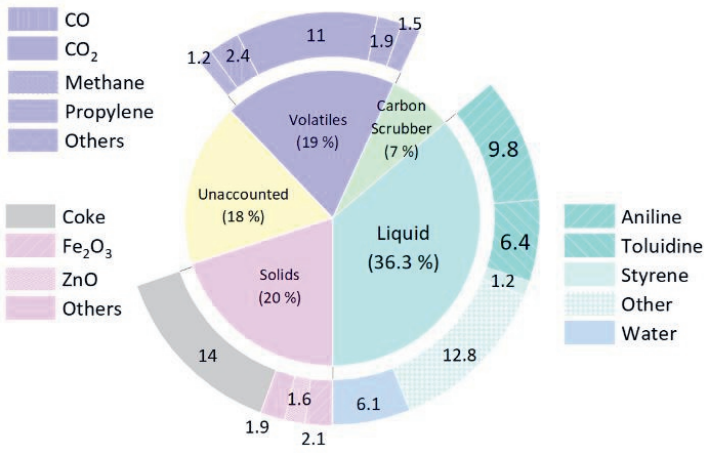

Figure 3.7. Mass balances for the ex-situ catalytic pyrolysis of EOL-1 PUR in the MPL using Alumina 8 as the catalyst. Operating conditions 139 g PUR per hour, R1 loaded with 400 g sand, and R2 loaded with 450 g catalyst, R1 500 °C, R2 550 °C, with a weight hourly space velocity (WHSV) of 0.31 h^{-1}, and a total operation time of 4 h. A comprehensive yield overview can be found in Table S3.4.24

The yields of aniline and toluidine versus time on stream (TOS) are illustrated in Figure 3.8. The yield initially increases with TOS, most likely due to the reactor's non-steady-state start-up, followed by relatively stable operation for 2 hours, with aniline and toluidine yields of 20% and 11 - 14%, respectively. After three hours of TOS, the yields are considerably reduced, most likely due to catalyst deactivation. The aniline/toluidine yields at 2 h and 3 h clearly demonstrate that, at scale, good yields of aniline and toluidine are achievable.

Scaling further, continuous kg-scale experiments were conducted in a two-stage pyrolysis unit (PPL) capable of processing 10 $kg_{feedstock}$ h^{-1}. For the upscaling experiments, 5 $kg_{feedstock}$ h^{-1} of EOL_2 polyurethane was fed via a conveyor screw system for a total of 3 h, with 10 kg of alumina 5 loaded in the first reactor and 15 kg alumina 5 in the second fluidized bed reactor. Over 3 h, products were collected and quantified. The liquid yield was 23 wt%, consisting of 16.9 wt% of organics and 5.6 wt% of water. The aniline yield on intake (wt%)/ N-based yield (%) was: 6.5/14, the toluidine yield was 6.3/11.6. Byproducts were aromatics BTX, and styrene. MDA was not detected. A total of 39% of gas-phase components were formed, including H_2, CO, CO_2, and small hydrocarbons (methane, ethane, ethylene, propane, and propylene). The solid yield was 28 wt% of which 26 wt% was coke and 1.4 wt% was minerals.

The nearly identical combined aniline and toluidine yields between continuous gram-scale and continuous kilogram-scale operation (27% and 26%, respectively) demonstrate the process upscaling potential. Although lower than the results from batch-milligram-scale experiments, all reported yields

in this work are far higher than those reported in the scientific literature and demonstrate a novel route for recycling rigid PUR foam. It is worth noting that these results are highly promising and unprecedented in both yield and scale, indicating that operating at scale can be further improved by optimizing the setup and conditions.

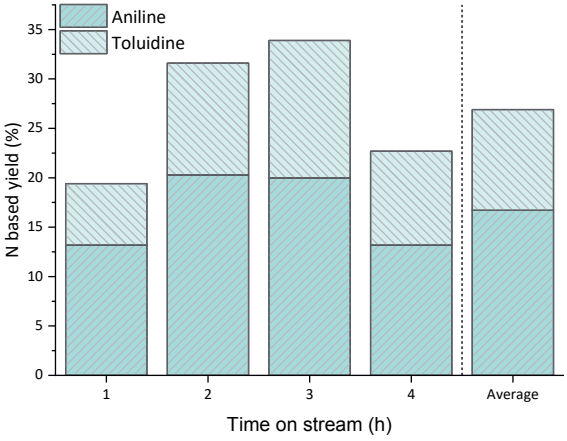

Figure 3.8. Aniline and toluidine yields versus TOS for the ex-situ catalytic pyrolysis of EOL_1 PUR in the miniplant using Alumina 8 as the catalyst. Operating conditions 139 g PUR per hour, R1 loaded with 400 g sand, and R2 loaded with 450 g catalyst, R1 500 °C, R2 550 °C, with a weight hourly space velocity (WHSV) of 0.31 h^{-1}, and a total operation time of 4 h. A comprehensive yield overview can be found in the section S3.3, Tables S3.4.16 – S3.4.18

Potential for climate change impact reduction and catalytic process performance metrics

The potential of the novel thermocatalytic chemical recycling process to reduce current climate change impacts was assessed with the environmental potential, an LCA-based methodology applicable to earlier stages of process development (Figure 3.9).[13,14] The environmental potential compares the impacts of an idealized, best-case recycling scenario that recovers aniline and toluidine with those of the real-world status quo, assumed here as waste incineration with energy recovery, when both processes treat 1 kilogram of PUR. Such a comparison provides an upper bound for the achievable climate change reduction through the recycling process and therefore gives guidance on whether a process is worth developing further.

For a non-catalytic pyrolysis of polyurethane, as described by Grittner *et al.*[35] (Table S3.4.1 and Figure 3.9), the potential for climate change reduction is 0.1 $kg_{CO2\text{-}eq}$ per $kg_{treatedPUR}$. In comparison, the upscaled thermal catalytic process in continuous operation increases the potential for climate change reduction to 0.6 $kg_{CO2\text{-}eq}$ per $kg_{treatedPUR}$, motivating its further development. Moreover, if these calculations are extended to the achieved yields in the batch mg setup, climate change could potentially be reduced by as much as 1.3 $kg_{CO2\text{-}eq}$ per $kg_{treatedPUR}$ (see supporting section for more details), highlighting the benefits from improved yields.

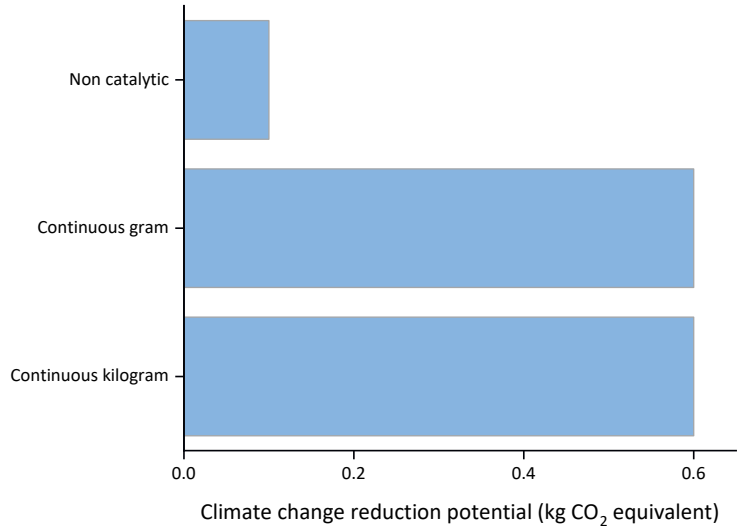

Figure 3.9. Environmental potential of the PUR recycling pathways to reduce climate change impacts in comparison to the current waste treatment practice of incineration with energy recovery for 1 kg of PUR treated. The environmental potential determines an upper bound for climate change reductions

A preliminary analysis focused on catalyst performance requirements with respect to economic margins derived from input (PUR) and output (aniline) prices was conducted to assess the economic feasibility of the developed process (see Section S7.2 for calculation details). The amount of catalyst used in the 4-hour run on the miniplant (556 g PUR input with 850 g catalyst) under unoptimized conditions, without catalyst reactivation, was compared to a maximum catalyst consumption based on the miniplant yields (16 wt% aniline and toluidine) using the calculated margin between input and output values. A 9437 $kg_{cat} \cdot ton_{prod}^{-1}$ was calculated for the 4-hour run against a maximum consumption of 867 $kg_{cat} \cdot ton_{prod}^{-1}$ for an economically neutral situation. Therefore, a minimal extension of the catalyst lifetime of 44 hours is required to achieve breakeven. Typical processes require a catalyst to run for at least 2.5 months to achieve a breakeven value.[36] However, less stringent catalyst lifetimes are required for this process due to the high product market prices even without taking into account potential value of other generated side products. Additionally, the results are likely to improve, as continuous gram-scale yields were obtained under non-optimized conditions. The best catalyst is currently a specialty catalyst, which likely will become less expensive upon bulk implementation. Long-term catalyst stability and regeneration potential has not been tested yet, but these catalyst performance targets seem within reach.[36]

An important is that large investment costs are expected to set up this value chain; the eventual viability will be determined by the realized yields of valuable outputs, such as aniline and toluidine, as well as the potential value of other cogenerated products. One important consideration is that the proposed thermocatalytic pyrolysis is currently the only viable closed-loop recycling option that can provide aniline to produce rigid PUR foam with the same product quality. Upcoming stricter regulations on recycled content, increased fees for waste disposal via incineration, and circularity targets could affect the potential investments.

3.3 Conclusions

In this work, we presented a novel method for chemically recycling end-of-life rigid MDA-based polyurethane foam via catalytic pyrolysis. Our developed process enables aniline recovery from PUR recycling to produce new polyurethane foam with chemical and physical properties equal to those of fossil-based PUR. The results presented in this paper demonstrate that the depolymerization of rigid polyurethane foam to aniline is feasible via catalytic pyrolysis using an alumina-based catalyst. A statistical analysis was performed to correlate the aniline yield to catalyst properties. For this reason, an extensive catalyst characterization was performed. The analysis of variance showed that γ-alumina catalysts with high Lewis acidity and preferably high surface area provide the best results for aniline yield. The yield could be increased from 40% to 51% by changing the surface area from 179 m^2/g to 218 m^2/g and the acidity from 330 µmol/g to 406 µmol/g.

Scaling was performed at batch milligram, gram, and continuous gram-, kilogram scales. The largest scale still allowed 26% aniline and toluidine molar yields at a 5 $kg_{feedstock}$ h^{-1} operation for 3 hours. It should be noted that further optimization is a critical factor in techno-economic analysis, as running efficiency is directly correlated with operational costs. Nevertheless, the continuous kilogram-per-hour operation (pilot plant) demonstrated the potential to reduce climate change impacts by 0.6 $kg_{CO2\text{-}eq}$ per $kg_{treatedPUR}$ compared to waste incineration even under non-optimized conditions. The ultimate climate benefits depend on the greenhouse gas emissions in the rest of the value chain and its energy demands. Preliminary techno-economic analysis of continuous gram-scale operation showed a positive balance at a catalyst lifetime of only 44 hours.

References

1. Kemona, A. & Piotrowska, M. Polyurethane recycling and disposal: Methods and prospects. *Polymers (Basel).* **12**, 1752 (2020).
2. Nikje, M. M. A., Garmarudi, A. B. & Idris, A. B. Polyurethane waste reduction and recycling: From bench to pilot scales. *Des. Monomers Polym.* **14**, 395–421 (2011).
3. Banik, J., Chakraborty, D., Rizwan, M., Shaik, A. H. & Chandan, M. R. Review on disposal, recycling and management of waste polyurethane foams: A way ahead. *Waste Management and Research* **41**, 1063–1080 (2023).
4. Zia, K. M., Bhatti, H. N. & Ahmad Bhatti, I. Methods for polyurethane and polyurethane composites, recycling and recovery: A review. *React. Funct. Polym.* **67**, 675–692 (2007).
5. Deng, Y. *et al.* Reviewing the thermo-chemical recycling of waste polyurethane foam. *J. Environ. Manage.* **278**, 111527 (2021).
6. Akindoyo, J. O. *et al.* Polyurethane types, synthesis and applications-a review. *RSC Adv.* **6**, 114453–114482 (2016).
7. Krupers, M. J., Bartelink, C. F., Gr, H. J. M. & M611er, M. Formation of rigid polyurethane foams with semi-fluorinated diblock copolymeric surfactants. *Polymer.* **39**, 2049–2053 (1998).
8. Datta, J., Kopczyńska, P., Simón, D. & Rodríguez, J. F. Thermo-Chemical Decomposition Study of Polyurethane Elastomer Through Glycerolysis Route with Using Crude and Refined Glycerine as a Transesterification Agent. *J. Polym. Environ.* **26**, 166–174 (2018).
9. Özkan, M. & Engell, S. Design of the Systemic Modelling and Analysis Framework. *https://circular-foam.eu/Outcomes/Deliverables.html* https://circular-foam.eu (2023).

10. Liu, B. *et al.* Opportunities in Closed-Loop Molecular Recycling of End-of-Life Polyurethane. *ACS Sustain. Chem. Eng.* **11**, 6114–6128 (2023).
11. Bulan, A. *et al.* Process for producing isocyanates. (2012) doi:US8,153,838B2.
12. Eiden, S. *et al.* Pyrolysis of polyurethane compound-containing material in order to recover raw materials. Patent US 2024/0254395 A1, (2024).
13. Meys, R. *et al.* Towards a circular economy for plastic packaging wastes – the environmental potential of chemical recycling. *Resour. Conserv. Recycl.* **162**, 105010 (2020).
14. Pillich, M., Schilling, J., Bosetti, L. & Bardow, A. What to do with polyurethane waste? The environmental potential of chemically recycling polyurethane rigid foam. *Green Chemistry* **26**, 10893–10906 (2024).
15. Bharti, K. & Kaur, R. A Review Of Chemical Recycling Pathways For Waste Polyurethane. *Metall. Mater. Eng.* 1781–1803 (2025) doi:10.63278/mme.vi.1767.
16. Van Belleghem, L. *et al.* Recovery of Polyol and Aromatic Amines from Rigid Polyurethane Foams via Ammonolysis. *JACS Au* **5**, 3444–3452 (2025).
17. van Akker, M. *et al.* Full Utilization of Hard-to-Recycle Mixed Plastic Waste by Conversion toward Pyrolysis Oil and BTX Aromatics on a Pilot Scale. *Energy and Fuels* **39**, 6438–6451 (2025).
18. Zheng, S. *et al.* Benzenoid Aromatics from Renewable Resources. *Chem. Rev.* **124**, 10701–10876 (2024).
19. Xu, S. *et al.* Insight into waste polyurethane pyrolysis pathways: Mechanism functions analysis and in-situ coupling online monitoring. *J. Anal. Appl. Pyrolysis* **177**, 106301 (2024).
20. Guo, X., Wang, L., Li, S., Tang, X. & Hao, J. Gasification of waste rigid polyurethane foam: optimizing operational conditions. *J. Mater. Cycles Waste Manag.* **17**, 560–565 (2015).
21. Guo, X., Wang, L., Zhang, L., Li, S. & Hao, J. Nitrogenous emissions from the catalytic pyrolysis of waste rigid polyurethane foam. *J. Anal. Appl. Pyrolysis* **108**, 143–150 (2014).
22. Terakado, O., Yanase, H. & Hirasawa, M. Pyrolysis treatment of waste polyurethane foam in the presence of metallic compounds. *J. Anal. Appl. Pyrolysis* **108**, 130–135 (2014).
23. Bozi, J. & Blazsó, M. Catalytic thermal decomposition of polyamides and polyurethanes mixed with acidic zeolites. *J. Anal. Appl. Pyrolysis* **97**, 189–197 (2012).
24. Anand, R., Maheswari, R., Hegde, S. G. & Rao, B. S. Alkylation of o-toluidine with methanol over acidic zeolites. *J. Mol. Catal. A Chem.* **192**, 253–262 (2003).
25. Nordquist, A. F., Pierantozzi, R. & of Pa Assignee, both. Process for the disproportionation of alkylated aromatic primary amines. (1989). Doi: 4,801,751.
26. Bozi, J. & Blazsó, M. Catalytic thermal decomposition of polyamides and polyurethanes mixed with acidic zeolites. *J. Anal. Appl. Pyrolysis* **97**, 189–197 (2012).
27. Marella, A. *et al.* Quinoline: A versatile heterocyclic. *Saudi Pharmaceutical Journal* **21**, 1–12 (2013).
28. Gluszynska, A. Biological potential of carbazole derivatives. *Eur. J. Med. Chem.* **94**, 405–426 (2015).
29. Granados-Correa, F. & Bulbulian, S. Surface characterization of γ-al2o3 powders and their co2+ adsorption properties. *Int. J. Appl. Ceram. Technol.* **10**, E295–E303 (2013).
30. Flego, C., O', W. & Parker, N. Characterization of γ-alumina and borated alumina catalysts. *Appl. Catal. A Gen.* **185**, 137–152 (1999).

31. Seki, T. & Onaka, M. Elucidation of basic properties of mesoporous alumina through the temperature-programmed desorption of carbon dioxide and heterogeneous basic catalysis of mesoporous alumina for the Knoevenagel reaction in supercritical CO2. *J. Mol. Catal. A Chem.* **263**, 115–120 (2007).
32. Wang, S., Li, X., Wang, S., Li, Y. & Zhai, Y. Synthesis of γ-alumina via precipitation in ethanol. *Mater. Lett.* **62**, 3552–3554 (2008).
33. Chauruka, S. R. *et al.* Effect of mill type on the size reduction and phase transformation of gamma alumina. *Chem. Eng. Sci.* **134**, 774–783 (2015).
34. He, S. *et al.* Novel Staged Free-Fall Reactor for the (Catalytic) Pyrolysis of Lignocellulosic Biomass and Waste Plastics. *Energy and Fuels* **38**, 8740–8748 (2024).
35. Grittner, N., Kaminsky, W. & Obst, G. Fluid bed pyrolysis of anhydride-hardened epoxy resins and polyether-polyurethane by the Hamburg process. *J. Anal. Appl. Pyrolysis* **25**, 293–299 (1993).
36. Lange, J. P. Performance metrics for sustainable catalysis in industry. *Nat. Catal.* **4**, 186–192 (2021).

3.4 Supporting information

State of the art overview

A summarized overview of all published work in which aniline is both mentioned and quantified on the (non)catalytic pyrolysis of rigid polyurethane is shown in Table S3.4.1 For work on the (non)catalytic thermal degradation of polyurethane, see Table S3.4.2.

Table S3.4.1.State-of-the-art on the (non)catalytic pyrolysis of polyurethane, in which aniline is mentioned and is quantified

Group [year]	Operating conditions and reactor bed (temperature)	Type of PUR (composition)	Scale	Catalyst	Volatiles (%)[a]	Oil[a] /aniline (%)	Solids[a] (%)
Grittner [1993][1]	Continuous fluidized bed (700 °C)	Model (polyether, MDI)	1.6 kg	No cat	65	15/0.9	15
Font [2000][2]	Batch fixed bed/pyroprobe (600 °C)	Model (polyol, MDI)	5.0 mg	No cat	*ND*	*ND/0.6*[b]	*ND*
Guo [2015][3]	Batch fixed bed (1100 °C)	End-of-life (not defined)	2.14 g	CaO[d]	*ND*[e]	*ND/4.5*[e]	*ND*
Stancin [2019][4]	Batch fixed bed/quartz tube (500 °C)	End-of-life (not defined)	0.2 mg	No cat	*ND*	*ND/0.9*[c]	*ND*
Kaminsky [2021][5]	Continuous fluidized bed (750 °C)	Model (polyethylene glycol, MDI)	10 kg	No cat	*ND*	*ND/0.4*	*ND*
Eiden [2022][6]	Batch fixed bed (500 °C)	Model (polyol, pMDI)	1.0 g	γ -Al_2O_3[i]	ND	[h]70/10	30
Eiden [2022][6]	Batch fixed bed (500 °C)	Model (polyol, pMDI)	1.0 g	B-Al_2O_3[i]	21	69/19	10
Zeller [2025][7]	Batch fixed bed (550 °C)	Model (polyether polyol, MDI)	1.5 – 4.5 g	No cat	25	62/4.4[k]	13
This work [2026]	Batch fixed bed (550 °C)	Post production (polyol, pMDI)	0.5 mg	Alumina 8[f]	ND	ND/26[g]	ND
This work [2026]	Continuous fluidized bed (500 °C)	End-of-life	556 g	Alumina 8	19	30/7.3[g]	26
This work [2026]	Continuous fluidized bed (612 °C)	End-of-life	15 kg	Alumina 5	39	17/6.5[g]	28

[a]Values rounded to zero decimals for simplicity
[b]Values shown are exclusively based on area integration and do not represent a complete mass balance
[c]Values shown are exclusively based on the total amount of harmful chemicals and do not represent a complete mass balance
[d]Catalyst considered in this work are: CaO, $CaCO_3$, NaOH, $Ca(OH)_2$
[e]Values depicted are exclusively based on the sum of nitrogen containing compounds and do not represent a complete mass balance
[f]Catalyst used in this work are: RuO_2, BaO, CaO, CdO, La_2O_3, MgO, Fe_2O_3, Tb_2O_3, Ga_2O_3, SrO, TiO_2, CeO_2, Y_2O_3, Nb_2O_5, Bentonite, ZrO_2, B_2O_3, Sepionite, HfO_2, α-Al_2O_3, Alumina 4, TH 100/150, ScFa 140, Sba 200, Scca 150/230, Scca 5/150, Alumina 0, Scca 150/200, Scca 5/200
[g]Depicted Yields are calculated on input via calibration of according products
[h]Depicted value is liquid yield of which 50% oil and 20% water
[i]Catalyst considered in this work are: γ-Al_2O_3, Hydrotalcite, Basic-Al_2O_3 precursor (MgO with Al_2O_3)
[j]Depicted values in italic are calculated on area integration
[k]Determined via calibration of according compound on GC-MS

Table S3.4.2. State-of-the-art on the (non)catalytic pyrolysis of polyurethane, in which aniline is mentioned and is quantified

Group [Year]	Type of feed (cat)	Origin feedstock (composition)	Technique
Lattimer [1990][8]	Post production (no cat)	Morthane CA-128 (polyester, MDI,TDI,HDI)	Py-CI-MS/MS
Takamoto [1994][9]	Post production (Char, activated carbon)	Reaction injection molding (polyol, MDI)	GC
Esperanza [1999][10]	EOL (no cat)	EOL Furniture waste (polyol, MDI,TDI NDI, HDI)	GC-MS/TCD, TGA
Moroi [2003][11]	Model ($FeCl_3$, $CrCl_3$)	PEDA/EG[b], MDI, metalCl (polyol, MDI, metalchlorides)	TGA
Pielichowski [2003][12]	Model (no cat)	Various diols, pMDI (MDI)	TGA-IR/MS
Moroi [2004][13]	Model (metal chlorides)[a]	PEDA/EG[b], MDI, MetalCl (polyol, MDI, metalchlorides)	TGA
Bozi [2012][14]	Model (NH_4NaY, HUSY)	PA6,6, PA-6, PUR_{eth}, PUR_{est} (polyamide, polyether, polyester, MDI)	Py-GC/MS, TGA-MS
Bozi [2013][15]	Model (NH_4Y, HUSY)	PA6,6, PA-6, PUR_{eth}, PUR_{est} (polyamide, polyether, polyester, MDI)	Py-GC/MS, TGA-MS
Terakado [2014][16]	Post production (various catalysts) [d]	Toyo tire & rubber (Polyol, MDI,TDI)	GC-MS, TGA
Guo [2015][17]	EOL (various catalysts) [e]	EOL PUR (polyol, MDI)	GC-FID/TCD
Pagacz [2016][18]	Model (no cat)	Sorbitol based, pMDI (polyether, MDI)	TGA-IR
He [2016][19]	Model (no cat)	Shandong Lecron, Energt-saving New Material Co. Ltd. (Polyether polyol, MDI)	GC-MS, TGA-FTIR
Guo [2016][20]	EOL (alkali, transition)[c]	EOL Refrigerator (polyol, MDI)	GC-MS/TCD
Yuan [2018][21]	Model compound (NiMoO4)[a]	LY-4110 & PAPI (polyol, MDI)	TGA-IR
Kumagai [2019][22]	Post production (Ni/Mg/Al)	Domestic market Japan (Polyol, TDI, MDI)	Py-GC/MS, TGA-IR
Yao [2020][23]	EOL (no cat)	EOL recycling plant (polyol, MDI)	TGA-IR/MS
Nishiyama [2020][24]	Model (no cat)	Commercial chemicals (butanediol, glycol, MDI)	Py-GC/MS
Eschenbacher [2021][25]	Post production (no cat)	Recticel, Unilin (Polyether polyol, TDI, MDI)	Py-GC/MS-FID, TGA
Xu [2024][26]	EOL (no cat)	Waste refrigerator (polyol, MDI)	TGA-IR/MS

[a]metals used in this work: manganese, cobalt, copper, iron, chromium
[b]PEDA/EG is a polyester (PEDA) bonded to a chain extender (EG)
[c]catalyst used in this work: NaOH, NaCO3, CaO, CaOH, CaCO3, MgO, MgCO3, Fe, FeCl3, MgO2
[d]Catalysts used in this work: $ZnCl_2$, $CuCl_2$, $FeCl_3$, $FeCl_2$, $Fe(NO_3)_3$, , $Cu(NO_3)_2$, $Zn(NO_3)_2$, La_2O_3, ZnO, Fe_2O_3, Nd_2O_3
[e]Catalyst used in this work: Fe, Ni:Mg:Fe 1:1:1, $FeCl_3$, MgO, CaO, $MgCO_3$, Na_2CO_3, $CaCO_3$, $Ca(OH)_2$, NaO

Materials & methods

New produced PUR (nPUR)

New rigid polyurethane refrigerator foam obtained from Covestro Germany was used as the feedstock for all batch milligram- and batch gram-scale reactions, including general catalyst screening, specific alumina-based analysis, and upscaling work. The feed was cryo-milled to powder prior to use using an IKA Tube Mill 100 control. Elemental analysis and metal content of the PUR were analyzed using a CHNS analyzer and XRF, respectively. The metal content was calculated based on the polyurethane ash content (0.8%). Results are shown in Table S3.4.3. Specific elements were used in the production of polyurethane. Cyclopentane as a blowing agent, silicon as an additive, and calcium oxide and titanium dioxide as whiteners. The presence of potassium, iron, and magnesium has not been attributed to any specific purpose. These elements are likely contaminants from transportation. It should be noted that the assumption was made that each impurity was in the oxygenated state and not in the elemental state.

Table S3.4.3. Chemical composition of nPUR refrigerator foam obtained from Covestro Germany

C[a] (%)	H[a] (%)	N[a] (%)	O[b] (%)
65.7	6.69	7.52	19.5

Silicon[c,d] (%)	CaO[c,d] (%)	K_2O[c,d] (%)	Fe_2O_3[c,d] (%)	MgO[c,d] (%)	TiO_2[c,d] (%)
0.206	0.144	0.144	0.0037	0.035	0.003

Average of 2 measurements
[b]Based on deduction of CHN
[c]Percentage calculated on absolute ash values determined via XRF multiplied by 0.8% ash content
[d]Impurity values below 25 ppm have been left out for brevity

End-of-life_1 PUR (EOL_1)

This End-of-life rigid polyurethane refrigerator foam was received from Covestro Germany and used for batch milligram, batch, and continuous gram- and kilogram-scale operations. The foam originates from the Turkish waste facility Arçelik. Covestro Germany received the waste and performed a pretreatment prior to use. The polyurethane has been milled and pressed into pellets without binder material to enable continuous gram-scale reactions, allowing PUR to be fed into the reaction via a feeding screw. A total impurity level of 18.3% was present in the feed. For use on batch milligram and gram reactions, an additional cryo-milling step was performed using an IKA Tube Mill 100 to reduce the particle size.

Elemental analysis and metal content of the PUR were analysed using a CHNS analyser and XRF, respectively. The absolute amount of metal content was calculated based on the polyurethane ash content (5.68%). Results are shown in Table S3.4.4. Specific elements were used in the production of

polyurethane. Cyclopentane as a blowing agent, silicon as an additive, calcium oxide, and titanium dioxide as whiteners. The presence of the remaining metals has been attributed to impurities originating from refrigerator metal parts and during transportation. It should be noted that the assumption was made that each impurity was in the oxygenated state and not in the elemental state.

Table S3.4.4. Chemical composition of end-of-life rigid polyurethane foam obtained from waste refrigerators (EOL_1)

C[a] (%)	H[a] (%)	N[a] (%)	S[a] (%)	O[b] (%)
64.5	6.95	6.62	0.42	21.5

Fe_2O_3[c,d] (%)	ZnO[c,d] (%)	TiO_2[c,d] (%)	CaO[c,d] (%)	CuO[c,d] (%)	Sillicon[c,d] (%)	Al_2O_3[c,d] (%)
2.12	1.60	0.700	0.425	0.227	0.164	0.084
K_2O[c,d] (%)	Yb_2O_3[c,d] (%)	Cr_2O_3[c,d] (%)	SrO[c,d] (%)	Sb_2O_3[c,d] (%)	MgO[c,d] (%)	V_2O_5[c,d] (%)
0.065	0.018	0.016	0.012	0.012	0.011	0.009
SnO_2[c,d] (%)	MnO[c,d] (%)	ZrO_2[c,d] (%)	V_2O_5[c,d] (%)	SnO_2[c,d] (%)		
0.008	0.007	0.005	0.009	0.008		

[a]Average of 2 measurements
[b]Based on deduction of CHNS.
[c]Percentage calculated on absolute ash values determined via XRF multiplied by 5.7% ash content
[d]Impurity Values below 25 ppm have been left out for brevity

End-of-life_2 PUR (EOL_2)

This End-of-life rigid polyurethane refrigerator foam was received from Covestro Germany and used for batch milligram, batch, and continuous gram- and kilogram-scale operations. The foam originates from the French waste facility Suez. Covestro Germany received the waste and performed a pretreatment prior to use. The polyurethane has been milled and pressed into pellets without binder material to enable continuous gram-scale reactions, allowing PUR to be fed into the reaction via a feeding screw. A total impurity level of 12.3% was present in the feed. For use on batch milligram and gram reactions, an additional cryo-milling step was performed using an IKA Tube Mill 100 to reduce the particle size.

Elemental analysis and metal content of the PUR were analysed using a CHNS analyser and XRF, respectively. The absolute amount of metal content was calculated based on the polyurethane ash content (2.66%). Results are shown in Table S3.4.5. Specific elements were used in the production of polyurethane. Cyclopentane as a blowing agent, silicon as an additive, calcium oxide, and titanium dioxide as whiteners. The presence of the remaining metals has been attributed to impurities that

originate from refrigerator metal parts. It should be noted that the assumption was made that each impurity was in the oxygenated state and not in the elemental state.

Table S3.4.5. Chemical composition of end of life rigid polyurethane foam obtained from waste refrigerators (EOL_2)

C[a] (%)	H[a] (%)	N[a] (%)	S[a] (%)	O[b] (%)
66.04	6.71	7.14	0.21	19.9

Fe_2O_3[c,d] (%)	CaO[c,d] (%)	TiO_2[c,d] (%)	Sillicon[c,d] (%)	CuO[c,d] (%)	Al_2O_3[c,d] (%)	MgO[c,d] (%)	
0.668	0.447	0.365	0.286	0.284	0.090	0.082	
K_2O[c,d] (%)	BaO[c,d] (%)	MnO[c,d] (%)	SrO[c,d] (%)	Cr_2O_3[c,d] (%)	SnO_2[c,d] (%)	TeO_2[c,d] (%)	V_2O_5[c,d] (%)
0.025	0.016	0.012	0.006	0.005	0.004	0.004	0.004

[a]Average of 2 measurements
[b]Based on deduction of CHNS
[b]Percentage calculated on absolute ash values determined by multiplying by 2.66% ash content
[d]Impurity Values below 25 ppm have been left out for brevity

Composition summary of used feedstocks

Figure 3.4.1. shows the IR spectra of all measured PUR samples. The graph shows a distinct MDI-based signal at 1500 cm^{-1} and the absence of a distinct TDI-based signal at 1080 cm^{-1} for all three feeds. A summary of the chemical compositions of all feeds is depicted in Table S3.4.6.

Table S3.4.6. Summary of chemical composition of PUR feeds, calculation details are according to calculation 3.4.1

Feed	N content from elemental analysis (%)	Inerts[a] (%)	Other impurities[b] (%)	Total amount of PUR present in feed (%)
nPUR	7.52	0.80	ND	99.2
EOL_1	6.62	5.68	18.32	76.0
EOL_2	7.14	2.66	12.34	85.0

[a]Average of 2 measurements determined via ash content
[b]Impurities include polystyrene, cyclopentane as blowing agent, and other unidentified end-of-life incorporated impurities

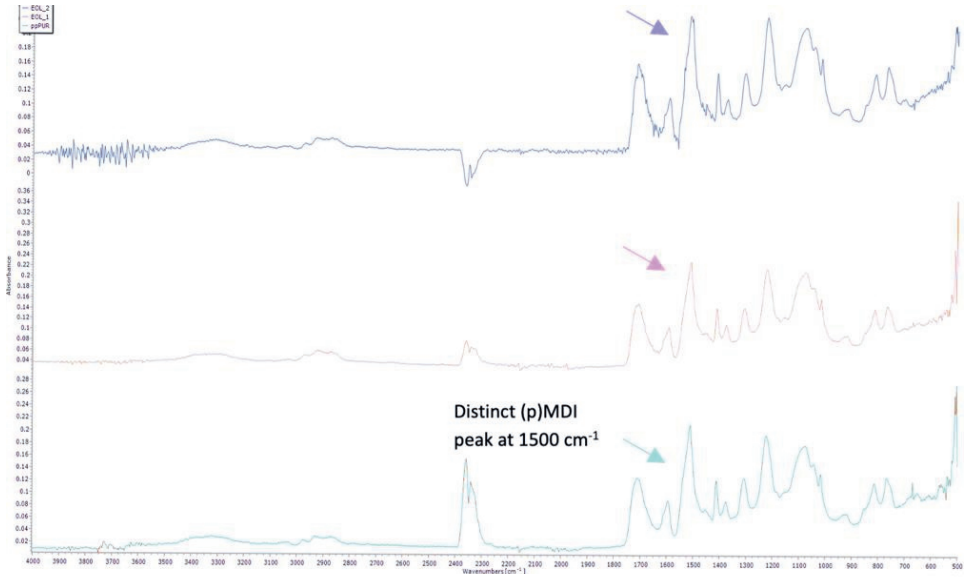

Figure 3.4.1. FTIR spectra of the three used feeds: nPUR,EOL_1, and EOL_2

Catalysts details

The catalysts used for the general catalyst screening, excluding alumina 4 and magnesium oxide, have been purchased from Sigma Aldrich. Netmag has kindly provided magnesium oxide. All the alumina oxides excluding α-alumina, alumina 0, and alumina 4 have been kindly provided samples by Sasol Germany. α-alumina, alumina 0, and alumina 4 have been purchased from Sigma Aldrich. The exact names of the catalysts have been depicted below

Table S3.4.7. Original names of used alumina based catalysts

Catalyst code	Commercial identifer
Alumina 0	Al_2O_3 from Sigma Aldrich (CAS: 1334-28-1)
Alumina 1	TH 100/150
Alumina 2	ScFa 140
Alumina 3	Scca 5/150
Alumina 4	Al_2O_3 from Sigma Aldrich (CAS 1334-28-1)
Alumina 5	Scca 150/200
Alumina 6	Sba 200
Alumina 7	Scca 150/230
Alumina 8	Scca 5/200

General catalyst screening analysis

Table S3.4.8. Chemical composition of the catalysts used for the general screening, determined via XRF

Catalyst[a,b]	Compound 1 (%)	Compound 2 (%)	Compound 3 (%)	Compound 4 (%)
RuO_2	RuO_2 (99.6)	CaO (0.394)	-	-
BaO	BaO (99.4)	SnO_2 (0.198)	CaO (0.189)	TeO_2 (0.172)
CaO	CaO (99.7)	SiO_2 (0.123)	-	-
CdO	CdO (98.4)	K_2O (1.38)	-	-
La_2O_3	La_2O_3 (99.2)	CaO (0.278)	TeO_2 (0.185)	SnO_2 (0.173)
MgO	MgO (89.3)	CaO (5.21)	Fe_2O_3 (3.86)	MnO (0.769)
Fe_2O_3	ND	-	-	-
Tb_2O_3	Tb_2O_3 (98.2)	MgO (1.05)	SiO_2 (0.225)	CaO (0.225)
Ga_2O_3	Ga_2O_3 (99.6)	CaO (0.13)	MgO (0.125)	-
SrO	SrO (99.7)	CaO (0.260)	-	-
TiO_2	TiO_2 (99.4)	K_2O (0.218)	Nd_2O_3 (0.202)	-
CeO_2	CeO_2 (99.3)	CaO (0.257)	TeO_2 (0.166)	SnO_2 (0.145)
Y_2O_3	Y_2O_3 (98.66)	SiO_2 (0.881)	CaO (0.318)	Dy_2O_3 (0.109)
Nb_2O_5	Nb_2O_5 (99.5)	CaO (0.348)	-	-
Bentonite	SiO_2 (42.9)	Fe_2O_3 (25.2)	Al_2O_3 (13.0)	CaO (11.0)
ZrO_2	ZrO_2 (96.8)	HfO_2 (2.20)	CaO (0.34)	CeO_2 (0.164)
B_2O_3[c]	CaO (49.7)	TiO_2 (28.1)	TeO_2 (10.5)	SnO_2 (8.72)
Sepionite	ND	-	-	-
HfO_2	HfO_2 (99.1)	SO_3 (0.441)	CaO (0.329)	SeO_2 (0.108)

[a]Only 4 main compounds have been depicted to maintain clarity
[d]Impurity Values below 25 ppm have been left out for brevity
[c]Mass of elemental Boron is not detectible via XRF, the compounds shown are relatively impurity levels

Alumina based catalyst analysis

Table S3.4.9. Chemical composition of the catalysts used in the alumina screening, determined via XRF

Catalyst[a,b]	Compound 1 (%)	Compound 2 (%)	Compound 3 (%)	Compound 4 (%)
α-Al_2O_3	Al_2O_3 (98.6)	CaO (0.575)	MgO (0.357)	SiO_2 (0.243)
Alumina 0	Al_2O_3 (99.1)	MgO (0.650)	CaO (0.150)	-
Alumina 1	Al_2O_3 (98.8)	CaO (0.120)	-	-
Alumina 2	Al_2O_3 (99.0)	MgO (0.710)	CaO (0.140)	TiO_2 (0.130)
Alumina 3	Al2O3 (98.9)	CaO (0.430)	MgO (0.350)	-
Alumina 4	Al2O3 (99.1)	MgO (0.692)	CaO (0.181)	-
Alumina 5	Al2O3 (98.5)	CaO (0.518)	TiO2 (0.392)	MgO (0.262)
Alumina 6	Al2O3 (98.9)	MgO (0.840)	CaO (0.140)	-
Alumina 7	Al2O3 (99.0)	MgO (0.635)	TiO2 (0.188)	CaO (0.173)
Alumina 8	Al_2O_3 (99.1)	MgO (0.660)	CaO (0.170)	-

[a]Only 4 main compounds have been depicted to maintain clarity
[d]Impurity Values below 25 ppm have been left out for brevity

Catalyst SEM and TEM analysis

The agglomerate and particle size of each catalyst were measured by SEM and TEM, respectively. For SEM, at least 60 particles were measured per sample, and for TEM, at least 200 particles were measured to ensure a reliable measurement (see Figures S3.4.2 & S3.4.3 below for examples). The images of alumina 4 and alumina 8 are shown below since alumina 4 was used for the general screening and alumina 8 was selected as the best performing catalyst.

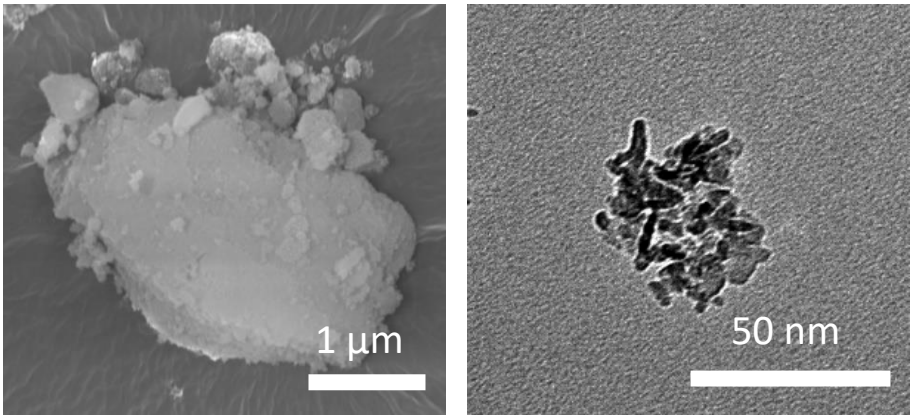

Figure 3.4.2. SEM (left) and TEM (right) image of Alumina 4

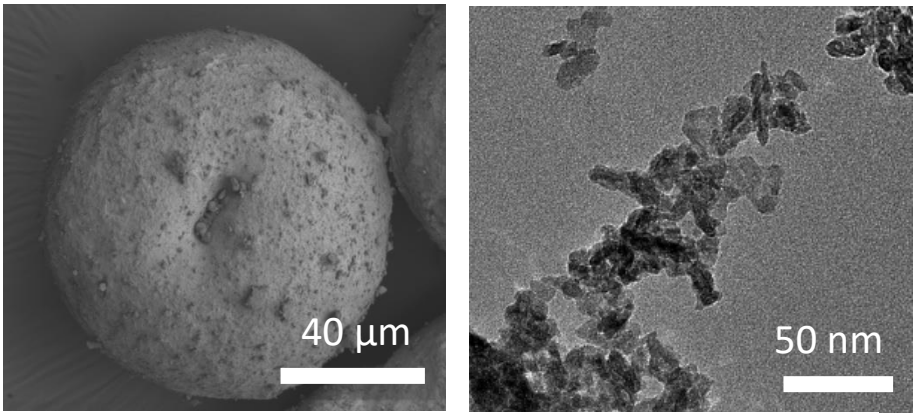

Figure 3.4.3. SEM (left) and TEM (right) image of Alumina 8

Structural characterization techniques

The chemical composition of the catalyst was measured on a Panalytical epsilon 3XLE. The nominal composition of elements was expressed as oxides, and the sum of the obtained concentrations was normalized to 100%. Approx. 1 g of catalyst was placed in a plastic holder with a 6 µm mylar film as the bottom.

Nitrogen physisorption experiments were conducted using a Micromeritics ASAP 2420 analyzer to determine the surface area. A 100 – 200 mg sample was placed in a BET tube with a filler rod and

sealed with a seal frit. The sample sorbents were degassed at 300 °C under a vacuum atmosphere for 12 hours prior to measurement. Adsorption isotherms were collected at -196 °C (77 K) over a relative pressure range of 0.01–1.00. The surface area was calculated using the Brunauer, Emmett, and Teller (BET) method, assuming a relative pressure between 0.03 and 0.30. The pore size distribution and pore volume were determined using the Barrett-Joyner-Halenda (BJH) method, while the micropore volume was calculated using the t-plot method.

All NH_3-temperature programmed desorption (NH_3-TPD) experiments were performed on a Micromeritics AutoChem II 2920 analyzer to determine the total acidity. A 100 - 200 mg sample was placed between quartz wool in a quartz U-tube. Before measurement, a pre-treatment step was performed by heating the sample to 550 °C with a helium flow of 50 mL/min for 30 minutes. Adsorption of 10 % NH_3 in He (50 mL/min) occurred at 100 °C for 120 minutes, followed by desorption between 100 – 900 °C at 10 °C/min with a helium flow of 50 mL/min for 15 minutes. The downstream gas was directed to a TCD detector for analysis. The concentration of NH_3 was determined by the intensities of m/z at 17.

CO_2-temperature-programmed desorption (CO_2-TPD) was performed on a Micromeritics AutoChem II 2920 analyzer to determine the total basicity. A 100 - 200 mg sample was placed between quartz wool in a quartz U-tube. Before measurement, a pre-treatment step was performed by heating the sample to 550 °C with a helium flow of 50 mL/min for 30 minutes. Adsorption of 10 % CO_2 in He (50 mL/min) occurred at 100 °C for 120 minutes, followed by desorption between 100 – 900 °C at 10 °C/min with a helium flow of 50 mL/min for 15 minutes. The downstream gas was directed to a TCD detector for analysis. The concentration of CO_2 was determined from the intensities at m/z 44.

The acidity ratio was determined via Pyridine Infrared (Py-IR). Experiments were conducted using a non-commercial device equipped with a Bruker Vertex 70 spectrophotometer coupled to an LN-MCT detector. Sample preparation involved pressing a waver from the catalyst (without a binder) and placing it in a custom holder. Prior to measurement, a pre-treatment step was carried out by heating the sample to 300 °C under reduced pressure for 8 hours. The sample was then cooled to room temperature, and a reference spectrum was recorded. Each spectrum was recorded with 128 scans and a resolution of 4 cm^{-1}. Pyridine adsorption was conducted at room temperature for 30 minutes, followed by removal of excess pyridine by vacuum for 30 minutes. A spectrum was recorded, and the reference spectrum was subtracted. The resulting spectra were expressed as absorbance in the spectral range between 1000 – 4000 cm^{-1}. Data processing was performed using OPUS 7.0 software.

The microstructure of the catalyst has been characterized using transmission electron microscopy (TEM) on a Tecnai T20 equipped with a LaB6 filament and a Cryo-EM Gatan 626 stage with a 4K CCD camera. An EDX Oxford Xmax T80 SDD was used as an EDX detector. The sample was prepared by sonication to suspend the catalyst in ethanol. 1 µL of the resulting well-dispersed sample was deposited on a TEM grid (copper or holy carbon) and dried for 5 min. Imaging was performed at 200 kev. Image processing was performed using Gatan software for the TEM image, TEM imaging, and analysis software (TIA) for STEM imaging, and INCA to obtain an EDX spectrum + mapping.

The microstructure of the fresh and regenerated catalysts was characterized with field emission gun scanning electron microscopy (FEM SEM) and energy dispersive X-ray spectroscopy (EDS) using a FEI

Nova NanoSEM 650 equipped with an EDAX EDS using an Octane Super detector. All samples were coated with a 12 nm gold layer to enhance conductivity.

The crystallinity of the catalysts was determined via powder X-ray diffraction (PXRD) measurements on a Bruker D8 Advance diffractometer with Cu Kα1 radiation (λ = 1.5418 Å) at 40 keV and 40 mA in the range 5° – 95° with a step size of 0.02°. The raw diffraction data were processed using Bruker DIFFRAC.EVA software.

All three feeds were measured by FTIR to confirm that the composition is solely MDI-based PUR, not a mixture of MDI- and TDI-based PUR. All infrared experiments were performed on a Shimadzu IRTracer-100 spectrophotometer. The data was processed in LabSolutions IR.

All milligram scale experiments performed in this study were carried out using a commercial Frontier Lab Tandem Microreactor (TMR, Rx 3050TR). A 0.5 mg sample and 2.5 mg catalyst (1:5 ratio) were brought together in a Frontier Lab Eco Cup (LF PY1-EC80F) and loaded into the reactor using a single-shot sampler (PY1-1040). The resulting oil was analyzed using an online gas chromatograph (Agilent Technologies 8890) coupled to a 5977B MSD and an FID 300 °C detector. The gas chromatograph was equipped with a 30 m × 0.25 mm capillary column (HP-5 MS) coated with a 0.25 µm film of 5% phenylmethyl polysiloxane. Helium was used as the carrier gas at a constant 1 mL/min flow rate. A Frontier Lab Microjet Cryo-Trap was connected to the column to separate all volatile gases. The initial oven temperature was set at 40 °C, with a ramp rate of 10 °C/min (maintained for 1 min) to reach a final column temperature of 300 °C, which was held for 5 min. The injector and detector temperatures were maintained at 300 °C. Data were collected in full-scan mode with mass-to-charge (m/z) ratios ranging from 35 to 500. Chromatographic peaks were identified using the NIST mass spectral data library. Quantification of the desired products was performed using the external calibration curve method.

Batch gram scale drop-down reactor

The gram-scale pyrolysis reactor was designed by He *et al.* at the University of Groningen. A detailed explanation of the machine can be found in earlier work. [27,28] The operation procedure was executed as follows: Prior to the pyrolysis process, a 30-minute carrier gas flush (100 mL/min) was performed to ensure that no oxygen was present in the reactor. Each heating zone was heated to the desired temperature, and the cold traps were cooled with a mixture of ethanol and liquid nitrogen. A 3.0 g sample and 3.0 g catalyst (1:1 ratio) were brought together in a steel tube and loaded into the preheat chamber of the reactor for 40 min at 200 °C. After 40 min, the sample was transferred to the first reactor and held at 550 °C for 30 min. After 30 minutes, the steel tube was transferred to a cooling zone, and the residue was collected for analysis. The vaporized feedstock passed to a second heating zone, followed by condensation in a 2-step cooling train. The remaining non-condensed gas was quenched through a potassium hydroxide solution to neutralize possible hydrogen cyanide formation. The resulting oil was analyzed using an offline gas chromatograph (Hewlett-Packard 6890) coupled to a 5973 MS detector. The gas chromatograph was equipped with a 30 m × 0.25 mm capillary column (HP-5 MS) coated with a 0.25 µm film of 5% phenylmethyl polysiloxane. Helium was used as the carrier gas at a constant flow rate of 1 mL/min. The initial oven temperature was set at 40 °C, with a ramp rate of 10 °C/min (maintained for 1 min) to reach a final column temperature of 300 °C, held for 5 min. The injector and detector temperatures were both kept at 300 °C. Quantification of the desired

products was performed using the external calibration curve method on an Agilent 8860 gas chromatograph equipped with an FID 300 °C detector. A 30 m × 0.25 mm capillary column (HP-5 MS) coated with a 0.25 µm film of 5% phenylmethyl polysiloxane was used. The initial oven temperature was set at 40 °C, with a ramp rate of 20 °C/min (maintained for 1 min) to reach a final column temperature of 350 °C.

Continuous gram per hour scale: mini plant reactor (MPL)

The MPL is a non-commercial, small-scale, continuously operated pyrolysis unit that processes between 100 and 300 g of feedstock per hour. Typical operating time for one experiment is 5 h. A scheme of the system is shown in Figure. S3.4.3.

The feedstock enters the initial fluidized-bed reactor (R1) via a dosing and transport conveyor screw system. R1 can be loaded with a fluidizable medium, such as a catalyst. Nitrogen gas is introduced at the base of R1 to fluidize the medium, while a minor nitrogen purge flow prevents backflow of pyrolysis vapors toward the feeding system. After R1, the mixture of pyrolysis vapors and nitrogen flows to the second reactor (R2), designated the catalytic upgrading reactor, which may operate in either a fluidized-bed or fixed-bed mode, typically with a catalyst. Vapors exiting R2, usually enriched with desired products, are condensed through a series of ethylene glycol and ethanol-cryogenic condensers to separate the condensable product from the non-condensable gas (product gas). A product gas recycle system is available, allowing the product gas to be redirected to either R1 or R2, if necessary; however, the gas recycle system is typically inactive in default operation. All components exposed to elevated temperatures are constructed from stainless steel.

The operation procedure was as follows: Prior to the pyrolysis process, both reactors were loaded with: 500 g of sand in the first reactor (R1) and 450 g of catalyst in the second reactor (R2). Each heating zone was heated to the desired temperature, R1 to 500 °C, and R2 to 550 °C. The gas flows were set to a desired flow of 120 L/h (fluidization gas; nitrogen flow over the feeding system). The reactor was flushed for 30 minutes at 120 L/h to ensure that no oxygen remained in the reactor. A feed rate of 150 g/h was applied based on daily calibration. The exact feed input was determined by weighing. 750 g of feed was added to R1 over 5 hours using a dosing and transport conveyor screw system. The pyrolysis vapors passed to R2, followed by condensation in a 2-step cooling train. The remaining non-condensed gas was quenched through a potassium hydroxide solution to neutralize possible hydrogen cyanide formation. A liquid sample was collected every hour, and the water/oil layers were separated using a separation funnel for analysis.

The resulting oil was analyzed using an offline gas chromatograph (Agilent 8860) coupled to a FID detector at 300 °C. The gas chromatograph was equipped with a 15 m × 0.25 mm capillary column (DB-5) coated with a 0.25 µm film of 5 % phenylmethyl polysiloxane. Helium was used as the carrier gas at a constant flow rate of 1.2 mL/min. The initial oven temperature was set at 55 °C, with a ramp rate of 50 °C/min to reach a final column temperature of 280 °C, which was held for 1.5 min. The injector and detector temperatures were both kept at 280 °C. Quantification of the desired products was obtained via the internal standard method.

The product gases were analyzed via online gas chromatography (Agilent 990) equipped with a TCD detector. A Poraplot Q UM 10 M x 0.25mm x 8 µm BF, CP-PORABOND Q 1M x 0.25 mm x 3 µm capillary

column. Helium was used as the carrier gas at a constant static pressure of 200 kPa. The column temperature was set at 80 °C. Quantification of the products was obtained via argon as an internal standard.

The solid residue was analyzed using thermogravimetric analysis (TGA) on a PerkinElmer TGA 4000 system. A 5.0 mg sample was placed in a pre-weighted crucible. The samples were heated from 35 °C to 900 °C at 10.00 °C/min under oxygen flow. The amount of coke present in the solid residue was calculated by use of Equation S3.4.1

$$Coke\ (\%) = \frac{Sample\ weight_{Tstart} - Sample\ weight_{Tend}}{Sample\ weight_{Tstart}} * 100 \qquad \text{(S3.4.1)}$$

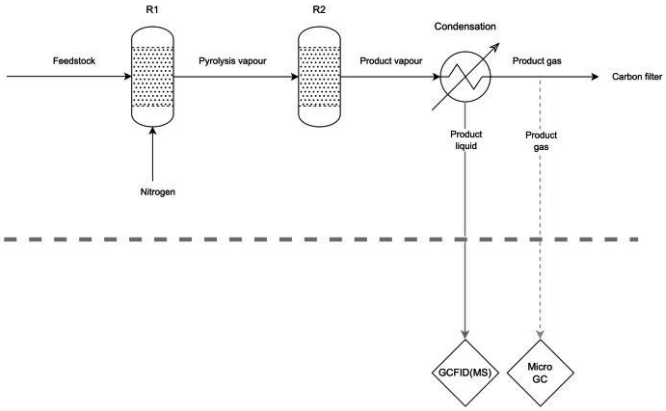

Figure. S3.4.3. Schematic representation of the streams and the methods of analysis for these streams in the BioBTX Mini Plant. The relative dimensions of the vessels do not indicate the real dimensions. The dotted lines represent a relatively small segment of the original stream to be analyzed

Continuous kilogram per hour scale: pilot plant reactor

The PPL operates in a similar fashion compared to the MPL. The pilot plant is capable of processing plastics or biomass at up to 10 kg/h (default: 5 kg/h). Unlike the MPL, which uses cryogenic condensation, the PPL is equipped with scrubbers to ensure optimal product recovery. The operation procedures and analysis techniques for the PPL are the same as those used with the MPL. See the work of Akker *et al*. [27] for extended details.

Calculation details

5 different yield calculations have been used in this paper to allow a fair comparison between feeds and state-of-the-art data.

(**S3.4.2**) Yield of nitrogen-containing compounds calculated as % based on the amount of nitrogen in the feed. Typical calculations like this use a polymer repetitive unit as the reference to calculate the yield. However, the exact composition of the feeds used in this paper is not known. Therefore, the nitrogen content of the feed was determined by elemental analysis. This yield is expressed in the paper as “N-based yield” with % as the unit. The calculation of this yield is shown in equation S3.4.2. Please

note that the amount of product produced (#Prod) is determined via calibration of the corresponding compound on a GC-FID basis.

$$N\ based\ yield\ (\%) = \frac{\#prod * Nt}{\#feed * Nf} * 100 \quad \text{(S3.4.2)}$$

In which:
#prod is the weight of the product produced
N_t is the calculated N content in the target molecule:
Aniline: 15.04 %
Toluidine: 13.07%
MDA: 14.13 %
#feed is the weight of the feed input
N_f is the N content in the feed, determined via elemental analysis

(**S3.4.3**) Yield based on area% integration. This yield is calculated by integrating all peaks identified via GC/MS FID. Please note that the quantitative data from the FID are used for calculations; the MS data are used only for product identification. The total integration has been used as 100% yield. From here, the yield of the target molecule is calculated by taking the area integration of the target molecule divided by the summed peak integration of all identified compounds. This yield is expressed in the paper as "*Yield on peak integration*" with % as the unit. Note that no GC calibration was performed to obtain this yield. The calculation of this yield is shown in equation S3.4.3.

$$Yield\ on\ peak\ integration\ (\%) = \frac{\#prod\ peak}{\#total\ peak} * 100 \quad \text{(S3.4.3)}$$

In which:
#prod peak is the peak integration of the target molecule
#total peak is the summed peak integration of all integrated compounds

(**S3.4.4**) yield based on weight input. This is a yield calculation in which the weight of the target molecule is divided by the weight of the polyurethane input. The amount of the target molecule produced (#Prod) is determined by calibrating the corresponding compound. The yield is expressed in the paper as "*Yield on input*" with wt% as unit. The calculation of this yield is shown in equation S3.4.4.

$$Yield\ on\ input\ (wt\%) = \frac{\#prod}{\#feed} * 100 \quad \text{(S3.4.4)}$$

In which:
#prod is the weight of product produced
#feed is the weight of feed input

(**S3.4.5**) Normalized yield on input. In the paper, 3 different feeds were tested to assess the process's robustness. These feeds vary in the amount of PUR present due to additives and contaminants. For this reason, the input-based yield, as defined in (**3.4.5**), has been calculated and normalized to 100% based on the amount of PUR present in the feed. The amount of PUR is shown in Table S3.4.6. This

yield is expressed in the paper as “Normalized yield on input” with % as the unit. The calculation of this yield is shown in equation S3.5. Please note that the amount of product produced (#Prod) is determined via calibration of the corresponding compound on a GC-FID basis.

$$Normalized\ yield\ on\ input\ (\%) = \frac{\#prod * 100}{\#feed * PUR\ in\ feed} * 100 \qquad \text{(S3.4.5)}$$

In which:
#prod is the weight of the product produced
#feed is the weight of the feed input

(**S3.4.6**) Product per kilogram of catalyst. The efficiency of the catalyst is determined via the calculation of the product produced per kilogram of catalyst. The catalyst efficiency is calculated according to equation S3.4.6.

$$\frac{Product}{Kilogram\ catalyst}\ (kg) = \frac{PPH * yield\ on\ input}{Tot.\ cat.\ add.} * 100 \qquad \text{(S3.4.6)}$$

In which:
PPH is the weight of PUR fed to the reactor per hour, which is 0.139 kg for the miniplant Yield on input is calculated according to equation S4 in section 3. Tot. cat. Add. Is the total weight of the catalyst added to the reactor, which is 0.450 kg for the miniplant

Pyrolysis results

The results shown in Table S3.4.10 originate from the thermal decomposition of nPUR, using mass spectrometry, catalyzed by alumina 4. Reaction conditions: 0.5 mg nPUR, catalyst-to-feed ratio of 5 to 1, 550 °C with a helium flow of 205 mL/min and a pyrolysis time of 10 seconds.

Table S3.4.10. Identified products from the thermal decomposition of nPUR catalyzed by alumina 4

#	Area integration[a] (%)	Match (%)	ID
1	13.5	4	Carbon dioxide
2	6.4	42	Acetone
3	2.2	58	Cyclopentane
4	40.8	97	Aniline
5	0.43	94	Aniline, N-methyl-
6	14.7	94	p-Toluidine
7	1.1	97	Benzenamine, 2,4-dimethyl-
8	0.90	93	Benzenamine, N-propyl-
9	1.4	93	Quinoline, 3-methyl-
10	2.0	86	1H-Indole, 4-methyl-
11	0.59	64	1H-Imidazole
12	2.2	87	Quinoline, 4-ethyl-
13	0.6	94	1H-Indole, 2,3-dimethyl-
14	1.5	64	Indolizine, 2-methyl-6-ethyl-

15	0.80	95	Acridine
16	0.46	86	Acridine, 9-methyl-
17	0.87	60	2-(4-Aminobenzyl)phenylamine
18	8.6	98	Benzenamine, 4,4'-methylenebis-
19	1.0	94	Benzenamine, 2,4'-methylenebis-

[a]Reaction conditions: 0.5 mg nPUR, catalyst-to-feed ratio of 5 to 1, 550 °C with a helium flow of 205 mL/min and a pyrolysis time of 10 seconds

Table S3.4.11. General catalyst screening pyrolysis results, calculated on area% according to calculation S3.4.2

Catalyst[a]	**Volatiles (%)**	**Aniline (%)**	**Toluidine (%)**	**MDA[b] (%)**	**N-containing (%)**
No cat	48	0.0	0.0	27	26
RuO_2	31	0.0	0.0	69	0.0
BaO	35	2.6	0.9	62	0.0
CaO	31	2.4	1.7	61	4.3
CdO	37	3.7	1.3	51	7.2
La_2O_3	23	1.9	2.5	72	0.8
MgO	27	3.2	2.9	59	8.3
Fe_2O_3	22	2.6	2.3	69	4.4
Tb_2O_3	43	4.5	2.5	48	2.7
Ga_2O_3	50	5.1	1.5	37	7.2
SrO	28	2.2	1.5	63	4.8
TiO_2	49	7.7	5.8	33	4.9
CeO_2	41	4.0	3.1	50	2.2
Y_2O_3	37	4.1	3.2	54	1.1
Nb_2O_5	49	7.7	5.8	33	4.9
Bentonite	52	13	3.2	30	0.9
ZrO_2	24	13	8.0	50	4.9
B_2O_3	30	19	4.3	40	6.1
Sepiolite	37	32	8.3	14	8.9
HfO_2	19	34	8.8	25	13
Alumina 4	22	41	15	9.5	13

[a]Reaction conditions: 0.5 mg nPUR, catalyst-to-feed ratio of 5 to 1, 550 °C with a helium flow of 205 mL/min and a pyrolysis time of 10 seconds
[b]4,4-MDA and 4,2-MDA isomers were observed during pyrolysis and grouped

Table S3.4.12. General catalyst screening pyrolysis results, calculated on input according to calculation S3.4.3

Catalyst[a]	Aniline[b,c] (wt%)	Toluidine[b,c] (wt%)	MDA[b,c,d] (wt%)	Total[b,c] (wt%)	ErrorAnT[e] (%)	Error MDA[f] (%)
No cat	0.0	0.0	3.5	3.5	-	0.5
RuO_2	0.0	0.0	12	12	-	1.6
BaO	0.8	0.3	29	30	0.6	3.0
CaO	1.0	0.8	28	29	0.2	0.3
CdO	1.3	0.6	19	21	1.2	0.8
La_2O_3	0.9	1.0	33	35	0.3	0.7
MgO	1.2	1.2	23	25	0.2	1.8
Fe_2O_3	1.9	0.6	10	12	0.6	0.2
Tb_2O_3	1.5	1.0	15	17	0.3	2.4
Ga_2O_3	1.9	1.1	13	16	0.8	2.2
SrO	2.2	0.9	31	34	1.4	2.8
TiO_2	1.9	1.5	13	17	0.9	4.4
CeO_2	1.9	1.6	23	27	0.2	1.1
Y_2O_3	2.5	1.4	20	24	1.4	0.6
Nb_2O_5	2.8	1.5	16	20	0.2	0.7
Bentonite	4.3	1.0	6.5	12	0.9	0.6
ZrO_2	4.1	2.6	20	27	1.8	0.8
B_2O_3	7.9	1.8	13	13	1.0	2.8
Sepiolite	10	0.3	5.1	16	0.6	0.2
HfO_2	17	4.1	6.5	27	0.4	1.3
Alumina 4	20	7.0	3.6	30	0.9	2.0

[a]Reaction conditions: 0.5 mg nPUR, catalyst-to-feed ratio of 5 to 1, 550 °C with a helium flow of 205 mL/min and a pyrolysis time of 10 seconds
[b]Determined via calibration curve of according compound
[c]Average of 2 measurements
[d]4,4-MDA and 4,2-MDA isomers were observed during pyrolysis and grouped
[e]Calculated yield percentage error of Aniline and Toluidine combined
[f]Calculated yield percentage error of MDA

Table S3.4.13. General catalyst screening pyrolysis results, N base yield calculated according to calculation S3.4.1

Catalyst[a]	Aniline[b,c] (wt%)	Toluidine[b,c] (wt%)	MDA[b,c,d] (wt%)	Total[b,c] (wt%)	Error AnT[e] (%)	Error MDA[f] (%)
No cat	0	0	5.5	5.5	-	0.7
RuO_2	0	0	23	23	-	3.1
BaO	1.5	0.6	54	56	1.2	5.4
CaO	2	1.3	52	55	0.4	0.6
CdO	2.5	1	36	39	2.3	1.6
La_2O_3	1.7	1.7	63	66	0.5	1.3
MgO	2.4	2	43	47	0.4	3.5
Fe_2O_3	3.9	1	19	23	1.1	0.4
Tb_2O_3	3.1	1.8	27	32	0.5	4.5
Ga_2O_3	3.7	1.8	25	30	1.5	4.1
SrO	4.3	1.6	58	64	2.8	5.1
TiO_2	3.7	2.5	25	31	1.8	8.2
CeO_2	3.7	2.7	43	50	0.3	2

Y_2O_3	4.9	2.4	38	45	2.7	1.2
Nb_2O_5	5.5	2.5	30	38	0.4	1.3
Bentonite	8.6	1.8	12	23	1.7	1.1
ZrO_2	8.1	4.5	37	50	3.4	1.3
B_2O_3	16	3.1	24	43	2	5.1
Sepiolite	20	0.6	9.5	30	1.3	0.4
HfO_2	33	7	12	52	0.6	2.7
Alumina 4	40	12	6.7	58	1.8	3.9

[a]Reaction conditions: 0.5 mg nPUR, catalyst-to-feed ratio of 5 to 1, 550 °C with a helium flow of 205 mL/min and a pyrolysis time of 10 seconds
[b]Determined via calibration curve of according compound
[c]Average of 2 measurements
[d]4,4-MDA and 4,2-MDA isomers were observed during pyrolysis and grouped
[e]Calculated yield percentage error of Aniline and Toluidine combined
[f]Calculated yield percentage error of MDA

Table S3.3.4.14. Alumina based catalyst screening pyrolysis results based on area% according to calculation S3.4.2

Catalyst[a]	**Volatiles (%)**	**Aniline (%)**	**Toluidine (%)**	**MDA[b] (%)**	**N-containing (%)**
α-Al_2O_3	43	4.08	4.21	44	4.6
Alumina 0	39	11	7.24	36	6.8
Alumina 1	26	34	16	10	15
Alumina 2	24	35	13	13	15
Alumina 3	23	36	13	14	13
Alumina 4	22	41	15	9.5	13
Alumina 5	24	34	12	9.8	19
Alumina 6	27	38	10	7.9	16
Alumina 7	24	44	14	1.7	17
Alumina 8	22	41	15	4.2	18

[a]Reaction conditions: 0.5 mg nPUR, catalyst-to-feed ratio of 5 to 1, 550 °C with a helium flow of 205 mL/min and a pyrolysis time of 10 seconds
[b]4,4-MDA and 4,2-MDA isomers were observed during pyrolysis and grouped

Table S3.4.15. Alumina based catalyst pyrolysis results, calculated on input according to calculation S3.4.3

Catalyst[a]	**Aniline[b,c] (wt%)**	**Toluidine[b,c] (wt%)**	**MDA[b,c,d] (wt%)**	**Total[b,c] (wt%)**	**Error AnT[e] (%)**	**Error MDA[f] (%)**
α-Al_2O_3	1.9	1.9	21	25	0.3	1.9
Alumina 0	4.9	3	12	20	0.4	4.9
Alumina 1	13	4.7	2.3	20	1.7	13
Alumina 2	15	6.4	4.4	26	1.8	15
Alumina 3	19	7.2	6.3	33	0.3	19
Alumina 4	20	7	3.6	30	0.9	20

Alumina 5	22	7.4	2.2	31	1.2	22
Alumina 6	23	7	3.8	34	2.2	23
Alumina 7	23	6.6	0.9	31	1.2	23
Alumina 8	26	8.7	2.7	37	0.9	26

[a]Reaction conditions: 0.5 mg nPUR, catalyst-to-feed ratio of 5 to 1, 550 °C with a helium flow of 205 mL/min and a pyrolysis time of 10 seconds
[b]Determined via calibration curve of according compound
[c]Average of 2 measurements
[d]4,4-MDA and 4,2-MDA isomers were observed during pyrolysis and grouped
[e]Calculated yield percentage error of Aniline and Toluidine combined
[f]Calculated yield percentage error of MDA

Table S3.4.16. Alumina based catalyst pyrolysis results, N based yield calculated according to calculation S3.4.1

Catalyst[a]	**Aniline[b,c] (wt%)**	**Toluidine[b,c] (wt%)**	**MDA[b,c,d] (wt%)**	**Total[b,c] (wt%)**	**Error AnT[e] (%)**	**Error MDA[f] (%)**
α-Al_2O_3	3.7	3.2	39	46	0.6	3.7
Alumina 0	9.7	5.2	23	38	0.8	9.7
Alumina 1	26	8.2	4.2	39	3.3	26
Alumina 2	30	11	8.2	49	3.4	30
Alumina 3	39	13	12	63	0.6	39
Alumina 4	40	12	6.7	58	1.8	40
Alumina 5	43	13	4.2	60	2.5	43
Alumina 6	46	12	7.1	66	4.1	46
Alumina 7	47	12	1.7	60	2.1	47
Alumina 8	51	15	5	71	1.8	51

[a]Reaction conditions: 0.5 mg nPUR, catalyst-to-feed ratio of 5 to 1, 550 °C with a helium flow of 205 mL/min and a pyrolysis time of 10 seconds
[a]Determined via calibration curve of according compound
[c]Average of 2 measurements
[d]4,4-MDA and 4,2-MDA isomers were observed during pyrolysis and grouped
[e]Calculated yield percentage error of Aniline and Toluidine combined
[f]Calculated yield percentage error of MDA

Table S3.4.17. Summary of chemical composition of PUR feeds and aniline, toluidine and MDA yields after catalytic pyrolysis using Alumina 8

Feed	**N cont.[a] (wt%)**	**Total Inerts[b] (wt%)**	**Other impurities[c] (wt%)**	**Total PUR in feed (wt%)**	**An yld (%N)**	**Tol yld (%N)**	**MDA yld[d] (%N)**
nPUR	7.52	0.80	0.00	99.2	51.4	15.0	5.0
EOL_1	6.62	5.68	18.32	76.0	33.1	9.1	2.2
EOL_2	7.14	2.66	12.34	85.0	31.6	9.1	5.7

[a]Calculated by elemental analysis
[b]average of 2 measurements determined via ash content
[c]Impurities include binders, and cyclopentane
[d]4,4-MDA and 4,2-MDA isomers were observed during pyrolysis and grouped

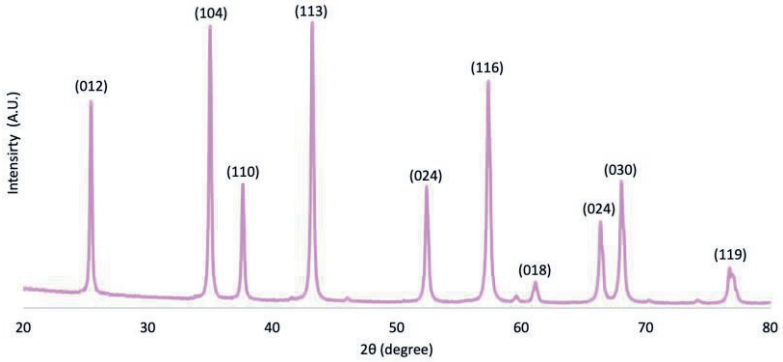

Figure S3.5.5: XRD analysis of Alpha alumina

Scale comparison

Table S3.4.18.Overview of results for the catalytic pyrolysis on various setups

Set-up[a]	Mode (Feed)	Temp. R1/R2 (°C)	Feed rate (g/h)	Tot. PUR (g)	Cat. Load (g)	An/Tol (N%)	MDA[f] (N%)
TMR[b]	in-situ (nPUR)	550/550	-	$5 \cdot 10^{-1}$	$2.5 \cdot 10^{-1}$	51/15	5.0
TMR[b]	in-situ (EOL_1)	550/550	-	$5 \cdot 10^{-1}$	$2.5 \cdot 10^{-1}$	33/9.1	2.2
Batch gram scale[c]	In-situ (nPUR)	550/550	-	3.0	3.0	10/4.4	2.7
Mini plant[d]	ex-situ (EOL_1)	500/550	139	556	450	17/10	ND
TMR[b]	in-situ (EOL_2)	550/550	-	$5 \cdot 10^{-1}$	$2.5 \cdot 10^{-1}$	32/9.1	5.7
Pilot plant[e]	In/ex-situ (EOL_2)	612/531	5000	15000	25000	14/12	0.0

[a]Alumina 8 was used as catalyst for all runs, excluding the pilot plant run where Alumina 5 is used
[b]Reaction conditions: 0.5 mg PUR, R1 loaded with 2.5 mg catalyst, and R2 loaded with inert material (SiC), R1 550 °C, R2 550 °C with a helium flow of 205 mL/min., and a total pyrolysis time of 10 s
[c]Operating conditions: 3.0 g PUR, R1 loaded with 3.0 g catalyst, R1 550 °C, R2 550 °C, and a total operation time of 2 h.
[d]Operating conditions: 139 g PUR per hour, R1 loaded with 400 g sand, and R2 loaded with 450 g catalyst, R1 500 °C, R2 550 °C, with a weight hour space velocity (WHSV) of 0.9 h^{-1}, and a total operation time of 4 h
[e]Operating conditions: 5 kg PUR per hour, R1 loaded with 10 kg catalyst, and R2 loaded with 15 kg catalyst, R1 612 °C, R2 531 °C, with a weight hour space velocity (WHSV) of 0.33 h^{-1}, and a total operation time of 3 h
[f]4,4-MDA and 4,2-MDA isomers were observed during pyrolysis and grouped

Statistical analysis of Alumina-based catalyst screening

Table S3.4.19. Input parameters for ANOVA analysis

Catalyst	Response (%)	Surface area (m^2/g)	Acidity (µmol/g)
Alumina 0	10.2	98.0	350
Alumina 1	24.5	147	329
Alumina 2	27.8	141	337
Alumina 3	39.0	147	204
Alumina 4	38.3	179	330
Alumina 5	41.4	197	221
Alumina 6	44.3	208	488
Alumina 7	45.6	242	412
Alumina 8	50.2	218	406
Alumina 0 duplicate	9.1	98.0	350
Alumina 1 duplicate	28.2	147	329
Alumina 2 duplicate	32.3	141	337
Alumina 3 duplicate	38.4	147	204
Alumina 4 duplicate	40.6	179	330
Alumina 5 duplicate	44.9	197	221
Alumina 6 duplicate	48.5	208	488
Alumina 7 duplicate	47.8	242	412
Alumina 8 duplicate	52.6	218	406

Table S3.4.20. Response surface fit summary

Source	Sequential p-value	Lack of Fit p-value	Adjusted R^2	Predicted R^2	
Linear	< 0.0001	0.0005	0.8364	0.7755	
2FI	0.1205	0.0007	0.8534	0.8071	
Quadratic	**< 0.086**	**0.0065**	**0.9225**	**0.8983**	**Suggested**
Cubic	0.0065		0.9719	0.9405	Aliased

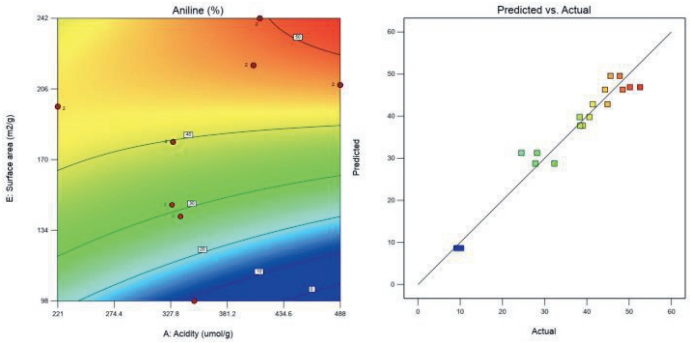

Figure S3.4.6. 2D response surface of surface area and acidity with respect to aniline yield (left). The red spots are the design points. And predicted vs actual of response surface of surface area and acidity with respect to the aniline yield (right)

Table S3.4.21. Final equation in terms of coded and actual factors for future modelling

Final Equation in Terms of Coded Factors[a]		**Final Equation in Terms of Actual Factors**[b]	
Aniline	=	Aniline	=
37.1		11.40593	
-3.66	A	-0.207415	Acidity
19.3	E	0.523975	Surface area
10.18	AE	0.001059	Acidity * Surface area
-9.62	E^2	-0.001857	Surface area^2

[a]The equation in terms of coded factors can be used to make predictions about the response for given levels of each factor. By default, the high levels of the factors are coded as +1 and the low levels are coded as -1. The coded equation is useful for identifying the relative impact of the factors by comparing the factor coefficients.

[b]The equation in terms of actual factors can be used to make predictions about the response for given levels of each factor. Here, the levels should be specified in the original units for each factor. This equation should not be used to determine the relative impact of each factor because the coefficients are scaled to accommodate the units of each factor and the intercept is not at the center of the design space

Large-scale results

Table S3.4.22. Alumina 8 based catalytic pyrolysis results of batch gram-scale pyrolysis calculated on input and on N-based content according to calculations (S3.4.3) and (S3.4.1), respectively

Gas[a] **(%)**	**Solid (%)**	**Oil (%)**	**Water (%)**
54	14	30	2

Aniline[b] **(wt%)**	**Toluidine**[b] **(wt%)**	**MDA**[b] **(wt%)**	**Aniline**[b] **(N%)**	**Toluidine**[b] **(N%)**	**MDA**[b,c] **(N%)**
5.2	2.5	1.4	10.3	4.4	2.7

[a]Gas production is calculated by difference

[b]Reaction condictions: 3.0 g PUR, R1 loaded with 3.0 g catalyst, R1 550 °C, R2 550 °C, and a total operation time of 2 h

[c]4,4-MDA and 4,2-MDA isomers were observed during pyrolysis and grouped

Table S3.4.23. Alumina 8 based catalyst pyrolysis results of continuous gram scale (miniplant) pyrolysis calculated via peak integration according to calculation (S3.4.2)

Time[a] (h)	An (%)	Tol (%)	MDA[b] (%)	N-cont. (%)	BTX (%)	Aromatics (%)	Styrene (%)	Volatiles (%)
1	34	21	0.0	21.5	2.6	10.0	3.8	6.9
2	33	27	0.0	24.3	2.5	8.1	3.3	1.7
3	29	31	0.0	24.0	2.5	8.3	3.8	1.8
4	26	28	1.0	30.2	2.3	7.0	4.0	1.4
Avg.	30	27	1.0	25.1	3.2	10.9	5.6	1.1

[a] Reaction conditions: 139 g PUR per hour, R1 loaded with 400 g sand, and R2 loaded with 450 g catalyst, R1 500 °C, R2 550 °C, with a weight hour space velocity (WHSV) of 0.9 h^{-1}, and a total operation time of 4 h

[b]4,4-MDA and 4,2-MDA isomers were observed during pyrolysis and grouped

Table S3.4.24. Alumina 8 based catalyst pyrolysis results of the continuous gram scale (miniplant) pyrolysis calculations of yield on input, theoretical yield, and production per kilogram catalyst according to calculations (S3.4.3, S3.4.1, and S3.4.5, respectively).

Time[d] (h)	An[a] (wt%)	Tol[a] (wt%)	An[b] (%)	Tol[b] (%)	An[c] (kg)	Tol[c] (kg)
1	5.81	3.12	13.2	6.2	0.018	0.010
2	8.94	5.75	20.3	11.3	0.028	0.018
3	8.82	7.02	20.0	13.9	0.027	0.022
4	5.79	4.82	13.2	9.5	0.018	0.015
Average	7.34	5.18	16.7	10.2	0.023	0.016

[a]Depicted Yields are calculated on input according to calculation (S3.4.3)

[b]Depicted Yields are calculated on N base according to calculation (S3.4.2)

[c]Depicted Depicted yields are calculated on product per kilogram catalyst according to calculation (S3.4.5)

[d]Reaction conditions: 139 g PUR per hour, R1 loaded with 400 g sand, and R2 loaded with 450 g catalyst, R1 500 °C, R2 550 °C, with a weight hour space velocity (WHSV) of 0.9 h^{-1}, and a total operation time of 4 h

Table S3.4.25. Alumina 8 based catalyst pyrolysis mass balance results of continuous gram scale (miniplant). Yields are based on input according to calculation S3.4.5

Mass balance[a] (%)	Gas fraction[b] (%)	Liquid fraction[b] (%)	Solid fraction (%)
Gas (18.6)	CH_4 (1.2)	Aniline (9.8)	Fe_2O_3 (2.1)
Liquid (36.3)	CO (2.4)	Toluidine (6.4)	ZnO (1.6)
Solid (19.7)	CO_2 (11.0)	Styrene (1.2)	Coke (14.0)
Carbon scrubber (7.4)	C_3H_6 (1.9)	Water (6.1)	Others (2.0)
Unaccounted (18.0)	Others (1.5)	Other (12.8)	

[a]Reaction conditions: 139 g PUR per hour, R1 loaded with 400 g sand, and R2 loaded with 450 g catalyst, R1 500 °C, R2 550 °C, with a weight hour space velocity (WHSV) of 0.9 h^{-1}, and a total operation time of 4 h; [b]Based on input via calibration of according compounds

Environmental potential calculation and techno-economic evaluation (TEA)

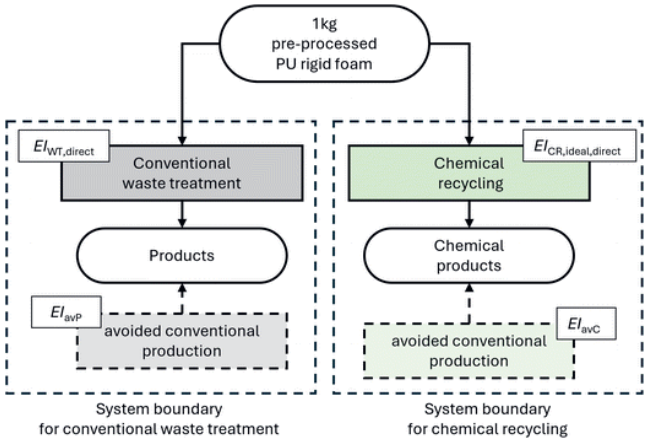

Figure S3.4.7 .System boundaries utilized for the calculations of the environmental potential, reproduced from Pillich et al.,[29] with permission from the Royal Society of Chemistry. The equation on top of the Fig. describes the environmental potential which is calculated by subtracting the environmental impacts of an ideal process from the environmental impacts of the current status-quo

The environmental potential is modelled according to the procedure described in Pillich *et al*.,[29] and is an LCA-based methodology to assess novel PUR recycling processes very early in the process development. The goal of the environmental potential is to compare a novel chemical recycling process against the current waste treatment status quo. Figure. S3.7 gives an overview of the system boundaries utilized to calculate the environmental potential. Any pretreatment, transport, and sorting are assumed to be required for both processes and hence, not modelled. Consequently, the stream entering the two systems is an already pre-processed PU rigid foam waste stream.

$$E_{\mathrm{Pot}} = \underbrace{(\mathrm{EI}_{\mathrm{WT,direct}} - \mathrm{EI}_{\mathrm{avP}})}_{\mathrm{EI}_{\mathrm{WT,net}}} - \underbrace{(\mathrm{EI}_{\mathrm{CR,ideal,direct}} - \mathrm{EI}_{\mathrm{avC}})}_{\mathrm{EI}_{\mathrm{CR,ideal,net}}} \qquad \text{(S3.4.7)}$$

The environmental potential can then be calculated by subtracting the environmental impacts of an ideal process, $EI_{\mathrm{CR,ideal,net}}$, from the environmental impacts of the current status-quo, $EI_{\mathrm{WT,net}}$, as shown in Eq. S1. In the case of conventional waste treatment, environmental impacts from the treatment itself, $EI_{\mathrm{WT,direct}}$, as well as from the avoided conventional production, $EI_{\mathrm{avP.}}$, can be directly taken from available data, literature, or databases, as these processes are well known. For chemical recycling, the processes are still under development, and only minimal data is available. Therefore, the environmental potential assumes an ideal chemical recycling process, where the reaction is assumed to be stochiometric with 100% conversion, all chemical products are assumed to be pure, and the rest is considered as waste; all other process aspects (e.g., preheating, separation, etc.) are neglected, and the only required heat input is the reaction enthalpy. Consequently, the ideal process causes environmental impacts only due to the thermodynamically minimal heat input and waste treatment of the residual outputs, $EI_{\mathrm{CR,ideal,direct}}$, and avoids the burdens of conventional chemical production of the recovered products, EI_{avC}. Such an ideal chemical recycling process

represents the best possible chemical process, and therefore, the environmental potential provides an upper bound on the reductions in environmental impacts that can be achieved, as no recycling process will be better than the ideal recycling process. If the environmental potential is positive, the novel recycling process presents an opportunity to reduce environmental impacts. Conversely, if the potential is negative, the novel recycling process cannot have lower impacts than the status quo waste treatment even under ideal conditions.

Preliminary techno-economic evaluation (TEA)

For this work, we calculate all environmental impacts with the Environmental Footprint 3.0 [30]method and utilize data from ecoinvent 3.11[31] and CarbonMinds [32], which is consistent with ecoinvent, for any required LCI data. More specifically, we assume the conventional waste treatment to be waste incineration with energy recovery and calculate environmental impacts from the treatment itself, $EI_{\mathrm{WT,direct}}$ with the waste incineration model provided by Doka[33], which is updated to be consistent with ecoinvent 3.11. We further assume the recovered energy from incineration to be in the form of electricity and heat for district heating, as modelled in Pillich *et al*., and use updated datasets from ecoinvent to calculate emissions form avoided conventional production, $EI_{\mathrm{avP.}}$. For the calculation of the environmental impacts from the ideal chemical recycling process, $EI_{\mathrm{CR,ideal,direct}}$ we assume the heat to be supplied by steam from natural gas and utilize the respective ecoinvent dataset. Further, we assume residual recycling wastes to be incinerated with energy recovery in the form of steam and model the emissions with the updated Doka model. For chemical products, we only consider the amounts of aniline and toluidine as measured in this work as product and take data from CarbonMinds to calculate the avoided emissions from conventional production, EI_{avC}. The environmental potential of the three investigated setups compared to conventional incineration with energy recovery is shown in Figure S3.5.9

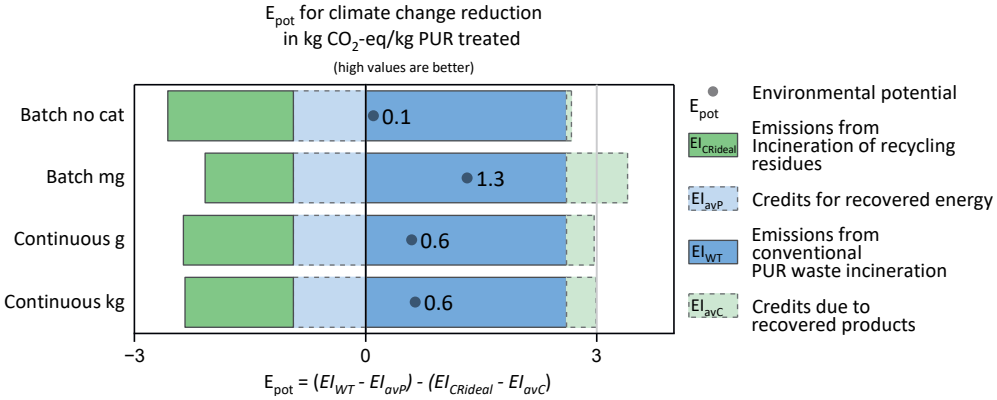

Figure S3.4.8.Environmental potential of the three investigated reactor and process types (Batch mg, continuous g and kg) with Alumina 8 as catalyst and a batch pyrolysis with no catalyst. The equation below shows the calculation of the environmental potential (E_{pot}) concerning the individual

As a first approximate techno-economic evaluation, the maximum catalyst consumption was calculated and compared to the mini-plant data over a 4-hour period.[34] A catalyst lifetime was calculated to determine the required stability for a feasible process.

The cost variables are listed in Table S3.4.26. The variables included are shown in the left column, and the variables excluded are shown in the right column. The majority has been excluded from the calculation for simplicity and brevity. It is assumed that waste collection, sorting, and preparation are ideal and that the plants already exist, so no costs are associated with these factors. Regarding the process, it is assumed that all produced solids, liquids, and gases, excluding aniline and toluidine, can be disposed of at no additional cost. Also, aniline and toluidine can be separated from the other products at no additional cost. This leaves only the purchasing costs for EOL PUR foam and the catalyst, against the selling costs of aniline and toluidine. It is assumed that the market price of aniline and toluidine is equal. The current market price of €1051 · ton^{-1} is used for the calculation [35] The actual market selling price of €100 · ton^{-1} is used for EOL PUR foam. [36]

Table S3.4.26. All variables considered for the techno-economic evaluation

Included	Excluded
Purchase cost EOL PUR feed	Plant capital costs
Purchase cost catalyst	Waste collection and preparation costs
Selling cost of Aniline	Gas & energy input reactor
Selling cost of Toluidine	Solid, liquid, gas, stream disposal
	Separation (distillation) costs

The maximum catalyst consumption (kg_{cat} · ton_{prod}) was calculated using PUR and catalyst market prices relative to those of aniline and toluidine. The results are shown in in Table S3.4.27. A production of 162 kg_{prod} · ton_{PUR}^{-1} (equation S3.7) was calculated via 16.2 wt% combined aniline and toluidine (AnT) yield on the miniplant, resulting in a PUR contribution of €617 · ton_{prod}^{-1} (equation S3.8) and a catalyst contribution of €434 · ton_{prod}^{-1} (equation S3.9). A maximum catalyst consumption of 867 kg_{cat} · ton_{prod}^{-1} was calculated via a usage of 0.867 ton_{cat} · ton_{prod}^{-1} (equation S3.10).

The miniplant processed 556 g of PUR with 850 g of catalyst over a 4-hour run, producing 16.2 wt% toluidine and aniline. This resulted in a catalyst consumption of 9473 kg_{cat} · $ton_{prod}^{-1,}$ as 90 g product was produced using 850 g catalyst (equation S3.11).

The catalyst lifetime was determined from the number of catalytic regeneration cycles required to reach breakeven (equation S3.12). It was calculated that the catalyst must remain stable for up to 11 runs of 4-hours, resulting in a lifetime of 44 hours to reach breakeven.

Table S3.4.27. Calculation of the maximum catalyst consumption

Product	Market price (€ · ton^{-1})	Production (kg · ton_{pur}^{-1})	Max usage (ton · ton_{prod}^{-1})	Contribution (€ · ton_{prod}^{-1})
PUR	100	-	6.17	617
Catalyst	500 [37]	-	0.867	434
An + tol	1051	162	-	-

[a]Yields used from miniplant data shown in Figure. 3.7

Table 3.4.28. Calculation of miniplant catalyst consumption data

Product	Market price (€ · ton^{-1})	Input (g)	Prod. (g)	Cat consumption (kg$_{cat}$ · ton$_{prod}^{-1}$)	Contribution (€ · ton$_{prod}^{-1}$)
PUR	100	556	-		
Catalyst	500 [37]	850	-	9437	4718
An + tol	1051	-	90		

$$Prod_{AnT}\left(\frac{kg_{prod}}{\text{ton}_{PUR}}\right) = Y_{AnT} * 1000 \quad \text{(S3.4.8)}$$

$$Contribution_{PUR}\left(\frac{€}{ton_{prod}}\right) = \frac{Mp_{pur}}{prod_{AnT}} * 1000 \quad \text{(S3.4.9)}$$

$$Max\ contribution_{cat}\left(\frac{€}{ton_{Prod}}\right) = margin = MP_{AnT} - Contribution_{PUR} \quad \text{(S3.4.10)}$$

$$Max\ usage\left(\frac{ton_{cat}}{ton_{prod}}\right) = \frac{MP_{cat}}{Contribution_{cat}} \quad \text{(S3.4.11)}$$

$$Prod_{AnT}\,(g) = Y_{AnT} * W_i \quad \text{(S3.4.12)}$$

$$Catalyst\ lifetime\ for\ breakeven\ (h) = \left(\frac{CC_{plant}}{CC_{ref}}\right) * 4 \quad \text{(S3.4.13)}$$

In which:

Y_{AnT} = Aniline and toluidine mini plant yield (0.162)

Mp_{pur} = Market price PUR (100 € ton^{-1})

Mp_{AnT} = Market price aniline and toluidine (1050 € ton^{-1})

MP_{cat} = Market price catalyst (1050 € ton^{-1})

w_i = weight input PUR in the miniplant (556 g)

CC_{ref} = The reference calculated catalyst consumption (kg$_{cat}$ · ton$_{prod}^{-1}$)

CC_{plant} = The calculated catalyst consumption of the miniplant (kg$_{cat}$ · ton$_{prod}^{-1}$)

References

1. Grittner, N., Kaminsky, W. & Obst, G. Fluid bed pyrolysis of anhydride-hardened epoxy resins and polyether-polyurethane by the Hamburg process. *J. Anal. Appl. Pyrolysis* 25, 293–299 (1993).
2. Font, R., Fullana, A., Caballero, J. A., Candela, J. & García, A. Pyrolysis study of polyurethane. *J. Anal. Appl. Pyrolysis* 58–59, 63–77 (2001).
3. Guo, X., Wang, L., Zhang, L., Li, S. & Hao, J. Nitrogenous emissions from the catalytic pyrolysis of waste rigid polyurethane foam. *J. Anal. Appl. Pyrolysis* 108, 143–150 (2014).

4. Stančin, H. *et al.* Experimental analysis of waste polyurethane from household appliances and its utilization possibilities. *J. Environ. Manage.* 243, 105–115 (2019).
5. Kaminsky, W. Chemical recycling of plastics by fluidized bed pyrolysis. *Fuel Communications* 8, 100023 (2021).
6. Eiden, S. *et al.* Pyrolysis of polyurethane compound-containing material in order to recover raw materials. (2024).
7. Zeller, M. *et al.* Characteristics of Polyurethane Pyrolysis—Experimental Investigations and Product Analyses for the Assessment of Chemical Recycling Potentials. *J. Appl. Polym. Sci.* 143, (2025).
8. Lattimer, R. P., Muenster, H. & Budzikiewicz, H. PYROLYSIS TANDEM MASS SPECTROMETRY (Py-MS/MS) OF A SEGMENTED POLYURETHANE. *J. Anal. Appl. Pyrolysis* 17, 237–249 (1990).
9. Takamoto, D. Y. & Petrich, M. A. Effect of Heterogeneous Secondary Pyrolysis Reactions on the Thermal Decomposition of Polyurethane Scrap. *Ind. Eng. Chem. Res* 33, 3004–3009 (1994).
10. Esperanza, M. M., García, A. N., Font, R. & Conesa, J. A. Pyrolysis of varnish wastes based on a polyurethane. *J. Anal. Appl. Pyrolysis* 52, 151–166 (1999).
11. Moroi, G. & Ciobanu, C. Aspects of polyesterurethane interaction with metallic ions. III. Thermal behavior of polyurethane interaction products with iron and chromium ions. *J. Anal. Appl. Pyrolysis* 70, 87–98 (2003).
12. Pielichowski, K. & Slotwinska, D. Flame-resistant modified segmented polyurethanes with 3-chloro-1,2- propanediol in the main chain - Thermoanalytical studies. *Thermochim. Acta* 410, 79–86 (2004).
13. Moroi, G. Influence of ion species on the thermal degradation of polyurethane interaction products with transition metal ions. *J. Anal. Appl. Pyrolysis* 71, 485–500 (2004).
14. Bozi, J. & Blazsó, M. Catalytic thermal decomposition of polyamides and polyurethanes mixed with acidic zeolites. *J. Anal. Appl. Pyrolysis* 97, 189–197 (2012).
15. Bozi, J., Mihályi, M. R. & Blazsó, M. Study on temperature dependence of catalytic thermal decomposition of polyamides and polyurethanes mixed with acidic zeolites. *J. Anal. Appl. Pyrolysis* 101, 103–110 (2013).
16. Terakado, O., Yanase, H. & Hirasawa, M. Pyrolysis treatment of waste polyurethane foam in the presence of metallic compounds. *J. Anal. Appl. Pyrolysis* 108, 130–135 (2014).
17. Guo, X., Wang, L., Li, S., Tang, X. & Hao, J. Gasification of waste rigid polyurethane foam: optimizing operational conditions. *J. Mater. Cycles Waste Manag.* 17, 560–565 (2015).
18. Pagacz, J. *et al.* Polyurethane foams chemically reinforced with POSS—Thermal degradation studies. *Thermochim. Acta* 642, 95–104 (2016).
19. He, J. J., Jiang, L., Sun, J. H. & Lo, S. Thermal degradation study of pure rigid polyurethane in oxidative and non-oxidative atmospheres. *J. Anal. Appl. Pyrolysis* 120, 269–283 (2016).
20. Guo, X., Zhang, W., Wang, L. & Hao, J. Comparative study of nitrogen migration among the products from catalytic pyrolysis and gasification of waste rigid polyurethane foam. *J. Anal. Appl. Pyrolysis* 120, 144–153 (2016).
21. Yuan, Y. *et al.* Highly efficient catalysts for reducing toxic gases generation change with temperature of rigid polyurethane foam nanocomposites: A comparative investigation. *Compos. Part A Appl. Sci. Manuf.* 112, 142–154 (2018).

22. Kumagai, S., Yabuki, R., Kameda, T., Saito, Y. & Yoshioka, T. Simultaneous recovery of H2-rich syngas and removal of HCN during pyrolytic recycling of polyurethane by Ni/Mg/Al catalysts. *Chemical Engineering Journal* 361, 408–415 (2019).
23. Yao, Z. *et al.* Probing the combustion and pyrolysis behaviors of polyurethane foam from waste refrigerators. *J. Therm. Anal. Calorim.* 141, 1137–1148 (2020).
24. Nishiyama, Y. *et al.* Temperature-dependent pyrolysis behavior of polyurethane elastomers with different hard- and soft-segment compositions. *J. Anal. Appl. Pyrolysis* 145, 104754 (2020).
25. Eschenbacher, A., Varghese, R. J., Weng, J. & Van Geem, K. M. Fast pyrolysis of polyurethanes and polyisocyanurate with and without flame retardant: Compounds of interest for chemical recycling. *J. Anal. Appl. Pyrolysis* 160, 105374 (2021).
26. Xu, S. *et al.* Insight into waste polyurethane pyrolysis pathways: Mechanism functions analysis and in-situ coupling online monitoring. *J. Anal. Appl. Pyrolysis* 177, 106301 (2024).
27. van Akker, M. *et al.* Full Utilization of Hard-to-Recycle Mixed Plastic Waste by Conversion toward Pyrolysis Oil and BTX Aromatics on a Pilot Scale. *Energy and Fuels* 39, 6438–6451 (2025).
28. He, S. *et al.* Novel Staged Free-Fall Reactor for the (Catalytic) Pyrolysis of Lignocellulosic Biomass and Waste Plastics. *Energy and Fuels* 38, 8740–8748 (2024).
29. Pillich, M., Schilling, J., Bosetti, L. & Bardow, A. What to do with polyurethane waste? The environmental potential of chemically recycling polyurethane rigid foam. *Green Chemistry* 26, 10893–10906 (2024).
30. Fazio, S. et al. *Supporting Information to the Characterisation Factors of Recommended Life Cycle Impact Assessment Methods*. vol. version 2 (2018).
31. Althaus, H.-J. *et al.* Swiss Centre for Life Cycle Inventories A joint initiative of the ETH domain and Swiss Federal Offices Life Cycle Inventories of Chemicals Data v2.0. *https://www.academia.edu/39728395/Swiss_Centre_for_Life_Cycle_Inventories_A_joint_initiative_of_the_ETH_domain_and_Swiss_Federal_Offices_Life_Cycle_Inventories_of_Building_Products_Data_v2_0_2007* www.ecoinvent.org. (2007).
32. Stellner et al. Methodology cm.chemicals version1.01 2022. https://www.carbon-minds.com/products/data/carbon-footprint-and-lca-data/database-and-methodology-versions/ (2022).
33. Doka, G. Swiss Centre for Life Cycle Inventories A joint initiative of the ETH domain and Swiss Federal Offices Life Cycle Inventories of Waste Treatment Services. *https://doka.ch/13_I_WasteTreatmentGeneral.pdf* www.ecoinvent.ch (2003).
34. Lange, J. P. Performance metrics for sustainable catalysis in industry. *Nat. Catal.* 4, 186–192 (2021).
35. Aniline daily market price. https://www.sunsirs.com/uk/prodetail-258.html.
36. Wholesale High Purity PU Scrap Polyurethane Foam Rubber Waste for Recycling Foaming Grade Mixed Color Industrial Use. https://www.alibaba.com/product-detail/Wholesale-High-Purity-PU-Scrap-Polyurethane_10000028735737.html?spm=a2700.galleryofferlist.normal_offer.d_image.461a13a016ryQD&priceId=51c9cd60e68c4a2da11fd59080ae86dd.



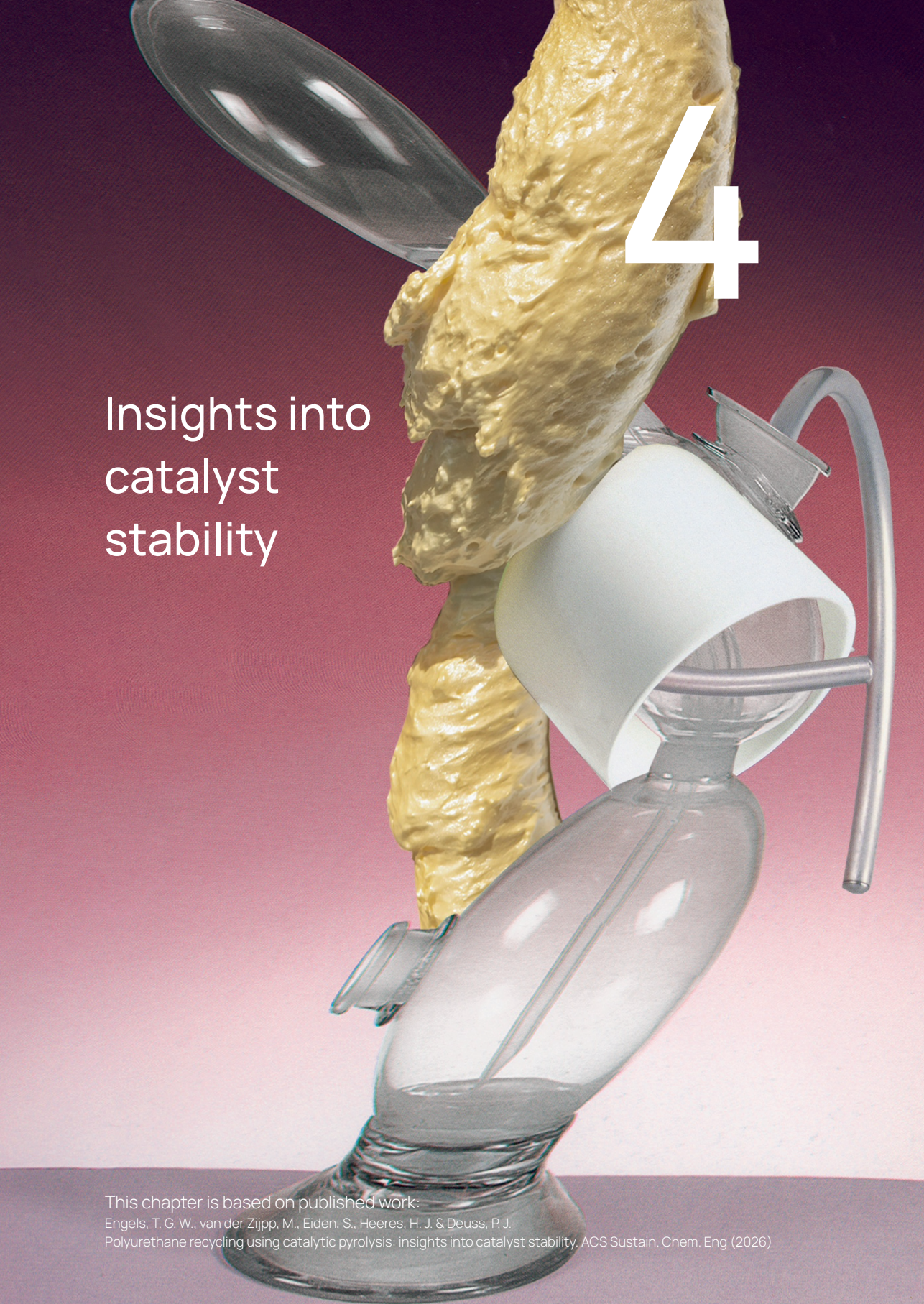

4

Insights into catalyst stability

This chapter is based on published work:

Engels, T. G. W., van der Zijpp, M., Eiden, S., Heeres, H. J. & Deuss, P. J.
Polyurethane recycling using catalytic pyrolysis: insights into catalyst stability. ACS Sustain. Chem. Eng (2026)

Abstract

Polyurethanes are widely used in many applications because of their versatility. However, efficient recycling remains challenging. Recent findings indicate that aniline recovery from rigid polyurethane foams via catalytic pyrolysis with an alumina-based catalyst is an attractive option. Techno-economic analyses show that catalyst costs are a major factor and that catalyst recycling is essential. Here, we report an extensive study on the recyclability of a selected alumina-based catalyst (Puralox 5/200) for the catalytic pyrolysis of PUR. Experiments with fresh and spent catalysts in a batch-operated staged free-fall reactor at gram scale (3.0 g nPUR, catalyst-to-feed ratio: 1 to 1, 550 °C) using virgin PUR showed differences in activity and chemoselectivity for aniline, indicative of catalyst deactivation. Spent catalyst characterization (TGA-MS, TEM-EDX, N_2 physisorption, TPD, and XRD) showed hard coke (14.4 wt%) on the catalyst. Catalyst regeneration was successfully demonstrated using an oxidative treatment at 550 °C, though some irreversible deactivation, including loss in acidity and BET surface area, as well as inorganic accumulation, was observed after 5 regeneration/recycles. Additional experiments to assess catalyst performance after multiple regeneration-recycles were carried out on a milligram scale in a tandem microreactor coupled to GC-MS/FID (catalyst-to-feed ratio of 5:1 at 550 °C), using rigid polyurethane (nPUR) and a contaminated end-of-life (EOL) feed. With nPUR, catalyst performance for aniline and toluidine formation declined in the first 4 cycles, then stabilized at half the original activity for 28 cycles, and finally dropped to very low levels. For EOL PUR, catalyst performance over multiple runs was significantly worse, and the catalyst was inactive after 18 cycles. We characterized the spent catalysts from both PUR feeds (a.o TEM-EDX), which showed that inorganic impurity accumulation contributes to catalyst deactivation.

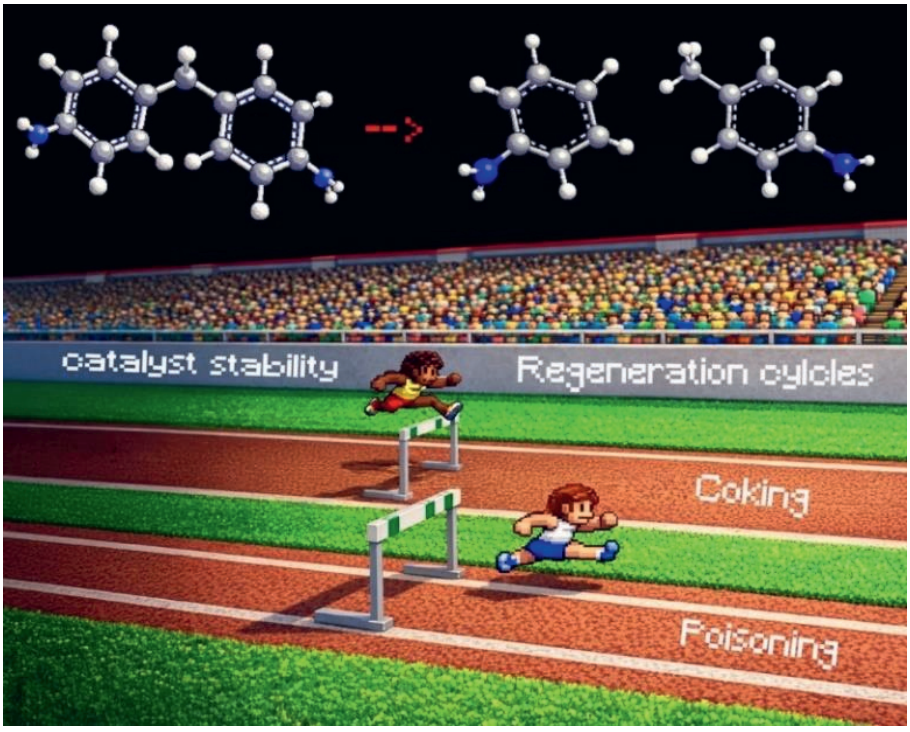

4.1. Introduction

Polyurethanes are highly versatile polymers with many important everyday applications, such as the use as insulation materials. A general pathway for the synthesis of a polyurethane foam is depicted in Figure 4.1 and involves the reaction of aniline, formaldehyde, and phosgene to form an (oligomeric) isocyanate (pMDI), which then is reacted with a polyol to give a polyurethane foam.[1] Typical additives include fillers (e.g. silica) to improve mechanical properties, pigments (e.g. iron oxide) to tailor optical characteristics, and blowing agents (e.g. cyclopentane) to reduce thermal conductivity, thereby improving insulation performance.[2]

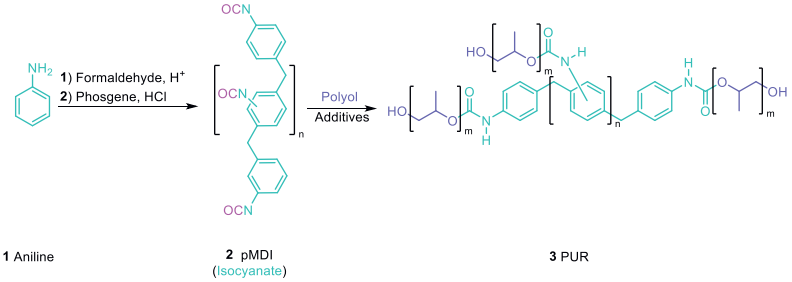

Figure 4.1 Chemistry of PUR foam formation

Waste plastic recycling is essential for reducing both environmental impact and dependence on fossil resources, and is a key element of future circular economies. However, end-of-life polyurethanes are currently mainly disposed of through landfilling (40%), mechanical recycling (25%), or incineration (35%). [3] A number of recycling options for polyurethanes have been investigated, including glycolysis, aminolysis, and catalytic pyrolysis.[4] Successful polyol recovery has been achieved via glycolysis (Figure 4.2*a*), and the recovered polyol was used to produce new PUR foam.[5] Recovering and reusing the isocyanate segment has not been widely reported due to the challenging downstream purification. Polymeric methylenedianiline (pMDA) has been recovered with 87 % purity via ammonolysis at a 300 g h^{-1} scale (Figure 4.2*b*).[6] It has been shown that the relevant product properties of PUR made with recovered pMDA differ from those obtained with virgin pMDA. As such, it is highly desirable to convert the N-containing segment in PUR to aniline (Figure 4.2*c*), which can more easily be used to make new PUR with identical properties than MDA or pMDA recovered from recycling by selective depolymerization.

Catalytic pyrolysis is a promising approach for converting plastics, such as rigid polyurethane foams, into low-molecular-weight building blocks via thermal and catalytic reactions in an oxygen-free environment at temperatures between 300 and 700 °C. In recent work, we demonstrated the successful recovery of aniline from rigid polyurethane foam via catalytic pyrolysis. An 51% N-based aniline yield was obtained from virgin PUR using alumina catalysts (550°C) in a tandem micro reactor (TMR) at mg scale. The process was scaled up to 5 kg/h of PUR feed in a continuous fluidized-bed setup using the best alumina-based catalyst identified in an extensive screening study (Puralox SCCa 5/200). Aniline was obtained at an average N-based yield of 14% for a 3-hour run using end-of-life polyurethane foam (EOL PUR). A cracking mechanism was proposed in which polyurethane retro-polymerizes into polyol and MDA. Aniline and toluidine are subsequently formed by catalytic cracking of the methylene bridge in 4,4'-methylenedianiline (MDA).

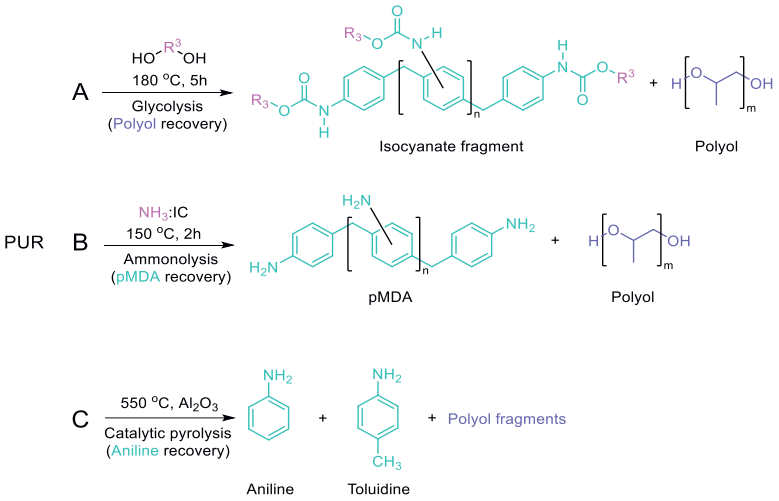

Figure 4.2. Strategies for the recovery of PUR building blocks from PUR. Polyol recovery was achieved via glycolysis (**A**)[5], pMDA recovery via ammonolysis (**B**)[6], and aniline recovery via catalytic pyrolysis (**C**)

Techno-economic analyses reveal that catalyst costs are a significant item and that catalyst recycling is essential.[7] However, potential catalyst deactivation was shown after 4 hours of operation, with a dedicated investigation into the stability of the alumina catalyst remaining to be performed. Moreover, explorations on catalyst use of multiple cycles for PUR recycling to aniline have not yet been performed. Here, we report experimental studies to determine the stability of a selected alumina-based catalyst for the conversion of PUR to aniline and modes of deactivation and factors that lie at the basis of this. Initial experiments were conducted in a batch-operated, staged, free-fall reactor using newly produced rigid polyurethane foam (nPUR) as the feed. After reaction, the spent catalyst was analyzed in detail to assess changes in catalyst structure (XRF, TGA-O_2/N_2, SEM, TEM-EDX, N_2 physisorption, NH_3-TPD, and XRD). In addition, five regeneration-recycle cycles were performed to gain insights into irreversible structural changes in the catalyst during oxidative regeneration. Long-term catalyst stability was tested by performing multiple reaction/regeneration cycles in a tandem microreactor coupled to a GC-FID using both nPUR and EOL PUR, followed by detailed catalyst characterization to identify deactivation pathways.

4.2. Experimental Section

Virgin PUR (nPUR) and end of life PUR (EOL PUR) were obtained from Covestro in Germany. The nPUR contained minimal amounts of impurities, see supporting information (section S2.5) for details. The EOL PUR was collected from a waste facility and pelletised before use in catalytic pyrolysis experiments. The alumina-based catalyst (Puralox SCCa 5/200) was obtained from Sasol Limited (Germany)[8] Further catalyst details are provided in the supporting information, section S4.5.

Elemental compositions were carried out via energy dispersive X-ray fluorescence (ED-XRF) on a Panalytical Epsilon 3^{XLE} instrument. Approximately 1 g of catalyst was placed in a plastic holder with a 6 µm mylar film as the bottom. The nominal composition of elements was expressed as oxides, and the sum of the obtained concentrations was normalized to 100%.

The catalyst microstructure was analyzed via nitrogen physisorption experiments (BET) using a Micromeritics ASAP 2420 analyzer. 100 - 200 mg of catalyst sample was placed in a tube with a filler rod and sealed. The sample was degassed at 300°C under a vacuum atmosphere for 12 h prior to measurement. The free space of the sample tubes was measured according to application note no. 104 from Micromeritics. Adsorption isotherms were collected at -196°C (77K) over a relative pressure range of 0.01–1 mbar. The surface area (S_{BET}) was calculated using the Brunauer-Emmett-Teller (BET) method, assuming a relative pressure of 0.03–0.30 mbar. The pore size distribution and pore volume were determined using the Barrett-Joyner-Halenda (BJH) method. The adsorption branch approach was used to avoid tensile strength effects that may lead to an artificial peak at 4 nm. [9]

The total acidity of the catalysts was determined using NH_3-temperature-programmed desorption (NH_3-TPD) experiments on a Micromeritics AutoChem II 2920 analyzer. The sample (100-200 mg) was placed between quartz wool in a quartz U-tube. Before measurement, a pre-treatment step was performed by heating the sample to 550 °C with a helium flow of 50 mL/min for 30 min. The adsorption step was carried out using 10% NH_3 in He (50 mL/min) at 100 °C for 120 min, followed by desorption from 100–900°C at 10 °C/min with a helium flow of 50 mL/min for 15 min. The downstream gas was directed to a TCD detector for analysis. The concentration of NH_3 was determined by the intensities of m/z at 17.

The catalyst basicities were measured using CO_2-temperature-programmed desorption (CO_2-TPD) on a Micromeritics AutoChem II 2920 analyzer. A sample (100-200 mg) was placed between quartz wool in a quartz U-tube. Before measurement, a pre-treatment step was performed by heating the sample to 550°C with a helium flow of 50 mL/min for 30 min. The adsorption step was carried out using 10% CO_2 in helium (50 mL/min) at 100°C for 120 min, followed by desorption from 100–900°C at 10°C/min with a helium flow of 50 mL/min for 15 min. The downstream gas was directed to a TCD detector for analysis. The CO_2 concentration was determined from the intensity at m/z 44.

Temperature-programmed oxidation (TPO) was performed using the Micromeritics AutoChem II 2920 Chemisorption Analyzer equipped with a thermal conductivity detector (TCD). The TPO measurements were performed with 10% O_2 in helium at a 30 mL/min flow rate in the temperature range of 25-600°C.

The catalyst's microstructure was characterized by transmission electron microscopy (TEM) on a Tecnai T20 equipped with a LaB_6 filament, a Cryo-EM Gatan 626 stage with a 4K CCD camera, and an Oxford Xmax T80 SDD EDX detector. The catalyst was suspended in ethanol under sonication. 1 μL of the resulting well-dispersed sample was deposited on a TEM grid (copper or holy carbon) and dried for 5 min under air at room temperature. Imaging was performed at 200 Kev. Image processing was performed using Gatan software for TEM imaging; TEM imaging and analysis software (TIA) for STEM imaging; and INCA to obtain an EDX spectrum and to map.

The microstructure of the fresh and regenerated catalysts was characterized with field emission gun scanning electron microscopy (FEM SEM) and energy dispersive X-ray spectroscopy (EDS) using a FEI Nova NanoSEM 650 equipped with an EDAX EDS using an Octane Super detector. All samples were coated with a 12 nm gold layer to enhance conductivity.

TGA experiments were performed on a Perkin-Elmer TGA 4000 system. A 5.0 mg sample was placed in a pre-weighted crucible. The samples were heated from 35 °C – 800 °C at 10.00 °C/min under oxygen or nitrogen flow.

The crystal structures were determined via Powder X-ray diffraction (PXRD) measurements carried out on a Bruker D8 Advance diffractometer with Cu Kα1 radiation (λ = 1.5418 Å) under 40 keV and 40 mA in the range 5° – 95° with a step size of 0.02°. The raw diffraction data were processed using Bruker DIFFRAC.EVA software.

The water content of the liquid products was determined using a two-component volumetric Karl Fischer titration. The experiments were conducted with the 702 Titrino SM Metrohm device. HydranalTM Titrant 5 served as the titrant, and HydranalMT Solvent was used as the solvent during titration. To ensure titrant accuracy, three measurements with tap water were performed as quality control. The water content in the oil was quantified through quadruplicate measurements.

For the batch milligram setup (TMR), product analyses by GC was conducted as follow. The initial oven temperature was set at 40 °C, with a ramp rate of 10 °C/min (maintained for 1 min) to reach a final column temperature of 300 °C, which was held for 5 min. The injector and detector temperatures were maintained at 300 °C. Data were collected in full-scan mode with mass-to-charge (m/z) ratios ranging from 35 to 500. Chromatographic peaks were identified using the NIST mass spectral data library. Quantification of the desired products was performed using the external calibration curve method. A series of dilutions was prepared for each product of interest: aniline, toluidine, and MDA. The dilutions were injected into the TMR using a microshot injector and measured by GC-FID. From here, an external calibration curve was generated to enable accurate yield calculations.

The product oils from experiments in the batch-staged free-fall reactor were analyzed using an offline gas chromatograph (Hewlett-Packard 6890) coupled to a 5973 MS detector. The gas chromatograph was equipped with a 30 m × 0.25 mm capillary column (HP-5 MS) coated with a 0.25 µm film of 5% phenylmethyl polysiloxane. Helium was used as the carrier gas at a constant 1 mL/min. The initial oven temperature was set at 40 °C, with a ramp rate of 10 °C/min (maintained for 1 min) to reach a final column temperature of 300 °C, held for 5 min. The injector and detector temperatures were both set to 300 °C. Quantification of the desired products was performed using the external calibration curve method on an Agilent 8860 gas chromatograph equipped with a FID detector. A 30 m × 0.25 mm capillary column (HP-5 MS) coated with a 0.25 µm film of 5% phenylmethyl polysiloxane was used. The initial oven temperature was set at 40 °C, with a ramp rate of 20 °C/min (maintained for 1 min) to reach a final column temperature of 350 °C.

All milligram scale experiments performed in this study were carried out using a commercial Frontier Lab Tandem Microreactor (Rx 3050TR). A 0.5 mg sample and 2.5 mg catalyst (1:5 wt ratio) were mixed, added in a Frontier Lab Eco Cup (LF PY1-EC80F) and loaded into the reactor using a single-shot sampler (PY1-1040). The pyrolysis products were analyzed using an online gas chromatograph (Agilent Technologies 8890) coupled to a 5977B MSD and an FID detector. A Frontier Lab Microjet Cryo-Trap was connected to the column to separate all volatile gases.

Details on the batch-operated staged free-fall pyrolysis reactor and its operation have been reported recently.[10,11] A representative experiment is described here. The set-up was flushed with nitrogen (100

mL/min) prior to the pyrolysis experiment to remove all oxygen. Each zone was heated to the desired temperature, and the two cold traps in the condensation system were cooled to -116 °C with a mixture of ethanol and liquid nitrogen. The polyurethane sample (3.0 g) and catalyst (3.0 g) were added to a steel tube (closed at the bottom and open at the top) and loaded into the reactor's preheating chamber, where they were held for 40 min at 200 °C. The latter time was obtained by optimization experiments. Subsequently, the sample was transferred to the pyrolysis reactor and held at 550 °C for 30 min. Then, the steel tube was transferred to the cooling zone, and the solid residue was collected for analysis. The pyrolysis vapors were condensed in a 2-step cooling train. The non-condensable gases were quenched with a potassium hydroxide solution to neutralize any hydrogen cyanide that might have formed. The product oils were analyzed by GC. The oil, water, and solid yields (wt%) were determined using equations 4.1 - 4.3, respectively. The gas yield (wt%) was calculated by difference according to equation 4.4.

$$Oil\ yield\ (wt\%) = \frac{w_{liq}}{w_f} \cdot (1 - water\ yield) \cdot 100 \tag{4.1}$$

$$Water\ yield\ (wt\%) = \frac{w_{liq}}{w_f} \cdot H_2O_{kf} \cdot 100 \tag{4.2}$$

$$Solid\ yield\ (wt\%) = \frac{w_r}{w_f} \cdot 100 \tag{4.3}$$

$$Gas\ yield\ (wt\%) = 100 - (oil\ yield + solid\ yield) \tag{4.4}$$

Here, w_f is the feed intake (g), w_{liq} is the liquid yield (g), H_2O_{kf} is the water content in the oil, determined by a Karl Fisher titration, and w_r is the solid residue in the tube after reaction (g) minus the catalyst intake (g).

The individual product yields (aniline, toluidine, and MDA) are expressed as input weight (Eq. 4.5) or on a nitrogen basis (Eq. 4.6).

$$Yield\ on\ input\ (wt\%) = \frac{w_i}{w_f} \cdot 100 \tag{4.5}$$

Here, w_i is the weight of an individual product *i* (g), as determined by GC, and w_f is the feed intake (g).

$$N\ based\ yield\ of\ component\ i\ (wt\%) = \frac{w_i \cdot N_i}{w_f \cdot N_f} \cdot 100 \tag{4.6}$$

Here, w_i is the weight of an individual product *i* (g), as determined by GC, w_f is the feed intake (g), N_i is the nitrogen content (wt %) of an individual product *i*, and N_f is the nitrogen content of the feed (wt%, as determined by elemental analysis).

The catalyst regeneration study at mg scale was performed by using a gas torch to heat the cup containing the spent catalyst to approximately 1000 °C for 10 s. The catalyst color was visually inspected to qualitatively assess the effect. Successful regeneration was associated with a visual color change from black to white. Please note that minor catalyst was lost during the recovery process due to the small scale**.** The catalyst regeneration study at g scale was performed in a Uhlig Metalclay

furnace. The spent catalyst was transferred into a ceramic cup and placed in the oven. The temperature was set to 120 °C, with a ramp rate of 10 °C/min, maintained for 60 min to reach 550 °C, then held at 550 °C for 300 min. Regeneration was associated with a visual color change from black to white.

4.3. Results & Discussion

Feedstock and catalyst characterization

nPUR and EOL PUR were used as feeds in this study, and detailed compositional data are given in the supporting information (section S4.5). The compositions of the two PUR feeds differ considerably. The nPUR is relatively clean (> 99% PUR), whereas the EOL PUR contained a significant amount of ash (2.66 wt%) as well as 12 wt% polystyrene. The catalyst used in this study is an alumina-based catalyst (Puralox SCCa 5/200), a semi-crystalline, mesoporous catalyst with a surface area of 218 m^2/g and a total acidity of 406 µmol/g. In addition to Al_2O_3, the sample contains small amounts of MgO (0.6 wt%) and CaO (0.2 wt%). The average particle size was measured using SEM and found to be 85 µm, in line with the supplier's product specifications. TEM also shows smaller particles, either those in the smaller fraction of the particle-size distribution or formed by attrition. A complete overview of relevant catalyst properties is provided in the supporting information (Section S4.5).

Experiments with fresh catalyst

Batch gram-scale experiments were conducted on a custom-made staged, fixed-bed, free-fall, slow pyrolysis setup developed by our group.[11] (Supporting information, section S4.6, Figure S4.6.2). The reactor has three independent heating zones: I) preheating, II) pyrolysis, and III) cooling. A stainless-steel tube loaded with catalyst and nPUR (*in-situ* approach) is introduced from the top of the reactor into the preheating zone (200 °C). The tube is then transported by gravity to the pyrolysis section (550 °C). The vapor phase is condensed in a cooling section, yielding a liquid and a permanent gas phase. After the reaction, the tube containing spent catalyst and organic solid residue is transferred to the cooling zone and subsequently removed from the reactor for analysis. Aniline, toluidine, and MDA concentrations in the liquid phase were determined by standard calibration and used to calculate the corresponding yields. Other low molecular weight N-containing side products in the liquid phase were calibrated using indole as the reference.

Initial experiments involved catalytic runs with nPUR using a fresh catalyst (Puralox SCCa 5/200) at an nPUR-to-catalyst ratio of 1:1 (wt basis) at a pyrolysis temperature of 550 °C. The experiments yielded 34 wt% liquid product (based on feed intake), which contained mainly organics and some water (2 wt% on feed). The solid residue, mainly coke on catalyst and char, was 14 wt% based on nPUR intake. The gas phase could not be quantified accurately and was estimated at 52 wt% by difference. The target compound, aniline, was obtained at 5.2 wt% on nPUR intake, corresponding to a 10.3% N-based yield. Byproducts were toluidine (2.5 wt% on feed, 4.4% N-based yield) and MDA (1.4 wt% on feed, 2.7% on N-basis). Figure 4.3 shows an overview of the results for the fresh catalyst, including the amounts of the three main components (aniline, toluidine, and MDA). In-depth ^1H- and ^{13}C-NMR and GC-MS fragmentation pattern analyses were performed to distinguish between the formation of toluidine and methylaniline. The latter is also an identified product of thermal PUR pyrolysis. The NMR data clearly indicate that the methyl group is attached to the aromatic ring, not the N-atom, indicating

toluidine formation. The aniline-to-toluidine ratio (2.15 +/- 0.3) is nearly constant across runs, indicating that catalyst deactivation does not significantly affect the relative amounts of aniline and toluidine. In addition, the aniline yields are lower than those reported earlier for mg-scale experiments by our group, but are in line with those from continuous kg-scale experiments (6.5% aniline, 6.3% toluidine).[7]

Experiments with spent catalyst

Catalyst stability was assessed by reusing the spent catalyst from the first run for a second pyrolysis experiment with nPUR under the same conditions, without an intermediate catalyst regeneration step. The results are shown in Figure 4.3 (yellow column, spent) and clearly demonstrate a 45% reduction in the combined yield of aniline, toluidine, and MDA compared to the run with fresh catalyst (Figure 4.3, yellow column, fresh). The chemo-selectivity shift from aniline and toluidine to MDA could be attributed to coking (*vide infra*), which mainly reduces the catalysts' cracking activity to convert MDA to aniline and toluidine, thereby reducing yields and altering selectivity. Thus, catalyst performance differs significantly between fresh and spent catalysts after a single run without regeneration.

A thermal (non-catalytic) experiment was performed under the same conditions to assess whether the spent catalyst was still active (Figure 4.3, yellow column, no cat). In this case, aniline, toluidine, and MDA are also formed, though with lower yields than in the experiment with the spent catalyst. Statistical tests showed equal aniline and toluidine yields when comparing the thermal run (no cat) to the spent catalyst run, indicating that the spent catalyst no longer contributes to aniline/toluidine (AnT) formation. In contrast, the MDA yields differ significantly, suggesting that the spent catalyst can still promote MDA formation. Thus, the spent catalyst showed significant MDA activity, though it is no longer active for aniline and toluidine formation.

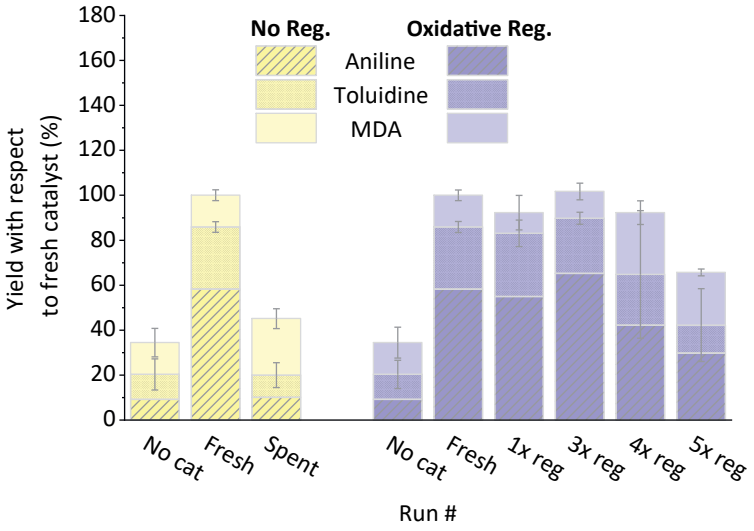

Figure 4.3. Overview of experiments in the staged free-fall reactor. Left: pyrolysis runs without regeneration of the catalyst, Right: sequential runs with oxidative regeneration/recycling (3.0 g nPUR, catalyst-to-feed ratio: 1 to 1, 550 °C)

Spent catalyst characterization

Visual images of the fresh and spent catalyst after one catalytic pyrolysis experiment are shown in Figure 4.5A. The catalyst's color has changed considerably from off-white for the fresh to black for the spent, indicating carbon deposition on the surface of the latter. To assess the presence of coke, the spent catalyst was characterized in detail using elemental analysis, BET, SEM, TEM-EDX, TGA, and XRD.

TGA-O_2 (Figure 4.4) exhibited twxo main weight-loss regions: one small at low temperature (5.8 wt%, centered at 115 °C), typically due to the release of moisture and low-molecular-weight compounds, and a second region centered at 570 °C (14.4 wt%). The latter indicates the presence of a hard coke.[12] Elemental analysis of the spent catalyst (supporting information, Table S4.6.6) indeed showed the presence of significant amounts of C (14.6 wt%), H (1.2 wt%) and N (1.7 wt%). The H/C ratio is 0.94 (on molar basis), further supporting the presence of a hard coke[13] with nitrogen incorporation in its structure. The surface area decreased from 218 m^2/g to 159 m^2/g, also indicating the formation of coke clogging the porous structure. XRD (Supporting information, Figure S4.6.4, Table S4.6.7) showed no clear change in crystallinity (55% to 63%) or changes in the principal alumina lattice plane shapes (311, 400, and 440).

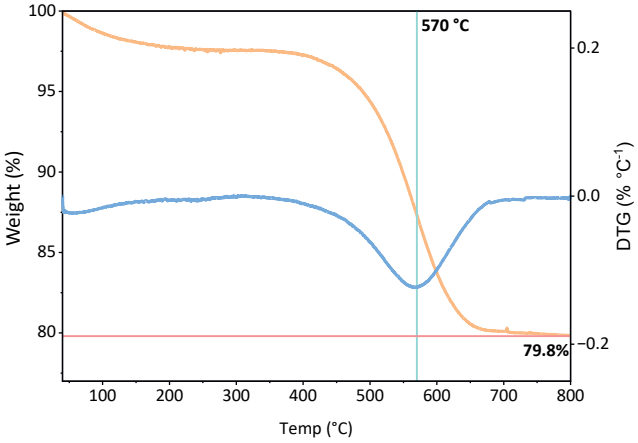

Figure 4.4. TGA-O_2 of the spent catalyst after a single nPUR conversion run in the batch staged free fall reactor

The spent catalyst was also analyzed by SEM and TEM-EDX, and the results were compared with those of the fresh catalyst (Figure 4.5B - D). It clearly shows the presence of carbon, which appears to be uniformly distributed across the catalyst particles (Figure 4.5C and D). TEM-EDX mapping of single particles (Figure 4.6E) also showed a homogeneous carbon distribution on the catalyst. This thereby confirms carbon deposition on at least the outer surface of the catalyst, potentially leading to partial pore blockage and a reduction in active sites.[14] Closer examination of the carbon deposits shows the presence of crystalline domains, as shown in Figure 4.6D, revealing a lattice spacing of 0.37 nm, larger than the typical graphite d-spacing of 0.33 nm.[15] This suggests that the carbonaceous deposit lacks the highly ordered, 3-dimensional crystalline graphite structure, possibly due to nitrogen incorporation, as shown by elemental analyses.

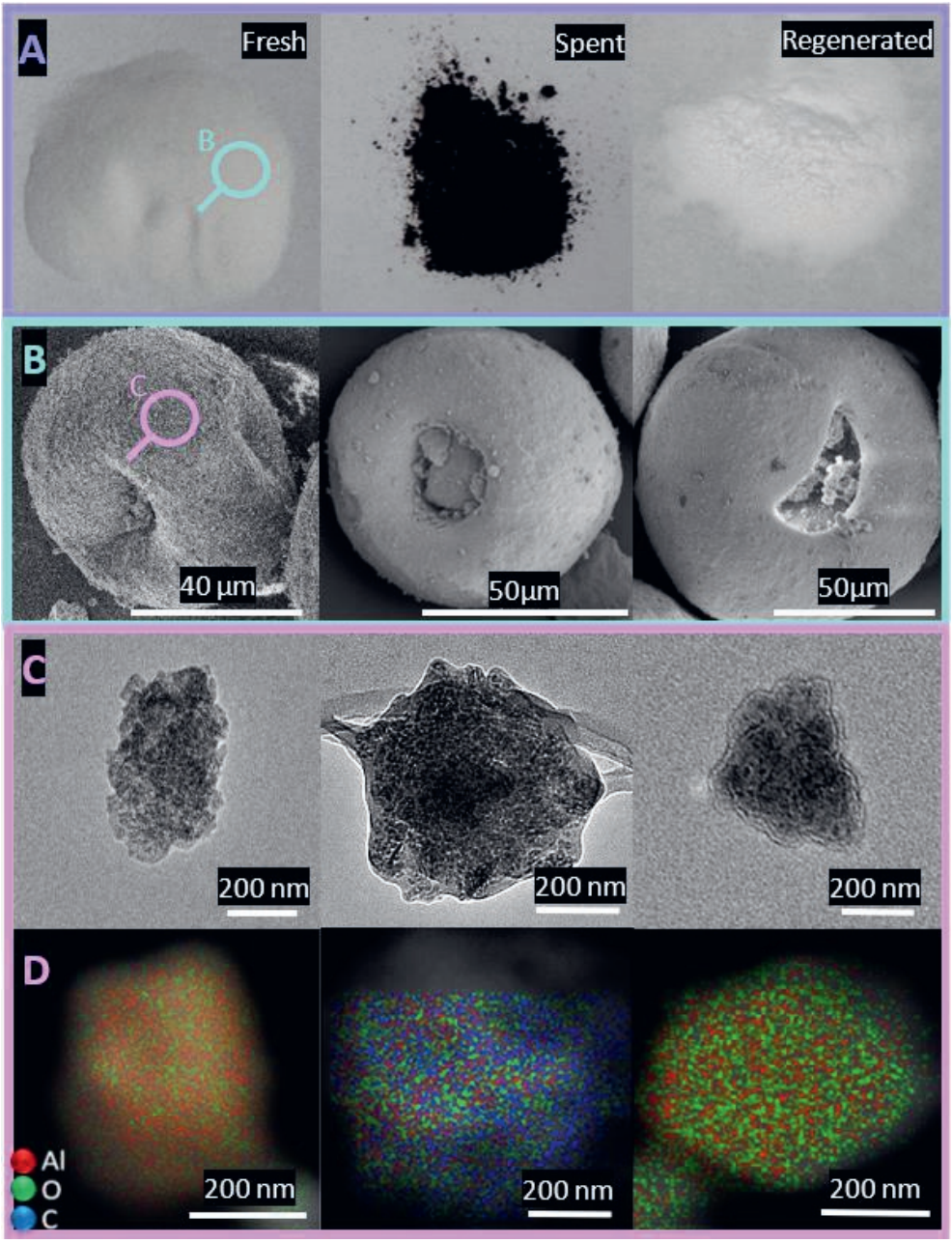

Figure 4.5. Analysis of fresh, spent, and regenerated puralox SCCa 5/200 catalyst after pyrolysis of nPUR. **A**) visual representation, **B**) scanning electron microscopy images, and **C**) transmission electron microscopy with **D**) energy dispersive X-ray spectroscopy analysis

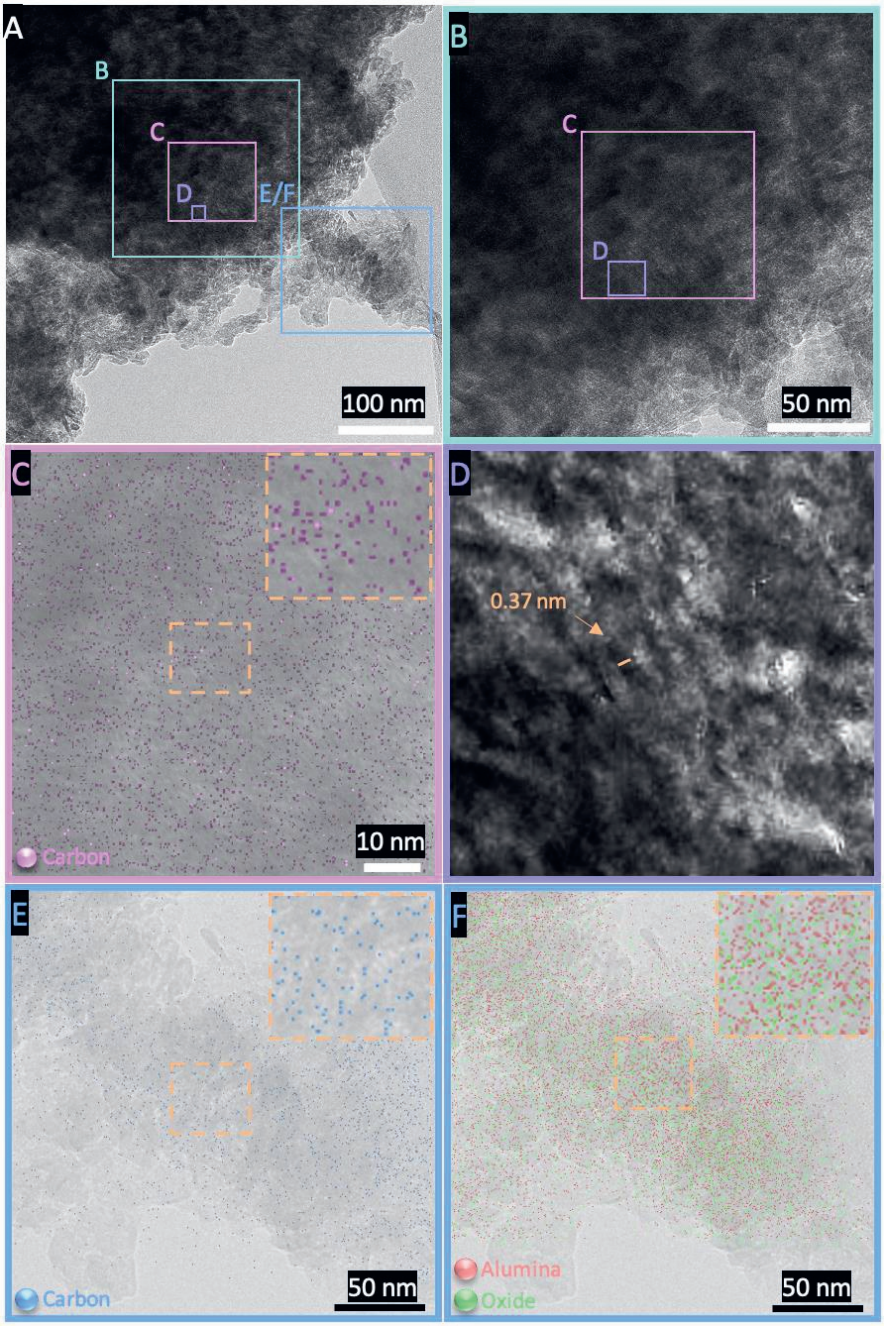

Figure 4.6. Representative transmission electron microscopy images of the spent catalyst. **A**) and **B**) General overview **C**) zoom-in images showing homogeneous carbon deposition **D**) carbon lattice spacing. **E**) and **F**) images of single stacked particles analyzed with energy dispersive X-ray spectroscopy

Experiments with the regenerated catalyst

The data in the previous paragraphs show that catalyst deactivation by coking occurs to a significant extent. To regenerate the catalyst and thus to remove the coke, oxidative treatments (550 °C for 5 h) were investigated. Regeneration/recycle was successful in the first three regeneration/recycle steps, as indicated by the aniline yields (Figure 4.3), which showed no significant reduction compared to the fresh catalyst. Regeneration/recycle steps 4 and 5 show a steady decrease in aniline yields, indicating irreversible catalyst deactivation (*vide infra*). However, the yields after the 4th and 5th runs are significantly higher than those in the non-catalytic runs (Figure 4.3), implying that the catalyst still remains active. The aniline-to-toluidine ratio (2.15 +/- 0.3) is about constant across runs, indicating that catalyst deactivation does not significantly affect the relative amounts of aniline and toluidine. The characterization results for single- and multiple-regeneration/recycle steps are shown in Figure 4.7. Here, the first run is marked as "fresh," and each regeneration cycle is numbered. For example, "Reg 3x" refers to the 4th run, in which the catalyst has been recycled/reused after three oxidative regeneration treatments. The results revealed that coke removal via an oxidative treatment is highly effective for reactivating the catalyst, though after several regeneration steps, the catalyst becomes less active and the aniline yield decreases. To identify changes in catalyst structure across multiple regeneration/recycling cycles, an in-depth analysis of catalyst properties after each regeneration/recycle has been conducted.

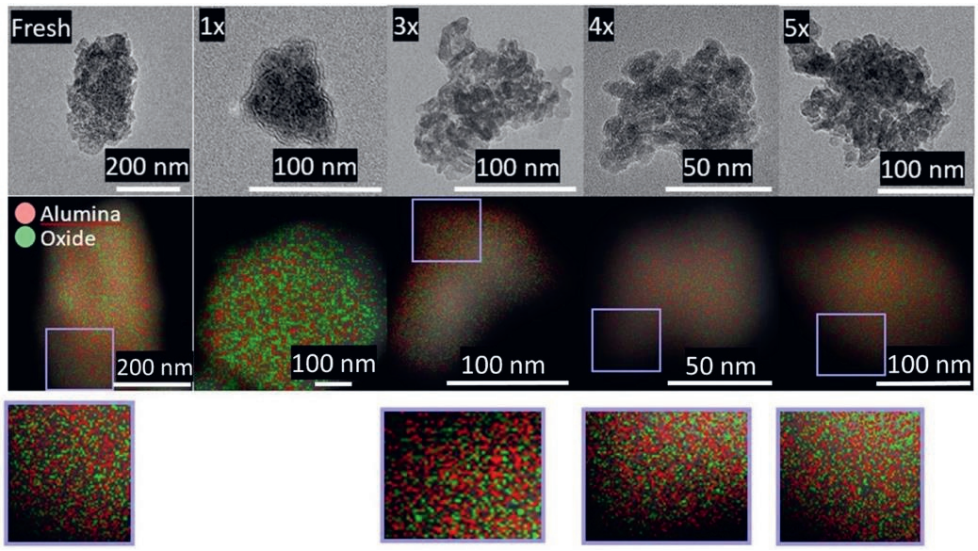

Figure 4.7. TEM-EDX images of catalyst particles after oxidative treatment. From left to right: Fresh, 1x, 3x, 4x, and 5x recycled

Characterization of the regenerated catalysts

The fresh and spent catalysts (before oxidative treatments) were analyzed using TGA-O_2 (Supporting information, Figure S4.6.5). The thermograms were similar across all catalysts, with the main weight-loss peak centered at 570 °C and 581 °C. The coke content was also very similar and ranged between

20.1% to 21.2%. The TGA-O_2 of a regenerated catalyst (Figure S4.6.8, Supporting Information) was identical to that of a fresh catalyst. Thus, it can be concluded that an oxidative treatment at 550 °C for 5 h is an effective method for coke removal, and that no significant differences in the amount or type of coke on the spent catalysts are observed.

Additional analyses were performed on spent catalysts after oxidative regeneration (XRD, SEM, TEM-EDX, XRF, NH_3-TPD, and N_2 physisorption) to identify irreversible structural changes during regeneration. SEM analysis showed that the average particle size of the catalysts did not change significantly (84 µm for the fresh and between 79 and 106 µm for the regenerated ones, see supporting information, Figure S4.6.7, Table S4.6.9). XRD analysis (Figure S4.6.6) showed no changes in the diffraction pattern or the appearance of new signals (e.g., from a Boehmite phase), indicating that phase transformation did not occur to a significant extent during pyrolysis. However, both the surface area and the acidity of the catalysts are affected by oxidative regeneration. A steady decrease in BET surface area was observed (from 218 m^2/g to 172 m^2/g), which points to structural changes in the catalyst. The same holds for the acidity, which is lowered from (406 µmol/g to 375 µmol/g) after 5 cycles (Figure 4.8). It is likely that these combined effects are responsible for the observed 50% reduction in the combined yield of aniline and toluidine, after 5 recycle steps (Figure 4.3). However, XRF analyses (Supporting information, Table S4.6.9) revealed that substantial amounts of inorganics are present in the regenerated catalysts, and that these amounts increase with each regeneration cycle. For example, the amount of SiO_2 increases from negligible to 3.58% after 5 cycles, CaO from 0.17% to 0.61% and MgO from negligible to 0.63%, leading to a reduction in the alumina content (from 99.7% to 93.2%). The inorganics that increase are also present as ash components in the nPUR feed (supporting information, Table S4.6.1), and imply that these are deposited on the catalyst surface during catalytic pyrolysis, thereby affecting the structural features and associated catalyst activity. The presence of SiO_2 on the catalyst after 5 cycles is also supported by XRD (supporting information, Figure S4.6.6, Table S4.6.9) and shows a clear Si (111) peak of SiO_2 at 2θ of 27°[16] (Supporting information, Table S4.6.1).

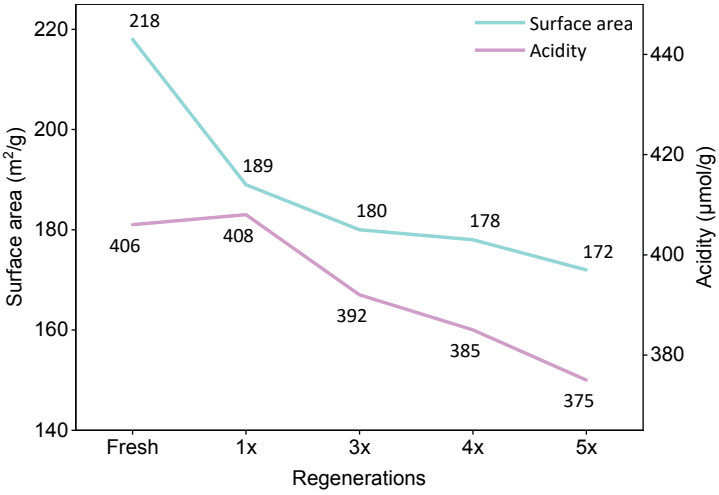

Figure 4.8. Surface area and acidities after each catalyst regeneration cycle and after oxidative treatment

Extended catalyst reuse/recycling in the TMR

Previous results showed that, in addition to reversible deactivation by coke formation, the catalyst irreversibly deactivated after 4 regeneration cycles. We further investigated extended regeneration cycles on a milligram scale in the TMR (0.5 mg feed, a catalyst-to-feed ratio of 5:1, at 550 °C). Here, the TMR was loaded with catalyst and PUR, and pyrolysis was initiated. After the run, the reactor was cooled and opened. The catalyst was regenerated by heating in air and reused for an experiment with fresh PUR. Catalyst stability was assessed by comparing aniline and toluidine yields in the recycled runs with those in the initial run. Aniline and toluidine yields based on input (wt%) are provided in the supplementary information section S4, Table S4.6.10.

Figure 4.9 (top, blue columns) shows the normalized combined aniline and toluidine yields using nPUR as the feed for 45 regeneration cycles. The horizontal purple line marked with "No cat ref. line AnT nPUR" shows the yield for a non-catalytic run, which tentatively may be considered the level for a fully deactivated catalyst (*vide infra*). For the first 4 regeneration cycles, the combined yield dropped from 100 (fresh) to 35%. In the next 28 regeneration steps, the yield stabilized at about 20% of the fresh catalyst activity, then declined to a low value for subsequent 13 cycles. This indicates a three-stage deactivation pattern: first, a steep decline; followed by a stabilization stage; and finally, full deactivation.

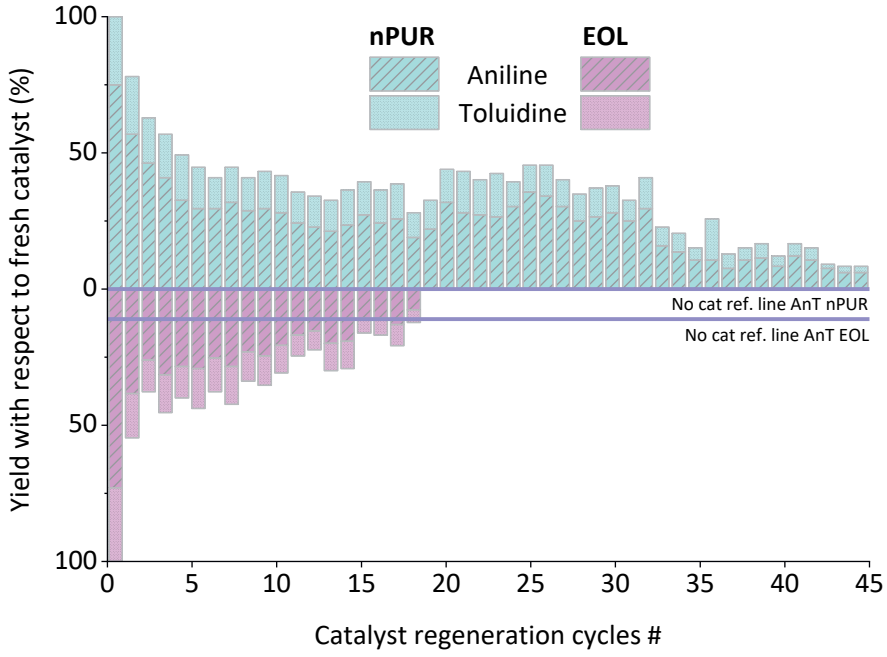

Figure 4.9. Catalyst activity for aniline and toluidine formation from nPUR (Blue) and EOL PUR (purple) in TMR experiments. Reaction conditions: ca. 0.5 mg nPUR or EOL PUR, catalyst-to-feed ratio of 5 to 1, 550 °C with a helium flow of 205 mL/min and a reaction time of 10 seconds. The purple lines represent non-catalytic yields and were used as reference line to identify complete catalyst deactivation

Statistical analyses of the data also confirm the presence of three distinct stages (Figure 4.10). No sound explanation for this deactivation behavior has been found yet. Different active sites may be present on the catalysts, with different reactivity and sensitivity to impurities in the feed. In the initial stage of deactivation, a specific type of active site is rather rapidly deactivated by impurities (e.g., silica and other metals, see Table S4.6.1 in the Supporting Information), as found for the g-scale downer experiments (*vide supra*). In the subsequent stage, catalytic activity remains constant, implying the presence of sites that remain active and are less prone to deactivation. Finally, these sites are also deactivated by (other) impurities or by substantial carbon deposition due to incomplete oxidative regeneration (*vide infra).*

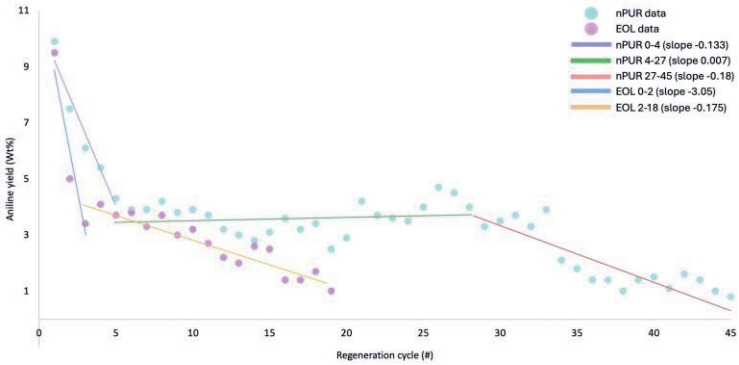

Figure 4.10. Comparison of aniline yields for the recycle runs in the TMR for nPUR and EOL PUR

TEM-EDX analysis (supporting information, Figure S4.6.12) of the 45-times-regenerated catalyst indeed shows extensive carbon deposition, with more than half of the sample weight being carbon. This implies that the oxidative regeneration steps between runs were far from quantitative, leading to carbon accumulation on the catalyst. This obscures the deactivation pattern and hampers drawing sound conclusions and a proper comparison with the data from the staged free-fall reactor. In addition, we cannot rule out that the carbon deposit itself, with embedded inorganics, is somewhat active in the reaction. As such, we tentatively conclude that contaminant deposition contributes to catalyst deactivation, though we cannot rule out effects of coke deposition in these extended TMR experiments.

Similar TMR recycling experiments as described for nPUR were carried out with EOL PUR feed, and the normalized combined aniline and toluidine yields are shown in Figure 9 (pink columns, downwards oriented). The deactivation pattern differs markedly from that obtained with nPUR, and the catalyst is inactive after 18 recycle runs. This is most likely due to the severe accumulation of impurities on the catalyst surface, stemming from the substantial amounts of elemental impurities present in the EOL-PUR feed (Supporting information, Table S4.6.2). This phenomenon was already observed for nPUR, but it is likely enhanced because EOL-PUR contains larger amounts of contaminants; see Figure S4.6.13 for details. This Figure depicts the different deactivation patterns for both PUR types, with trendlines generated using a statistical approach. The initial drop in activity is slightly higher for EOL-PUR than for nPUR. However, while nPUR shows a stabilization phase during extended recycling runs, EOL-PUR shows a rapid decline, which was attributed to extensive impurity accumulation on the catalyst surface

leading to deactivation. However, as with nPUR, carbon deposition obscures the analyses because coke formation is less than quantitative during the oxidative workup of spent catalyst. Indeed, TEM-EDX analysis (at.%) of the catalyst after 18 regeneration steps using EOL-PUR (Supporting information, Figure S4.6.13, and Table S4.6.12) revealed only 19% remaining alumina, large amounts of carbon, and substantial amounts of iron (6.61%). Iron is a common catalyst poison for various catalytic transformations, and it can block catalyst pores and active sites and promote coke formation.[17] The iron content is by far lower in the spent catalyst from the nPUR experiments (0.49 at%). This may be one factor responsible for the remarkable difference in catalyst deactivation profiles between nPUR and EOL-PUR (Figure 9 and 10). Elemental mapping did not detect potassium on the spent catalyst surface, despite its presence in the feedstock (ICP, see Tables S1 and S2 in the supporting information). This is most likely because the trace amounts accumulating on the catalyst over time do not exceed the TEM-EDX detection limit of about 1 wt%. Consequently, we cannot conclude the influence of potassium on catalyst deactivation.

Comparison of milligram scale (TMR) vs gram scale (downer) catalyst performance

Direct comparison of catalyst performance, particularly the extent of deactivation, between the milligram- and gram-scale reactors is challenging because the two systems operate at i) different PUR-to-catalyst loadings (1:1 for the downer and 1:5 for the TMR) and ii) different heating and heating-up times. The cumulative catalyst consumption is 6 kg PUR converted per kg catalyst for the downer recycle experiments and 3.6 kg PUR converted per kg catalyst for the TMR experiments. Combined with the experimentally obtained aniline and toluidine yields, the catalyst amount required to produce a ton of product is still far too high and not on par with TEA values. Further testing will be required in dedicated units, e.g., an FCC-type concept with intermediate catalyst regeneration by oxidative treatment to reduce catalyst consumption, which is beyond the scope of this study.

To compare extents of catalyst deactivation in both units, catalyst performance was assessed by plotting the combined aniline and toluidine yield versus the cumulative PUR throughput per unit catalyst mass (g PUR/g cat), and the results are shown in Figure S4.6.14, Supporting Information. It shows a steady decreasing trend for the TMR system, indicative of progressive catalyst deactivation. For the downer, a different trend was observed, with relatively stable yields up to a cumulative PUR throughput of 5 per unit catalyst mass, followed by a substantial drop. As such, the two units show different deactivation trends, which may be due to differences in heating time, PUR-to-catalyst loadings, and coke levels remaining after oxidative treatment (negligible for the g-scale reactor and significant for the mg reactor (*vide supra*)).

4.4. Conclusions

We conducted extensive studies to experimentally determine the stability of a selected alumina-based catalyst for converting PUR to aniline via catalytic pyrolysis. Virgin PUR (nPUR) was pyrolyzed in a batch-operated staged free-fall reactor, and it was shown that the catalyst deactivates to some extent, as indicated by changes in activity and chemoselectivity when using a spent catalyst. Spent catalyst characterization shows that coke formation is the main cause of catalyst deactivation. Oxidative treatment of the spent catalyst was highly effective at removing coke, suggesting that coke formation may be a reversible form of catalyst deactivation. Subsequent testing across multiple regeneration cycles in the g-scale downer reactor shows that irreversible deactivation occurs to some extent, due

to decreased acidity and BET surface area, attributed to deposition of inorganics from the PUR feed on the catalyst. Extended recycle runs in a TMR also support this, showing that EOL-PUR, with higher inorganic content, deactivates much faster than nPUR. However, incomplete oxidative regeneration due to experimental limitations led to coke accumulation on the catalyst surface, obscuring the TMR results. The findings reported here imply that coke formation is likely not a major issue for further scale-up, though optimizing the oxidative treatment process (e.g., severity, such as temperature and time) is required. Further attention should be given to impurity handling in the PUR feed to avoid irreversible activation, e.g., by developing effective pretreatments to remove inorganic impurities.

References

1. Bulan, A. *et al.* Process for producing isocyanates. (2012) doi:US8,153,838B2.
2. Alshammari, B. A. *et al.* Impact of Hybrid Fillers on the Properties of High Density Polyethylene Based Composites. *Polymers (Basel).* **14**, 3427 (2022).
3. Datta, J., Kopczyńska, P., Simón, D. & Rodríguez, J. F. Thermo-Chemical Decomposition Study of Polyurethane Elastomer Through Glycerolysis Route with Using Crude and Refined Glycerine as a Transesterification Agent. *J. Polym. Environ.* **26**, 166–174 (2018).
4. Liu, B. *et al.* Opportunities in Closed-Loop Molecular Recycling of End-of-Life Polyurethane. *ACS Sustain. Chem. Eng.* **11**, 6114–6128 (2023).
5. Shin, S. R., Kim, H. N., Liang, J. Y., Lee, S. H. & Lee, D. S. Sustainable rigid polyurethane foams based on recycled polyols from chemical recycling of waste polyurethane foams. *J. Appl. Polym. Sci.* **136**, 47916 (2019).
6. Van Belleghem, L. *et al.* Recovery of Polyol and Aromatic Amines from Rigid Polyurethane Foams via Ammonolysis. *JACS Au* **5**, 3444–3452 (2025).
7. Engels, T. G. W. *et al.* Chemical recycling of rigid polyurethane foam via thermocatalytic conversion to aniline. (2026).
8. Sasol Limited. High Purity Aluminas. https://products.sasol.com/pic/products/home/grades/ZA/5puralox-and-catalox/index.html (2026).
9. Groen, J. C., Peffer, L. A. A. & Pérez-Ramírez, J. Pore size determination in modified micro- and mesoporous materials. Pitfalls and limitations in gas adsorption data analysis. *Microporous and Mesoporous Materials* **60**, 1–17 (2003).
10. van Akker, M. *et al.* Full Utilization of Hard-to-Recycle Mixed Plastic Waste by Conversion toward Pyrolysis Oil and BTX Aromatics on a Pilot Scale. *Energy and Fuels* **39**, 6438–6451 (2025).
11. He, S. *et al.* Novel Staged Free-Fall Reactor for the (Catalytic) Pyrolysis of Lignocellulosic Biomass and Waste Plastics. *Energy and Fuels* **38**, 8740–8748 (2024).
12. Anekwe, I. M. S. & Isa, Y. M. Unlocking catalytic longevity: a critical review of catalyst deactivation pathways and regeneration technologies. *Energy Advances* **4**, 1075–1113 (2025).
13. Behera, B., Gupta, P. & Ray, S. S. Structure and composition of hard coke deposited on industrial fluid catalytic cracking catalysts by solid state 13C nuclear magnetic resonance. *Appl. Catal. A Gen.* **466**, 123–130 (2013).
14. He, S. *et al.* A time- and space-resolved catalyst deactivation study on the conversion of glycerol to aromatics using H-ZSM-5. *Chemical Engineering Journal* **434**, 134620 (2022).

15. Legin-Kolar, M. & Ugarkovic, D. Petroleum coke structure: Influence of feedstock composition. *Carbon N. Y.* **31**, 383–390 (1993).
16. Kumar, G., Chen, J. W., Ma, H. H., Huang, X. F. & Huang, M. H. Facet-dependent electrical conductivity properties of a 4H-SiC wafer. *J. Mater. Chem. C Mater.* **10**, 10424–10428 (2022).
17. Argyle, M. D. & Bartholomew, C. H. Heterogeneous catalyst deactivation and regeneration: A review. *Catalysts* **5**, 145–269 (2015).

4.5. Supporting information

Newly produced PUR (nPUR) and end-of-life PUR (EOL)

Newly rigid polyurethane refrigerator foam was obtained from Covestro Germany and used as the feedstock for all batch milligram- and batch gram-scale reactions. The feed was cryo-milled to a powder prior to use using an IKA Tube Mill 100 control. Elemental analysis and metal content of the PUR were analyzed using a CHNS analyzer and XRF, respectively. The ash content (0.8%) was obtained via combustion under air in a dedicated oven at 3.0 g scale. The content of various metals in the ash was determined by XRF. Results are shown Table S4.6.1. It is assumed that the inorganics are present in the oxidized form, which is not necessarily the case.

Table S4.6.1. Chemical composition of nPUR refrigerator foam obtained from Covestro Germany

C[a] (%)	H[a] (%)	N[a] (%)	O[b] (%)
65.7	6.69	7.52	19.5

Sillicon[c,d] (%)	CaO[c,d] (%)	K_2O[c,d] (%)	Fe_2O_3[c,d] (%)	MgO[c,d] (%)	TiO_2[c,d] (%)
0.206	0.144	0.144	0.0037	0.035	0.003

[a]Average of 2 measurements; [b]By difference; [c]Percentage calculated on absolute ash values determined via XRF; [d]Impurities below 25 ppm have been left out for brevity

Table S4.6.2. Chemical composition of end-of-life rigid polyurethane foam (EOL) obtained from waste refrigerators

C[a] (%)	H[a] (%)	N[a] (%)	S[a] (%)	O[b] (%)
66.04	6.71	7.14	0.21	19.9

Fe_2O_3[c,d] (%)	CaO[c,d] (%)	TiO_2[c,d] (%)	Sillicon[c,d] (%)	CuO[c,d] (%)	Al_2O_3[c,d] (%)	MgO[c,d] (%)	
0.668	0.447	0.365	0.286	0.284	0.090	0.082	
K_2O[c,d] (%)	BaO[c,d] (%)	MnO[c,d] (%)	SrO[c,d] (%)	Cr_2O_3[c,d] (%)	SnO_2[c,d] (%)	TeO_2[c,d] (%)	V_2O_5[c,d] (%)
0.025	0.016	0.012	0.006	0.005	0.004	0.004	0.004

[a]Average of 2 measurements; [b]By difference; [c]Percentage calculated on absolute ash values determined via XRF; [d]Impurity values below 25 ppm have been left out for brevity

Table S4.6.3. Summary of chemical composition of PUR feeds

Feed	N content from elemental analysis (%)	Ash content[a] (%)	Other impurities[b] (%)	Total amount of PUR present in feed (%)
nPUR	7.52	0.80	0.00	99.2
EOL_2	7.14	2.66	12.34	85.0

[a]Average of 2 measurements; [b]Impurities include binder material, polystyrene, cyclopentane as blowing agent, and other unidentified end-of-life incorporated impurities

Catalyst details

The alumina-based catalyst (Puralox SCCa 5/200) consists of 99.1% Al_2O_3, 0.66% MgO, and 0.17% CaO as measured via XRF (See Table S4.6.8). Relevant catalyst properties measured experimentally by us are shown in Table S4.6.4. The particle size distribution of the catalyst was measured by SEM with at least 60 particles measured per sample (see Table S4.6.4 below for examples).

Table S4.6.4. Experimentally obtained properties of the alumina-based Puralox SCCa 5/200 catalysts

Property	Value	Unit
Al_2O_3 content[a]	99.1	%
Particle size[b]	84 ± 28	µm
Surface area[c]	218	m^2/g
Total pore volume[d]	382	cm^3/g
Total acidity[e]	406	µmol/g
Acid site density[f]	1.86	$µmol/m^2$
Basicity[g]	187	µmol/g
Basic site density[f]	0.86	$µmol/m^2$
Brønsted/Lewis ratio[h]	0/100	-

Crystallinity[i]	54.5	%
Crystal size[j]	53.5	Å

[a]Determined via XRF; [b]Obtained via SEM analysis, measurement of 85 particles; [c]Calculated via N_2 physisorption; [d]Determined via p/p^0 at 0.99 from isotherm plot; [e]Obtained via NH_3-TPD; [f]Calculated using $\frac{Total\ acidity/basicity}{Surface\ area}$; [g]Obtained by CO_2-TPD; [h]Calculated from Py-IR experiments; [i]Calculated using Bruker DIFFRAC.EVA software

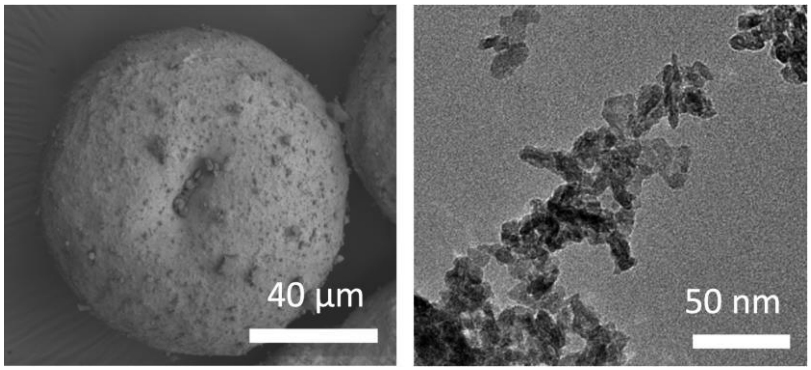

Figure S4.6.1. SEM (left) and TEM (right) image of Puralox SCCa 5/200

Staged free-fall reactor (batch gram scale)

Gram scale experiments were performed on a staged free-fall reactor developed in-house (Figure S4.6.2). A detailed description of the reactor is given in earlier work: Van Akker, M. *et al.* Full Utilization of Hard-to-Recycle Mixed Plastic Waste by Conversion toward Pyrolysis Oil and BTX Aromatics on a Pilot Scale. *Energy and Fuels* **39**, 6438–6451 (2025). And He, S. *et al.* Novel Staged Free-Fall Reactor for the (Catalytic) Pyrolysis of Lignocellulosic Biomass and Waste Plastics. *Energy and Fuels* **38**, 8740–8748 (2024).

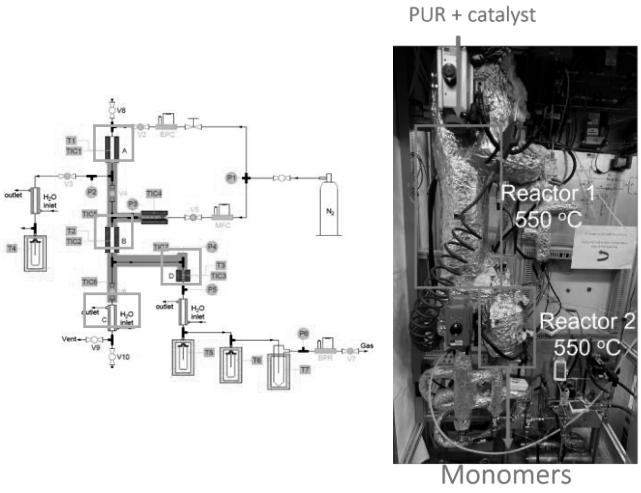

Figure S4.6.2. Schematic representation (left) of the staged free-fall reactor (batch gram-scale setup), obtained from ref. [2] **A**) pre-heating zone, **B)** pyrolysis zone 1, **C**) cooling zone, **D**) Optional catalyst bed (not used in the research reported in this manuscript) and visual representation of the staged freefall reactor (right)

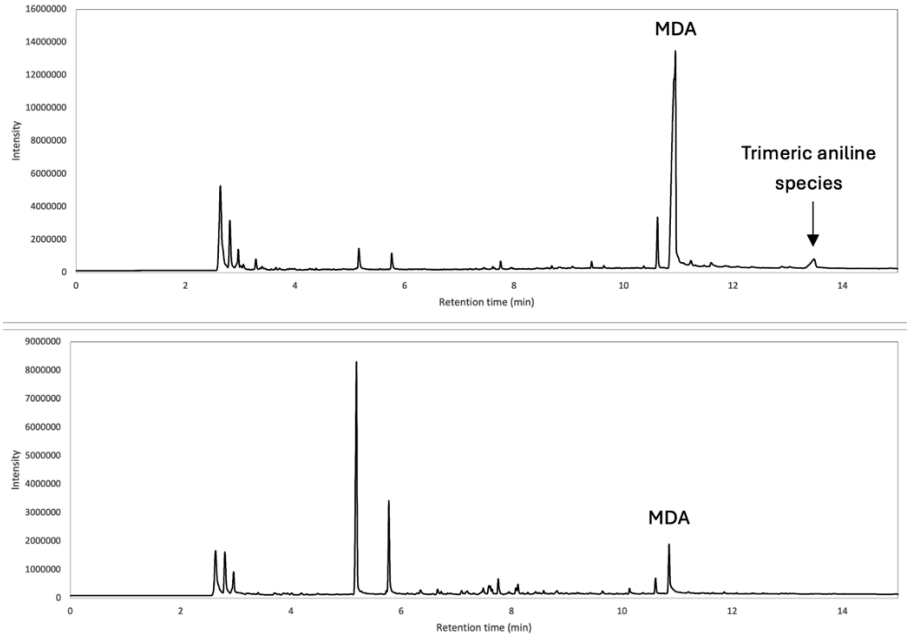

Figure S4.6.3 Example of a GC-MS measurement for a catalyst where higher MDA fragments were observed (top) and a representative GC-MS chromatogram for the catalyst 5/200 used in this work (bottom)

Statistical validation of thermally regenerated catalyst yields (purple columns)

The aniline, toluidine, and MDA yields for the fresh and regeneration runs (purple columns in Figure 4.3) were analyzed to determine whether the observed yields differ statistically. The results are shown in Table S4.6.5. Here, the range is the mean ± standard deviation.

Table S4.6.5. Statistical analysis for the combined aniline and toluidine and MDA yields of the pyrolysis results shown in Figure 4.3

Run	AnT yield ranges (wt%)	MDA yield ranges (wt%)	Are the yields statistically equal to the fresh catalyst? (AnT/MDA)
Fresh	7.35 – 7.65	0.98 – 1.52	N/A
1x	6.52 – 8.08	0.12 – 1.54	Yes/Yes
3x	7.34 – 8.46	0.72 – 1.27	Yes/Yes
4x	5.70 – 8.10	2.07 – 2.73	Yes/No
5x	2.20 – 5.40	2.08 – 2.12	No/Yes

Spent catalyst characterization data for g-scale experiments

Elemental analysis of the spent catalyst is shown in Table S4.6.6, the cat characterization data of the fresh, spent, 2x used, 3x used, and regenerated data are shown in Table S4.6.7. The BET and XRD results are shown in Table S4.6.7, and Figure S4.6.4.

Table S4.6.6. CHNSO results of the Spent catalyst

C[a] (%)	H[a] (%)	N[a] (%)	S[a] (%)	O[b] (%)
14.57	1.15	1.67	ND	82.61

[a]Average of 2 measurements; [b]by difference

Table S4.6.7. Relevant property data of the alumina catalyst, fresh, spent, and 1x regeneration results

	Surface area[a] (m^2/g)	Total acidity[b] (µmol/g)	Acid site density[c] (µmol/m^2)	Particle size[d] (µm)	Crystallinity[e] (%)
Fresh	218	406	1.86	84	55
Spent	159	ND	-	ND	63
2x reused	141	ND	-	ND	66
Regenerated	189	409	2.17	79	56

[a]Determined at P/P_0 = 0.99 with an average of 2 measurements; [b]Obtained byNH_3-TPD; [c]Calculated using $\frac{Total\ acidity}{Surface\ area}$; [d]Obtained by SEM imaging, average of minimal 60 particles; [e]Calculated using Bruker DIFFRAC.EVA software

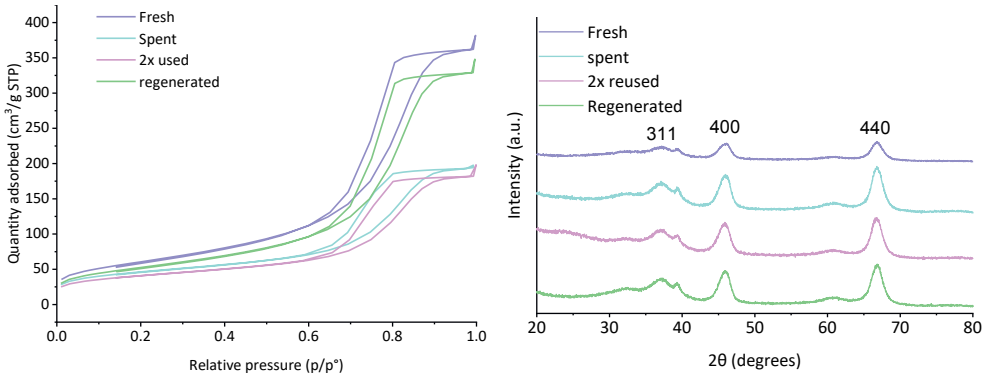

Figure S4.6.4. Nitrogen physisorption data (left) for fresh, spent, and regenerated catalyst after oxidative regeneration and XRD results (right) of fresh catalyst, spent and reused catalyst prior to regeneration, and oxidatively regenerated catalyst

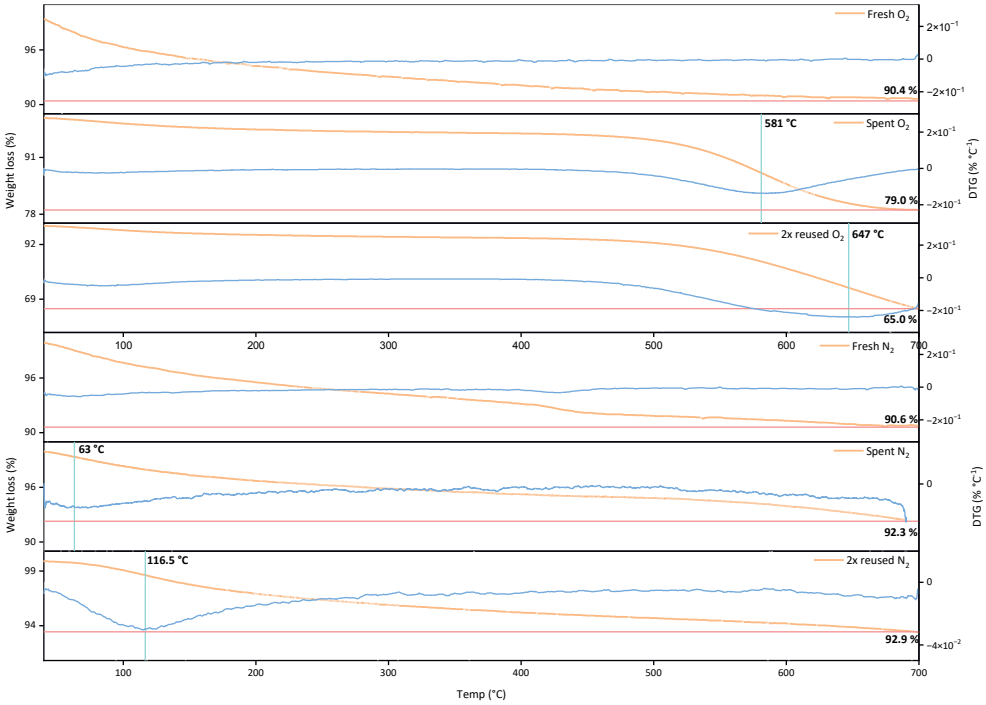

Figure S4.6.5. TGA-O_2 of relevant spent catalysts prior to oxidative treatment. From top to bottom: fresh-O_2, spent-O_2, 2x reused-O_2

Catalyst data for regeneration studies in the gram-scale reactor

Elemental analysis (XRF) and cat characterization data of the oxidatively regenerated catalysts are shown in Table S4.6.8 and Table S4.6.9, respectively. XRD data are given in Figure S4.6.6. The SEM and TEM images are shown Figure S4.6.7 and Figure 4.4 of the manuscript. The coke has been identified via TGA-O_2 (Figure S4.6.8). Please note that regeneration cycle 2 is not included in the data due to a system defect. However, the catalyst was passed through the pyrolysis cycle and used in the next regeneration experiment.

Table S4.6.8. Elemental analysis of the catalyst of each regeneration cycle

Regeneration (#)	Compound 1 (%)	Compound 2 (%)	Compound 3 (%)	Compound 4 (%)
Fresh	Al_2O_3 (99.7)	CaO (0.17)	-	-
1x reg.	Al_2O_3 (98.3)	SiO_2 (1.11)	CaO (0.22)	K_2O (0.15)
3x reg.	Al_2O_3 (95.1)	SiO_2 (3.00)	MgO (0.68)	K_2O (0.36)
4x reg.	Al_2O_3 (94.5)	SiO_2 (3.42)	MgO (0.71)	CaO (0.43)
5x reg.	Al_2O_3 (93.2)	SiO_2 (3.58)	Y_2O_3 (1.10)	MgO (0.63)

[a]Only the 4 main compounds have been depicted for clarity; [b]Impurities below 250 ppm are not provided

Table S4.6.9. Relevant property data of the alumina catalyst regeneration results

	Surface area[a] (m^2/g)	Total acidity[b] (µmol/g)	Acid site density[c] (µmol/m^2)	Particle size[d] (µm)	Crystallinity[e] (%)
Fresh	218	406	1.86	84	54
1x reg.	189	408	2.17	79	56
3x reg.	180	392	2.18	106	57
4x reg.	178	385	2.16	80	57
5x reg.	172	375	2.18	93	57

[a]Determined at P/P_0 = 0.99 with an average of 2 measurements; [b]Obtained by NH_3-TPD; [c]Calculated using $\frac{\text{Total acidity}}{\text{Surface area}}$; [d]Obtained by SEM imaging, average of at least 50 agglomerates; [e]Calculated using Bruker DIFFRAC.EVA software

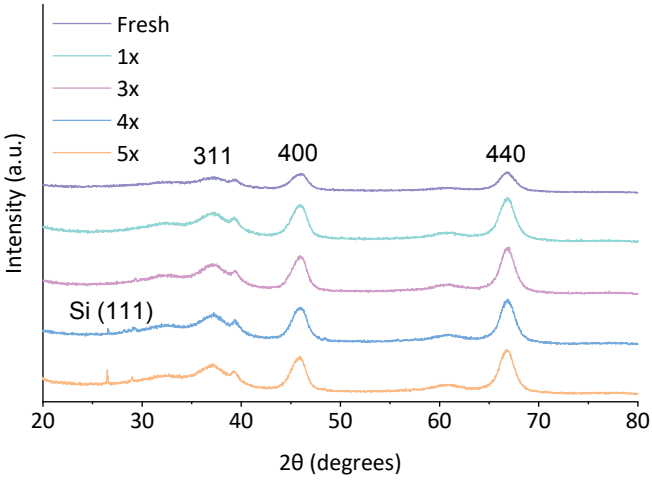

Figure S4.6.6. XRD analysis of oxidatively regenerated catalysts. From top to bottom: Fresh, 1x, 3x, 4x, and 5x regenerated catalyst

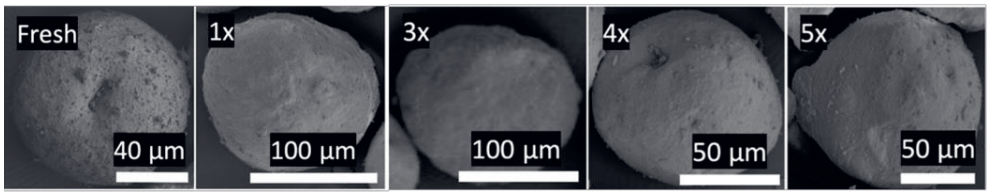

Figure S4.6.7. SEM images of representative catalyst particles after oxidative treatment. From left to right: Fresh, 1x, 3x, 4x, and 5x

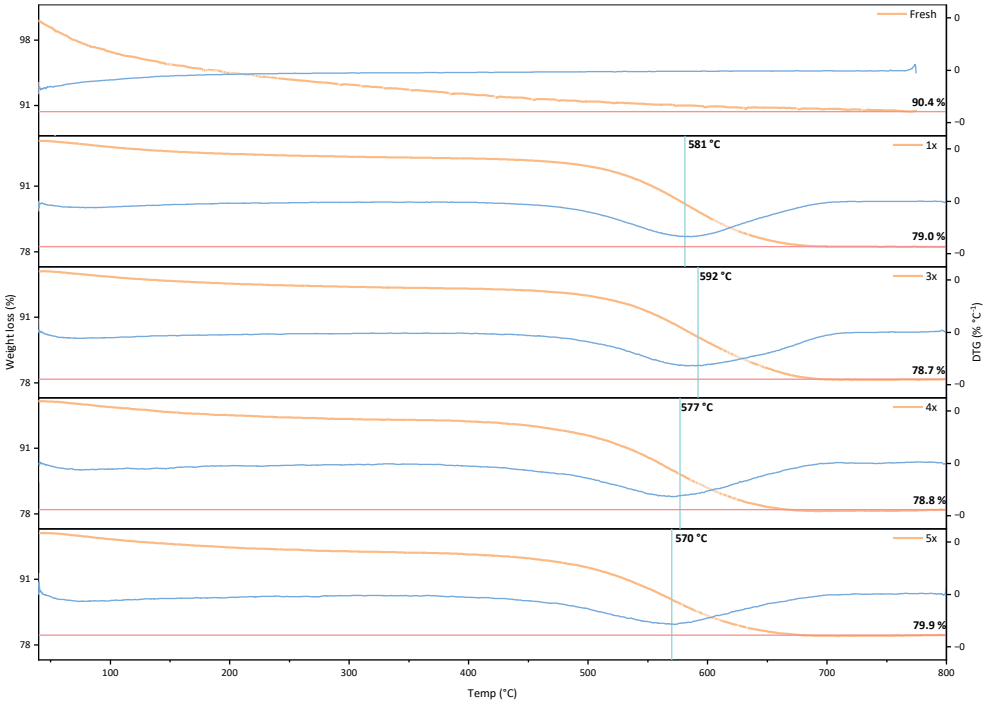

Figure S4.6.8. TGA-O_2 results of the spent catalysts prior to oxidative treatment. From top to bottom: fresh, 1x, 3x, 4x, and 5x thermally regenerated catalyst

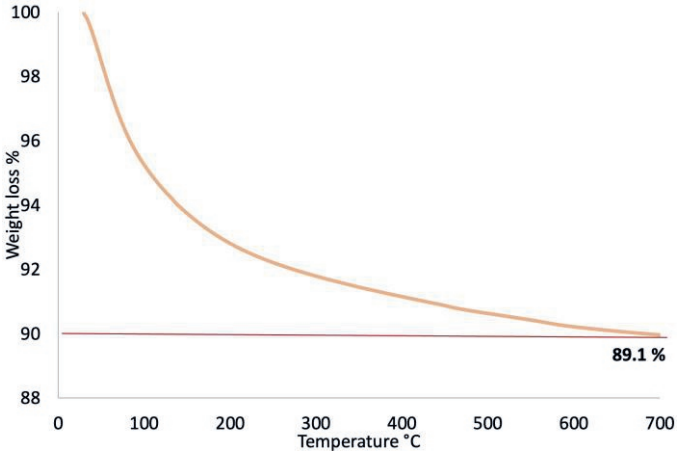

Figure S4.6.9. TGA-O_2 results of an oxidative regenerated catalyst after 1 catalytic cycle

Table S4.6.10. Batch milligram scale catalytic pyrolysis results of post-production PUR (nPUR), and end-of-life PUR (EOL) yield on input using equation 4.5 in section 4.2

Regeneration[a] (#)	An yld nPUR (wt%)	Tol yld nPUR (wt%)	An yld EOL (wt%)	Tol yld EOL (wt%)
No cat	0.0	0.0	0.8	0.6
Fresh	9.9	3.3	9.5	3.5
1	7.5	2.8	5.0	2.1
2	6.1	2.2	3.4	1.5
3	5.4	2.1	4.1	1.8
4	4.3	2.2	3.7	1.5
5	3.9	2.0	3.8	1.9
6	3.9	1.5	3.3	1.6
7	4.2	1.7	3.7	1.8
8	3.8	1.6	3.0	1.4
9	3.9	1.8	3.2	1.4
10	3.7	1.8	2.7	1.3
11	3.2	1.5	2.2	1.0
12	3.0	1.5	2.0	0.9
13	2.8	1.5	2.6	1.3
14	3.1	1.7	2.5	1.3
15	3.6	1.6	1.4	0.7
16	3.2	1.6	1.4	0.8
17	3.4	1.7	1.7	1.0
18	2.5	1.2	1.0	0.6
19	2.9	1.4	-	-
20	4.2	1.6	-	-
21	3.7	2.0	-	-
22	3.6	1.7	-	-
23	3.5	2.1	-	-
24	4.0	1.2	-	-
25	4.7	1.3	-	-
26	4.5	1.5	-	-
27	4.0	1.3	-	-
28	3.3	1.3	-	-
29	3.5	1.4	-	-
30	3.7	1.3	-	-
31	3.3	1.0	-	-
32	3.9	1.5	-	-
33	2.1	0.9	-	-
34	1.8	0.9	-	-
35	1.4	0.6	-	-
36	1.4	2.0	-	-
37	1.0	0.7	-	-
38	1.4	0.6	-	-
39	1.5	0.7	-	-
40	1.1	0.5	-	-
41	1.6	0.6	-	-
42	1.4	0.6	-	-
43	1.0	0.2	-	-
44	0.8	0.3	-	-
45	0.8	0.3	-	-

[a] Reaction conditions: 0.5 mg nPUR, catalyst-to-feed ratio of 5 to 1, 550 °C with a helium flow of 205 mL/min., and a pyrolysis time of 10 s

The aniline to toluidine for both the nPUR and EOL PUR runs based on the results shown in Table S4.6.10 have been analyzed. The analysis for nPUR is shown in Figure S4.6.10 and for EOL PUR in Figure S4.6.11. For nPUR (Figure S4.6.10), the mean aniline-toluidine ratio is 2.41 with a standard deviation of 0.65. A clear trend is absent. For EOL PUR (Figure S4.6.11), Visually, there appears to be a slight downward trend. However, statistical analysis shows this is not significant (p=0.07), and only 17% of the variation is explained by run order.

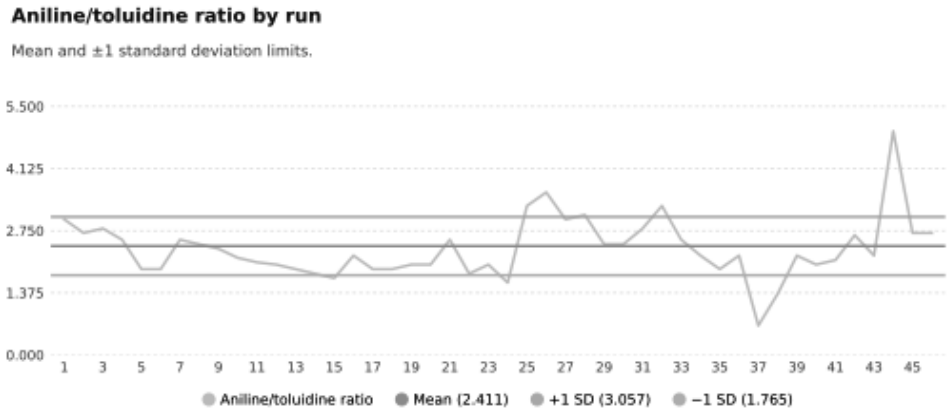

Figure S4.6.10. Aniline-to-toluidine ratio for nPUR for recycling experiments in the TMR

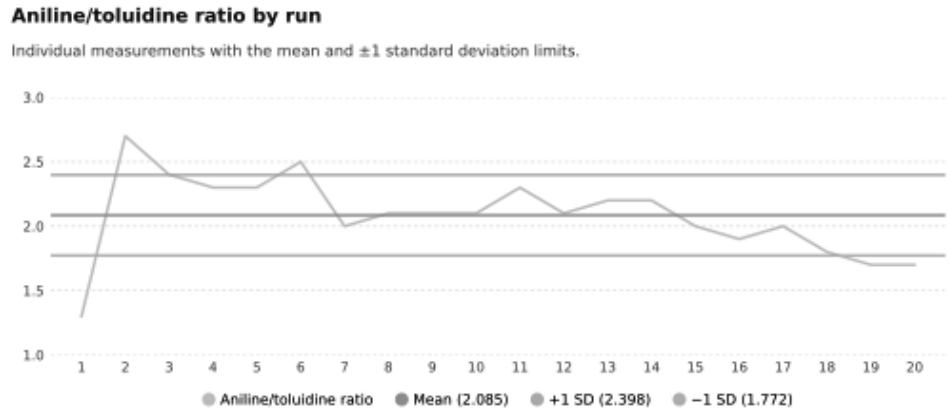

Figure S4.6.11. Aniline-to-toluidine ratio for EOL PUR for recycling experiments in the TMR

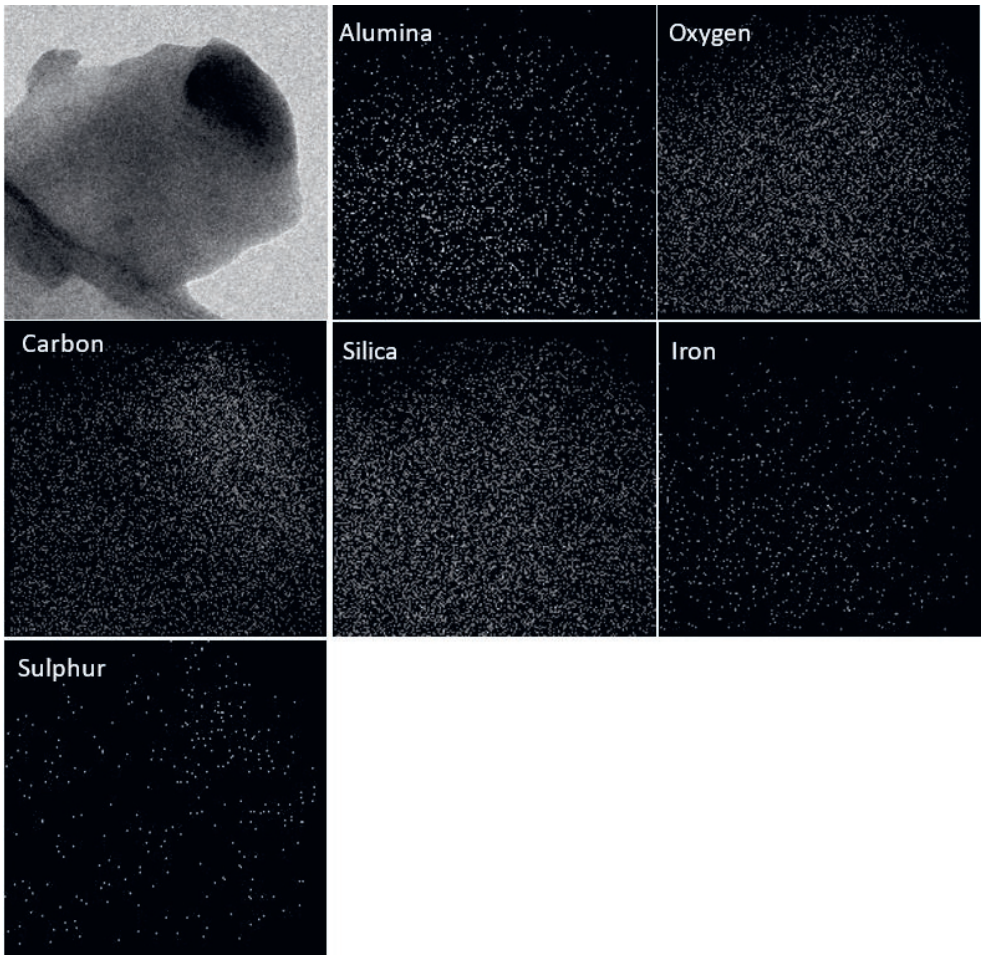

Figure S4.6.12. TEM-EDX results of the catalyst after 45 regeneration cycles with the pyrolysis of nPUR. The analysis was performed after oxidative treatment. Reaction conditions: 0.5 mg nPUR, catalyst-to-feed ratio of 5 to 1, 550 °C with a helium flow of 205 mL/min and a pyrolysis time of 10 seconds

Table S4.6.11. Element quantification of TEM-EDX results shown in Figure S4.6.11

Element	Atomic%
Al	2.49
O	30.76
C	54.34
Si	11.47
Fe	0.49
S	0.17
Mg	0.29

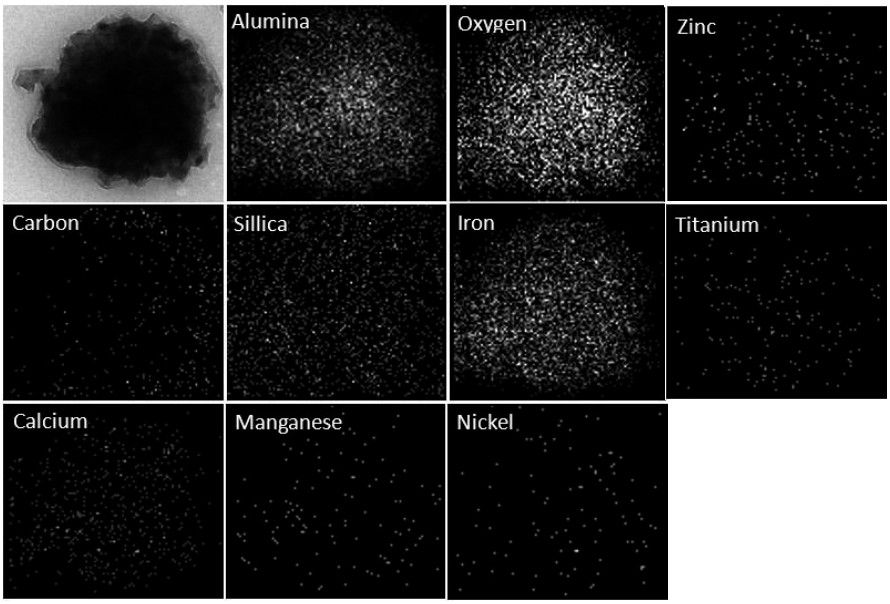

Figure S4.6.13. TEM-EDX results of the catalyst after 18 regeneration cycles with the pyrolysis of EOL PUR. The analysis was performed after oxidative treatment. Reaction conditions: 0.5 mg EOL PUR, catalyst-to-feed ratio of 5 to 1, 550 °C with a helium flow of 205 mL/min and a pyrolysis time of 10 seconds. Please note that nickel originates from sample cup leaching over time

Table S4.6.12. Element quantification of TEM-EDX results shown in Figure S4.6.13

Element	Atomic%
Al	19.01
O	38.90
C	31.01
Si	3.24
Fe	6.61
Ca	0.72
Mn	0.09
Ni	0.07
Ti	0.09
Zn	0.25

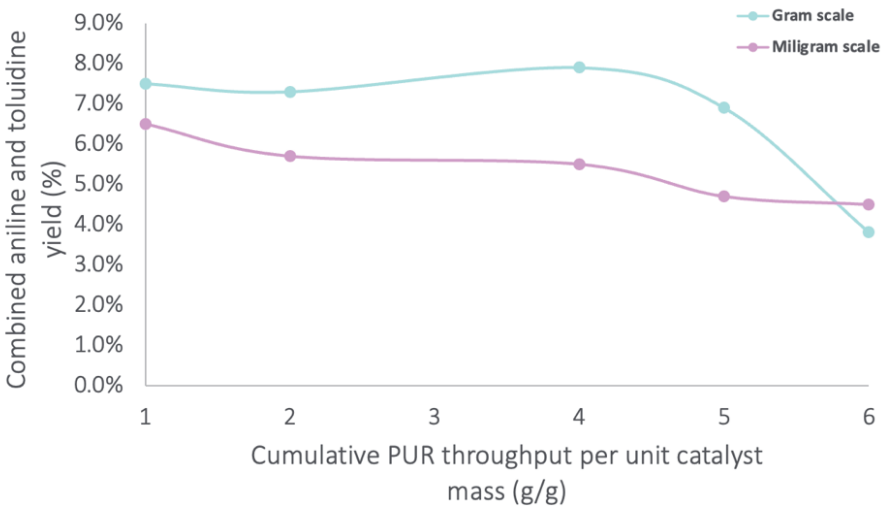

Figure S4.6.14. TMR (milligram scale) vs. downer (gram scale) catalyst performance based on cumulative PUR throughput per unit catalyst mass



Mechanistic insights using ^{13}C and deuterium model compounds

5



This chapter is based on submitted work:

Engels, T. G. W., Talkami, L., Heeres, A., Heeres, H. J. & Deuss, P. J.

Catalytic pyrolysis of rigid polyurethane to aniline: Mechanistic insights using ^{13}C and deuterium model compounds (2026)

Abstract

Recent research highlighted the successful recovery of aniline from the polymeric methylenedianiline (pMDA) segment (~50 wt%) of rigid polyurethane foam at a continuous kilogram scale via catalytic pyrolysis (550 °C) using an alumina-based catalyst (SCCa 5/200). In this work, we explored the mechanistic steps involved in the chemocatalytic recycling strategy described above by performing model studies with D- and ^{13}C- labelled 4,4'-methylenedianiline (MDA)- derivatives in a tandem micropyrolysis reactor. The presence of a catalyst promotes aniline and toluidine formation, as well as additional N-containing side products (ethylaniline, ethyltoluidine, acridine, and methylacridine). Analysis of the pyrolysis product when using D-labelled rigid PUR model compounds implied that the hydrogens from the alcohol and in particular α-hydrogens are available for conversion of the MDA methylene bridge into aniline and toluidine. Catalytic pyrolysis results of ^{13}C labelled model compounds showed that N-containing side products form via homo- or cross-coupling-reactions. A 3-step mechanism for the formation of aniline and toluidine was proposed based on these observations. First, depolymerization of PUR occurs to form polyol and pMDA-derived fragments. Secondly, polyol fragments decompose, yielding CO, CO_2, propene, and acetone. The latter provides hydrogen atoms to crack the methylene bridge of the intermediate MDA, forming aniline and toluidine. In addition, it is shown that in particular toluidine is involved in the formation of N-containing side products, which also hints at its role as coke precursor.

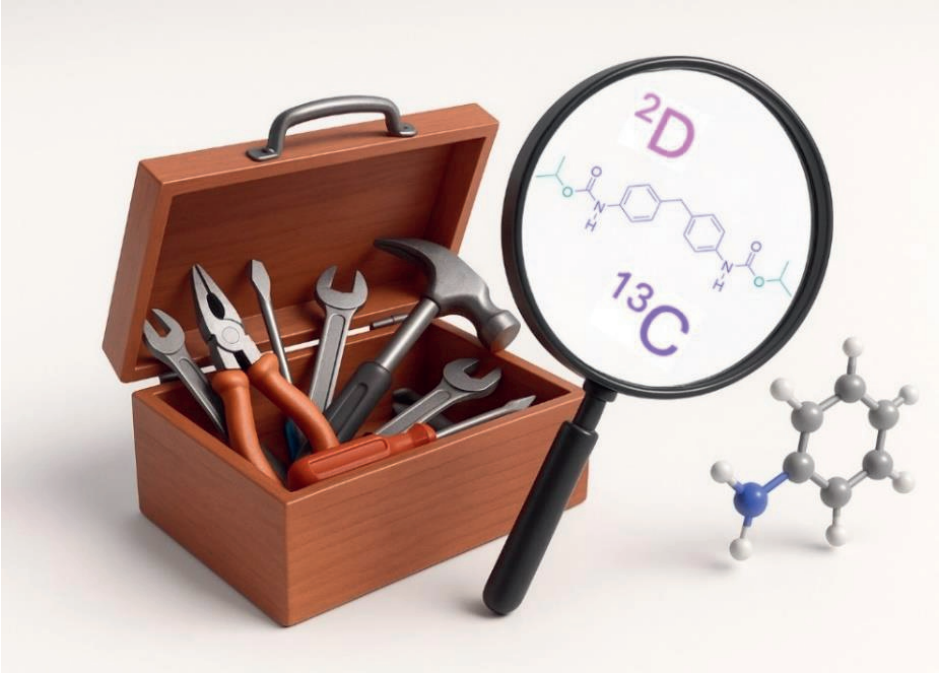

5.1. Introduction

Recycling plastic waste has become crucial for minimizing environmental harm and reducing reliance on fossil fuels, thereby promoting a future circular economy. Polyurethanes are highly adaptable materials used in many applications, though challenging to recycle. This thermoset is often used for insulation, with current waste management methods including landfill (40%), mechanical processing (25%), and energy recovery through incineration (35%).[1] The absence of an efficient circular pathway has led to a significant focus on recycling initiatives. In the ideal case, recovering base chemicals such as aniline from polyurethane waste can reduce climate change impacts by 5.6 kg CO_{2eq} per kg PUR treated.[2]

Polyurethanes are conventionally produced through the reaction of an isocyanate with a polyol, thereby forming the characteristic carbamate bond (–NH–CO–O–). In the case of rigid polyurethane foams, polymeric methylene diphenyl diisocyanate (pMDI) is used as the isocyanate component, which is derived from polymeric methylene dianiline (pMDA), obtained via the acid-catalyzed condensation of aniline with formaldehyde (Figure 5.1, A).[3]

Recently, our group[4] demonstrated that aniline may be obtained in 51% (N-based) yield from virgin PUR (nPUR) via catalytic pyrolysis (550 °C) at batch milligram scale (TMR) using a specific alumina catalyst. Upscaling to continuous operation in a fluidized-bed reactor (5 kg $h^{-1}_{feedstock}$), produced aniline in 14% (N-based) yield from end-of-life PUR.

Thermal pyrolysis of polyurethanes has been studied using model, commercial, and end-of-life feedstocks, and a 4-step degradation pathway has been proposed (Figure 5.1, B).[5–21] Initially, small molecules (H_2O, blowing agents) volatize (100 – 200 °C), followed by retro-polymerization via chain scission (200 - 350 °C), cleaving PUR into isocyanate- and polyol segments. The polyol fragment decomposes into aliphatic alcohols, ethers, alkanes, and alkenes (200–350 °C), and the isocyanate segment into primary amines and CO_2 (350 – 600 °C). The thermal decomposition of PUR is influenced by its formulation (type of polyol, isocyanate, additives, and their content)[12,22–32] and the pyrolysis conditions (temperature, heating rate, carrier gas).[33–38]

Introduction of a catalyst to the thermal degradation process of rigid polyurethane foam has a pronounced effect on the product formation. Reported examples are, **I**) the degradation temperature is decreased upon addition of metal ions (e.g. Cobalt)[39,40], **II**) 4'4 methylene diisocyanate (MDI) and other nitrogen containing aromatics are observed when using zeolites [41,42], **III**) the gas and char yield are higher when using metal salts (e.g. $FeCl_3$ or $ZnCl_2$, respectively)[43], and **IV**) gas formation like NO_x, HCN, CO, and CO_2 can be suppressed by the use of metal oxides (e.g. CaO).[44–47] (A comprehensive overview of all published work is provided in the supplementary information section 5.5).

Bozi *et al.*[41] proposed a mechanism for the formation of aniline from MDI-based models via catalytic pyrolysis with zeolites at 500 °C using a micro-pyrolyzer (Figure 5.1, C). Aniline and toluidine form through the cleavage of the polyurethane polymer chain via a β-CH transfer reaction, followed by further fragmentation facilitated by the acidic sites of the HUSY catalyst. Unfortunately, a clear description of the origin of the hydrogen equivalents required for the formation of aniline and toluidine from the MDI fragment was not provided, and the aniline to toluidine ratio was not quantified.

In our previous work on the catalytic pyrolysis of PUR using alumina catalysts.[4,48] Aniline and toluidine were formed in a 3:1 ratio, which is inconsistent with the expected 1:1 ratio based on the molecular structure of pMDA. A detailed investigation on catalyst deactivation showed mainly hard coke on the catalyst. However, the origin of coke formation was not identified. To correlate the 3-to-1 aniline-to-toluidine ratio with coke evolution, a fundamental understanding of the reaction pathways involved in PUR pyrolysis is necessary. In addition, this knowledge may assist rational catalyst design and may provide tools to increase product yields and tune product ratios upon demand.

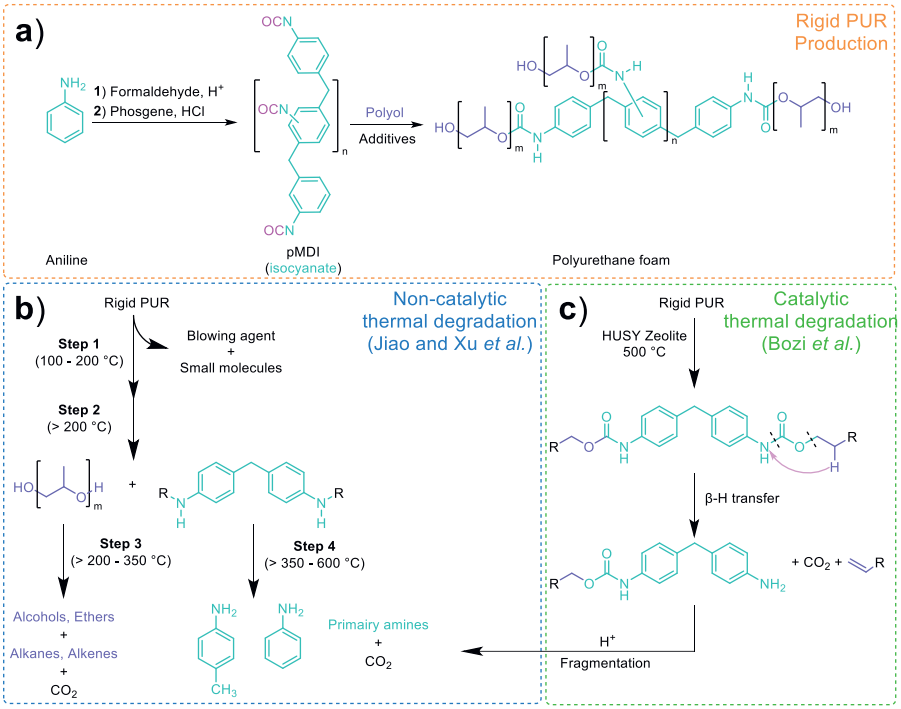

Figure 5.1. Schematic chemical production route of rigid polyurethane foam highlighted in orange (a)[3], non-catalytic thermal decomposition of PUR highlighted in blue (b)[15,21], and zeolite-catalyzed pyrolysis by Bozi *et al.* [41] highlighted in green (c)

In this pioneering work, we aim to gain advanced insight into the degradation pathways of rigid polyurethane foam by establishing the origins of the main- and N-containing side-products via non-catalytic and catalytic pyrolysis of specifically designed and synthesized model compounds (deuterium-, ^{13}C-, and non-labelled). Changes in isotopic distribution and label locations were identified through careful analysis of the products' fragmentation patterns. Based on the data, a reaction mechanism is proposed for the catalytic pyrolysis of PUR foams with a selected alumina catalyst.

5.2. Experimental

Unless otherwise indicated, reagents and substrates were used as received. Standard chemicals were purchased from Sigma Aldrich, commercially available labelled compounds were obtained from

Cambridge Isotopes, and technical-grade solvents were purchased from Boom B.V. Meppel. Dry solvents were collected at room temperature at 6 bar operational pressure from a dry solvent purification system (MBraun SPS 800). Inert-atmosphere experiments were either performed using standard Schlenk techniques with dry P_2O_5-nitrogen gas or in the glovebox.

The alumina-based catalyst (Puralox SCCa 5/200) used in this study was obtained from Sasol Limited (Germany)[49] It is a semi-crystalline, mesoporous catalyst with 99% purity and a pore volume of 0.59 cm^3/g. Other elements present include 0.6% magnesium oxide and 0.2% calcium oxide. The catalyst has an average particle size of 84 µm. The catalyst has a surface area of 218 m^2/g with an acidity of 406 µmol/g. Catalyst characterization data are consistent with Sasol's literature values.[49] A complete overview of relevant catalyst properties is provided in Section S2.1. [4]

1. Diisopropyl (methylenebis(3,1-phenylene))dicarbamate

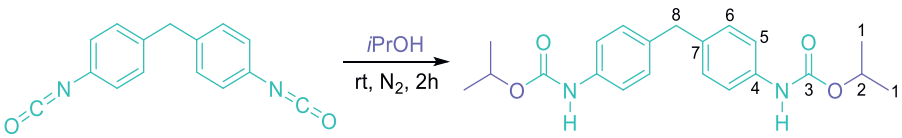

4.0 mmol **99%**

4,4'-methylenediphenyl diisocyanate (4.0 mmol, 1.0 g) was dissolved in 25 mL isopropanol under nitrogen at room temperature, and the reaction progress was monitored by TLC using n-hexane/ethyl acetate 70:30 ratio. TLC analysis indicated the formation of a single product after 2 h reaction time. The reaction mixture was concentrated *in vacuo*, affording a white solid in 99% yield.

^{1}H-NMR (400 MHz, $CDCl_3$): δ 7.27 (d, *J* = 7.24 Hz, 4H, C5-**H**), 7.09 (d, *J* = 8.45 Hz, 4H, C6-**H**), 6.46 (bs, 2H, N-**H**), 5.00 (m, 2H, C2-**H**), 3.88 (s, 2H, C8-**H**), 1.28 (d, *J* = 7.25 Hz, 12H, C1-**H**)

^{13}C-NMR (400MHz, $CDCl_3$): δ 153.01 (C3), 136.31 (C4 or 7), 136.26 (C4 or 7), 129.35 (C6), 118.97 (C5), 68.66 (C2), 40.38 (C8), 21.88 (C1)

HRMS (ESI) m/z: $[M+H]^+$ calcd for $C_{21}H_{27}N_2O_4$ 371.1965; found 371.1959

^{1}H, ^{13}C, COSY, and HSQC NMR data is available in the supplementary information section 5.5, Figures S5.5.2 – S5.5.5

2. Diethyl-(methylenebis(4,1-phenylene))dicarbamate

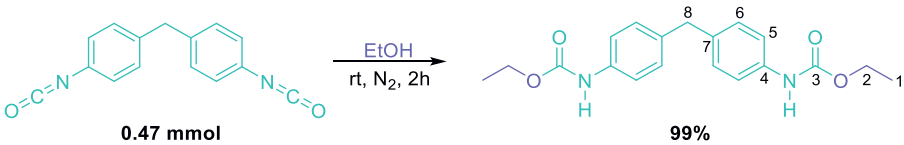

0.47 mmol **99%**

4,4'-methylenediphenyl diisocyanate (0.47 mmol, 118 mg) was dissolved in 1 mL ethanol at room temperature, and the reaction progress was monitored by TLC using n-hexane/ethyl acetate 80:20 ratio. TLC analysis indicated the formation of a single product after 2 h reaction time. The reaction mixture was concentrated *in vacuo* (40 °C, 0.2 mbar), affording a white solid in 99% yield.

^{1}H-NMR (400 MHz, CD_3COCD_3): δ 9.46 (bs, 2H, N-**H**), 7.46 (d, *J* = 8.75 Hz, 4H, C5-**H**), 7.07 (d, *J* = 9.11 Hz, 4H, C6-**H**)**,** 4.07 (q, *J* = 7.17 Hz, 4H, C2-**H**), 3.76 (s, 2H, C8-**H**), 1.21 (t, *J* = 6.81 Hz, 6H, C1-**H**)

^{13}C-NMR (400MHz, CD_3COCD_3): δ 153.01 (C3), 137.56 (C4 or 7), 135.76 (C4 or 7), 129.23 (C6), 118.28 (C5), 60.38 (C2), 40.24 (C8), 14.83 (C1)

^{1}H and ^{13}C NMR data is available in the supplementary information section 5.5, Figures S5.5.6 – S5.5.7

3. Diisopropyl (methylenebis(3,1-phenylene))dicarbamate

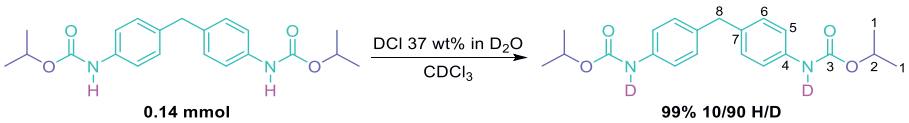

0.14 mmol **99% 10/90 H/D**

Model compound **2** (0.14 mmol, 50 mg) was dissolved in 1 mL dry $CDCl_3$ followed by addition of 1 mL 35 wt% DCl in D_2O. The chloroform layer was washed 3 times with D_2O. The chloroform layer was separated from the D_2O layer and concentrated *in vacuo* (40 °C, 0.2 mbar). The resulting mixture was a white solid with a 99% yield. The amount of deuterated labeling was 90%, based on ^{1}H integration at 6.5 ppm, and confirmed by NMR.

The dry solid has been measured in dry DCM to prevent H/D exchange between the amine and the solvent. External locking with $CDCl_3$ was performed using a manual signal search.

^{1}H-NMR (400 MHz, DCM): δ 8.31 (d, *J* = 6.44 Hz, 4H, C5-**H**), 8.11 (d, *J* = 8.23 Hz, 4H, C6-**H**), 7.75 (bs, 0.09H, N-**H**), 6.00 (m, 2H, C2-**H**)**,** 4.88 (s, 2H, C8-**H**), 2.28 (d, *J* = 5.81 Hz, 12H, C1-**H**)

^{13}C-NMR (400MHz, DCM): δ 153.22 (C3), 136.10 (C4 or 7) 136.03 (C4 or 7), 129.3 (C6), 118.7 (C5), 68.6 (C2), 40.5 (C8), 22.0 (C1)

D-NMR (400 MHz, DCM): δ 6.76 (2D, N-**D**)

HRMS (ESI) m/z: $[M+Na]^+$ calcd for $C_{21}H_{24}D_2N_2O_4$ Na 395.1910; found 395.1905

^{1}H, ^{13}C, and ^{1}D NMR data is available in the supplementary information section 5.5, Figures S5.5.8 – S5.5.10

4. Di(ethyl-^{13}C) (methylenebis(4,1-phenylene))dicarbamate

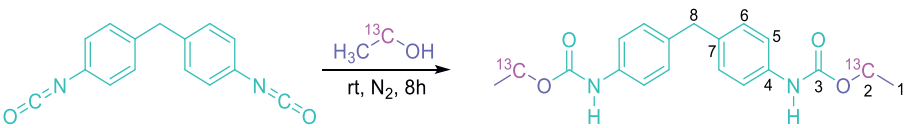

0.47 mmol **99% 5/95 ^{12}C/^{13}C**

4,4'-methylenediphenyl diisocyanate (0.47 mmol, 118 mg) was dissolved in 1 mL ethanol-^{13}C at room temperature, and the reaction progress was monitored by TLC using n-hexane/ethyl acetate 80:20 ratio. TLC analysis indicated the formation of a single product after 8 h reaction time. The reaction mixture was concentrated *in vacuo* (40 °C, 0.2 mbar), affording a white solid in 99 % yield.

^{1}H-NMR (400 MHz, $(CD_3)_2SO$): δ 8.48 (s, 2H, N-**H**), 7.47 (d, *J* = 8.34 Hz, 4H, C5-**H**), 7.14 (d, *J* = 9.20 Hz, 4H, C6-**H**)**,** 4.31 (q, *J* = 7.07, 2H, ^{13}C2-**H**)**,** 4.13 (q, *J* = 7.07, 0.10H, ^{12}C2-**H**), 3.94 (q, *J* = 7.07, 2H, ^{13}C2-**H**), 3.87 (s, 2H, C8-**H**), 1.23 (m, 6H, C1-**H**)

^{13}C-NMR (400MHz, $(CD_3)_2SO$): δ 205.3 (C3), 137.42 (C4 or 7), 135.83 (C4 or 7), 129.91 (C6), 118.33 (C5), 60.17 ($^{13}C2$), 40.17 (C8), 14.18 (C1), 13.77 (C1)

^1H, and ^{13}C NMR data is available in the supplementary information section 5.5, Figures S5.5.11 – S5.5.12

5. Bis(propan-2-yl-1,1,1,3,3,3-d_6) (methylenebis(4,1-phenylene))dicarbamate

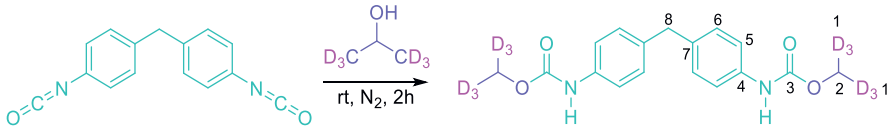

0.38 mmol **99% 4/96 H/D**

4,4'-Methylenediphenyl diisocyanate (0.38 mmol, 94.7 mg) was dissolved in 1 mL isopropanol (dimethyl-D_6) at room temperature, and the reaction progress was monitored by TLC using n-hexane/ethyl acetate 70:30 ratio. TLC analysis indicated the formation of a single product after 2 h reaction time. The reaction mixture was concentrated *in vacuo* (40 °C, 0.2 mbar), affording a white solid in 99% yield.

^1H-NMR (400 MHz, $CDCl_3$): δ 7.27 (d, *J* = 8.30 Hz, 4H, C5-**H**), 7.01 (d, *J* = 8.12 Hz, 4H, C6-**H**), 6.48 (bs, 2H, N-**H**), 4.97 (s, 2H, C2-**H**), 3.87 (s, 2H, C8-**H**)

^{13}C-NMR (400MHz, $CDCl_3$): δ 153.26 (C3), 136.13 (C4 or 7), 136.10 (C4 or 7), 129.4 (C5), 118.6 (C5), 68.4 (C2), 40.4 (C6)

D-NMR (400 MHz, $CDCl_3$): δ 1.21 (12D, C1-**D**)

HRMS (ESI) m/z: $[M+Na]^+$ calcd for $C_{21}H_{14}D_{12}N_2O_4$ Na 405.2538; found 405.2532

^1H, ^{13}C, and NMR data is available in the supplementary information section 5.5, Figures S5.5.13 – S5.5.15

*Note that C1 could not be observed due to long relaxation delay combined with C-D splitting

6. Diethyl 4,4'-methylene-^{13}C bis(1,4-phenylene)diurethane

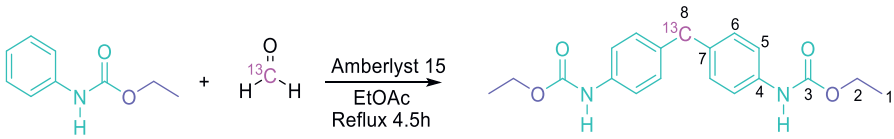

6.05 mmol **8.38 mmol** **46.2% 2/98 $^{12}C/^{13}C$**

phenylurethane (6.05 mmol, 1.01 g), 20% formaldeyde-*^{13}C* solution (8.38 mmol, 0.26 g), Amberlyst 15 (0.25 g), and EtOAc (25 mL) were mixed. The reaction mixture was heated to reflux and stirred for 4.5 h. The catalyst was collected by filtration, and the filtrate was concentrated *in vacuo* (40 °C, 0.2 mbar). The crude product was purified by flash column chromatography (25% EtOAc in heptane). Fractions containing product were combined and concentrated *in vacuo*, affording a white solid in 46.2% yield.

^1H NMR (400 MHz, $CDCl_3$): δ 7.29 (d, *J* = 8.0 Hz, 4H, C5-**H**), 7.09 (dd, *J* = 3.9 Hz, 4H, C6-**H**), 6.67 (bs, 1.5H, N-**H**), 4.21 (q, *J* = 7.1 Hz, 4H, C2-**H**), 4.03 (s, 1H, $^{13}C8$-**H**), 3.86 (s, 0.02H, $^{12}C8$-**H**), 3.71 (s, 1H, $^{13}C8$-**H**), 1.29 (t, *J* = 7.1 Hz, 6H, C1-**H**).

^{13}C NMR (101 MHz, $CDCl_3$): δ 153.73 (C3), 136.45 (C4 or 7), 136.03 (C4 or 7), 129.39 (C6), 118.89 (C5), 61.16 (C2), 40.53 (^{13}C8), 14.56 (C1).

^{1}H, and ^{13}C NMR data is available in the supplementary information section 5.5, Figures S5.5.16 – S5.5.17

7. Diisopropyl 4,4-methylene-d_2 diphenylenedicarbamate

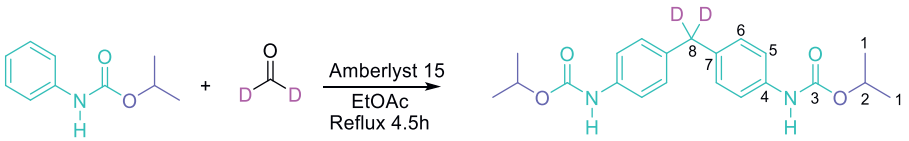

5.58 mmol **8.75 mmol** **13.5% 1/99 H/D**

Isopropyl N-phenylcarbamate (5.58 mmol, 1.03 g), 20% aqueous formaldhyde-*d_2* solution (8.75 mmol, 0.28 g), Amberlyst 15 (1.03 g), and EtOAc (20 mL) were mixed. The reaction mixture was heated to reflux and stirred for 4.5 h. The catalyst was collected by filtration, and the filtrate was concentrated *in vacuo* (40 °C, 0.2 mbar). The crude product was purified by flash column chromatography (0-10% TBME in heptanes). Fractions containing product were combined and concentrated *in vacuo*, affording a white solid in 13.5% yield.

^{1}H NMR (400 MHz, $CDCl_3$): δ 7.29 (d, *J* = 8.0 Hz, 4H, C5-**H**), 7.08 (d, *J* = 8.5 Hz, 4H, C6-**H**), 6.69 (bs, 2H, N-**H**), 5.01 (m, 2H, C2-**H**), 1.28 (d, *J* = 6.3 Hz, 12H, C1-**H**)

^{13}C NMR (151 MHz, $CDCl_3$): δ 153.42 (C3), 136.21 (C4 or 7), 136.10 (C4 or 7), 129.37 (C6), 118.89 (C5), 68.64 (C2), 39.86 (C8), 22.13 (C1)

D-NMR (400 MHz, $CDCl_3$): δ 3.86 (2D, C8-**D**)

^{1}H, ^{13}C, and ^{1}D NMR data is available in the supplementary information section 5.5, Figures S5.5.18 – S5.5.20

8. bis(propan-2-yl-d_7) (methylenebis(4,1-phenylene))dicarbamate

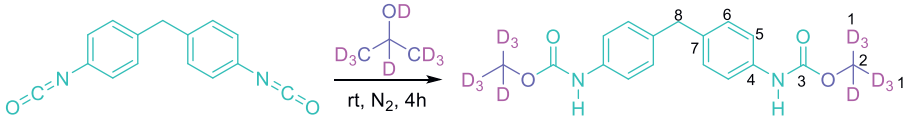

0.41 mmol **99%**
4/96 H/D (C1-**D**)
1/99 H/D (C2-**D**)

4,4'-methylenediphenyl diisocyanate (0.41 mmol, 102.5 mg) was dissolved in 1 mL isopropanol dimethyl-D_8 at room temperature, and the reaction progress was monitored by TLC using n-hexane/ethyl acetate 70:30 ratio. TLC analysis indicated the formation of a single product after 4 h reaction time. The reaction mixture was concentrated *in vacuo* (40 °C, 0.2 mbar), affording a white solid in 99 % yield.

^{1}H-NMR (400 MHz, $CDCl_3$): δ 7.26 (d, *J* = 7.71 Hz, 4H, C5-**H**), 7.07 (d, *J* = 8.33 Hz, 4H, C6-**H**), 3.86 (s, 2H, C8-**H**)

^{13}C-NMR (600MHz, $CDCl_3$): δ 153.22 (C3) 136.14 (C4 or 7), 136.06 (C4 or 7), 129.37 (C6), 118.70 (C5), 67.97 (C2), 40.5 (C8), 21.05 (C1)

D-NMR (400 MHz, $CDCl_3$): δ 4.93 (2D, C2-**D**) 1.21 (12D, C1-**D**)

HRMS (ESI) m/z: $[M+Na]^+$ calcd for $C_{21}H_{12}D_{14}N_2O_4$ Na 407.2664; found 407.26604

^1H, ^{13}C, and ^1D NMR data is available in the supplementary information section 5.5, Figures S5.5.21 – S5.5.23

All pyrolysis experiments in this study were performed using a commercial Frontier Lab Tandem Microreactor (TMR, Rx 3050TR). 0.5 mg of the sample and 2.5 mg of catalyst (1:5 ratio) were combined in a Frontier Lab Eco Cup (LF PY1-EC80F) and loaded into the reactor using a single-shot sampler (PY1-1040). A pyrolysis time of 10 seconds was used to ensure that all material had been transferred from the reactor to the online gas chromatograph coupled to mass spectrometry (GC-MS). The vapor was analyzed using an online gas chromatograph (Agilent Technologies 8890) coupled to a 5977B MSD and an FID detector at 300 °C. The gas chromatograph was equipped with a 30 m × 0.25 mm capillary column (HP-5 MS) coated with a 0.25 µm film of 5 % phenylmethyl polysiloxane. Helium was used as the carrier gas at a constant flow rate of 1 mL/min. A Frontier Lab Microjet Cryo-Trap was connected to the column to separate all permanent gases. The initial oven temperature was set at 40 °C, with a ramp rate of 10 °C/min (maintained for 1 min) to reach a final column temperature of 300 °C, which was held for 5 min. The injector and detector temperatures were maintained at 300 °C. Data were collected in full-scan mode with mass-to-charge (m/z) ratios ranging from 35 to 500. Chromatographic peaks were identified using the NIST mass spectral data library. Quantification of the desired products was performed using the external calibration curve method.

5.3. Results and Discussion

Model compound synthesis

Initially, two urethane model compounds (**1** and **2**) were synthesized to represent the structure of the rigid MDI-based polyurethane framework. These two models vary in the alcohol segment (EtOH- and *i*PrOH-based) to investigate the influence of structural changes on the alcohol segment on the thermal degradation. Literature[28] previously explored changes in decomposition temperature upon changes on the polyol segment using TGA.[28] It was shown that polyether-type PUR (using tetrahydrofuran) and polyester-type PUR (using butanediol adipate) based PUR showed 2 main weight loss regions. The first weight loss (between 341 – 351 °C) showed a minor difference of 10 °C, while the second weight loss (382 - 414 °C) showed a 32 °C higher temperature for the butanediol adipate-based PUR. Additionally, CO_2 evolution was observed for the butanediol adipate-based PUR sample, which was absent for the polyether-based PUR sample.

For further insights into bond-breaking events the synthesized model compound series was extended with isotopically Labelled model compounds. Models **1**-**5** and **8** (Figure 5.2, A) were successfully synthesized in high yields (>99%) by dissolving 4,4'-methylene diphenyl diisocyanate (MDI) with (labelled) isopropanol (*i*PrOH) or ethanol (EtOH), for 2 h at room temperature under nitrogen. Models **6** and **7** (Figure 5.2, B) were prepared by adding phenylurethane or Isopropyl N-phenylcarbamate to formaldhyde-d_2, affording the desired structures in 46.2% and 13.5% yields, respectively, due to

challenging workup procedures. For the four deuterated (**3, 5, 7, 8**) and two carbon-enriched (**4, 6**) model compounds, the H/D and $^{12}C/^{13}C$ ratios for each model compound were determined by NMR.

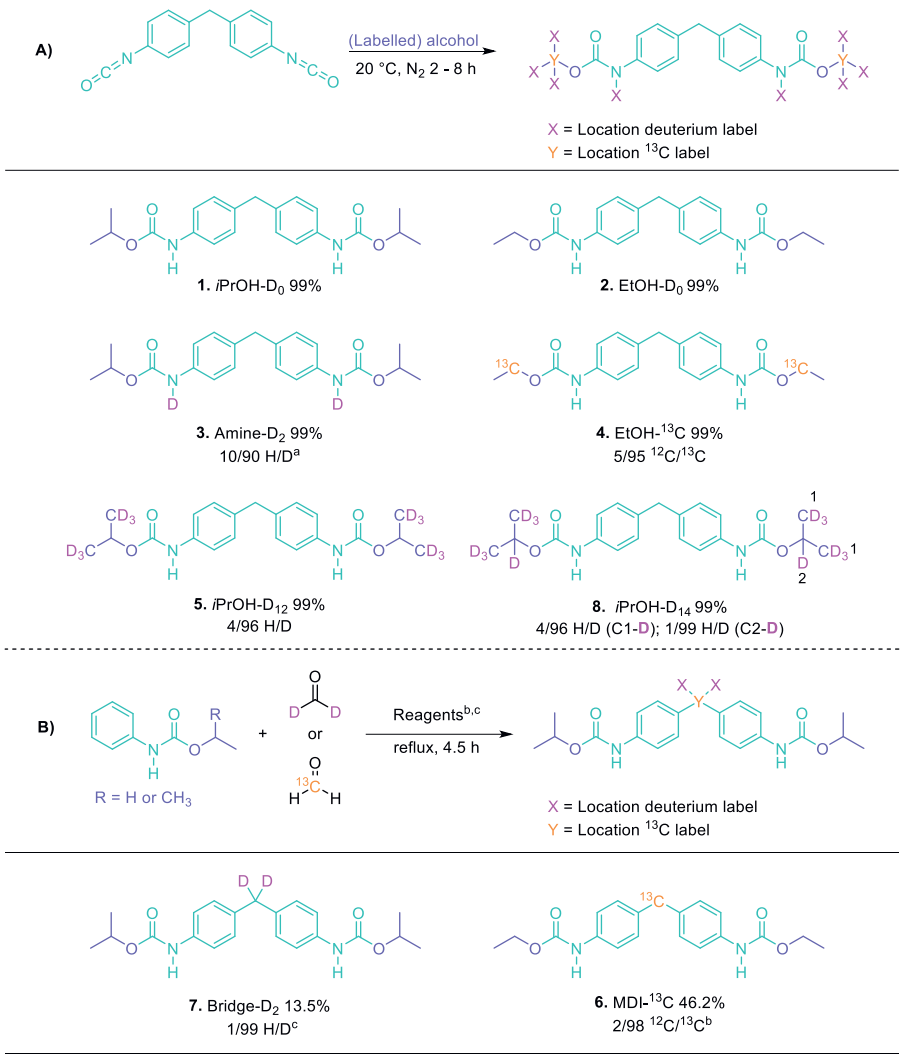

Figure 5.2. Synthesized model compounds: non-labelled (**1** and **2**), deuterated (**3**, **5**, **7**, and **8**), and carbon-enriched (**4** and **6**). Compounds **1**, **2**, **4**, **5**, **8** have been synthesized via route A. Compounds **6** and **7** have been synthesized via route B. Compound **3** has been synthesized using compound **1**. General reaction conditions: MDI (0.14 – 4.0 mmol), 1 – 25 mL alcohol (EtOH or iPrOH), at 20 °C under N_2 for 2 - 8 h. [a]Prepared via H/D exchange of model 1. using D_2O and $CDCl_3$. [b]Reaction conditions: Phenylurethane (6.05 mmol), 20% formaldeyde-^{13}C solution (8.38 mmol), Amberlyst 15 (0.25 g), EtOAc (25 mL), 4.5 hours, reflux. [c]Reaction conditions: Isopropyl N-phenylcarbamate (5.58 mmol), 20% aqueous formaldhyde-d^2 solution (8.75 mmol), Amberlyst 15, EtOAc, 4.5 hours, reflux. For specific reaction conditions, see section 2.2

Non-catalytic and catalytic pyrolysis of unlabelled model components

Models *i*PrOH-D_0 (**1**) and EtOH-D_0 (**2**) were subjected to non-catalytic and catalytic (1:5 model:puralox SCCa 5/200) pyrolysis at 550 °C in a microreactor coupled to an online GC-MS/FID. The goal of this experiment was to identify the main and N-containing side products and to gain insight into how structural changes in the polyol segment affect product composition. The yields of specific products were obtained by quantifying the products using calibration curves. Yields are expressed as mol% input corrected for the theoretical production of multiple molecules per model compound (e.g. 2 anilines can be formed from one model compound). Detailed yield calculations are described in the supplementary information section 5.5, calculation S5.5.1, and a comprehensive product overview with calculated yields is available in Section S5.5.

Results for the non-catalytic and catalytic pyrolysis of both model *i*PrOH-D_0 (**1**) and EtOH-D_0 (**2**) are shown in Figure 5.2. The main products identified from the non-catalytic pyrolysis of *i*PrOH-D_0 (**1**) were propene, isopropanol, and MDI (3%) as sole N-containing product. Introduction of a catalyst led to the formation of propene and acetone with as main N-containing products aniline (37%), toluidine (5%) as well as several other N-containing side products (5%). Thus, distinct differences in product formation are evident between catalytic and non-catalytic experiments, and aniline and toluidine are formed only in the presence of a catalyst.

In the case of EtOH-D_0 (**2**), non-catalytic pyrolysis produced ethane, ethene, ethanol, acetaldehyde, and MDI (20%). The effect of changing the alcohol segment on product formation was clearly evident: the *i*PrOH-based model produced propene and isopropanol, whereas the EtOH-based model yielded ethene and ethanol. As for *i*PrOH-D_0 (**1**), selectivity changed when using a catalyst, forming ethanol , acetaldehyde , aniline (31%), toluidine (10%), MDA (3%), and N-containing side products (9%).

The products from the non-catalytic pyrolysis of both models were consistent with the retro-polymerization pathway described in the literature.[15,21] Formation of primary amines is also described in literature, which was absent for our non-catalytic pyrolysis experiments. In contrast, the catalytic runs did show aniline and toluidine formation (Summed yields of 42% and 44% for *i*PrOH-D_0 (**1**) and EtOH-D_0 (**2**), respectively).

Based on a hydrogen balance, the formation of toluidine and aniline from MDA requires 2 additional hydrogen atoms to form. The presence of aniline and toluidine in the catalytic runs, together with the hydrogen balance, indicate that the catalyst most likely promotes MDA bridge cracking into aniline and toluidine via hydrogen addition.

N-containing side products (acridine, indole, ethylaniline, and ethyltoluidine) were observed for both models upon addition of a catalyst, indicating that the catalyst facilitates additional side reactions (e.g., alkylation and intermolecular rearrangements). The origin of side products is reflected in the aniline-to-toluidine ratio. Based on the model compound, two aromatic ring structural motifs, simple cracking of the methylene linkage should yield equimolar amounts of aniline and toluidine. The 3:1 and 7:1 ratios, together with the formation of additional nitrogen-containing byproducts, indicate that toluidine is prone to secondary transformations involving further condensation towards acridine formation for both models (3.4% and 2.1% calculated on mol% with indole as reference compound for

*i*PrOH-D_0 (**1**) and EtOH-D_0 (**2**), respectively), which has also been described as a precursor to coke formation.[50]

The results revealed that the introduction of a catalyst promotes the formation of aniline and toluidine, as well as unwanted N-containing side products. Additionally, it could be concluded that the side-product distribution was influenced by the type of polyol segment in the model. The catalytic pyrolysis results of *i*PrOH-D_0 (**1**) showed mainly the formation of acridine and methylacridine, whereas for EtOH-D_0 (**2**), additional N-containing side products (ethylaniline and ethyltoluidine) were observed. Other products observed were propene and acetone. These eight main identified compounds (propene, acetone, aniline, toluidine, ethylaniline, ethyltoluidine, acridine, and methylacridine were identified as compounds of interest, and the formation of these molecules has been further investigated by looking at changes to their isotope and fragmentation patterns (see section S4) using D- and ^{13}C labelled models as substrate for catalytic pyrolysis.

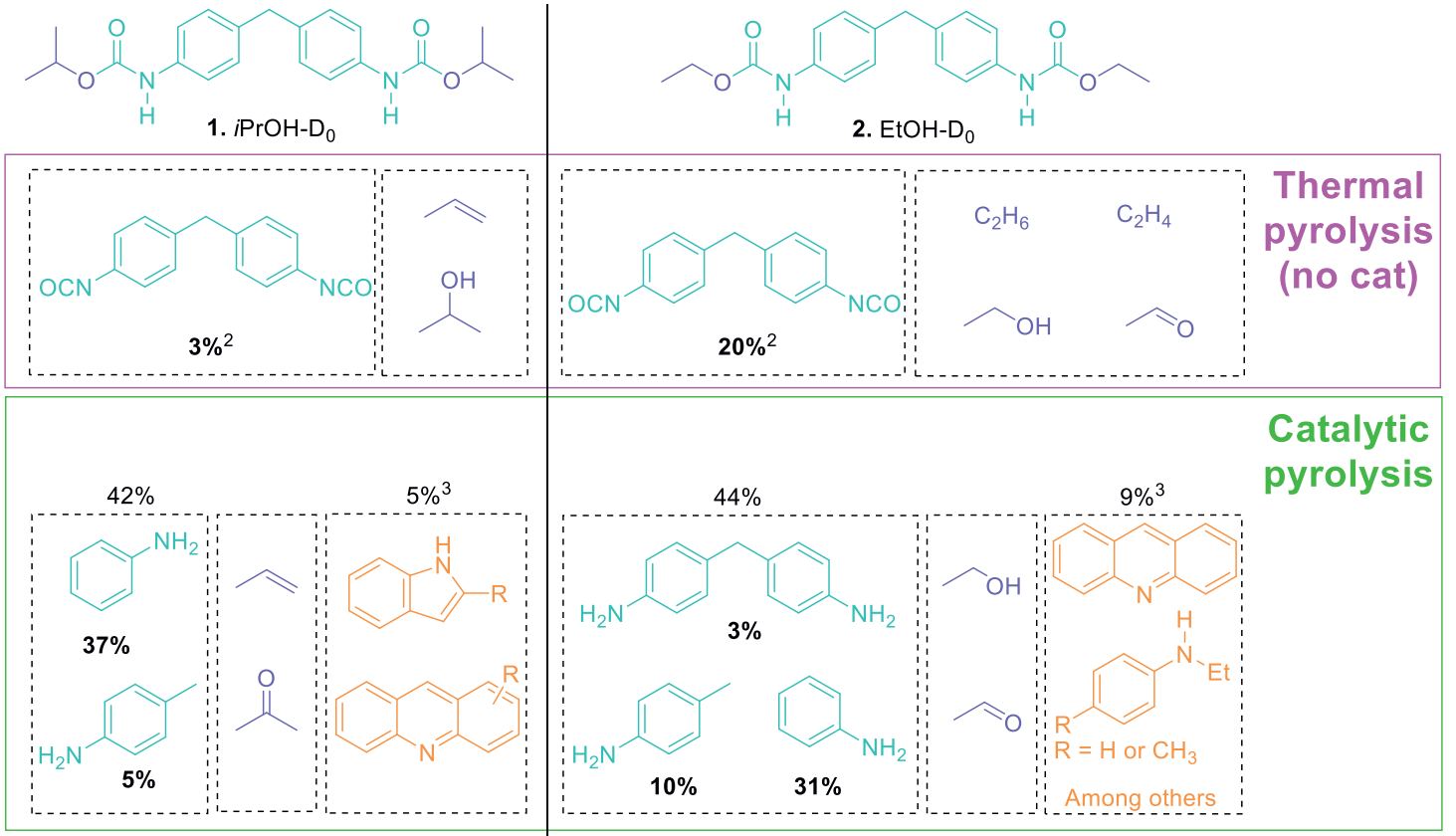

Figure 5.3. Thermal (pink) and catalytic (green) pyrolysis of model compounds **1** (iPrOH-D_0, left) and **2** (EtOH-D_0 right). [1]All depicted values are rounded to a whole number and are an average of 2 measurements, [2]yields are calibrated on MDA as reference compound and the molecular mass of MDI has been used for the yield calculation, [3]Yields are calibrated on indole as reference compound

Catalytic pyrolysis of deuterated model compounds

In section 3.2, it was hypothesized that aniline and toluidine most likely form via the cracking of the methylene bridge of MDA with hydrogen atom equivalents originating from the polyol fragment. Further evidence for the origin of aniline and toluidine formation was obtained by investigating hydrogen-transfer dynamics. For this purpose, deuterated model compounds amine-D_2 (**3**), bridge-D_2 (**7**), *i*PrOH-D_{12} (**5**), and *i*PrOH-D_{14} (**8**) were pyrolyzed under identical conditions to non-deuterated model *i*PrOH-D_0 (**1**). The hydrogen atoms for each product formed (propene, acetone, aniline, and toluidine) were traced upon using specific deuterium-labelled model compounds. For initial insight, the molecular ion isotopologue intensity ratio (M_{x+0}) is used which is calculated according to equation 5.1 in which I_{M+i} is the mass peak intensity and M_{x+i} is the mass peak intensity ratio, n is the maximum amount of deuterium observed in a component This number represents the amount of non-deuterated product present in the pyrolysis mixture and is the value noted in between brackets for each model under discussion to give an initial indication of the labelling extend. For example, propene formed from *i*PrOH-D_0 has a molecular mass intensity ratio (M_x) of 86 which is noted in the text as *i*PrOH-D_0 (86). An extended explanation of the labelling interpretations can be found in Section S5.5.

$$M_{x+i} = \frac{I_{M+i}}{\sum_{i=0}^{n} I_{M+i}} \cdot 100 \tag{5.1}$$

Product analysis for deuterated model components

Catalytic pyrolysis results with model compounds amine-D_2 (**3**), *i*PrOH-D_{12} (**5**), bridge-D_2 (**7**), and *i*PrOH-D_{14} (**8**) are shown in Figure 5.4. The model compounds are shown on the x-axis, and the isotopologue intensity ratio of a specific formed product on the y-axis. The products derived from the segment representing the polyol (*i*PrOH) are shown in purple (propene and acetone) and from the isocyanate segment (MDI) in blue (aniline and toluidine). The molecular ion isotopologue intensity ratio (M_x) representing the amount of non-deuterated species is shown in the blue columns.

For example, propene (m/z 42, blue column) formed from *i*PrOH-D_{12} (4th row, entry **a**) has 5 isotopomers represented by the colors blue, orange, green, red, and lightblue (m/z 42, 43, 45, 46, 47, respectively). The M_x in this case is 18, as the blue column (m/z 42) has an intensity of 18. Please note that the results are relative peak heights that are not calibrated for differences in ionization.

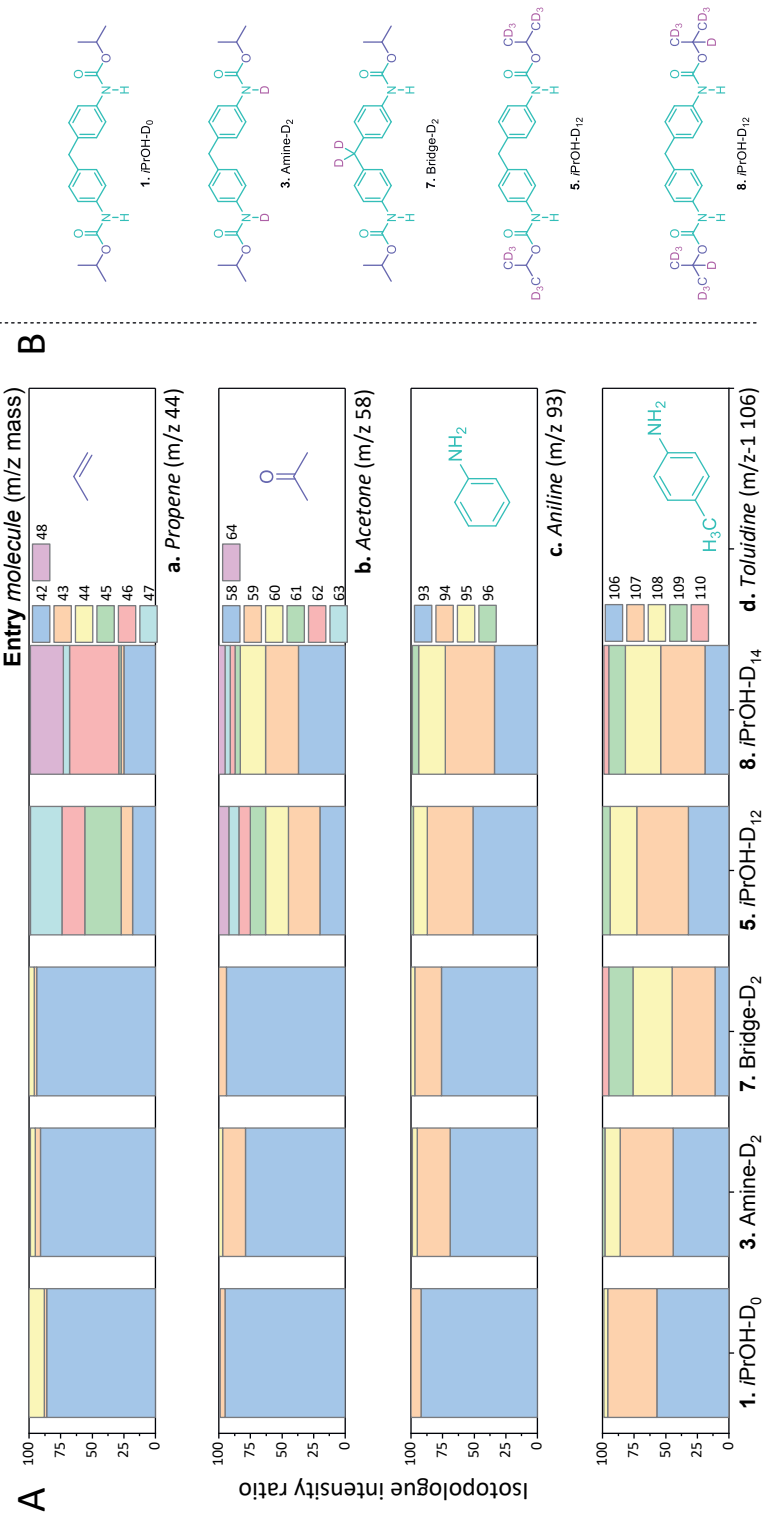

Figure 5.4. **A**) MS intensity ratios of all investigated model compounds (iPrOH-D_0 (**1**), amine-D_2 (**3**), bridge-D_2 (**7**), iPrOH-D_{12} (**5**), and iPrOH-D_{14} (**8**)). The molecules of interest are shown on the right with the alcohol fragments (propene and acetone) highlighted in purple, entries **a** and **b** and the isocyanate fragments (aniline and toluidine) in blue, entries **c** and **d**. The mass peak intensity ratios are color-coded and calculated according to equation 5.1. The molecular mass intensity ratio (M_x) which defines the amount of non-deuterated compound is indicated in blue. **B**) the model compounds that have been pyrolyzed to obtain the products of interest: iPrOH-D_0 (**1**), Amine-D_2 (**3**), Bridge-D_2 (**7**), iPrOH-D_{12} (**5**), and iPrOH-D_{14} (**8**)

First, the isotopologue distribution patterns of the alcohol derived fragments shown in entry **a** and **b** (propene and acetone) have been analyzed with GC-MS for all model compounds (*i*PrOH-D_0, amine-D_2, bridge-D_2, *i*PrOH-D_{12}, and *i*PrOH-D_{14}). An M_x of 86 was observed for propene (entry **a**) formed via non-deuterated model compound *i*PrOH-D_0 (86). Propene formed from isocyanate-labelled models amine-D_2 (91) and bridge-D_2 (94) showed an M_x close to that of the non-deuterated model (*i*PrOH-D_0). In contrast, the polyol-labelled models showed 5 deuterated species for *i*PrOH-D_{12} (18) and 6 deuterated species for *i*PrOH-D_{14} (25). The M_{x+i} intensity ratios for both models (*i*PrOH-D_{12} and *i*PrOH-D_{14}) were similar. The major isotopomer is observed at m/z 46 for iPrOH-D_{14} and at m/z 45 for *i*PrOH-D_{12}, confirmed significant deuterium enrichment and the origin of propene from the alcohol fragments. The fragmentation patterns of propene showed a wide mass distribution (m/z 37 – 44 for *i*PrOH-D_0), making more detailed analysis difficult. The fragmentation patterns of propene formed by *i*PrOH-D_0, Bridge-D_2, and *i*PrOH-D_{14} are shown the supplementary section S5.5 Figure S5.5.24 as examples.

Similar results were observed for acetone (entry **b**) formed from *i*PrOH-D_0 (95) and Bridge-D_2 (94). The lower M_x of amine-D_2 (79) was attributed to some H/D exchange between N-D group and the O-H group keto-enol tautomer of acetone. Significantly lower M_x were observed with *i*PrOH-D_{12} (20) and *i*PrOH-D_{14} (37), containing both 7 isotopomers with the amount of isotopomers being more distributed for *i*PrOH-D_{12} compared to *i*PrOH-D_{14}.

Analysis of the polyol-derived products (propene and acetone) showed expected results with some additional H/D exchange for acetone. However, the absence of exchange from the Bridge-D_2 to the polyol indicated a unidirectional hydrogen atom flow from the polyol to the isocyanate segment. Consequently, the fragmentation patterns of the isocyanate derived fragments shown in entry **c** and **d** (aniline and toluidine) were analyzed in a similar fashion as propene and acetone using GC-MS for all model compounds (*i*PrOH-D_0, amine-D_2, bridge-D_2, *i*PrOH-D_{12}, and *i*PrOH-D_{14}).

Aniline (entry **c**) resulted in a significantly lower M_x for all labelled models (average 58) compared to the non-deuterated model (92). Amine-D_2 (69), and bridge-D_2 (76) contained both 3 isotopomers and *i*PrOH-D_{12} (61) and *i*PrOH-D_{14} (34) 4 isotopomers. Notably, the amount of isotopomers was more distributed over m/z 93 – 95 for *i*PrOH-D_{12}, and *i*PrOH-D_{14} compared to Amine-D_2, and bridge-D_2, indicating more deuterium incorporation with the polyol labelled models compared to the isocyanate labelled models.

Similar results were observed for toluidine (entry **d**). As expected, the models amine-D2 (44), bridge-D2 (11), iPrOH-D12 (32), and iPrOH-D14 (19) showed a clear increase in deuterated species compared to the non-deuterated model *i*PrOH-D_0 (57).

The increase in deuterium incorporation in aniline and toluidine with the polyol labelled models (*i*PrOH-D_{12} and *i*PrOH-D_{14}) combined with the retention of non-deuterated propene and acetone with the isocyanate labelled models (amine-D_2 and bridge-D_2) implied that most likely, there is a unidirectional hydrogen atom flow from the alcohol segment to the isocyanate segment during the catalytic pyrolysis process. Subsequent comparison between the aniline deuterated-to-non-deuterated ratio (D/ND) showed that the hydrogen atoms on the alcohol segments are more mobile compared to those of the isocyanate hydrogen atoms, as it was observed that the ratio order from

least to most deuterated was model **1** (*i*PrOH-D_0, 8/92) < **7** (bridge-D_2, 24/76), **3** (amine-D_2, 31/69), **5** (*i*PrOH-D_{12}, 49/51), **8** (*i*PrOH-D_{14} 66/34).

To understand the observed mobility a relationship with bond strengths was sought via DFT calculations using non-deuterated model *i*PrOH-D_0 as representative structure. Calculation details can be found in Section S5.5. Bond dissociation energy calculations (Table 5.1 and Figure 5.5) showed a decrease in bond energy for CH_2 < NH < CH < CH_3 < Ar-H^{NH} < Ar-H^{CH2}. The C-H bonds on the polyol segment (bond 2 and 3) are considered weaker, with the isopropanoyl α-C-H bond (3) weaker than the methyl C-H bond (2), indicating that the α-hydrogen atom is indeed the most mobile hydrogen and is most likely to be available to provide hydrogen atom equivalents required for the MDA cracking reaction. The lowest C-H bond energy is found for the methylene bridge hydrogens (4. The higher amount of deuterated species for aniline and toluidine formed with bridge-D_2, combined with the lowest bond energy, indicates that the methylene bridge hydrogens participate in the formation of aniline and toluidine. The highest bond energies were found on the aromatic hydrogens (5 and 6), rendering them immobile, as experimentally proven by the absence of evidence for deuterium exchange (*vide infra*).

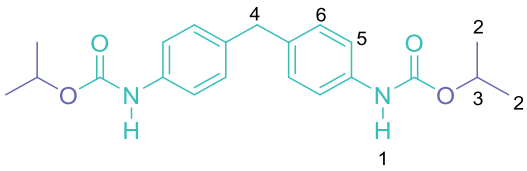

Figure 5.5. Bond number assignment for the calculated bond energies

Table 5.1. Calculated bond energies of C-H and N-H bond in model **1** (iPrOH-D_0).

Bond	Representing bond	Type of bond	Bond energy (kcal/mol)
1	N-H	NH	160.15
2	Methyl CH_3	CH_3	171.30
3	Isopropanoyl α-C-H	CH	165.97
4	Methylene bridge	CH_2	148.01
5	Ar-H near N-H	Ar-H^{NH}	180.81
6	Ar-H near Methylene bridge	Ar-H^{CH2}	180.87

Based on the results, it can be concluded that the hydrogen atoms required to crack the methylene bridge of MDA into aniline and toluidine primarily originates from the polyol segment rather than the isocyanate segment. Specifically, the hydrogen in the α-position of the isopropyl moiety and secondly those from the β-position of the isopropyl segment are available to participate as confirmed by the larger amount of deuterated aniline and toluidine species on model *i*PrOH-D_{14}, compared to *i*PrOH-D_{12}.

Analysis of the aniline and toluidine fragmentation patterns

As previously discussed, the required hydrogen atoms to form aniline and toluidine most likely originate from the alcohol segment representing the polyol. Consequently, formation of aniline and

toluidine via cracking of the isocyanate methylene bridge has been further investigated by identifying the locations of deuterium atoms on both aniline and toluidine. For this experiment, models *i*PrOH-D_0 (**1**), amine-D_2 (**3**), bridge-D_2 (**7**), *i*PrOH-D_{12} (**5**), and *i*PrOH-D_{14} (**8**) were pyrolyzed, and the aniline and toluidine fragmentation patterns for each model were analyzed via GC-MS. The two highest m/z mass peaks were compared to identify the location of the deuterium label. So for example, the three peaks with the highest intensity for aniline are m/z 93, 66, and 33 of which m/z 93 and 66 have the highest masses. For this reason, m/z 93 and 66 have been analyzed to a further extent. For toluidine m/z 107 and 77 have been investigated.

As the MDA bridge is located between the para positions of both aromatic rings, it is expected that external hydrogen atom should end up in the para position for both aniline and toluidine, thus in the case of deuterium resulting in para-labelled aniline and a methyl-group-labelled toluidine. The first two largest m/z peaks for both aniline and toluidine have been analyzed for models *i*PrOH-D_0, amine-D_2, bridge-D_2, *i*PrOH-D_{12}, and *i*PrOH-D_{14} as shown in Figure 5.6. Aniline fragmentates from a m/z 93 into a m/z 66 five-membered ring via HCN removal.[51] It is expected that both m/z 93 and m/z 66 should have a mirror isotope pattern as that would mean that the deuterium label is located on the ring rather than the HCN. Results showed indeed nearly identical patterns for all models, confirming that the label is bound to the aniline ring rather than the amine itself. The bond energies supported by the scrambling in Figure 5.6 showed no exchange between deuterium and the ortho/meta positions. For this reason, the deuterium atom is indeed most likely positioned on the para position of the aromatic ring. Ionization of toluidine exists in the metastable form $[C_7H_8N]^+$ with a m/z 106 and typically forms the base peak instead of m/z 107. The metastable species fragmentates from m/z 106 into a 6-membered ring with an m/z of 77 via cleavage of $HN{=}CH_2$.[52] Also in this case, a mirror isotope pattern was expected. The fragmentation patterns showed similar results as aniline, a nearly mirror image is visible upon comparison of m/z 106 to m/z 77, indicating that the deuterium atoms are located on the methyl-ring fragment rather than the released amine fragment.

Overall the results from the experiments with deuterium labelled model compound show that aniline and toluidine form via cracking of the methylene bridge in MDA with hydrogen atoms that mostly originate from the isopropyl moiety α-positioned hydrogen and secondly the β-position. End-of-life rigid polyurethane foams have a similar structure. Their isocyanate component is typically a polymeric methylene dianiline (pMDA) moiety, while the polyol is usually a polypropylene oxide-based structure with both α- and β-positioned hydrogens. Consequently, when these foams undergo catalytic pyrolysis under the same conditions as outlined in this study, they are likely to decompose through pathways similar to those of the model compounds examined here.

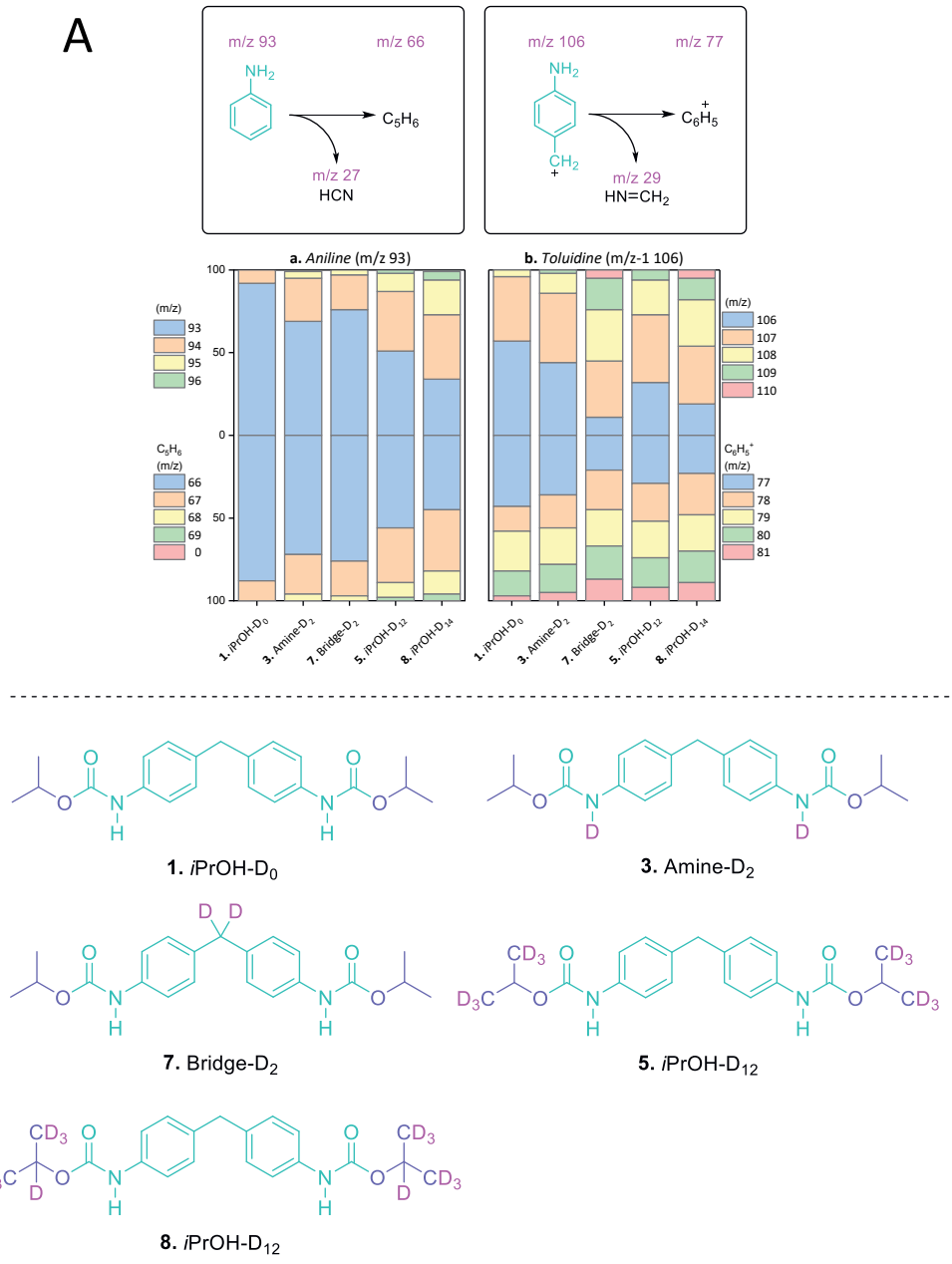

Figure 5.6. **A**) Normalized MS intensity ratios of aniline (left) and toluidine (right). The model compounds are displayed on the x-axis (rows 1-5) with M + X, X = 0-4, color-coded, and the molecular mass is indicated in blue. The molecular mass for both molecules is shown on top (m/z 93, and 107), and the second main peak on the bottom (m/z 66, and 77) for aniline and toluidine, respectively. **B**) the model compounds that have been pyrolyzed to obtain the products of interest: iPrOH-D_0 (**1**), Amine-D_2 (**3**), Bridge-D_2 (**7**), iPrOH-D_{12} (**5**), and iPrOH-D_{14} (**8**)

Origin of N-containing side products

Next, we focused on N-containing side products ethylaniline, ethyltoluidine, acridine, and methylacridine, as the origin of these products could not be unequivocally determined from the deuterium-labeling experiments. For this reason, the ^{13}C-labelled model compounds EtOH-^{12}C (**2**), EtOH-^{13}C (**4**), and MDI-^{13}C (**6**) were subjected to catalytic pyrolysis to trace carbon movement. Note that model EtOH-^{12}C (**2**) is the same model compound as EtOH-D_0 (**2**) but the name is changed to ^{12}C instead of D_0 for clarity as the focus of this section is on carbon labelling rather than deuterium labelling.

For this set of experiments, the EtOH-based model design (**2**) was chosen because the short-chain alcohol produced significantly more and different N-containing side products than the more bulky *i*PrOH-based model (**1**). Analysis of the results was performed in a similar fashion compared to the deuterium-labeling experiments. The mass spectrometry intensities were compared to identify which products contained ^{13}C atoms. The nitrogen-containing main and side products identified were aniline (m/z 93), toluidine (m/z-1 106), ethylaniline (m/z 121), ethyltoluidine (m/z 135), acridine (m/z 179), and methylacridine (m/z 193). It should be noted that acetaldehyde, and diethyl ether arising from the labelled alcohol segments were also observed. However, equal masses for acetaldehyde and CO_2 peaks rendered the detailed analysis unreliable. For diethylether, a double ^{13}C incorporated species was observed which was assigned to a dimerization reaction between two ethanol fragments that originate from the ^{13}C labelled model EtOH-^{13}C (**4**). The data is provided in the supplementary information section S5.5.

The isotope distributions of the nitrogen-containing products from catalytic pyrolysis results with models EtOH-^{12}C (**2**), EtOH-^{13}C (**4**), and MDI-^{13}C (**6**) are shown in Figure 5.7. The main N-containing products, aniline and toluidine, are shown in blue (entries **a** and **b**), cross reaction products, ethylaniline and ethyltoluidine, are multicolored (entries **c** and **d**), and the other side products, acridine and methylacridine, are shown in orange (entries **e** and **f**). Each column represents the isotopologue intensity ratio of a specific formed product with the molecular ion isotopologue intensity ratio (M_x) shown in blue.

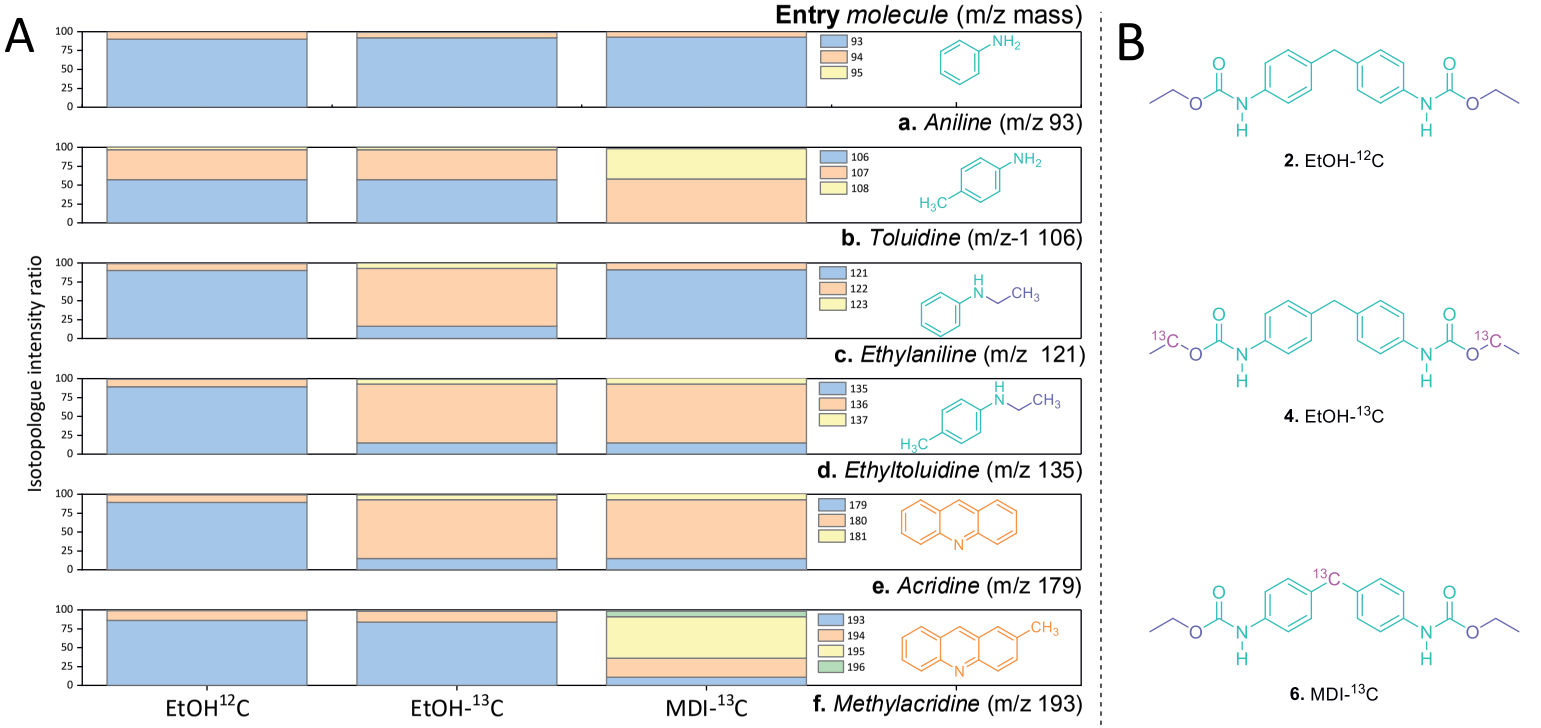

Figure 5.7. **A**) MS intensity ratios of all investigated model compounds (EtOH-^{12}C (**2**), EtOH-^{13}C (**4**), and MDI-^{13}C (**6**)). The molecules of interest are shown on the right with the isocyanate fragments (aniline and toluidine) in blue entries **a** and **b**, the cross reaction between alcohol and isocyanate segments (ethylaniline and ethyltoluidine) in blue/purple entries **c** and **d**, and the N-containing side products (acridine and methyl acridine) in orange, entry **e** and **f**. The mass peak intensity ratios are color-coded and calculated according to equation 5.1. The molecular mass intensity ratio (M_x) which defines the amount of non-deuterated compound is indicated in blue. **B**) the model compounds that have been pyrolyzed to obtain the products of interest: EtOH-^{12}C (**2**), EtOH-^{13}C (**4**), and MDI-^{13}C (**6**).

No ^{13}C was observed in the aniline and toluidine formed, except for toluidine from MDI-^{13}C (**6**). This compound showed an identical pattern to that of toluidine formed via EtOH-^{12}C (**2**) and EtOH-^{13}C (**4**), with an additional ^{13}C present. From the results, it can be concluded that aniline and toluidine are formed via the expected cracking of the MDA bridge pathway.

Identical patterns were observed for cross-reaction products (ethylaniline and ethyltoluidine) formed from EtOH-^{13}C (**4**). In addition, ethyltoluidine formed from MDI-^{13}C (**6**) showed ^{13}C incorporation. These two observations clearly show that both side products arise from alkylation of a polyol fragment by the amine of the isocyanate fragments.

N-containing side products, acridine and methyl acridine, showed only ^{13}C incorporation for the MDI-^{13}C model (**6**). Furthermore, methylacridine from MDI-^{13}C (**6**) showed mainly double ^{13}C incorporation. The results show that these side products arise from the isocyanate segment, possibly via a recombination of formed toluidine and aniline or via an intermolecular mechanism in the case of acridine. The acridine is single-labelled, indicating formation through a reaction between aniline and toluidine. The double-labelled methylacridine implies that it is formed from two toluidine fragments, as shown in Figure 5.8. The results also provide a rationale for the experimentally observed higher amount of aniline relative to toluidine. It suggests that side products most likely form via reactions between toluidine and other fragments.

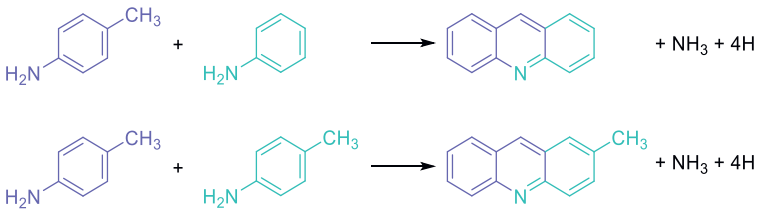

Figure 5.8. Reaction schemes for the formation of N-containing side products, acridine (top), and methylacridine (bottom)

Proposed mechanism for product formation

The combined results from this work using the various PUR model compounds led to the proposal of a 3-step mechanism for the formation of aniline and toluidine from the PUR (Figure 5.9). Step 1 involves the retro polymerization of PUR into a polyol and an isocyanate fragment, as discussed in the literature[53], which can be facilitated by Lewis acid sites on the catalyst. In the second step, the polyol segment most likely cleaves into smaller molecules, including CO, CO_2, propene, and acetone, releasing hydrogen atoms (**step 2**). Catalytic decomposition of the remaining MDA structure (or in the case of PUR pMDA) by cleavage of the methylene bridges to form aniline and toluidine occurs on the catalyst surface using the hydrogen atoms released in step 2 (**step 3**).

The N-containing side products form via deamination of MDA, followed by an intramolecular rearrangement forming acridine (**step 4**). The results also indicated that two aniline molecules may recombine to form acridine (**step 5**). The other side product, methyl acridine, is formed via recombination of two toluidine molecules (**step 6**). Overall, consuming more toluidine equivalents than aniline results in higher aniline than toluidine in the product mixture.

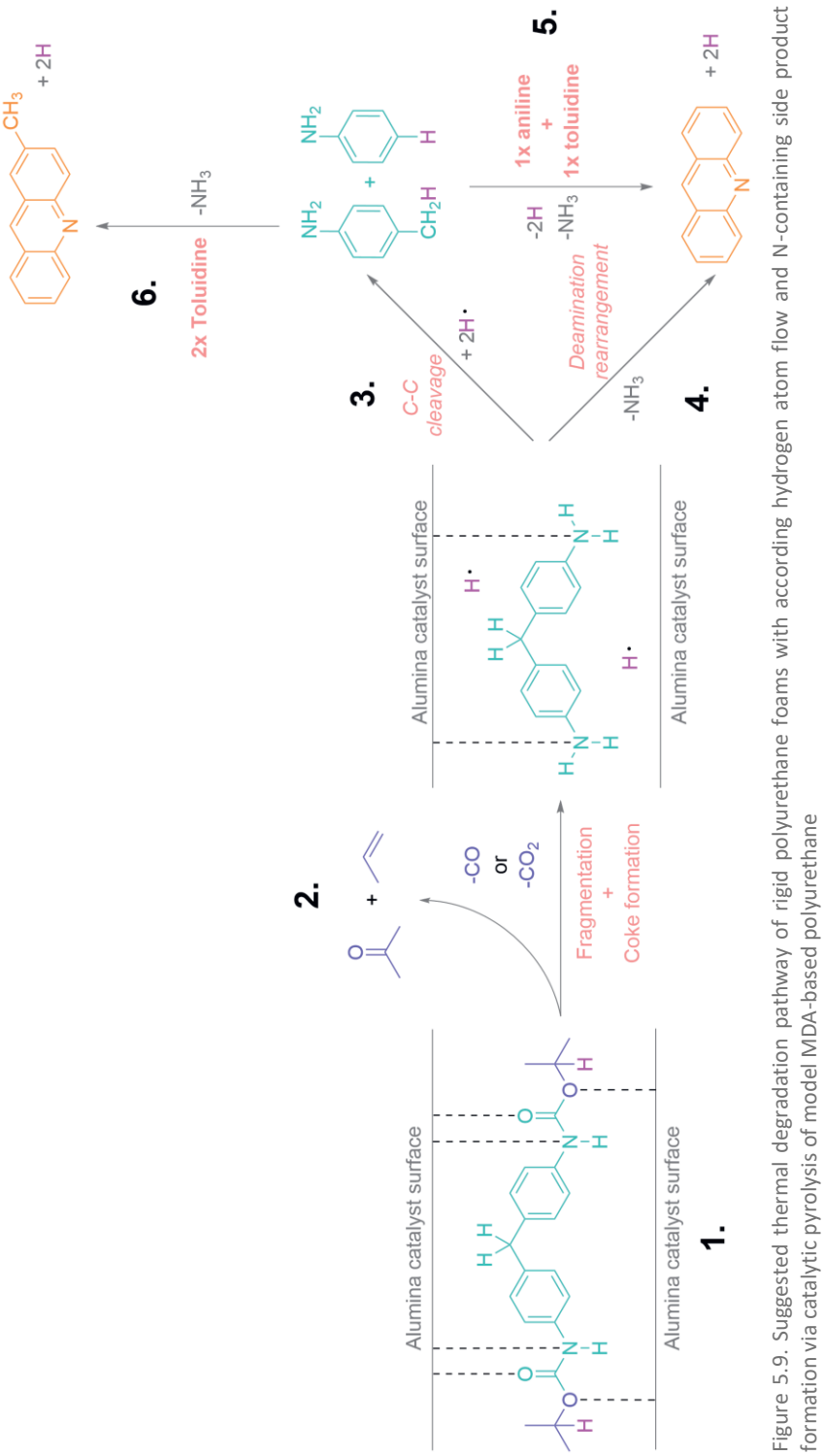

Figure 5.9. Suggested thermal degradation pathway of rigid polyurethane foams with according hydrogen atom flow and N-containing side product formation via catalytic pyrolysis of model MDA-based polyurethane

5.4. Conclusions

In this work, we aimed to gain advanced insight into the depolymerization pathways of rigid polyurethane foam via non-catalytic and catalytic pyrolysis using model compounds (D-, ^{13}C-, and unlabelled).

Initial work showed that the presence of a catalyst promotes the formation of aniline and toluidine, as well as additional N-containing side products (ethylaniline, ethyltoluidine, acridine, and methylacridine). The origin of aniline and toluidine formation from MDA was elucidated by investigating hydrogen atom-transfer dynamics. The results showed a unidirectional hydrogen atom flow from the polyol segment to the isocyanate segment, with the α-hydrogen (calculated to have low bond energy) of the isopropanoyl moiety most likely contributing to the cracking of the methylene bridge of MDA, thereby forming aniline and toluidine. ^{13}C results showed that N-containing side products form via **I**) cross reaction between polyol- and isocyanate fragments (ethylaniline and ethyltoluidine) or **II**) homocoupling between isocyanate fragments (aniline and toluidine) occurs to form acridine and methylacridine. These N-containing side products are well-known coke precursors which showed that most likely the larger conversion of toluidine into side products explains the 3 to 1 aniline to toluidine ratio. This is in line with results obtained with PUR meaning that this explanation can be extended to catalytic pyrolysis of PUR to aniline and toluidine.

The combined results enabled the establishment of a mechanism that explains the origin of the main products (aniline and toluidine) and the N-containing side products (ethylaniline, ethyltoluidine, acridine, and methylacridine). First, the catalyst interacts with the polyurethane foam lone pairs, forming polyol and pMDA derived fragments. Secondly, polyol fragments decompose to give CO, CO_2, propene, and acetone, releasing hydrogen equivalents for the third step, which is the cracking of the methylene bridge of MDA, thereby forming N-containing side products such as acridine via an intermolecular rearrangement, or breaking into aniline and toluidine, which may recombine to form acridine. Methyl acridine likely forms through the recombination of two toluidine fragments. These side products most likely further react towards coke.

The structural resemblance between the synthesized models and end-of-life rigid polyurethane foam allows the obtained results to be extrapolated to industrially produced polyurethane foam case studies.

References

1. Datta, J., Kopczyńska, P., Simón, D. & Rodríguez, J. F. Thermo-Chemical Decomposition Study of Polyurethane Elastomer Through Glycerolysis Route with Using Crude and Refined Glycerine as a Transesterification Agent. *J. Polym. Environ.* **26**, 166–174 (2018).
2. Pillich, M., Schilling, J., Bosetti, L. & Bardow, A. What to do with polyurethane waste? The environmental potential of chemically recycling polyurethane rigid foam. *Green Chemistry* **26**, 10893–10906 (2024).
3. Bulan, A. *et al.* Process for producing isocyanates. (2012) doi:US8,153,838B2.
4. Engels, T. G. W. *et al.* Chemical recycling of rigid polyurethane foam via thermocatalytic conversion to aniline. (2026).

5. Dyer, E., Earl Newborn, G. & Total, O. Degradation of Methylenebis- (4-phenyl Isocyanate) Carbamates. *JACS* **80**, 5495–5498 (1958).
6. Grassie, N. & Zulfiqar, M. THERMAL DEGRADATION OF THE POLYURETHANE FROM 1,4-BUTANEDIOL AND METHYLENE BIS(4-PHENYL ISOCYANATE). *J Polym Sci Polym Chem Ed* **16**, 1563–1574 (1978).
7. Yang, W. P., Macosko, C. W. & Wellinghoff, S. T. Thermal degradation of urethanes based on 4,4'-diphenylmethane diisocyanate and 1,4-butanediol (M DI/B DO). *Polymer (Guildf).* **27**, 1235–1240 (1986).
8. Voorhees, K. J. Mechanisms of Pyrolysis for a Specifically Labeled Deuterated Urethane. *J. Polym. Sci., Polym. Chem. Ed.* **20**, 1457–1467 (1982).
9. Lattimer, R. P., Muenster, H. & Budzikiewicz, H. PYROLYSIS TANDEM MASS SPECTROMETRY (Py-MS/MS) OF A SEGMENTED POLYURETHANE. *J. Anal. Appl. Pyrolysis* **17**, 237–249 (1990).
10. Shieh, Y.-T., Chen, H.-T., Liu, K.-H. & Twu, Y.-K. Thermal Degradation of MDI-Based Segmented Polyurethanes. *J Polym Sci A: Polym Chem* **37**, 4126–4134 (1999).
11. Herrera, M., Wilhelm, M., Matuschek, G. & Kettrup, A. Thermoanalytical and pyrolysis studies of nitrogen containing polymers. *J. Anal. Appl. Pyrolysis* **58–59**, 173–188 (2001).
12. Camino, G. *et al.* Mechanism of Expandable Graphite Fire Retardant Action in Polyurethanes. *ACS Symposium Series* **797**, 90–109 (2001).
13. Pielichowski, K., Kulesza, K. & Pearce, E. M. Thermal Degradation Studies on Rigid Polyurethane Foams Blown with Pentane. *J. Appl. Polym. Sci.* **88**, 2319–2330 (2003).
14. Rosu, D., Tudorachi, N. & Rosu, L. Investigations on the thermal stability of a MDI based polyurethane elastomer. *J. Anal. Appl. Pyrolysis* **89**, 152–158 (2010).
15. Jiao, L., Xiao, H., Wang, Q. & Sun, J. Thermal degradation characteristics of rigid polyurethane foam and the volatile products analysis with TG-FTIR-MS. *Polym. Degrad. Stab.* **98**, 2687–2696 (2013).
16. Sun, L., Li, K., Xue, W. & Zeng, Z. Thermal degradation of reactive polyurethane hot melt adhesive based on MDI. *J. Adhes. Sci. Technol.* **32**, 1253–1263 (2018).
17. Stančin, H. *et al.* Experimental analysis of waste polyurethane from household appliances and its utilization possibilities. *J. Environ. Manage.* **243**, 105–115 (2019).
18. Li, M., Jiang, L., He, J. J. & Sun, J. H. Kinetic triplet determination and modified mechanism function construction for thermo-oxidative degradation of waste polyurethane foam using conventional methods and distributed activation energy model method. *Energy* **175**, 1–13 (2019).
19. Yao, Z. *et al.* Probing the combustion and pyrolysis behaviors of polyurethane foam from waste refrigerators. *J. Therm. Anal. Calorim.* **141**, 1137–1148 (2020).
20. Zeller, M. *et al.* Thermogravimetric studies, kinetic modeling and product analysis of the pyrolysis of model polymers for technical polyurethane applications. *J. Anal. Appl. Pyrolysis* **171**, 105976 (2023).
21. Xu, S. *et al.* Insight into waste polyurethane pyrolysis pathways: Mechanism functions analysis and in-situ coupling online monitoring. *J. Anal. Appl. Pyrolysis* **177**, 106301 (2024).
22. Pielichowski, K. & Slotwinska, D. Flame-resistant modified segmented polyurethanes with 3-chloro-1,2- propanediol in the main chain - Thermoanalytical studies. *Thermochim. Acta* **410**, 79–86 (2004).

23. Nishiyama, Y. *et al.* Temperature-dependent pyrolysis behavior of polyurethane elastomers with different hard- and soft-segment compositions. *J. Anal. Appl. Pyrolysis* **145**, 104754 (2020).
24. Kumagai, S. *et al.* Effects of hard- and soft-segment composition on pyrolysis characteristics of MDI, BD, and PTMG-based polyurethane elastomers. *J. Anal. Appl. Pyrolysis* **126**, 337–345 (2017).
25. Backus, J. K., Bernard, D. L., Darr, W. C. & Saunders, J. H. Flammability and thermal stability of isocyanate-based polymers. *J. Appl. Polym. Sci.* **12**, 1053–1074 (1968).
26. Foti, S., Maravigna, P. & Montaudo, G. MECHANISMS OF THERMAL DECOMPOSITION IN TOTALLY AROMATIC POLYURETHANES. *J. Polym. Sci. A1* **19**, 1679–1687 (1981).
27. Chambers, J., Jicny, J. & Reese, C. B. The Thermal Decomposition of Polyurethanes and Polyiso cyanurates. *Fire Mater.* **5**, 133–141 (1981).
28. Herrera, M., Matuschek, G. & Kettrup, A. Thermal degradation of thermoplastic polyurethane elastomers (TPU) based on MDI. *Polym. Degrad. Stabil.* **78**, 323–331 (2002).
29. N. Ketata, C. Sanglar & M.F. Grenier-Loustalot. Thermal Degradation of Polyurethane Bicomponent Systems in Controlled Atmospheres. *Polymers and Polymer Composites* **13**, 1–26 (2005).
30. Eschenbacher, A., Varghese, R. J., Weng, J. & Van Geem, K. M. Fast pyrolysis of polyurethanes and polyisocyanurate with and without flame retardant: Compounds of interest for chemical recycling. *J. Anal. Appl. Pyrolysis* **160**, 105374 (2021).
31. Xu, D., Yu, K. & Qian, K. Thermal degradation study of rigid polyurethane foams containing tris(1-chloro-2-propyl)phosphate and modified aramid fiber. *Polym. Test.* **67**, 159–168 (2018).
32. Pagacz, J. *et al.* Polyurethane foams chemically reinforced with POSS—Thermal degradation studies. *Thermochim. Acta* **642**, 95–104 (2016).
33. Ohtani, H. *et al.* Characterization of polyurethanes by high-resolution pyrolysis-capillary gas chromatography. *J. Anal. Appl. Pyrolysis* **12**, 115 (1987).
34. Lattimer, R. P., Polce, M. J. & Wesdemiotis, C. MALDI-MS analysis of pyrolysis products from a segmented polyurethane. *J. Anal. Appl. Pyrolysis* **48**, 1–15 (1998).
35. Esperanza, M. M., García, A. N., Font, R. & Conesa, J. A. Pyrolysis of varnish wastes based on a polyurethane. *J. Anal. Appl. Pyrolysis* **52**, 151–166 (1999).
36. Font, R., Fullana, A., Caballero, J. A., Candela, J. & García, A. Pyrolysis study of polyurethane. *J. Anal. Appl. Pyrolysis* **58–59**, 63–77 (2001).
37. Wang, X. *et al.* Soot formation during polyurethane (PU) plastic pyrolysis: The effects of temperature and volatile residence time. *Energy Convers. Manag.* **164**, 353–362 (2018).
38. Guo, X., Wang, L., Li, S., Tang, X. & Hao, J. Gasification of waste rigid polyurethane foam: optimizing operational conditions. *J. Mater. Cycles Waste Manag.* **17**, 560–565 (2015).
39. Moroi, G. Influence of ion species on the thermal degradation of polyurethane interaction products with transition metal ions. *J. Anal. Appl. Pyrolysis* **71**, 485–500 (2004).
40. Moroi, G. & Ciobanu, C. Aspects of polyesterurethane interaction with metallic ions. III. Thermal behavior of polyurethane interaction products with iron and chromium ions. *J. Anal. Appl. Pyrolysis* **70**, 87–98 (2003).
41. Bozi, J. & Blazsó, M. Catalytic thermal decomposition of polyamides and polyurethanes mixed with acidic zeolites. *J. Anal. Appl. Pyrolysis* **97**, 189–197 (2012).

42. Bozi, J., Mihályi, M. R. & Blazsó, M. Study on temperature dependence of catalytic thermal decomposition of polyamides and polyurethanes mixed with acidic zeolites. *J. Anal. Appl. Pyrolysis* **101**, 103–110 (2013).
43. Terakado, O., Yanase, H. & Hirasawa, M. Pyrolysis treatment of waste polyurethane foam in the presence of metallic compounds. *J. Anal. Appl. Pyrolysis* **108**, 130–135 (2014).
44. Guo, X., Zhang, W., Wang, L. & Hao, J. Comparative study of nitrogen migration among the products from catalytic pyrolysis and gasification of waste rigid polyurethane foam. *J. Anal. Appl. Pyrolysis* **120**, 144–153 (2016).
45. Guo, X., Wang, L., Zhang, L., Li, S. & Hao, J. Nitrogenous emissions from the catalytic pyrolysis of waste rigid polyurethane foam. *J. Anal. Appl. Pyrolysis* **108**, 143–150 (2014).
46. Yuan, Y. *et al.* Highly efficient catalysts for reducing toxic gases generation change with temperature of rigid polyurethane foam nanocomposites: A comparative investigation. *Compos. Part A Appl. Sci. Manuf.* **112**, 142–154 (2018).
47. Kumagai, S., Yabuki, R., Kameda, T., Saito, Y. & Yoshioka, T. Simultaneous recovery of H2-rich syngas and removal of HCN during pyrolytic recycling of polyurethane by Ni/Mg/Al catalysts. *Chemical Engineering Journal* **361**, 408–415 (2019).
48. Engels, T. G. W., Van Der Zijpp, M., Eiden, S., Heeres, H. J. & Deuss, P. J. Polyurethane recycling using catalytic pyrolysis: insights into catalyst stability. (2026).
49. Sasol Limited. High Purity Aluminas. https://products.sasol.com/pic/products/home/grades/ZA/5puralox-and-catalox/index.html (2026).
50. Griffin, R. R., Scaroni, A. W. & Walker, P. L. Cokes and graphites produced from anthracene, acridine, and phenazine. *Carbon N. Y.* **29**, 991–998 (1991).
51. Kenneth, L., Rinehart, J., Buchholz, A. & Lear, G. Mass spectral fragmentation of aniline-1-carbon-13. *J. Am. Chem. Soc.* **90**, 1073–1075 (1968).
52. Selim, E. T. M., Rabbih, M. A. & Fahmey, M. A. Electron impact mass spectrometry of [C7H8N]+ and [C6H7]+ and [C6H7]+ fragment ions produced from o-toluidine and N-methylaniline. *Organic Mass Spectrometry* **27**, 919–923 (1992).
53. Jiao, L., Xiao, H., Wang, Q. & Sun, J. Thermal degradation characteristics of rigid polyurethane foam and the volatile products analysis with TG-FTIR-MS. *Polym. Degrad. Stab.* **98**, 2687–2696 (2013).

5.5. Supporting information

Table S5.5.1 summarizes the available literature on the non-catalytic thermal degradation of rigid polyurethane. For catalytic thermal degradation of rigid polyurethane, see Table 5.5.2 Full names of the chemicals abbreviated in the tables can be found in Table.5.5.0

Table 5.5.0. Abbreviation list for Tables S5.5.1 and S5.5.2

Abbreviation	Full name
Bayer Desmocoll 540	PUR synthesized from polyol with MDI or TDI
BDO	1,4-butanediol
HMDI	Hexanmethylene diisocyanate
HDI	Hexamethyleen diisocyanate
IPDI	Isophorone diisocyanate
MDI	Methyleen diisocyanate
NDI	Napthalene 1,5-diisocyanate
pBA	Polymeric 1,4-butanediol
pDEA	Polydiethylene glycol adipate
pEO	Poly(ethylene orthophtalate)
pHA	Poly-1,6-hexanediol adipate
pMDI	Polymeric methylene diisocyanate
pTDI	Polymeric toluene diisocyanate
pTHF	Polymeric tetrahydrofuran
PU-EMDI	Toluidine-based polyurethane
PU-EpTI	pMDI-based polyurethane
pTMEG	Poly(tetrahydrofurandiol)
PTMG	Poly(oxytetramethylene glycol)
THF	Tetrahydrofuran
TDI	Toluene diisocyanate
PAPI	Polymethylenepolyphenylisocyanate
PEA copolyester	Adipic acid, ethylene glycol, diethylene glycol (1:0.5:0.6 molar ratio)
Rokopol RF551, PCC Rokita S.A	Sorbitol based polyether polyol
XDI	Xylene diisocyanate

Table S5.5.1. Available literature on the non-catalytic thermal degradation of rigid polyurethanes (For abbreviation list see Table S5.5.0)

Group [Year]	Type of feed	Origin feedstock (polyol, cyanate)	Technique	Key insights
Dyer [1958][1]	Model	Not stated (Hexamethylene glycol, MDI)	GC, IR	Heterolytic scission of urethane bond primary decomposition pathway
Backus [1968][2]	Model	Commercial sources (Various co-reactants, MDI-3.0)	[a]TGA, [b]DTA	Thermal degradation behavior dictated by chemical structure and formulation
Grassie [1972][3]	Model	Department of Fibre Science, Strathclyde (BDO, MDI)	[c]TVA, [d]DSC	stepwise cleavage of urethane linkages into according segments primary decomposition pathway
Foti [1981][4]	Model	Commercial products (polyol, Various isocyanates, MDI)	Py-GC/MS, TGA	Thermal resistance controlled by structural motive
Chambers [1981][5]	Model	Not stated (various polyols, various cyanates, MDI)	GC/MS, TGA, [e]DTA, IR	Thermal degradation behavior dictated by chemical structure and formulation
Voorhees [1982][6]	Model	Not stated (Trimethylolpropane, PAPI)	[f]Py-GC/MS	Thermal degradation proceeds via specific kinetic processes (chain scission vs side-group elimination)
Yang [1986][7]	Model	Dow chemicals, freeport TX (BDO, MDI)	TGA, [g]GPC	Thermal degradation above 170 °C via first-order dissociation
Ohtani [1987][8]	Model	Not stated (pBA,pHA,pDEA, TDI, IPDI, HMDI, MDI)	Py-GC/MS	Pyrolysis conditions (temp, flow-rate, carrier gas) influence diisocyanate recovery
Lattimer [1990][9]	Model	Morthane CA-128 (polyester, MDI,TDI,HDI)	Py-MS/MS	PUR proceeds via 2-stage thermal decomposition pathway
Lattimer [1998][10]	Model	Not stated (pBA, BDO, MDI)	[h]MALDI-MS	Low temp pyrolysis promotes oligomeric product formation, and high temp promote dehydration to unsaturated species
Esperanza [1999][11]	[i]EOL	EOL Furniture waste (polyol, MDI, TDI, NDI, HDI)	GC-MS/TCD, TGA	Pyrolysis of waste yields complex distribution of products
Shieh [1999][12]	Model	Various suppliers (BDO, polyester polyol, MDI)	TGA-IR GPC	Thermal degradation involves scission of NH, CH bonds in hard segments
Font [2001][13]	Commercial	Bayer (Desmocoll540)	GC/MS, TGA	Higher temperature results in more light hydrocarbons
Hererra [2001][14]	Commercial	Not stated (rigid PUR, not specified)	GC/MS, [j]HPLC	Nitrogen content and polymer architecture influence onset and degradation pathways
Camino [2001][27]	Commercial	Impercial chemical industries (polyol, pMDI)	TGA, FTIR	Char arises from the presence of fire retardants in PUR
Hererra [2002][15]	Commercial	Not stated (Various co-reactants, MDI)	TGA-IR/MS	Thermal degradation behavior depends on type of soft segment (polyether or polyester)
Pielichowski [2003][16]	Commercial	Various suppliers (polyol, pMDI, pTDI)	TGA-IR	Hard and soft segment breakdown determines the weight loss behavior and thermal stability of PUR
Ketata [2004][17]	Model	Not stated (PU-EpTI, PU-EMDI)	TGA/FR-IR, MALDI-TOF	Thermal decomposition occurs via multiple competing reactions with product distribution determined via chemical structure and atmosphere
Pielichowski [2004][18]	Model	Various suppliers (Various co-reactants, pMDI)	TGA-IR/MS	Changes in backbone structure influences thermal resistance of PUR

Rosu [2010][19]	Model	Institute of macromolecular chemistry Romania (PEA copolyester MDI)	TGA-IR/MS	Thermal decomposition via multistage through urethane bond scission and soft segment breakdown
Jiao [2013][20]	Commercial	Shanghai Saikun rubber and plastic products Co. LTD. China (polyether, polyol, isocyanates)	TGA-IR/MS	Thermal decomposition via 2-stage with first step urethane cleavage at 200 °C
Pagacz [2016][21]	Model	Not stated (Rokopol RF551, PCC Rokita S.A., pMDI)	TGA-IR	Thermal degradation is lowered from 200 to 150 °C via foam modification (silsesquioxanes)
Kumagai [2017][22]	Model	Various suppliers (PTMG, BDO, XDI, MDI)	Py-GC/MS, [k]EGA-MS, TGA	Pyrolysis behavior depends on the structure and ratio of hard and soft segments
Sun [2018][23]	Model	Various suppliers (pBA, pTMEG, pEO, MDI)	Py-GC/MS, TGA	Thermal decomposition behavior involves multi stage with urethane scission and evolution of volatiles
Jiang [2018][24]	EOL	EOL rigid polyurethane waste (not specified)	Py-GC/MS, TGA	Waste PUR involves a complex multistage decomposition pathway
Stancin [2019][25]	EOL	EOL refrigerator waste (not specified)	Py-GC/MS	Thermal degradation showed significant amounts of hazardous compounds
Li [2019][26]	Model	Shandong lecron energy-saving new material Co. Ltd. (polyol, pMDI)	TGA	Thermo-oxidative degradation of PUR follows a multi-stage kinetic model
Wang [2018][28]	EOL	EOL refrigerator waste (not specified)	GC-MS/TCD, [l]TEM, [m]XRD,TGA,	Soot formation via thermal evolution is strongly dependent on pyrolysis temperature and volatiles residence time
Xu [2018][29]	Model	Various suppliers (Polyether polyol, pMDI)	GC-MS,TGA, FTIR	Incorporation of a flame-retardant and aramid fiber alters the onset degradation and volatile product formation
Yao [2020][30]	EOL	EOL recycling plant (not specified)	TGA-IR/MS	Waste foam exhibits a multistage thermal decomposition pathway including urethane bond scission
Nishiyama [2020][31]	Model	Various suppliers (BDO, glycol, MDI)	Py-GC/MS	Pyrolysis behavior depends on the structure and ratio of hard and soft segments
Eschenbacher [2021][32]	Commercial	Unilin Belgium (polyalcohol glycerol, MDI)	Py-GC/MS, TGA	Pyrolysis of PUR with and without chlorinated flame-retardants results in distinct volatile and char yields
Zeller [2023][33]	Commercial	Chemicals from BASF (BDO, pTHF MDI)	Py-GC/MS, TGA	Thermal decomposition occurs via structure dependent two step pathway described by a kinetic model
Xu [2024][34]	EOL	EOL refrigerator waste (not specified)	TGA-IR/MS	Waste PUR pyrolysis follows 3 mechanisms

[a]Thermogravimetric analysis; [b]Differencial thermal analysis; [c]Thermal volatilization analysis; [d]Differencial scanning calorimetry; [e]Derivative thermogravimetric analysis; [f]Pyrolysis gas chromatography mass spectrometry; [g]Gel permeation chromatography; [h]Matrix-assisted laser desorption/ionization mass spectrometry; [i]End-of-life; [j]High performance liquid chromatography; [k]Evolved gas analysis; [l]Transmission electron microscopy; [m]X-ray diffraction

Table S5.5.2.. Available literature on the catalytic thermal degradation of rigid polyurethanes (For abbreviation list see Table S5.5.0)

Group [Year]	Type of feed (cat)	Origin feedstock (polyol, cyanate)	Technique	Key insights
Takamoto [1994][35]	Fresh/commercial (Char, activated carbon)	Reaction injection molding (polyol, MDI)	GC	Thermal decomposition is influenced by secondary heterogeneous pyrolysis reactions on char and volatiles
Moroi [2003][36]	Model ($FeCl_3$, $CrCl_3$)	PEDA/EG[b], MDI, metalCl (polyol, MDI, metalchlorides)	TGA	Thermal decomposition pathway is altered by the introduction of transition metal ions
Moroi [2004][37]	Model (metal chlorides)[a]	PEDA/EG[b], MDI, MetalCl (polyol, MDI, metalchlorides)	TGA	Thermal decomposition pathway is altered by the introduction of transition metal ions
Bozi [2012][38]	Fresh/commercial (NH_4NaY, HUSY)	PA6,6, PA-6, PUR_{eth}, PUR_{est} (BDO, polyamide, polyether, polyester, MDI)	Py-GC/MS TGA-MS	Pyrolysis product distribution is altered (aromatic enhancement) by presence of acidic Y-type zeolite
Bozi [2013][39]	Fresh/commercial (NH_4Y, HUSY)	PA6,6, PA-6, PUR_{eth}, PUR_{est} (polyamide, polyether, polyester, MDI)	Py-GC/MS TGA-MS	Thermally induced chemical transformations promoted by acidic zeolites
Terakado [2014][40]	Fresh/commercial (various catalysts) [d]	Toyo tire & rubber (Polyol, MDI,TDI)	GC-MS, TGA	An increase in gas and char yield was observed for decomposition in the presence of metallic salts
Guo [2014][41]	EOL (CaO)	EOL PUR (polyol, MDI)	GC-MS/TCD	Nitrogen in waste PUR evolves as N_2 with suppression of NO_x in presence of CaO
Guo [2015][42]	EOL (various catalysts)[e]	EOL PUR (polyol, MDI)	GC-FID/TCD	Temperature has greater influence on gas production than catalyst type or air flow
Guo [2016][43]	EOL (alkali, transition)[c]	EOL Refrigerator (polyol, MDI)	GC-MS/TCD	N migrated into volatile products upon pyrolysis of waste PUR
Yuan [2018][44]	Model compound ($NiMoO_4$)[a]	LY-4110 & PAPI (polyol, pMDI)	TGA-IR	Formation of toxic gasses (CO, NO_x, HCN) suppressed by incorporation of specific metal oxides
Kumagai [2019][45]	Fresh/commercial (Ni/Mg/Al)	Domestic market Japan (Polyol, TDI, MDI)	Py-GC/MS, TGA-IR	Ni/Al/Mg-based catalyst converts waste PUR into H_2-rich syngas while suppressing HCN formation
Our work [2026]	Model ($Al2O_3$)	Sigma Aldrich, Cambridge isotopes (various alcohols, MDI)	Py-GC/MS, TGA-MS	Thermal decomposition shows unidirectional proton flow from soft segment to hard segment with alpha proton key role in cracking mechanism

[a]metals used in this work: manganese, cobalt, copper, iron, chromium
[b]PEDA/EG is a polyester (PEDA) bonded to a chain extender (EG)
[c]catalyst used in this work: NaOH, NaCO3, CaO, CaOH, CaCO3, MgO, MgCO3, Fe, FeCl3, MgO2
[d]Catalysts used in this work: $ZnCl_2$, $CuCl_2$, $FeCl_3$, $FeCl_2$, $Fe(NO_3)_3$, , $Cu(NO_3)_2$, $Zn(NO_3)_2$, La_2O_3, ZnO, Fe_2O_3, Nd_2O_3
[e]Catalyst used in this work: Fe, Ni:Mg:Fe 1:1:1, $FeCl_3$, MgO, CaO, $MgCO_3$, Na_2CO_3, $CaCO_3$, $Ca(OH)_2$, NaO

Materials and NMR spectra

Sasol kindly provided the alumina-based catalyst with the code Puralox SCCa 5/200. The catalyst is of high purity, as determined by XRF, consisting of 99% Al_2O_3, 0.66% MgO, and 0.17% CaO. Other impurities found were (ppm): 171 Fe_2O_3, 151 Ga_2O_3, 143 V_2O_5, 92 TiO_2, 41 TeO_2, 27 SnO_2, 14 ZnO, 13 MnO, and 8 Eu_2O_3. The catalyst specifications are shown in Table S5.5.3 The agglomerate and particle size of the catalyst were measured by SEM and TEM, respectively. For SEM, at least 60 particles were measured per sample, and for TEM, at least 200 particles were measured to ensure a reliable measurement (see Figure S5.5.3 below for examples).

Table S5.5.3. Properties of the alumina-based Puralox SCCa 5-200 catalysts

Property	Value	Unit
Purity[a]	99.1	%
Agglomerate size[b]	84 ± 28	µm
Particle size[c]	15 ± 4	nm
Surface area[d]	218	m^2/g
Total pore volume[e]	382	cm^3/g
Total acidity[f]	406	µmol/g
Acid site density[g]	1.86	$\mu mol/m^2$
Basicity[h]	187	µmol/g
Basic site density[g]	0.86	$\mu mol/m^2$
Brønsted/Lewis ratio[i]	0/100	-
Crystallinity[j]	54.5	%
Crystal size[j]	53.5	Å

[a]Determed via XRF

[b]Obtained via SEM analysis, measurement of 85 particles

[c]Obtained via TEM analysis, measurement of 200 particles

[d]Calculated via N_2 physisorption

[e]Determined via p/p^0 at 0.99 from isotherm plot

[f]Obtained via Ammonia Thermal programmed desorption (NH_3-TPD)

[g]Calculated via $\frac{Total\ acidity/basicity}{Surface\ area}$

[h]Obtained via Carbon dioxide Thermal programmed desorption (CO_2-TPD)

[i]Calculated via Py-IR experiments

[j]Calculated via Bruker DIFFRAC.EVA software

The ^1H, ^{13}C, COSY, and HSQC NMR spectra of model compound **1** (Diisopropyl (methylenebis(3,1-phenylene))dicarbamate) is shown in Figure S5.5.2 and Figure S5.5.5, respectively. Note that all synthesized model compounds in this manuscript have been confirmed in similar fashion.

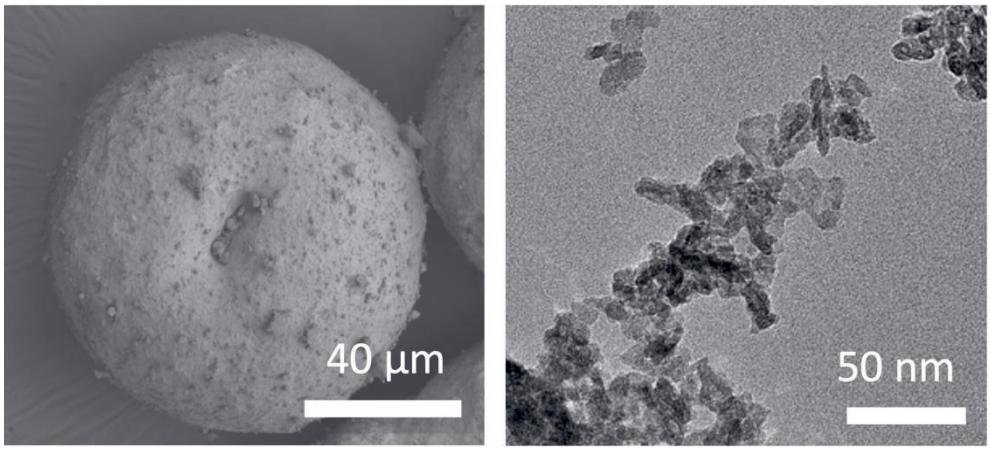

Figure S5.5.1. SEM (left) and TEM (right) image of Puralox SCCa 5/200

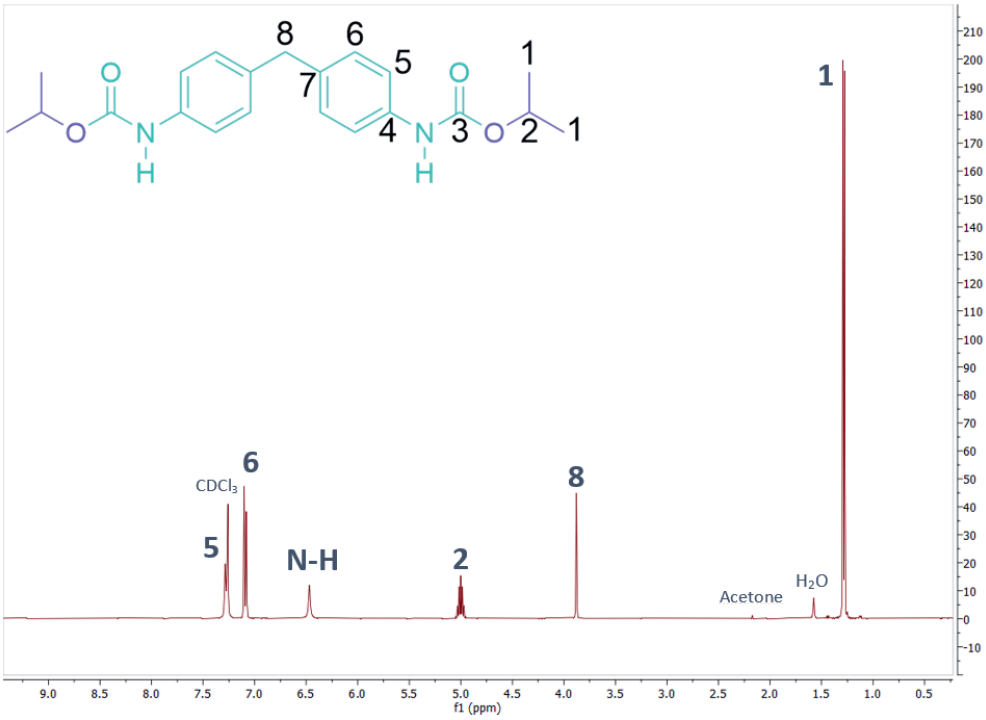

Figure S5.5.2. ^{1}H NMR spectra of model compound **1** Diisopropyl (methylenebis(3,1-phenylene))dicarbamate

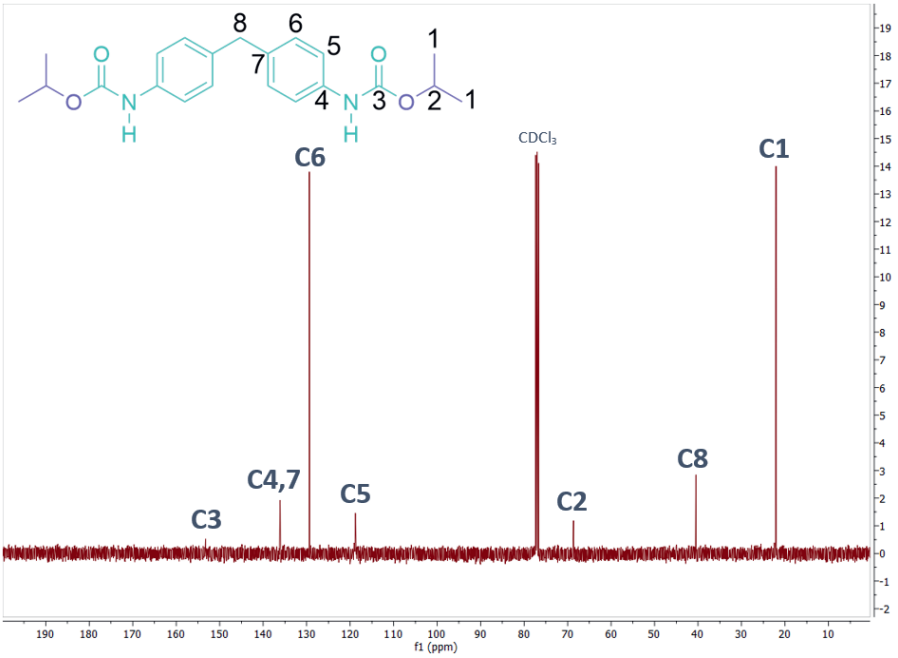

Figure S5.5.3. ^{13}C NMR spectra of model compound **1** Diisopropyl (methylenebis(3,1-phenylene))dicarbamate

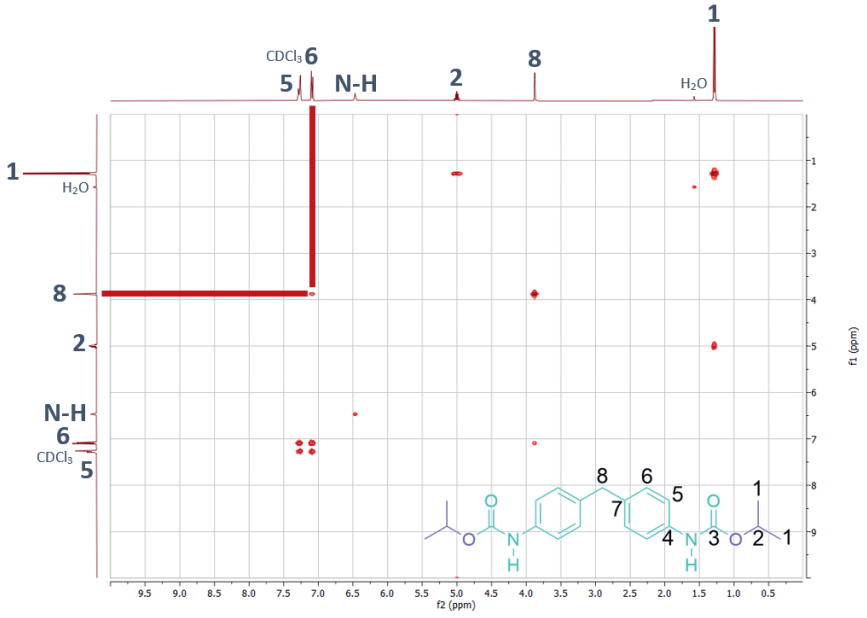

Figure S5.5.4. COSY NMR spectra of model compound **1** Diisopropyl (methylenebis(3,1-phenylene))dicarbamate

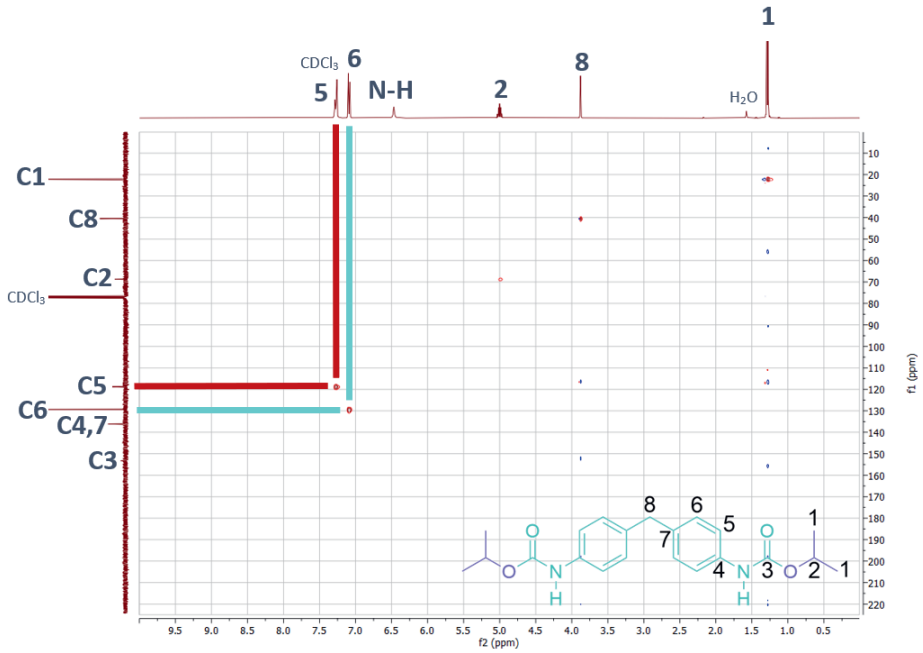

Figure S5.5.5. HSQC *N*MR spectra of model compound **1** Diisopropyl (methylenebis(3,1-phenylene))dicarbamate

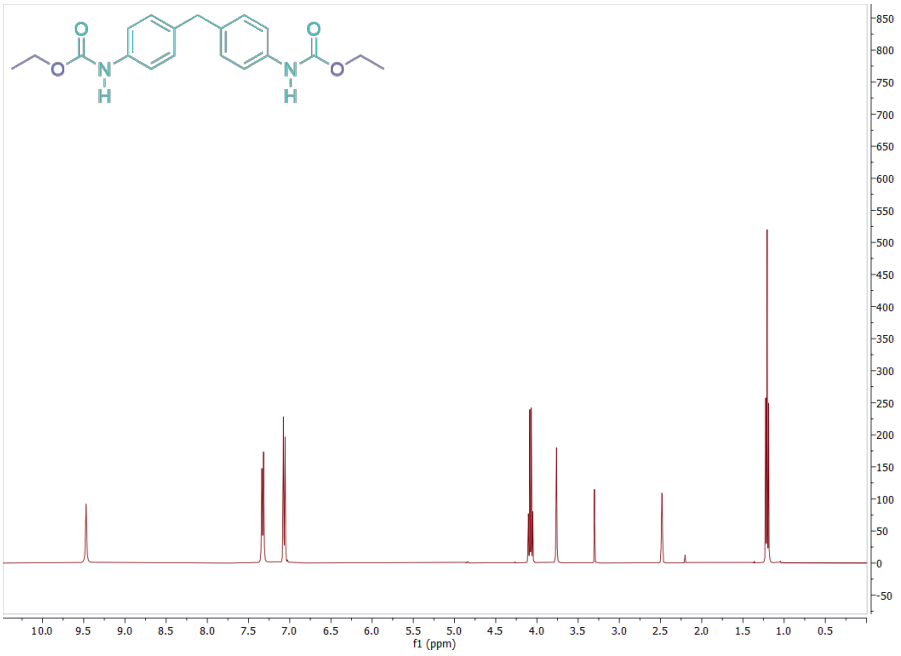

Figure S5.5.6. ^{1}H NMR spectra of model compound **2** Diethyl-(methylenebis(4,1-phenylene))dicarbamate)

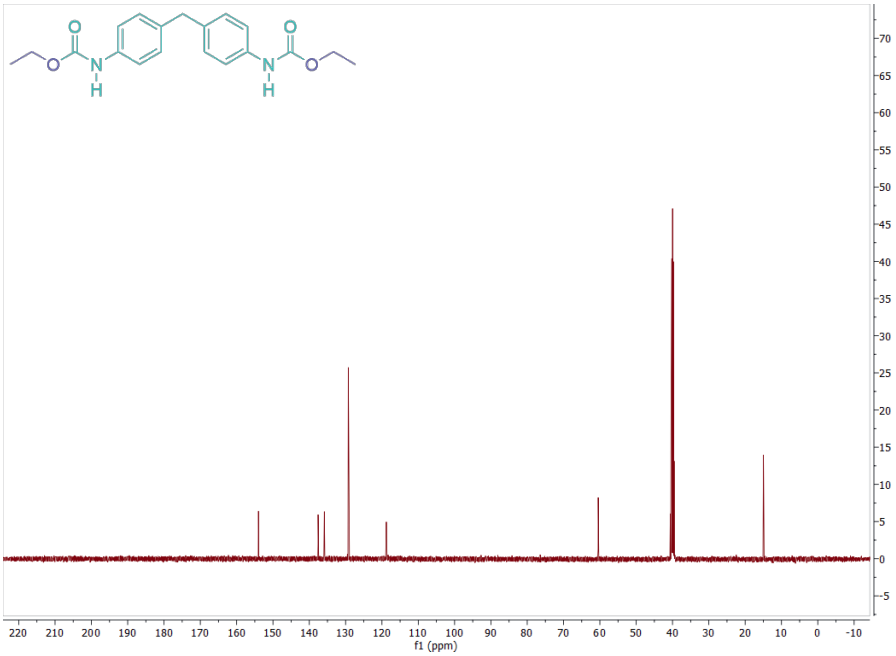

Figure S5.5.7. ^{13}C NMR spectra of model compound **2** Diethyl-(methylenebis(4,1-phenylene))dicarbamate)

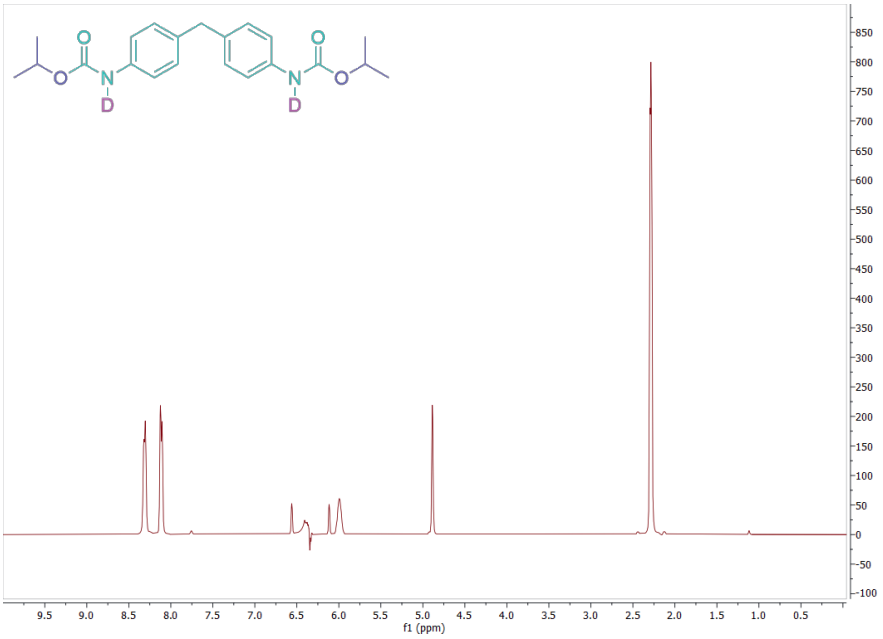

Figure S5.5.8 ^{1}H NMR spectra of model compound **3** Diisopropyl (methylenebis(3,1-phenylene))dicarbamate

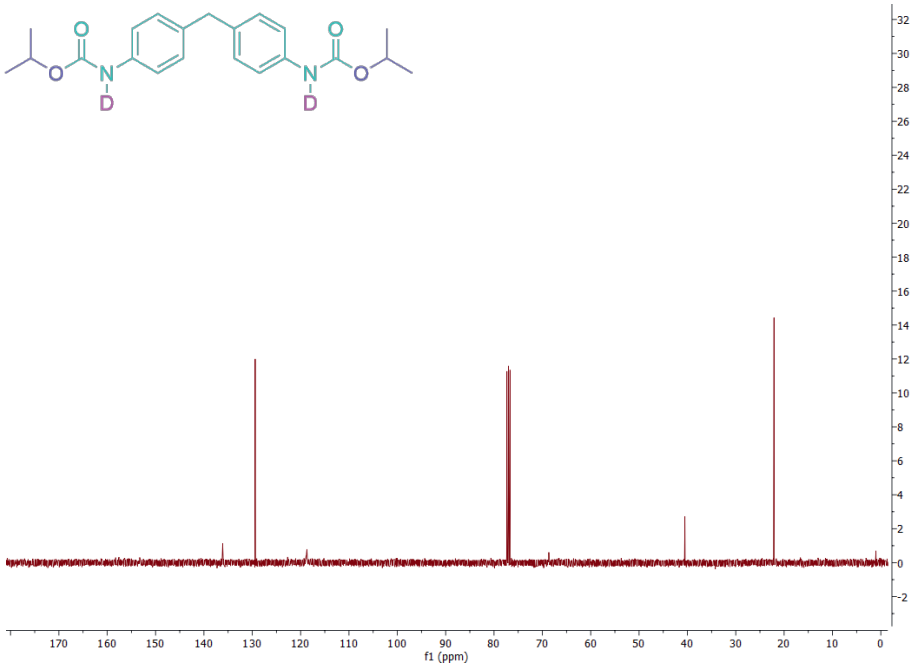

Figure S5.5.9. ^{13}C NMR spectra of model compound **3** diisopropyl (methylenebis(3,1-phenylene))dicarbamate

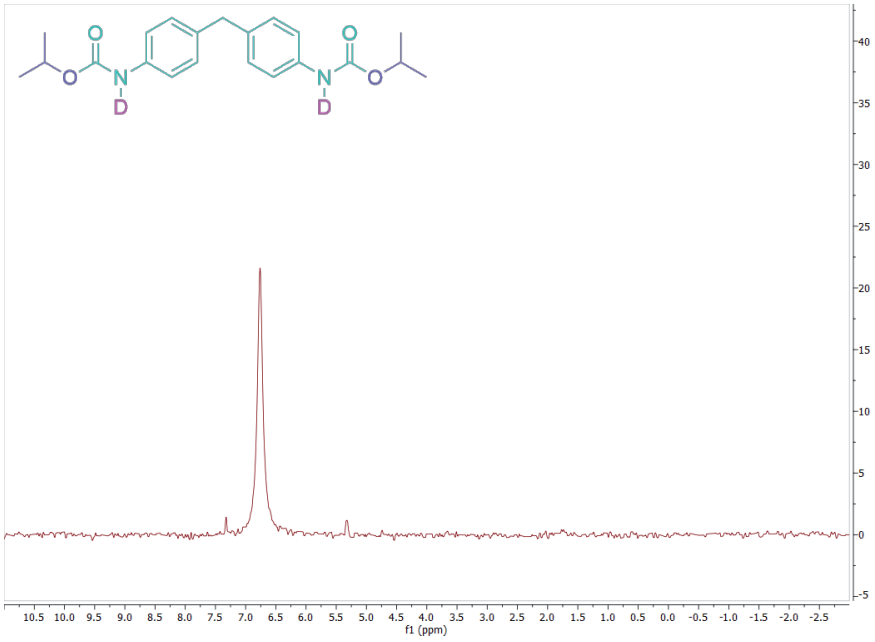

Figure S5.5.10.^{1}D NMR spectra of model compound **3** diisopropyl (methylenebis(3,1-phenylene))dicarbamate

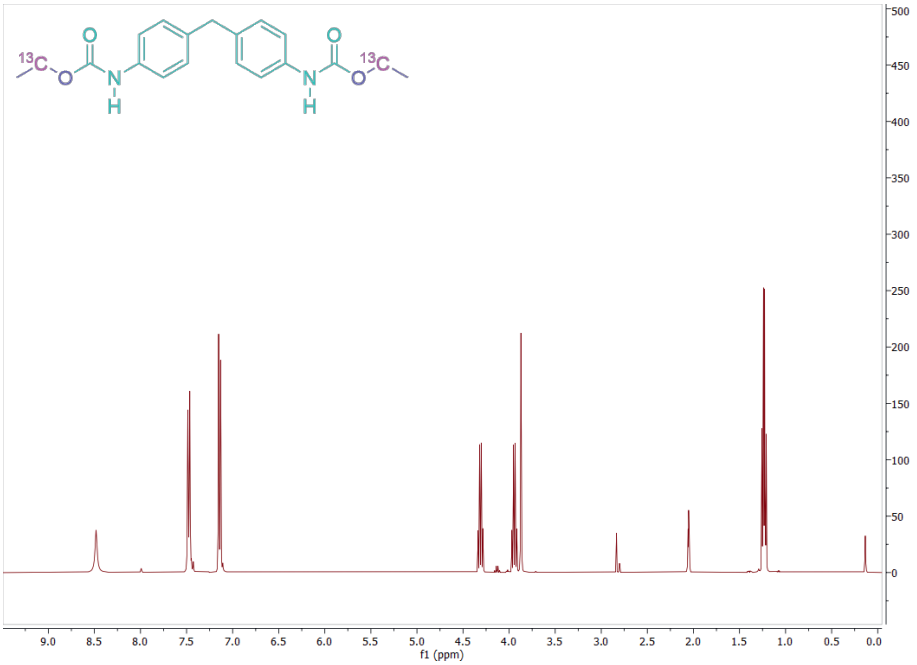

Figure S5.5.11.^{1}H NMR spectra of model compound **4** di(ethyl-13C) (methylenebis(4,1-phenylene))dicarbamate

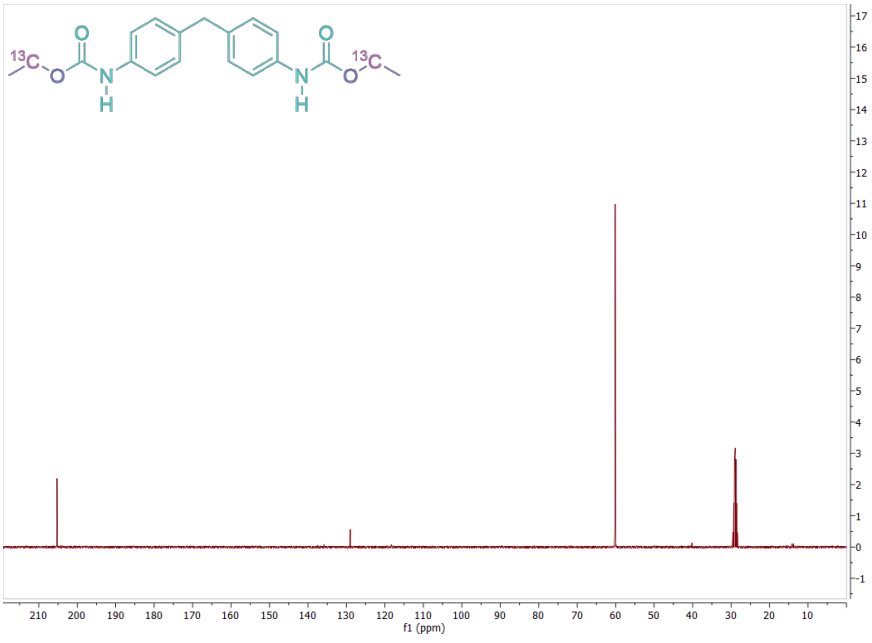

Figure S5.5.12. ^{13}C NMR spectra of model compound **4** di(ethyl-13C) (methylenebis(4,1-phenylene))dicarbamate

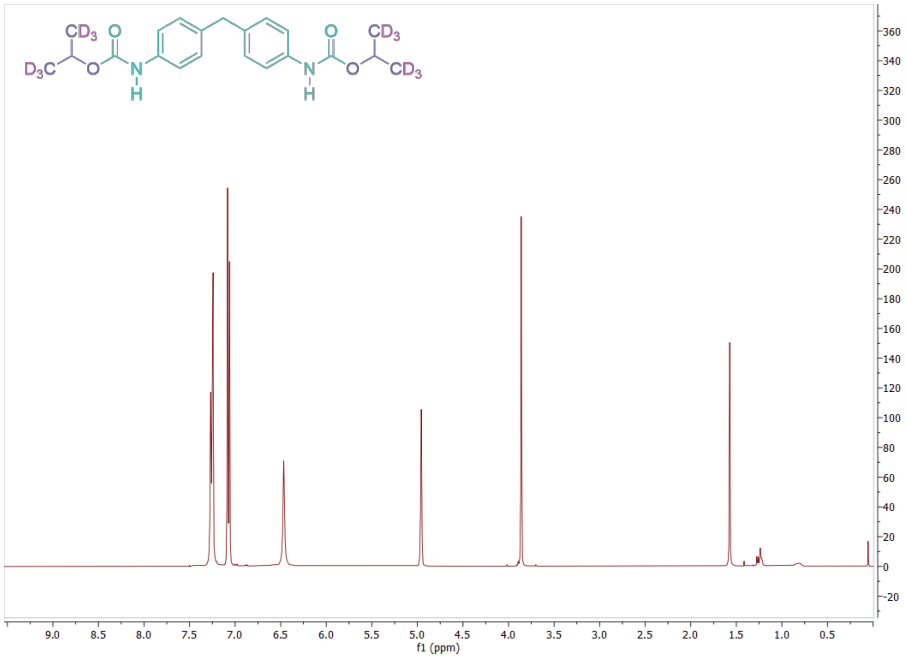

Figure S5.5.13. ^{1}H NMR spectra of model compound **5** bis(propan-2-yl-1,1,1,3,3,3-d6) (methylenebis(4,1-phenylene))dicarbamate

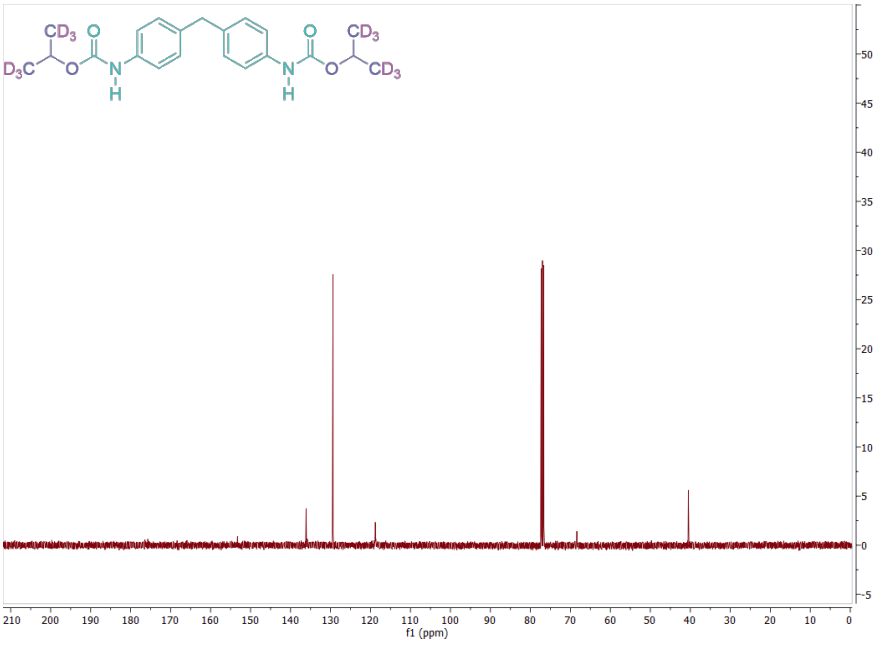

Figure S5.5.14.^{13}C NMR spectra of model compound **5** bis(propan-2-yl-1,1,1,3,3,3-d6) (methylenebis(4,1-phenylene))dicarbamate

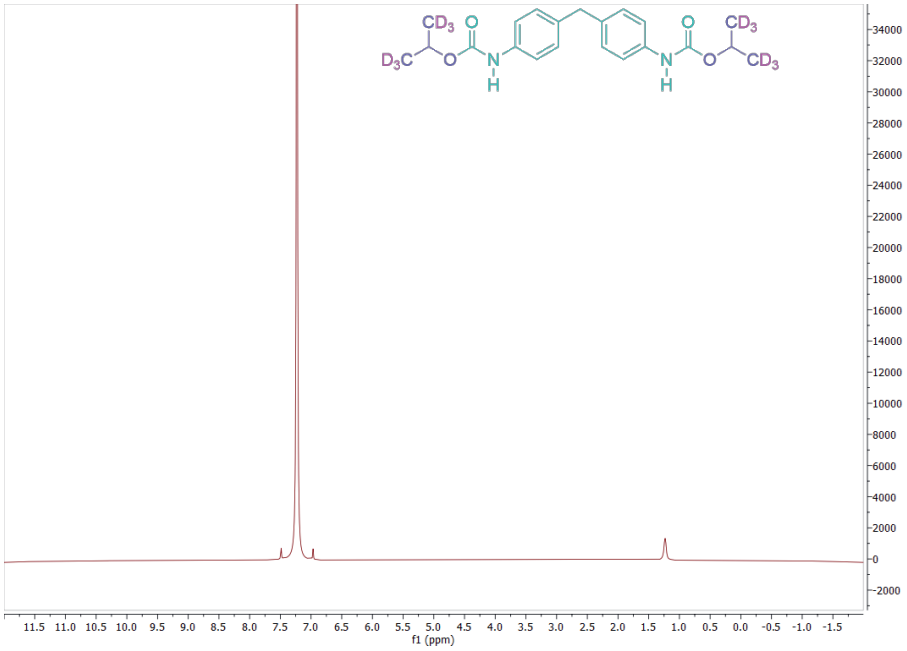

Figure S5.5.15. ^{1}D NMR spectra of model compound **5** bis(propan-2-yl-1,1,1,3,3,3-d6) (methylenebis(4,1-phenylene))dicarbamate

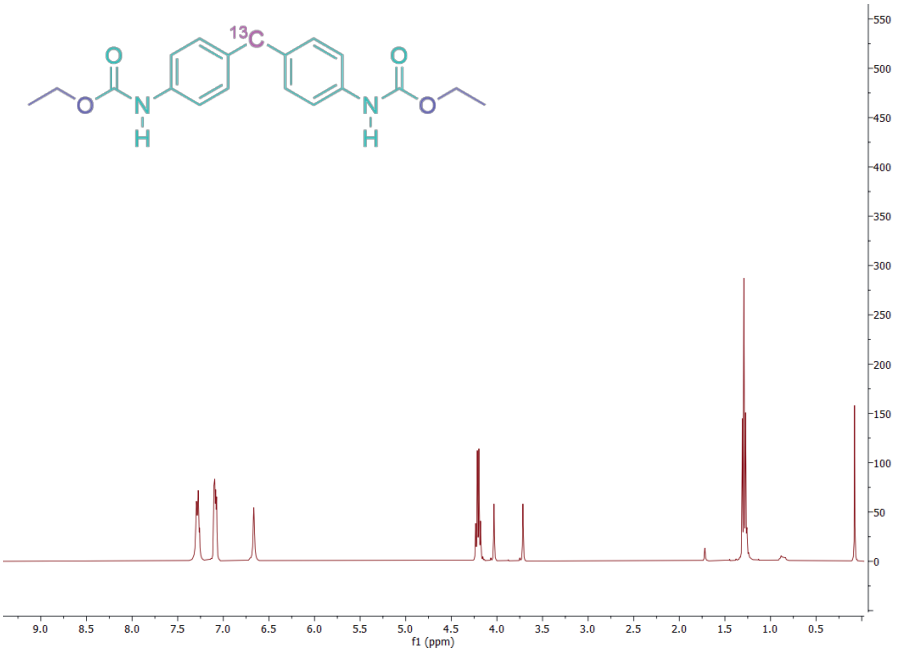

Figure S5.5.16.^{1}H NMR spectra of model compound **6** Diethyl 4,4'-methylene-13C bis(1,4-phenylene)diurethane

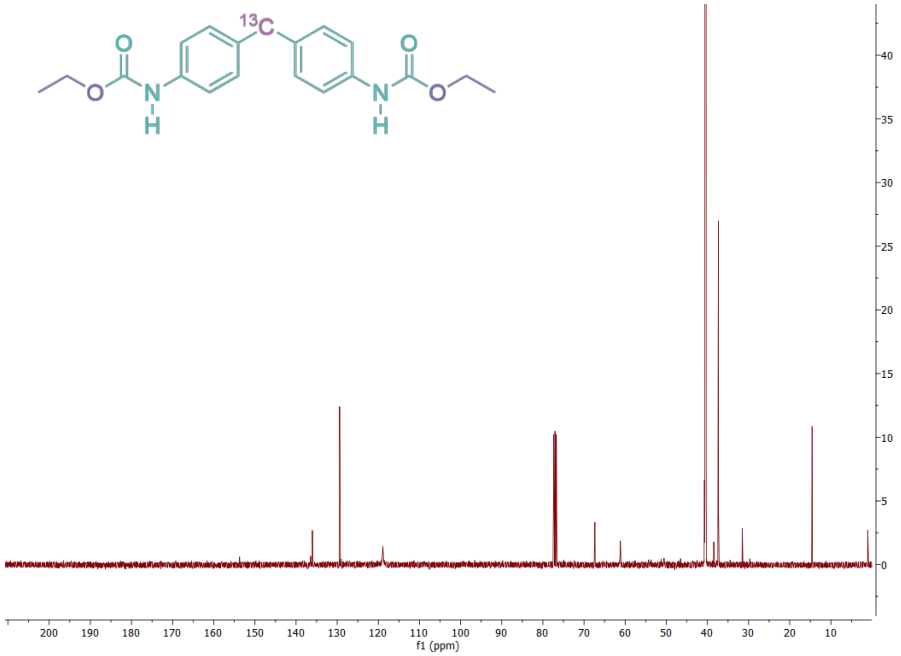

Figure S5.5.17. ^{13}C NMR spectra of model compound **6** Diethyl 4,4'-methylene-13C bis(1,4-phenylene)diurethane

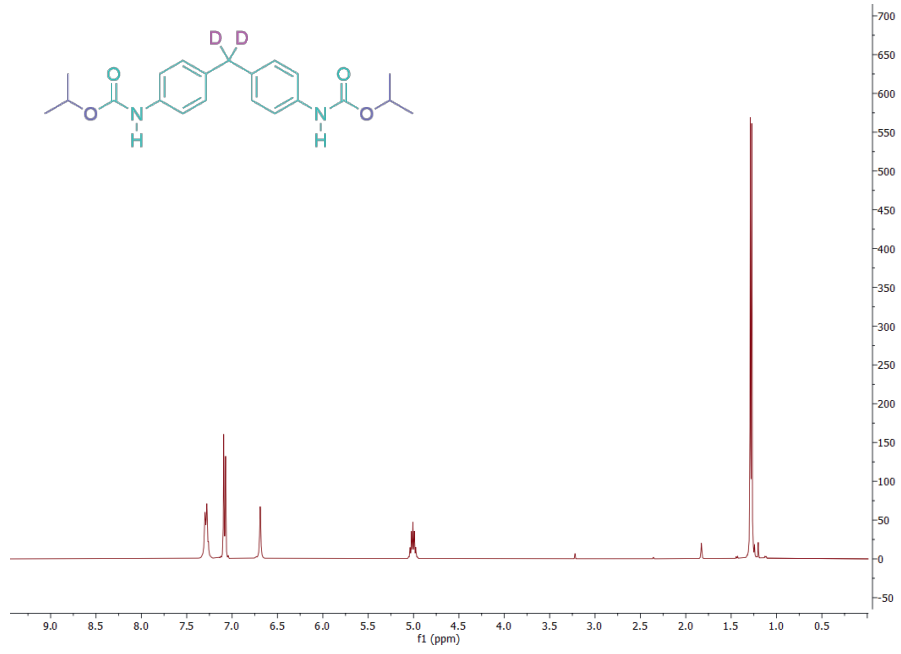

Figure S5.5.18. ^{1}H NMR spectra of model compound **7** Diisopropyl 4,4-methylene-d_2 diphenylenedicarbamate

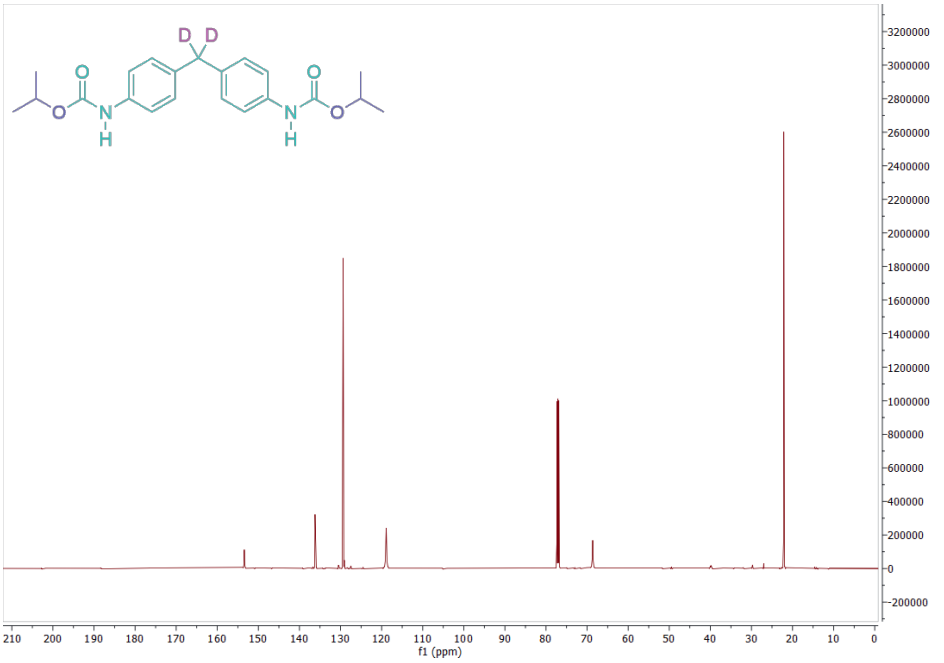

Figure S5.5.19. ^{13}C NMR spectra of model compound **7** Diisopropyl 4,4-methylene-d_2 diphenylenedicarbamate

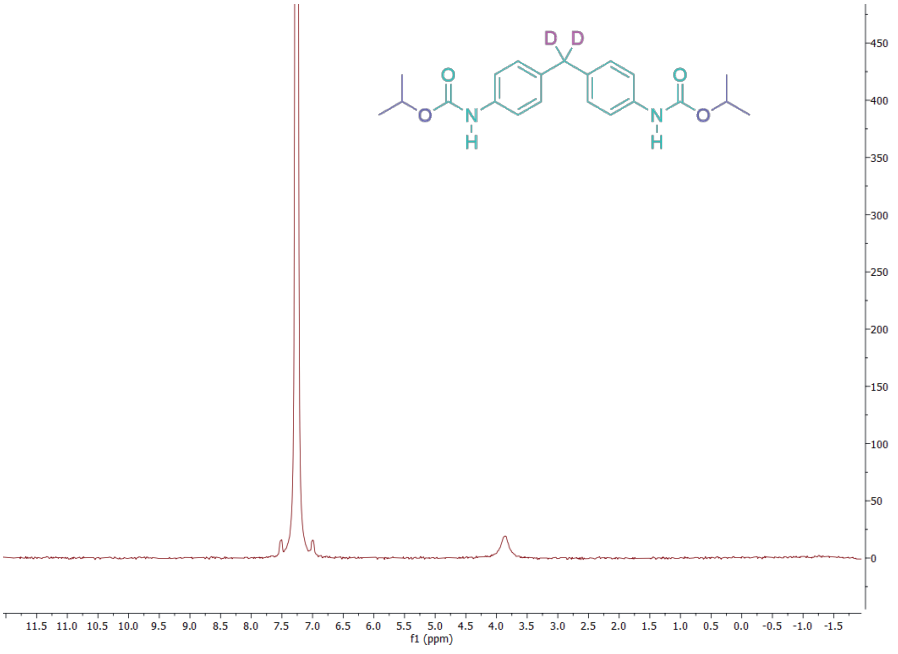

Figure S5.5.20. ^{1}D NMR spectra of model compound **7** Diisopropyl 4,4-methylene-d_2 diphenylenedicarbamate

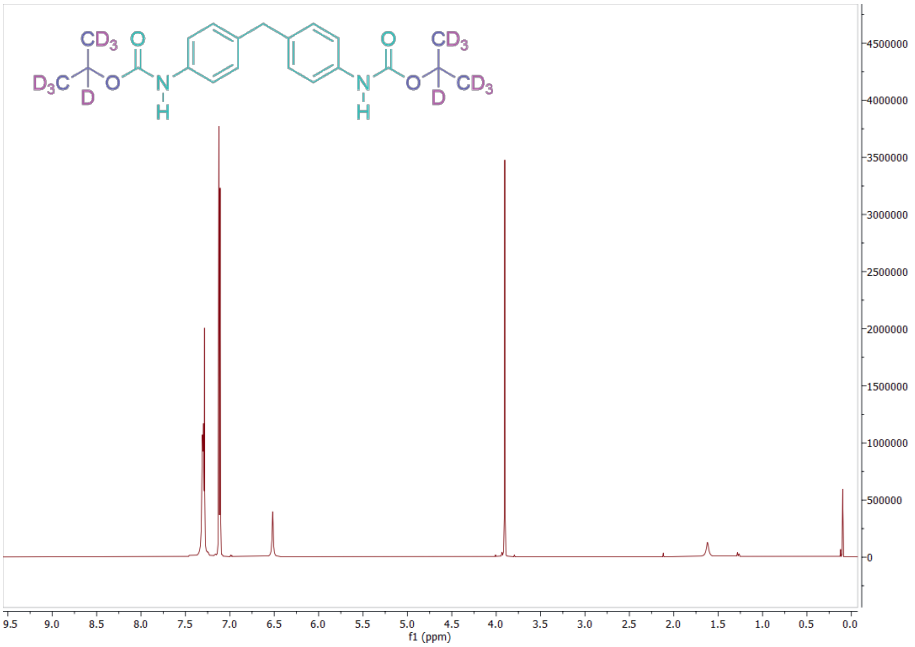

Figure S5.5.21. ^{1}H NMR spectra of model compound **8** bis(propan-2-yl-d7) (methylenebis(4,1-phenylene))dicarbamate

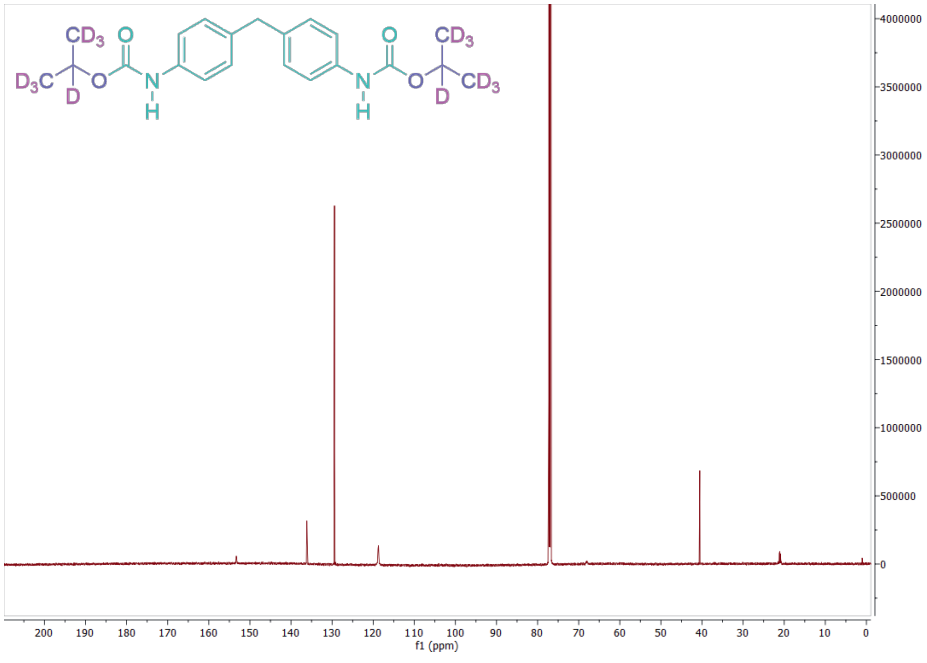

Figure S5.5.22 ^{13}C DMR spectra of model compound **8** bis(propan-2-yl-d7) (methylenebis(4,1-phenylene))dicarbamate

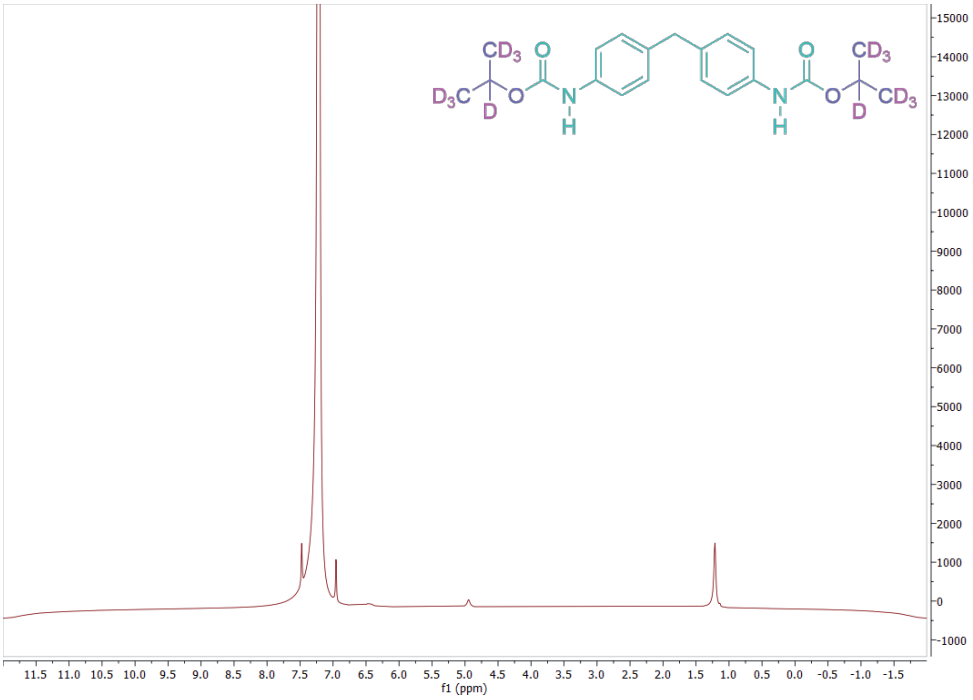

Figure S5.5.23. [1]D NMR spectra of model compound **8** bis(propan-2-yl-d7) (methylenebis(4,1-phenylene))dicarbamate

Calculation details

(**S5.5.1**) Yield in this work is based on mol% input. This yield is calculated by dividing the amount of target molecules produced by the amount of input molecules. The yield corrects for 2 aniline molecules that can be produced from 1 model compound molecule. The yield is expressed in the paper as "Mol% yield" with % as the unit. The Calculation is shown in Equation S5.5.1.

$$Mol\ \%\ yield\ (\%) = \frac{\#\mathrm{prod} * \#\mathrm{molm}}{2\ (\#\mathrm{molp} * \#\mathrm{model})} \quad \text{(S5.5.1)}$$

In which:

#prod is the amount of product produced in miligram

#model is the amount of model feed input in miligram

#molm is the molecular weight of the model compound

#molp is the molecular weight of the product:

- Aniline: 93 g/mol
- Toluidine: 107 g/mol
- Acridine: 149 g/mol
- MDA 198 g/mol

The 2 stands for 2 aromatic rings in the model compound that can be converted in 2 aniline molecules.

Non-catalytic and catalytic pyrolysis of models 1 and 2

Models 1. and 2. were pyrolyzed with and without a catalyst to demonstrate the catalyst's role in the process. Product identification for non-catalytic and catalytic pyrolysis of model 1. is shown in Table S5.5.5 and Table S5.5.6, respectively with the yields in Table S5.5.9. The product identification for non-catalytic and catalytic pyrolysis of model 2 is shown in Table S5.5.7, and Table S5.5.8, respectively with the yields in Table S5.5.10.

Models 1, 7, and 8 have been thermally (non-catalytic) pyrolyzed at batch milligram scale. The products identified via GC-MS were propene, isopropanol, and Methylene diphenyl diisocyanate (MDI). The 9 fragmentation patterns of the products formed upon non-catalytic pyrolysis of the three models are shown in Figure S5.5.24

Table S5.5.4. Identified products from the thermal decomposition of model **1** without a catalyst

#	Area integration[a] (%)	Match (%)	ID
1	39.1	83	Propene
2	3.09	90	isopropylalcohol
3	41.8	90	isopropylalcohol
4	15.9	99	Benzene, 1,1'-methylenebis[4-isocyanato-

Table S5.5.5.Identified products from the thermal decomposition of model **1** catalyzed by Puralox SCCa 5/200

#	Area integration[a] (%)	Match (%)	ID
1	32.0	90	Propene
2	8.39	64	Acetone
3	0.30	64	Diisopropyl ether
4	45.7	97	Aniline
5	8.56	94	Toluidine
6	1.76	97	Acridine
7	0.15	86	Acridine, 9-methyl-
8	2.67	81	Acridine, 9-methyl-
9	0.034	70	2-(4-Methylphenyl)-1H-indole
10	0.443	90	1H-Indole, 1-methyl-2-phenyl-

[a]Reaction conditions: 0.5 mg model, catalyst-to-feed ratio of 5 to 1, 550 °C with a helium flow of 205 mL/min and a pyrolysis time of 10 seconds

Table S5.5.6. Identified products from the thermal decomposition of model **2** without a catalyst

#	Area integration[a] (%)	Match (%)	ID
1	5.13	83	Ethylene
2	0.74	90	Ethane
3	7.17	91	Acetaldehyde
4	33.4	91	Ethanol
15	53.6	96	Benzene, 1,1'-methylenebis[4-isocyanato-

[a]Reaction conditions: 0.5 mg model, catalyst-to-feed ratio of 5 to 1, 550 °C with a helium flow of 205 mL/min and a pyrolysis time of 10 seconds

Table S5.5.7. Identified products from the thermal decomposition of model **2** catalyzed by Puralox SCCa 5/200

#	Area integration[a] (%)	Match (%)	ID
1	4.96	80	Acetaldehyde
2	5.01	87	Ethanol
3	2.76	90	Ethyl ether
4	0.0727	38	Tetrahydro-4H-pyran-4-ol
5	0.102	64	Benzene
6	42.56	95	Aniline
7	16.5	95	Toluidine
8	5.57	97	Benzenamine, N-ethyl-
9	0.762	81	Pyridine, 3-ethyl-5-methyl-
10	1.40	96	Benzenamine, 3,4-dimethyl-
11	0.447	70	1H-Indole, 2,3-dihydro-1,2-dimethyl-
12	2.42	96	N-Ethyl-p-toluidine
13	0.222	70	Benzenamine, N-ethyl-3-methyl-
14	0.308	94	Quinoline
15	0.338	83	Isoquinoline
16	0.104	83	Benzenamine, N,N-diethyl-4-methyl-
17	0.469	70	Quinoline, 2-methyl-
18	0.107	95	Quinoline, 8-methyl-
19	0.0664	38	Quinoline, 3-methyl-
20	0.0896	41	Formamide, N-(2-acetylphenyl)-
21	0.212	96	Quinoline, 2,7-dimethyl-
22	0.0242	30	Quinoline, 5,8-dimethyl-
23	0.0221	64	Quinoline, 3-ethyl-
24	0.100	43	Quinoline, 2,7-dimethyl-
25	0.0622	49	3,5-Dimethyl-4-phenylpyridine
26	1.14	97	Acridine
27	2.24	83	Acridine, 9-methyl-
28	0.144	78	1H-Indole, 1-methyl-2-phenyl-
29	0.157	38	2,2-Diphenylpropionitrile
30	0.0464	78	1H-Indole, 1-methyl-2-phenyl-
31	10.9	99	Benzenamine, 4,4'-methylenebis-
32	0.710	72	1-Ethyl-4-methoxy-9H-pyrido[3,4-b]indole
33	0.0927	78	Benzenamine, 4,4'-methylenebis[N,N-dimethyl-

[a]Reaction conditions: 0.5 mg model, catalyst-to-feed ratio of 5 to 1, 550 °C with a helium flow of 205 mL/min and a pyrolysis time of 10 seconds

Table S5.5.8 Catalytic pyrolysis results of model **1** with and without a catalyst, calculated on aromatic mol% according to equation 5.1

Mode[a,b]	Aniline	Toluidine	MDA[c]	N-others[e]
Thermal	0.00	0.00	3.44[d]	0.00
Catalytic	36.8	5.3	0.00	4.50

[a]Reaction conditions: 0.5 mg model, catalyst-to-feed ratio of 5 to 1, 550 °C with a helium flow of 205 mL/min and a pyrolysis time of 10 seconds

[b]Average of 2 measurements

[c]4,4-MDA and 4,2-MDA isomers were observed during pyrolysis and grouped

[d]MDI was formed instead of MDA

[e]Depicted yields are calibrated on indole as reference compound, and the molecular mass of acridine has been used for the yield calculation

Table S5.5.9. Catalytic pyrolysis results of model **2** with and without a catalyst, calculated on aromatic mol% according to equation 5.1

Mode[a,b]	Aniline	Toluidine	MDA[c]	N-others[e]
Thermal	0.00	0.00	20.2[d]	0.0400
Catalytic	30.5	9.69	2.62	8.90

[a]Reaction conditions: 0.5 mg model, catalyst-to-feed ratio of 5 to 1, 550 °C with a helium flow of 205 mL/min and a pyrolysis time of 10 seconds

[b]Average of 2 measurements

[c]4,4-MDA and 4,2-MDA isomers were observed during pyrolysis and grouped

[d]MDI was formed instead of MDA

[e]Depicted yields are calibrated on indole as reference compound and the molecular mass of acridine has been used for the yield calculation

DTF calculation details

All quantum chemical calculations were carried out using density functional theory (DFT). Geometry optimizations of all reactants, intermediates, and products were performed without symmetry constraints using the B3LYP functional together with the 6-311++G(d,p) basis set. Frequency calculations were subsequently carried out at the same level of theory to confirm that the optimized structures correspond to true minima on the potential energy surface (no imaginary frequencies). Thermal corrections to 298.15 K were included where relevant. Solvent effects were neglected unless otherwise stated, and all calculations were performed in the gas phase. Bond dissociation energies (BDEs) were calculated from the electronic energies of the optimized species according to: BDE(AB) = E0(A) + E0(B) – E0(AB) where (E) represents the total electronic energy including zero-point energy corrections obtained from vibrational frequency calculations.

Labelling interpretation

Identification of label incorporation was performed via two steps. In the first step, the molecular ion peak (M) as well as the M+X were established for each molecule of interest. The M/M+X ratio was used to quantify the amount of labelling. In the second step, the fragmentation pattern of each molecule was investigated to determine the label's location. Each experiment has been performed in duplicate to ensure data accuracy, and the fragment structures have been confirmed in the literature to verify the correct interpretation of the fragmentation patterns. Calculation details for the ratios and MS intensity values of each experiment are provided in sections 5.3, equation 5.1.

Quantification and location of labels

The mass peak (*M*) was used to identify label incorporation, and the first fragmentation peak following the main peak was investigated to determine the label's location. For example, aniline has a fragmentation pattern at m/z *93*, 66, and 39, with m/z *93* corresponding to the molecular mass peak. Deuterium has a m/z 2, so if a proton were exchanged for a deuterium atom, the corresponding mass would be *M*+1, for two deuterium atoms, *M*+2, etc. For the identification of scrambling, the MS intensity of the *93* peak has been summed with the MS intensities of m/z 94 – 99 (1x – 6x deuterium) and normalized to 1 to allow comparison with the non-deuterated model.

The non-deuterated model (**1.**) is used as a reference to indicate if the target molecule is deuterated or not. E.g., for aniline, the *M* peak (m/z *93*) accounts for 0.92 and the M+1 (m/z 94) for 0.08. The m/z 94 peak (0.08) is assigned to the combined natural abundances of ^{13}C (1.1%), ^{2}H (0.015%), and ^{15}N (0.36%). Subsequently, all deuterated model compounds have been compared to these values to identify the presence of deuterium after the reaction.

Aniline has a typical fragmentation pattern of m/z *93*, 66, 39. The 93 peak has been summed to its M+X peaks and normalized to 1. This approach has also been applied for the second central peak (m/z 66). Subsequently, the ratios have been compared to the m/z *93* pattern to identify the location of the labelled atom. For toluidine, the fragmentation pattern is m/z *107,* 77, 52. Here, the peaks for m/z *107* and 77 have been investigated.

Fragmentation patterns of propene, acetone, and MDA formed by *i*PrOH-D_0, Bridge-D_2, and *i*PrOH-D_{14}

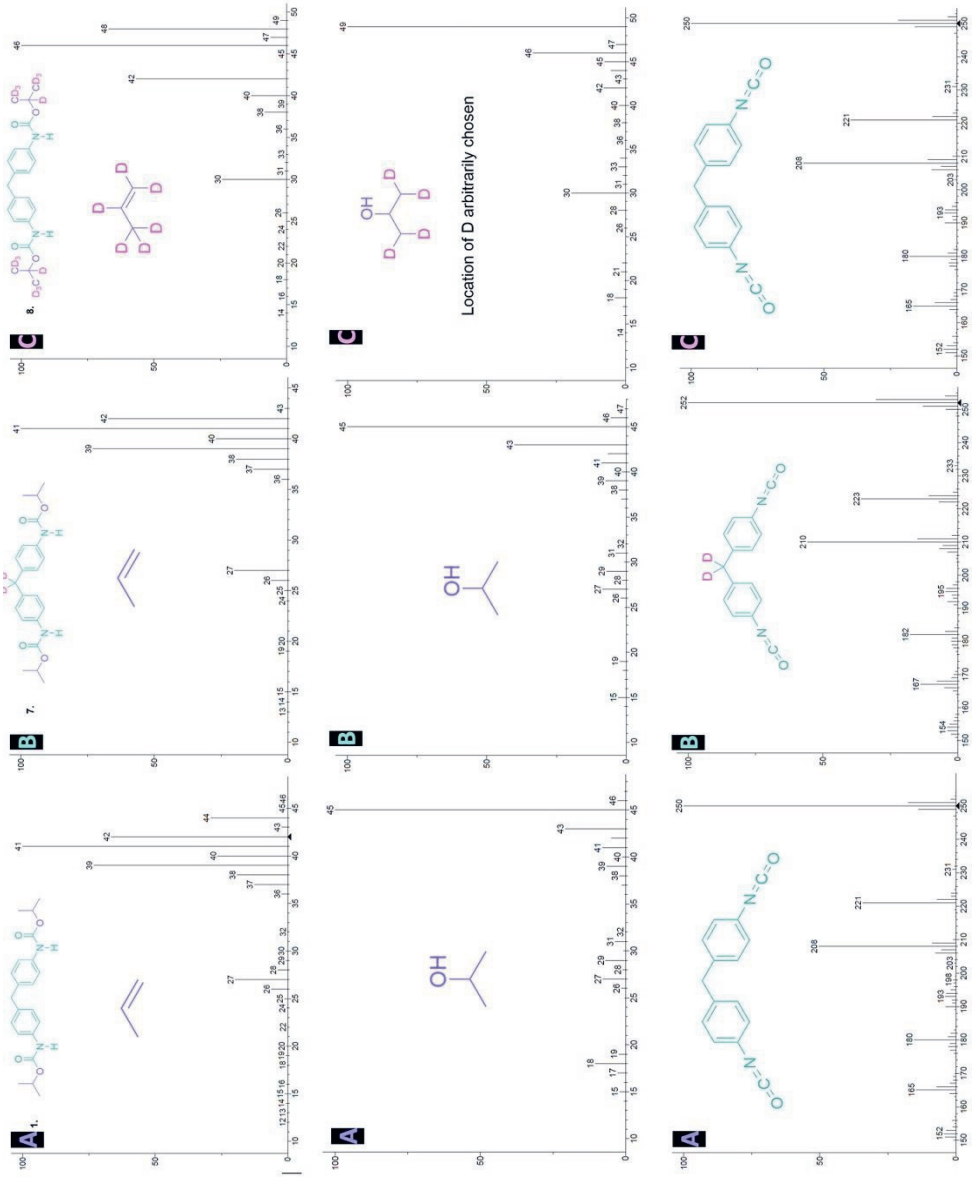

Figure S5.5.24. GC-MS fragmentation patterns of: propene, isopropanol, and Methylene diphenyl diisocyanate (MDI) formed from the non-catalytic pyrolysis of: A) model 1 (MDI + IPA), B) model 7 (MDI-D_2 + IPA), and C) Model 8 (MDI + IPA-D_{14})

MS intensity data

Non-deuterated model 1. and deuterated models 3. 5. 7. 8.

Table S5.5.10. MS integration intensities of model **1:** non-deuterated (top), non-deuterated duplicate (middle), and average value that is used for ratio calculations (bottom)

Molecule (M)	M	M+1	M+2	M+3	M+4	M+5	M+6
Propene (42)	47	1.0	15	0.1	0.1		
Acetone (58)	31	1.8	0.2				
Aniline (93)	100	8.0	0.2				
Toluidine (106)	100	68	5.0	0.2			
Acridine (179)	100	15	1.0	0.1	0.1		
Methylacridine (193)	100	16	2	0.3	0.8	0.3	0.3
Molecule (M)	**M**	**M+1**	**M+2**	**M+3**	**M+4**	**M+5**	**M+6**
Propene (42)	66	2.3	0.6				
Acetone (58)	30	1.0					
Aniline (93)	100	9.0	0.4				
Toluidine (106)	100	70	6.0	0.2			
Acridine (179)	100	14	1.0				
Methylacridine (193)	100	19	1.7				
Molecule (M)	**M**	**M+1**	**M+2**	**M+3**	**M+4**	**M+5**	**M+6**
Propene (42)	57	1.7	7.8	0.1	0.1	0.0	0.0
Acetone (58)	31	1.4	0.1	0.0	0.0	0.0	0.0
Aniline (93)	100	8.5	0.3	0.0	0.0	0.0	0.0
Toluidine (106)	100	69	6	0.2	0.0	0.0	0.0
Acridine (179)	100	15	1.0	0.1	0.1	0.0	0.0
Methylacridine (193)	100	18	1.9	0.2	0.4	0.2	0.2

Table S5.5.11.MS integration intensities of model **3:** 2D amine (top), 2D amine duplicate (middle), and average value that is used for ratio calculations (bottom)

Molecule (M)	M	M+1	M+2	M+3	M+4	M+5	M+6
Propene (42)	67	2.8	4.0				
Acetone (58)	28	5.0	0.6				
Aniline (93)	100	31.0	4.0	0.3			
Toluidine (106)	100	90	23	3.2	0.3		
Acridine (179)	100	43	8.0	1.2			
Methylacridine (193)	48	46	21	8	2.5	1.9	
Molecule (M)	**M**	**M+1**	**M+2**	**M+3**	**M+4**	**M+5**	**M+6**
Propene (42)	67	3.2	3				
Acetone (58)	25	7.0	1.1				
Aniline (93)	100	44.0	8.0	1.0			
Toluidine (106)	100	98	31	5.0	0.7		
Acridine (179)	100	59	17.0	3.1	0.5		
Methylacridine (193)	100	65	21	4	1.8		
Molecule (M)	**M**	**M+1**	**M+2**	**M+3**	**M+4**	**M+5**	**M+6**
Propene (42)	67	3.0	3.3	0.0	0.0	0.0	0.0
Acetone (58)	27	6.0	0.9	0.0	0.0	0.0	0.0

Aniline (93)	100	38	6.0	0.7	0.0	0.0	0.0
Toluidine (106)	100	94	27	4.1	0.5	0.0	0.0
Acridine (179)	100	51	13	2.2	0.3	0.0	0.0
Methylacridine (193)	74	56	21	6.0	2.2	1.0	0.0

Table S5.5.12. MS integration intensities of model **5:** 12D (top), 12D duplicate (middle), and average value that is used for ratio calculations (bottom)

Molecule (M)	**M**	**M+1**	**M+2**	**M+3**	**M+4**	**M+5**	**M+6**	**M+7**
Propene (42)	61	34	0.0	100	61	85	3.6	0.0
Acetone (58)	17	21	15	10	7.0	6.0	5.0	0.2
Aniline (93)	100	63	17	2.9	0.3			
Toluidine (106)	81	100	47	12	2.0			
Acridine (179)	100	77	29	7.0	1.3			
Methylacridine (193)	100	75	36	10.8	4.00	2.3	1.8	
Molecule (M)	**M**	**M+1**	**M+2**	**M+3**	**M+4**	**M+5**	**M+6**	**M7**
Propene (42)	61	31	0.0	100	63	87	3.6	0.1
Acetone (58)	17	21	16	10	8	7	9	0.5
Aniline (93)	100	79	27	5	0.7			
Toluidine (106)	74	100	53	15	3.0			
Acridine (179)	100	83	46	12	2.9	0.9		
Methylacridine (193)	66	60	33	13	6	5	1.8	
Molecule (M)	**M**	**M+1**	**M+2**	**M+3**	**M+4**	**M+5**	**M+6**	**M+7**
Propene (42)	61	33	0.0	100	62	86	3.6	0.1
Acetone (58)	17	21	16	10	7.5	6.5	7.0	0.4
Aniline (93)	100	71	22	4.0	0.5	0.0	0.0	0.0
Toluidine (106)	78	100	50	14	2.5	0.0	0.0	0.0
Acridine (179)	100	80	38	10	2.1	0.5	0.0	0.0
Methylacridine (193)	83	68	35	12	5.0	3.7	1.8	0.0

Table S5.5.13. MS integration intensities of model **7:** 14D (top), 14D duplicate (middle), and average value that is used for ratio calculations (bottom)

Molecule (M)	**M**	**M+1**	**M+2**	**M+3**	**M+4**	**M+5**	**M+6**	**M+7**
Propene (42)	64	5.0	0.0	8.0	100	12	66	2.2
Acetone (58)	11	18	15	11	10	12	18	1.2
Aniline (93)	86	100	54	14	3.0			
Toluidine (106)	54	100	82	38	10	2.2		
Acridine (179)	86	100	59	18	6.0	0.5		
Methylacridine (193)	89	100	64	27	8.0	2.00	0.3	
Molecule (M)	**M**	**M+1**	**M+2**	**M+3**	**M+4**	**M+5**	**M+6**	**M7**
Propene (42)	63	5.0	0.0	1.8	100	11	68	1.0
Acetone (58)	100	61	45	1.1	0.7			
Aniline (93)	88	100	52	13	2.5	0.2		
Toluidine (106)	56	100	82	39	11	2.3	0.2	
Acridine (179)	100	60	23	6.0	0.8			
Methylacridine (193)	83	100	68	31	10	2.9	0.8	
Molecule (M)	**M**	**M+1**	**M+2**	**M+3**	**M+4**	**M+5**	**M+6**	**M7**

Propene (42)	64	5.0	0.0	4.9	100	12	67	1.6
Acetone (58)	56	40	30	6.1	5.4	6.0	9.0	0.6
Aniline (93)	87	100	53	14	2.8	0.1	0.0	0.0
Toluidine (106)	55	100	82	39	11	2.3	0.1	0.0
Acridine (179)	93	80	41	12	3.4	0.3	0.0	0.0
Methylacridine (193)	86	100	66	29	9.0	2.5	0.6	0.0

Table S5.5.14. MS integration intensities of model **7:** 2D bridge (top), 2D bridge duplicate (middle), and average value that is used for ratio calculations (bottom)

Molecule (M)	**M**	**M+1**	**M+2**	**M+3**	**M+4**	**M+5**	**M+6**
Propene (42)	66	0.3	0.5				
Acetone (58)	31	2.2					
Aniline (93)	100	26	3.6	0.1			
Toluidine (106)	28	100	94	59	19	3.0	0.3
Acridine (179)	100	74	24	5.0	1.6	0.9	0.9
Methylacridine (193)	81	100	79	38	12	2.1	0.3
Molecule (M)	**M**	**M+1**	**M+2**	**M+3**	**M+4**	**M+5**	**M+6**
Propene (42)	66	3.2	5.0				
Acetone (58)	32	1.7					
Aniline (93)	100	30	4.0	0.5			
Toluidine (106)	36	100	87	51	14	2.00	
Acridine (179)	100	64	18	3.8	0.6	0.24	1.8
Methylacridine (193)	81	100	79	38	12	2.1	0.2
Molecule (M)	**M**	**M+1**	**M+2**	**M+3**	**M+4**	**M+5**	**M+6**
Propene (42)	66	1.8	2.75	0.0	0.0	0.0	0.0
Acetone (58)	32	2.0	0.0	0.0	0.0	0.0	0.0
Aniline (93)	100	28	3.8	0.3	0.0	0.0	0.0
Toluidine (106)	32	100	91	55	17	2.5	0.2
Acridine (179)	100	69	21	4.4	1.1	0.57	1.4
Methylacridine (193)	81	100	79	38	12	2.1	0.3

^{12}C non-labelled model 2. and carbon-13 models 4. And 6.

Table S5.5.15. MS integration intensities of model **2:** ^{12}C (top), ^{12}C duplicate (middle), and average value that is used for ratio calculations (bottom)

Molecule (M)	**M**	**M+1**	**M+2**	**M+3**	**M+4**	**M+5**	**M+6**
Acetaldehyde (44)	81	1.9	0.2				
Diethylether (74)	63	2.8	0.2				
Aniline (93)	100	14	0.8				
Toluidine (106)	100	72	8	0.4			
Ethylaniline (121)	39	4.0	0.2				
Ethyltoluidine (135)	40	5.0	0.3				
Acridine (179)	10	14	1.2				
Methylacridine (193)	100	15	1.2				
Molecule (M)	**M**	**M+1**	**M+2**	**M+3**	**M+4**	**M+5**	**M+6**
Acetaldehyde (44)	87	1.9	0.2				

Diethylether (74)	66	3.0	0.2				
Aniline (93)	100	8.0	0.2				
Toluidine (106)	100	68	5	0.2			
Ethylaniline (121)	37	3.7	0.1				
Ethyltoluidine (135)	38	4.0					
Acridine (179)	100	15	1.3	0.4			
Methylacridine (193)	100	15	1.2				
Molecule (M)	**M**	**M+1**	**M+2**	**M+3**	**M+4**	**M+5**	**M+6**
Acetaldehyde (44)	84	1.9	0.2	0.0	0.0	0.0	0.0
Diethylether (74)	65	2.9	0.2	0.0	0.0	0.0	0.0
Aniline (93)	100	11	0.5	0.0	0.0	0.0	0.0
Toluidine (106)	100	70	7	0.3	0.0	0.0	0.0
Ethylaniline (121)	38	3.9	0.2	0.0	0.0	0.0	0.0
Ethyltoluidine (135)	39	4.5	0.2	0.0	0.0	0.0	0.0
Acridine (179)	55	15	1.3	0.2	0.0	0.0	0.0
Methylacridine (193)	100	15	1.2	0.0	0.0	0.0	0.0

Table S5.5.16. MS integration intensities of model **4:** ^{13}C polyol (top), ^{13}C polyol duplicate (middle), and average value that is used for ratio calculations (bottom)

Molecule (M)	**M**	**M+1**	**M+2**	**M+3**	**M+4**	**M+5**	**M+6**
Acetaldehyde (44)	100	6.0					
Diethylether (74)	0.0	10	67	1.8			
Aniline (93)	100	8.0	0.3				
Toluidine (106)	100	70	6	0.2			
Ethylaniline (121)	7.0	37	3.3				
Ethyltoluidine (135)	9.0	44	4.0				
Acridine (179)	100	16	1.6	0.2			
Methylacridine (193)	100	17	1.6				
Molecule (M)	**M**	**M+1**	**M+2**	**M+3**	**M+4**	**M+5**	**M+6**
Acetaldehyde (44)	100	6.0					
Diethylether (74)	0.0	10	68	1.7			
Aniline (93)	100	8.0	0.3				
Toluidine (106)	100	70	6	0.2			
Ethylaniline (121)	8.0	37	3.3				
Ethyltoluidine (135)	10	52	4.0	0.2			
Acridine (179)	100	16	1.5	0.2			
Methylacridine (193)	100	17	1.6	0.2			
Molecule (M)	**M**	**M+1**	**M+2**	**M+3**	**M+4**	**M+5**	**M+6**
Acetaldehyde (44)	100	6.0	0.0	0.0	0.0	0.0	0.0
Diethylether (74)	0.0	10	68	1.8	0.0	0.0	0.0
Aniline (93)	100	8.0	0.3	0.0	0.0	0.0	0.0
Toluidine (106)	100	70	6	0.2	0.0	0.0	0.0
Ethylaniline (121)	7.5	37	3.3	0.0	0.0	0.0	0.0
Ethyltoluidine (135)	10	48	4.0	0.1	0.0	0.0	0.0
Acridine (179)	100	16	1.6	0.2	0.0	0.0	0.0
Methylacridine (193)	100	17	1.6	0.1	0.0	0.0	0.0

Table S5.5.17. MS integration intensities of model **6.:** ^{13}C bridge (top), ^{13}C bridge duplicate (middle), and average value that is used for ratio calculations (bottom)

Molecule (M)	**M**	**M+1**	**M+2**	**M+3**	**M+4**	**M+5**	**M+6**
Acetaldehyde (44)	28	1.2					
Diethylether (74)	68	3.4	0.25	0.5			
Aniline (93)	100	8.0	0.1				
Toluidine (106)	0.0	100	70	5.0			
Ethylaniline (121)	39	3.7					
Ethyltoluidine (135)	7.0	39	3.8				
Acridine (179)	28	100	14	1.5	0.9	0.6	
Methylacridine (193)	21	46	100	14	1.2	0.6	0.6
Molecule (M)	**M**	**M+1**	**M+2**	**M+3**	**M+4**	**M+5**	**M+6**
Acetaldehyde (44)	85	3.1					
Diethylether (74)	68	3.1					
Aniline (93)	100	8.0	0.3				
Toluidine (106)	0.0	100	68	4.0			
Ethylaniline (121)	38	3.9	0.2				
Ethyltoluidine (135)	8.0	39	3.8				
Acridine (179)	28	100	14	1.5	0.7	0.6	
Methylacridine (193)	21	47	100	13	1.1		
Molecule (M)	**M**	**M+1**	**M+2**	**M+3**	**M+4**	**M+5**	**M+6**
Acetaldehyde (44)	57	2.2	0.0	0.0	0.0	0.0	0.0
Diethylether (74)	68	3.3	0.1	0.3	0.0	0.0	0.0
Aniline (93)	100	8.0	0.2	0.0	0.0	0.0	0.0
Toluidine (106)	0.0	100	69	5	0.0	0.0	0.0
Ethylaniline (121)	39	3.8	0.1	0.0	0.0	0.0	0.0
Ethyltoluidine (135)	7.5	39	3.8	0.0	0.0	0.0	0.0
Acridine (179)	28	100	14	1.5	0.8	0.6	0.0
Methylacridine (193)	21	46	100	14	1.2	0.6	0.6

Calculated ratios per target molecule based on MS intensities
Non-deuterated model 1. and deuterated models 3. 5. 7. 8.

Table S5.5.18. MS integration intensities of **propene** with compound mass (**44**)

Mass	**42**	**43**	**44**	**45**	**46**	**47**
*i*PrOH-D_0 (**1.**)	86	2	12	0	0	0
Amine D_2 (**3.**)	91	4	4	0	0	0
Bridge-D_2 (**7.**)	94	2	4	0	0	0
*i*PrOH-D_{12} (**5.**)	18	9	0	29	18	25
*i*PrOH-D_{14} (**8.**)	25	2	0	2	39	5
Mass	**48**	**49**				
*i*PrOH-D_0 (**1.**)	0	0				
Amine D_2 (**3.**)	0	0				
Bridge-D_2 (**7.**)	0	0				
*i*PrOH-D_{12} (**5.**)	1	0				
*i*PrOH-D_{14} (**8.**)	26	1				

Table S5.5.19. MS integration intensities of **acetone** with compound mass (**58**)

Mass	58	59	60	61	62	63
*i*PrOH-D_0 (**1.**)	95	4	0	0	0	0
Amine D_2 (**3.**)	79	18	3	0	0	0
Bridge-D_2 (**7.**)	94	6	0	0	0	0
*i*PrOH-D_{12} (**5.**)	20	25	18	12	9	8
*i*PrOH-D_{14} (**8.**)	37	26	20	4	4	4
Mass	**64**	**65**				
*i*PrOH-D_0 (**1.**)	0	0				
Amine D_2 (**3.**)	0	0				
Bridge-D_2 (**7.**)	0	0				
*i*PrOH-D_{12} (**5.**)	8	0				
*i*PrOH-D_{14} (**8.**)	6	0				

Table S5.5.20.MS integration intensities of **aniline** with compound mass (**93**) top, and first fragmentation mass (**66**) bottom

Mass	93	94	95	96	97
*i*PrOH-D_0 (**1.**)	92	08	0	0	0
Amine D_2 (**3.**)	69	26	4	0	0
Bridge-D_2 (**7.**)	76	21	3	0	0
*i*PrOH-D_{12} (**5.**)	51	36	11	2	0
*i*PrOH-D_{14} (**8.**)	34	39	21	5	0
Mass	**66**	**67**	**68**	**69**	**70**
*i*PrOH-D_0 (**1.**)	88	12	0	0	0
Amine D_2 (**3.**)	72	24	4	0	0
Bridge-D_2 (**7.**)	76	21	3	0	0
*i*PrOH-D_{12} (**5.**)	56	33	9	2	0
*i*PrOH-D_{14} (**8.**)	45	37	14	4	1

Table S5.5.21. MS integration intensities of **Toluidine** with compound mass (**107**) top, and first fragmentation mass (**77**) bottom

Mass	106	107	108	109	110	111	112
*i*PrOH-D_0 (**1.**)	57	39	3	0	0	0	0
Amine D_2 (**3.**)	44	42	12	2	0	0	0
Bridge-D_2 (**7.**)	11	34	31	19	6	1	0
*i*PrOH-D_{12} (**5.**)	32	41	21	6	1	0	0
*i*PrOH-D_{14} (**8.**)	19	35	28	13	4	1	0
Mass	**77**	**78**	**79**	**80**	**81**	**82**	
*i*PrOH-D_0 (**1.**)	43	15	24	15	2	0	
Amine D_2 (**3.**)	36	20	22	17	5	0	
Bridge-D_2 (**7.**)	21	24	22	20	13	0	
*i*PrOH-D_{12} (**5.**)	29	23	22	18	7	0	
*i*PrOH-D_{14} (**8.**)	23	25	22	19	11	0	

Table S5.5.22. MS integration intensities of **Acridine** with compound mass (**179**) top, and first fragmentation mass (**152**) bottom

Mass	179	180	181	182	183	184	185

*i*PrOH-D_0 (**1.**)	87	13	1	0	0	0	0
Amine D_2 (**3.**)	60	31	8	1	0	0	0
Bridge-D_2 (**7.**)	51	35	11	2	1	0	1
*i*PrOH-D_{12} (**5.**)	44	35	16	4	1	0	0
*i*PrOH-D_{14} (**8.**)	40	35	18	5	1	0	0
Mass	**152**	**153**	**154**	**155**	**156**	**157**	
*i*PrOH-D_0 (**1.**)	66	31	3	0	0	0	
Amine D_2 (**3.**)	53	33	12	2	0	0	
Bridge-D_2 (**7.**)	48	34	14	4	1	0	
*i*PrOH-D_{12} (**5.**)	44	35	16	5	1	0	
*i*PrOH-D_{14} (**8.**)	37	35	18	8	2	0	

Table S5.5.23.MS integration intensities of **Methylacridine** with compound mass (**193**) top, first fragmentation mass (**179**) middle, and second fragmentation mass (**152**) bottom

Mass	**193**	**194**	**195**	**196**	**197**	**198**	**199**	**200**
*i*PrOH-D_0 (**1.**)	83	15	2	0	0	0	0	0
Amine D_2 (**3.**)	46	35	13	4	1	1	0	0
Bridge-D_2 (**7.**)	26	32	25	12	4	1	0	0
*i*PrOH-D_{12} (**5.**)	40	33	17	6	2	2	1	0
*i*PrOH-D_{14} (**8.**)	29	34	23	10	3	1	0	0
Mass	**179**	**180**	**181**	**182**	**183**	**184**		
*i*PrOH-D_0 (**1.**)	83	14	2	0	1	0		
Amine D_2 (**3.**)	58	31	8	3	0	0		
Bridge-D_2 (**7.**)	49	30	9	5	7	0		
*i*PrOH-D_{12} (**5.**)	40	32	16	7	3	2		
*i*PrOH-D_{14} (**8.**)	31	32	21	11	5	1		
Mass	**152**	**153**	**154**	**155**	**156**	**157**		
*i*PrOH-D_0 (**1.**)	57	20	11	10	2	0		
Amine D_2 (**3.**)	43	29	17	11	0	0		
Bridge-D_2 (**7.**)	35	28	20	13	3	1		
*i*PrOH-D_{12} (**5.**)	34	26	20	12	9	0		
*i*PrOH-D_{14} (**8.**)	34	30	21	11	3	0		

^{12}C non-labelled model 2. and carbon-13 models 4., and 6.

Table S5.5.24. MS integration intensities of **Acetaldehyde** with compound mass (**44**)

Mass	**44**	**45**	**46**	**47**	**48**	**49**	**50**
Ref ^{12}C (**2.**)	98	2	0	0	0	0	0
Polyol ^{13}C (**4.**)	94	6	0	0	0	0	0
Carbamate ^{13}C (**6.**)	96	4	0	0	0	0	0

Table S5.5.25. MS integration intensities of **Diethylether** with compound mass (**74**)

Mass	**74**	**75**	**76**	**77**	**78**	**79**	**80**
Ref ^{12}C (**2.**)	95	4	0	0	0	0	0
Polyol ^{13}C (**4.**)	0	13	85	2	0	0	0
Carbamate ^{13}C (**6.**)	95	5	0	0	0	0	0

Table S5.5.26. MS integration intensities of **Aniline** with compound mass (**93**)

Mass	93	94	95	96	97	98	99
Ref ^{12}C (**2.**)	90	10	0	0	0	0	0
Polyol ^{13}C (**4.**)	92	7	0	0	0	0	0
Carbamate ^{13}C (**6.**)	93	7	0	0	0	0	0

Table S5.5.27. MS integration intensities of **Toluidine** with compound mass (**106**)

Mass	106	107	108	109	110	111	112
Ref ^{12}C (**2.**)	57	40	4	0	0	0	0
Polyol ^{13}C (**4.**)	57	40	3	0	0	0	0
Carbamate ^{13}C (**6.**)	0	58	40	3	0	0	0

Table S5.5.28. MS integration intensities of **Ethylaniline** with compound mass (**121**)

Mass	121	122	123	124	125	126	127
Ref ^{12}C (**2.**)	90	9	0	0	0	0	0
Polyol ^{13}C (**4.**)	16	77	7	0	0	0	0
Carbamate ^{13}C (**6.**)	91	9	0	0	0	0	0

Table S5.5.29. MS integration intensities of **Ethyltoluidine** with compound mass (**135**)

Mass	135	136	137	138	139	140	141
Ref ^{12}C (**2.**)	89	10	0	0	0	0	0
Polyol ^{13}C (**4.**)	15	78	6	0	0	0	0
Carbamate ^{13}C (**6.**)	15	78	8	0	0	0	0

Table S5.5.30. MS integration intensities of **Acridine** with compound mass (**179**)

Mass	179	180	181	182	183	184	185
Ref ^{12}C (**2.**)	78	20	2	0	0	0	0
Polyol ^{13}C (**4.**)	85	14	1	0	0	0	0
Carbamate ^{13}C (**6.**)	19	69	10	1	1	0	0

Table S5.5.31. MS integration intensities of **Methylacridine** with compound mass (**193**)

Mass	193	194	195	196	197	198	199
Ref ^{12}C (**2.**)	86	13	1	0	0	0	0
Polyol ^{13}C (**4.**)	84	14	1	0	0	0	0
Carbamate ^{13}C (**6.**)	11	25	55	7	1	0	0

References

1. Voorhees, K. J. Mechanisms of Pyrolysis for a Specifically Labeled Deuterated Urethane. *J. Polym. Sci., Polym. Chem. Ed.* **20**, 1457–1467 (1982).
2. Yang, W. P., Macosko, C. W. & Wellinghoff, S. T. Thermal degradation of urethanes based on 4,4'-diphenylmethane diisocyanate and 1,4-butanediol (M DI/B DO). *Polymer (Guildf)* **27**, 1235–1240 (1986).
3. Lattimer, R. P., Muenster, H. & Budzikiewicz, H. PYROLYSIS TANDEM MASS SPECTROMETRY (Py-MS/MS) OF A SEGMENTED POLYURETHANE. *J Anal Appl Pyrolysis* **17**, 237–249 (1990).
4. Esperanza, M. M., García, A. N., Font, R. & Conesa, J. A. Pyrolysis of varnish wastes based on a polyurethane. *J Anal Appl Pyrolysis* **52**, 151–166 (1999).
5. Shieh, Y.-T., Chen, H.-T., Liu, K.-H. & Twu, Y.-K. Thermal Degradation of MDI-Based Segmented Polyurethanes. *J Polym Sci A: Polym Chem* **37**, 4126–4134 (1999).
6. Font, R., Fullana, A., Caballero, J. A., Candela, J. & García, A. Pyrolysis study of polyurethane. *J Anal Appl Pyrolysis* **58–59**, 63–77 (2001).
7. Herrera, M., Matuschek, G. & Kettrup, A. Thermal degradation of thermoplastic polyurethane elastomers (TPU) based on MDI. *Polym. Degrad. Stabil.* **78**, 323–331 (2002).
8. Pielichowski, K., Kulesza, K. & Pearce, E. M. Thermal Degradation Studies on Rigid Polyurethane Foams Blown with Pentane. *J. Appl. Polym. Sci.* **88**, 2319–2330 (2003).
9. Pielichowski, K. & Slotwinska, D. Flame-resistant modified segmented polyurethanes with 3-chloro-1,2- propanediol in the main chain - Thermoanalytical studies. *Thermochim Acta* **410**, 79–86 (2004).
10. Rosu, D., Tudorachi, N. & Rosu, L. Investigations on the thermal stability of a MDI based polyurethane elastomer. *J Anal Appl Pyrolysis* **89**, 152–158 (2010).
11. Jiao, L., Xiao, H., Wang, Q. & Sun, J. Thermal degradation characteristics of rigid polyurethane foam and the volatile products analysis with TG-FTIR-MS. *Polym Degrad Stab* **98**, 2687–2696 (2013).
12. Pagacz, J. *et al.* Polyurethane foams chemically reinforced with POSS—Thermal degradation studies. *Thermochim Acta* **642**, 95–104 (2016).
13. Jiang, L. *et al.* Pyrolytic behavior of waste extruded polystyrene and rigid polyurethane by multi kinetics methods and Py-GC/MS. *Fuel* **222**, 11–20 (2018).
14. Stančin, H. *et al.* Experimental analysis of waste polyurethane from household appliances and its utilization possibilities. *J Environ Manage* **243**, 105–115 (2019).
15. Li, M., Jiang, L., He, J. J. & Sun, J. H. Kinetic triplet determination and modified mechanism function construction for thermo-oxidative degradation of waste polyurethane foam using conventional methods and distributed activation energy model method. *Energy* **175**, 1–13 (2019).
16. Yao, Z. *et al.* Probing the combustion and pyrolysis behaviors of polyurethane foam from waste refrigerators. *J Therm Anal Calorim* **141**, 1137–1148 (2020).
17. Nishiyama, Y. *et al.* Temperature-dependent pyrolysis behavior of polyurethane elastomers with different hard- and soft-segment compositions. *J Anal Appl Pyrolysis* **145**, (2020).
18. Zeller, M. *et al.* Thermogravimetric studies, kinetic modeling and product analysis of the pyrolysis of model polymers for technical polyurethane applications. *J Anal Appl Pyrolysis* **171**, (2023).

19. Xu, S. *et al.* Insight into waste polyurethane pyrolysis pathways: Mechanism functions analysis and in-situ coupling online monitoring. *J Anal Appl Pyrolysis* **177**, (2024).
20. Takamoto, D. Y. & Petrich, M. A. Effect of Heterogeneous Secondary Pyrolysis Reactions on the Thermal Decomposition of Polyurethane Scrap. *Ind. Eng. Chem. Res* **33**, 3004–3009 (1994).
21. Moroi, G. & Ciobanu, C. Aspects of polyesterurethane interaction with metallic ions. III. Thermal behavior of polyurethane interaction products with iron and chromium ions. *J. Anal. Appl. Pyrolysis* **70**, (2003).
22. Moroi, G. Influence of ion species on the thermal degradation of polyurethane interaction products with transition metal ions. *J Anal Appl Pyrolysis* **71**, 485–500 (2004).
23. Bozi, J. & Blazsó, M. Catalytic thermal decomposition of polyamides and polyurethanes mixed with acidic zeolites. *J Anal Appl Pyrolysis* **97**, 189–197 (2012).
24. Bozi, J., Mihályi, M. R. & Blazsó, M. Study on temperature dependence of catalytic thermal decomposition of polyamides and polyurethanes mixed with acidic zeolites. *J Anal Appl Pyrolysis* **101**, 103–110 (2013).
25. Terakado, O., Yanase, H. & Hirasawa, M. Pyrolysis treatment of waste polyurethane foam in the presence of metallic compounds. *J Anal Appl Pyrolysis* **108**, 130–135 (2014).
26. Guo, X., Wang, L., Li, S., Tang, X. & Hao, J. Gasification of waste rigid polyurethane foam: optimizing operational conditions. *J Mater Cycles Waste Manag* **17**, 560–565 (2015).
27. Guo, X., Zhang, W., Wang, L. & Hao, J. Comparative study of nitrogen migration among the products from catalytic pyrolysis and gasification of waste rigid polyurethane foam. *J Anal Appl Pyrolysis* **120**, 144–153 (2016).
28. Yuan, Y. *et al.* Highly efficient catalysts for reducing toxic gases generation change with temperature of rigid polyurethane foam nanocomposites: A comparative investigation. *Compos Part A Appl Sci Manuf* **112**, 142–154 (2018).
29. Kumagai, S., Yabuki, R., Kameda, T., Saito, Y. & Yoshioka, T. Simultaneous recovery of H2-rich syngas and removal of HCN during pyrolytic recycling of polyurethane by Ni/Mg/Al catalysts. *Chemical Engineering Journal* **361**, 408–415 (2019).



6

Catalyst-structure-performance relations for the depolymerization of polyurethanes to aniline using amorphous silica alumina (ASA) catalysts

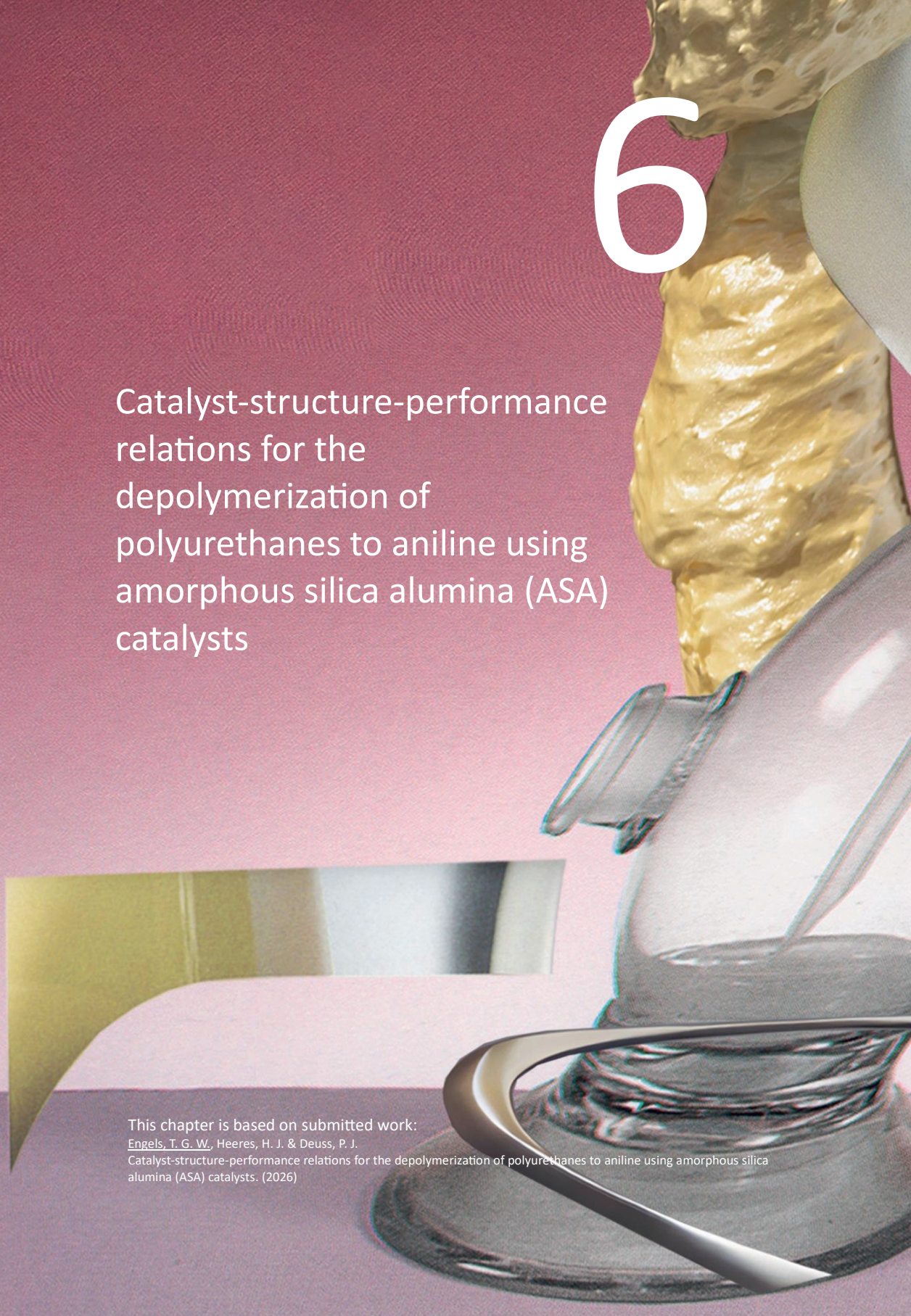

This chapter is based on submitted work:
Engels, T. G. W., Heeres, H. J. & Deuss, P. J.
Catalyst-structure-performance relations for the depolymerization of polyurethanes to aniline using amorphous silica alumina (ASA) catalysts. (2026)

Abstract

Polyurethanes are versatile, widely produced polymers that are, however, difficult to recycle. A possible approach involves the catalytic conversion of waste polyurethane to chemicals, from which new PUR can be synthesized, such as aniline. In this study, we report catalyst structure-performance relations for a set of eight amorphous silica-alumina catalysts used to convert polyurethanes into aniline, via in situ catalytic pyrolysis. Experiments were performed at a milligram scale in a tandem microreactor at 550 °C. The best results were obtained with a catalyst having a 95 to 5 alumina-to-silica ratio and a high-pore volume, yielding a combined aniline and toluidine yield of 36% based on nitrogen content in the feed. Catalyst-structure performance data showed a clear relationship between combined aniline and toluidine yield and the Brønsted/Lewis acidity ratio, along with catalyst pore width. Based on these findings, a catalyst mode of action is proposed in which the polyurethane undergoes Lewis acid-catalyzed retro-polymerization to a polyol and isocyanate group, followed by cracking of the methylene bridge of 4,4'-methylenedianiline (MDA), which is enhanced by the presence of Brønsted acidic sites in addition to the Lewis acid site. These findings will further guide the design and optimization of catalysts for polyurethane conversion to aniline as a recycling pathway.



6.1 Introduction

Polyurethanes (PUR) are used in everyday life products such as adhesives, coatings, shock absorbers, and insulators, among other applications.[1–4] However, polyurethane recycling is still in its infancy, and PUR waste is predominantly disposed of in landfills or incinerated (accounting for 75% of disposal).[5] Chemical recycling of PUR into monomeric building blocks is attracting significant interest at the moment.[6] Recent findings have shown that the polyol units in PUR may be recovered using glycolysis, as shown in Figure 6.1.[7] In contrast, recovering and reusing the isocyanate segment is more challenging, among other issues, due to downstream purification challenges. Polymeric methylenedianiline (pMDA) has been obtained in about 90% yield with 87% purity via ammonolysis at a 300 g h^{-1} scale.[8] It has been shown that the relevant product properties of PUR made with recovered pMDA differ from those of PUR made with virgin pMDA due to differences in quality. To overcome this issue and avoid excessive downstream processing, the conversion of the N-containing segment of PUR to aniline offers a more attractive approach. From aniline, virgin methylene diphenyl diisocyanate (MDI) can be synthesized as the isocyanate intermediate to produce PUR of the same quality as the original product.[9]

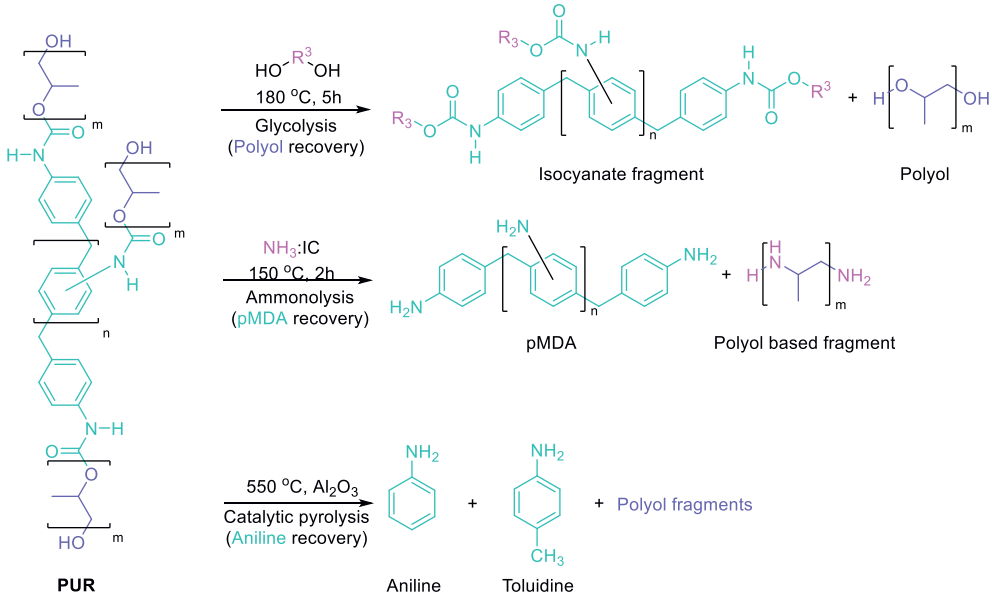

Figure 6.1. Chemical recycling options for PUR: polyol recovery (top) via Glycolysis by Shins et al. 2019 J. Appl. Polym. Sci., pMDA recovery via Ammonolysis by Van Belleghem et al 2025, JACS Au (middle), and aniline recovery via Catalytic pyrolysis by Engels *et al.* 2026 ChemRevxiv (bottom)

In previous work,[10] we demonstrated that aniline can be obtained from post-production rigid PUR foam based on pMDI (nPUR) with specific alumina catalysts, with yields up to 50% at the milligram scale (tandem microreactor (TMR)) at 550 ˚C. In addition, significant amounts of toluidine were formed, typically in a 3.5:1 aniline-to-toluidine ratio. The catalytic process was upscaled from batch milligram to continuous operation at 5 $kg_{feedstock}$ h^{-1}, achieving over 25 N% combined aniline and

toluidine yield (based on the calculated nitrogen content in the feed). Exploratory catalyst research on a range of alumina-based catalysts with varying properties showed that high surface area and high Lewis acidity achieved the highest combined aniline and toluidine yield. However, these alumina catalysts exhibit predominantly Lewis acidity, and the potential role of Brønsted acidity on catalyst performance was not explored. Bozi *et al.* [11] explored the influence of Brønsted acidity on the pyrolysis of PUR at 500 °C by using various zeolites. The group reported the formation of a wide range of N-containing aromatic compounds, though only limited amounts of aniline and toluidine were observed using catalysts with high Brønsted acidity. However, it was postulated that Brønsted sites are essential to promote methylene bridge cracking. For this reason, tuning the amount of Brønsted acidity may positively affect catalyst performance and, in turn, increase the yield of the desired N-containing products.

We here report a study on the use of amorphous silica-alumina (ASA) catalysts for the catalytic pyrolysis of PUR to aniline and toluidine. ASA's have a milder acidic character compared to zeolites, with Lewis acidity ranging from 174 – 410 µm/g and Brønsted acidity from 5 – 44 µm/g. Additionally, these catalysts lack the specific, well-defined micropore structure typically found in zeolites and are amorphous, with pores primarily in the meso range.[12,13] ASA catalysts have been used for various reactions, including hydrocracking, hydrotreating, dehydrogenation, isomerization, and alkylation.[14] Relevant catalyst properties (acidity, pore size distribution, surface area) may be tuned by, among other factors, the catalyst synthesis protocol, the silica-to-alumina ratio, and post-treatments. For example, it has been shown that lowering the alumina content typically increases surface area and acidity [15,16] Relevant examples of the use of ASA catalyst are provided in the supporting information (Section S6.5, Table S6.5.1).

A total of 8 ASA catalysts with different properties were used to pyrolyze nPUR at the mg scale (TMR) operated at 550 °C, with aniline and toluidine, as well as methylene diphenyl diisocyanate (MDI), as the molecules of interest. The catalysts were characterized in detail using various techniques (ED-XRF, BET, Py-IR, ^{27}Al NMR). Catalyst performance was compared to a benchmark catalyst (SCCa 5/200) from previous studies from our group[10]. The latter is a semi-crystalline, mesoporous alumina (99.2 wt%) promoted by MgO (0.6 wt%) and CaO (0.2 wt%) with a surface area of 218 m²/g and a total acidity of 406 µmol/g. Finally, catalyst performance data were modeled using relevant catalyst properties to obtain catalyst structure-performance relations.

6.2. Experimental section

nPUR based on pMDI was obtained from Covestro, Germany. The nPUR contained had a purity of >99% and a nitrogen content of 7.5 wt%, as determined by elemental analysis. Further details on the feed composition are provided in the supporting information (Table S6.5.2). The amorphous silica-alumina-based catalysts were obtained from Sasol Limited (Germany). Further details on the catalysts are provided in section 6.5, Table S6.5.3.

Elemental compositions were determined using energy dispersive X-ray fluorescence (ED-XRF) on a Panalytical Epsilon 3^{XLE} instrument. Approximately 1 g of catalyst was placed in a plastic holder with a 6 µm mylar film as the bottom. The nominal composition of elements was expressed as oxides, and the sum of the obtained absolute values were normalized to 100%.

Nitrogen physisorption experiments were carried out on a Micromeritics ASAP 2420 analyzer. 100-200 mg of the catalyst sample was placed in a tube with a filler rod, then sealed. The sample was degassed at 300°C under a 0.01-1 mbar atmosphere for 12 h prior to measurement. Adsorption isotherms were collected at -196°C (77K) over a relative pressure range of 0.01 – 1 mbar. The surface area (S_{BET}) was calculated using the Brunauer-Emmett-Teller (BET) method. The pore size distribution and pore volume were determined using the Barrett-Joyner-Halenda (BJH) method. The adsorption branch approach was used to avoid tensile-strength effects that could lead to an artificial peak at 4 nm.[17]

Solid-state ^{27}Al NMR spectra were recorded on a Bruker BioSpin AVANCE NEO 600 MHz (14.1 T) spectrometer equipped with a 3.2 mm double-resonance HX broadband CPMAS probe at a MAS frequency rate of 15 kHz and a temperature setpoint of 296 K**.** The corresponding Larmor frequencies were 600.130 and 156.375 MHz for ^{1}H and ^{27}Al, respectively. All samples were loaded into 3.2 mm zirconia rotors without additional inserts. ^{1}H and ^{27}Al chemical shifts were referenced to aqueous sodium trimethylsilylpropanesulfonate (DSS) and aluminium nitrate, respectively, using the indirect method by measuring the adamantane ^{13}C signals and setting the high-frequency adamantane peak to δ 40.49 ppm[1]. Single-pulse ^{27}Al MAS NMR experiments were performed using a pulse of 1.1 µs corresponding to a π/6 flip-angle, 128 scans (except for catalysts coded 40HPV and 70HPV, where 256 scans were used) and a recycle delay of 2 s. Peak deconvolution was performed using the dmfit procedure with a Gaussian-Lorentz algorithm.

The Brønsted and Lewis acidities were determined by Pyridine Infrared (Py-IR) experiments using an in-house built device equipped with a Bruker Vertex 70 spectrophotometer coupled to an LN-MCT detector. Sample preparation involved pressing a wafer from the catalyst (without a binder). Before measurement, a pre-treatment was carried out by heating the sample to 350 °C under 1 mbar for 8 h. The sample was then cooled to room temperature, and a reference spectrum was recorded (128 scans and a resolution of 4 cm^{-1}). Pyridine adsorption was conducted at room temperature for 30 minutes, followed by removal of excess pyridine under vacuum (1 mbar) for 30 minutes. A spectrum was recorded, and the reference spectrum was subtracted. This process was repeated for temperatures of 150 °C, 250 °C, and 350 °C to distinguish between acid site binding strengths. Data processing was performed using OPUS 7.0 and Origin software.

The Brønsted acid [B] and Lewis acid concentrations [L] were calculated in accordance with the literature, using equations 1 and 2, respectively.[18] The experimental concentrations recorded at room temperature were used to calculate the Brønsted-to-Lewis acidity ratio according to equation 6.3. The total acidity (Equation 6.4) was calculated as the sum of the Brønsted and Lewis acidity values, obtained from Equations 6.1 and 6.2, respectively. The acid site density was calculated via the combination of total acidity obtained by py-IR and the surface area via BET (Equation 6.5)

$$[B] = 0.47 \cdot \frac{A_i}{w} \quad \left(\frac{\mu mol}{g}\right) \tag{6.1}$$

$$[L] = 0.36 \cdot \frac{A_i}{w} \quad \left(\frac{\mu mol}{g}\right) \tag{6.2}$$

$$\frac{B}{L} ratio = \frac{[B]}{[L]} \tag{6.3}$$

$$T_a = [L] + [B] \left(\frac{\mu mol}{g}\right) \tag{6.4}$$

$$Acid\ site\ density\ = \frac{T_a}{S_{BET}} \qquad \left(\frac{\mu mol}{m^2}\right) \tag{6.5}$$

In which [B] is the Brønsted acid concentration, [L] is the Lewis acid concentration, A_i is the integrated peak area, w is the sample weight in miligram, T_a is the total acidity in µmol/g determined via TPD, and the S_{BET} is the surface area in µmol/m^2 as determined by BET.

All NH_3-temperature programmed desorption (NH_3-TPD) experiments were performed on a Micromeritics AutoChem II 2920 analyzer to determine the total acidity. A sample (100-200 mg) was placed between quartz wool in a quartz U-tube. Before measurement, a pre-treatment step was performed by heating the sample to 550 °C with a helium flow of 50 mL/min for 30 minutes. Adsorption of 10 % NH_3 in He (50 mL/min) occurred at 100 °C for 120 minutes, followed by desorption between 100 – 900 °C at 10 °C/min with a helium flow of 50 mL/min for 15 minutes. The downstream gas was directed to a TCD detector for analysis. The concentration of NH_3 was determined by the intensities of the peak at m/z at 17.

All milligram-scale experiments in this study were performed using a Frontier Lab Tandem Microreactor (TMR, Rx 3050TR). The reactor was operated using an in-situ mode (Figure 6.2. Schematic illustration of TMR setup running in in-situ mode). In this configuration, the well-mixed catalyst and PUR are loaded together into the device and pyrolyzed in the first reactor at the preset temperature. The second reactor is filled with an inert material (SiC).

A PUR sample (0.5 mg) and catalyst (2.5 mg, 1:5 ratio) were added to a Frontier Lab Eco Cup (LF PY1-EC80F) and loaded into the reactor using a single-shot sampler (PY1-1040). The vapor phase exiting the microreactor was analyzed using an online gas chromatograph (GC, Agilent Technologies 8890) coupled to a 5977B MSD and an FID detector at 300 °C. The GC was equipped with a 30 m × 0.25 mm capillary column (HP-5 MS) coated with a 0.25 µm film of 5% phenylmethyl polysiloxane. Helium was used as the carrier gas at a constant flow rate of 1 ml/min. A Frontier Lab Microjet Cryo-Trap was connected to the column to separate all volatile gases. The initial oven temperature was set at 40 °C, with a ramp rate of 10 °C/min (maintained for 1 min) to reach a final column temperature of 300 °C, which was held for 5 min. The injector and detector temperatures were maintained at 300 °C. Data were collected in full-scan mode with mass-to-charge (m/z) ratios ranging from 35 to 500. Chromatographic peaks were identified using the NIST mass spectral data library. Quantification of the desired N-containing products (aniline, toluidine, and MDA) was performed using an external calibration method. A series of dilutions of each compound was injected into the TMR using a microshot injector to obtain an external calibration curve, which was used to quantify products and calculate yields.

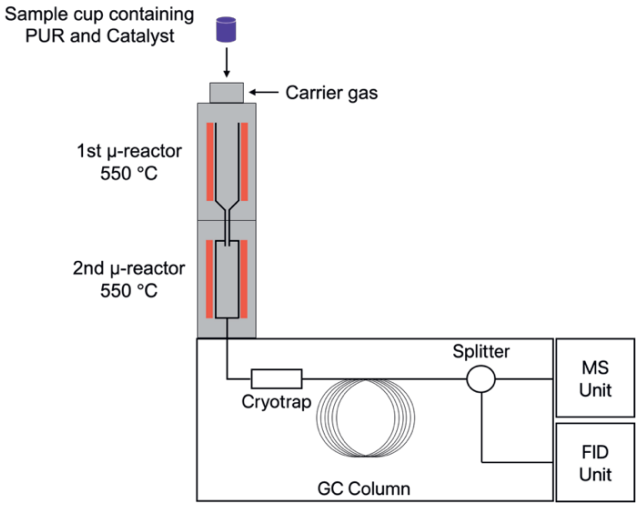

Figure 6.2. Schematic illustration of TMR setup running in in-situ mode

The individual product yields (aniline, toluidine, and MDA) are expressed on feed input weight (Equation 6.6) with wt% as the unit or on a nitrogen basis (Equation 6.7) with N% as the unit.

$$Yield\ on\ input\ (wt\%) = \frac{w_i}{w_f} \cdot 100 \tag{6.6}$$

Here, w_i is the weight of an individual product *i* (g), as determined by GC, and w_f is the feed intake (g).

$$N\ based\ yield\ of\ component\ i\ (N\%) = \frac{w_i \cdot N_i}{w_f \cdot N_f} \cdot 100 \tag{6.7}$$

Here, w_i is the weight of an individual product *i* (g), as determined by GC, w_f is the feed intake (g), N_i is the nitrogen content (wt %) of an individual product *i*, and N_f is the nitrogen content of the feed (wt%, as determined by elemental analysis).

Multi-variable regression was used to model the experimental data, and for this purpose, the Design-Expert Version 7.0.0 software package was employed. Equation 6.8 is used to model the experimental data.

$$y = b_0 + \sum_{i=1}^{n} b_i x_i + \sum_{i=1}^{n} b_{ii} x_i^2 + \sum_{i=j}^{n-1} \sum_{j=i+1}^{n} b_{ij} x_{ij} + e \tag{6.8}$$

Where *y* is the dependent variable (summed aniline and toluidine yield), x_i and x_j are the independent variables (in this case catalyst properties like acidity, acid site density, surface area, Lewis acidity, Brønsted acidity, pore width, Lewis/Brønsted ratio, pore volume, and alumina content), b_o, b_i, b_{ii} and b_{ij} are the regression coefficients of the model whereas e is the model error. The best regression equation was obtained by backward elimination of non-significant parameters. A parameter was considered statistically relevant when the p-value was less than 0.05.

6.3. Results and discussion

Catalytic pyrolysis experiments

Catalytic experiments using nPUR were carried out in duplicate at milligram scale (0.5 mg nPUR, 2.5 mg catalyst) in a TMR in an in situ mode at 550 °C. The latter temperature was selected based on a preliminary screening with alumina catalysts.[10] Aniline, toluidine, and MDA yields were determined and compared with those from thermal pyrolysis experiments. Eight ASA catalysts with alumina-to-silica loadings ranging from 95/5 to 30/70 were investigated. Four belonged to the standard pore volume (SPV) category, while the other four exhibited a higher pore volume (HPV) after post-treatment. A comprehensive yield overview for all catalysts is provided in the supporting information (section S6.5, Tables S6.5.4 and S6.5.5).

Thermal pyrolysis (non-catalytic) of nPUR yielded low amounts of the desired N-containing monomers (5.5 N% MDA, no aniline, and no toluidine). Chemoselectivity shifted from MDA to aniline and toluidine with the ASA catalysts (Figure 6.3), indicating a positive catalytic effect. The highest combined aniline and toluidine yield (35.6 N%) was achieved using catalyst 5HPV. On average, the combined aniline and toluidine yield is higher for the HPV catalyst series (29.8 N%) than for the SPV series (25.4 N%), suggesting that pore volume is a relevant indicator of catalyst performance. The aniline yield with the best catalyst in the ASA series (29.6 N%) is higher than that of the best catalyst in the alumina catalyst series (Puralox SCCa 5/200, 21.8 N%), as reported in literature.[10] A comprehensive yield overview for all catalysts is provided in the supporting information (section S6.5, Tables S6.5.4 and S6.5.5). Notably, no MDA was observed for any of the ASA catalysts, unlike the 2.8 N% MDA observed for a typical alumina-only catalyst (Puralox SCCa 5/200). A possible explanation is the higher Brønsted acidity of the ASA catalysts (*vide infra*), which may promote the conversion of MDA to aniline and toluidine. Small amounts of side products, such as indole derivatives, quinoline, and acridine, were also observed with the ASA catalyst, similar to the alumina catalysts in our previous studies.[19–21] These N-containing side products originate from **I**) cross reactions between polyol- and isocyanate fragments forming ethylaniline and ethyltoluidine or **II**) homocoupling between isocyanate fragments (aniline and toluidine) to form acridine and methylacridine[22].

Regarding the nitrogen balance, the highest combined aniline and toluidine yield (35.6 N%) was achieved with catalyst 5HPV. The remaining nitrogen is present in the liquid phase as low molecular weight N-containing byproducts such as (substituted) indoles (ca. 20% N based on GC calibration), and 1.7% N in the coke. The remaining N is in the form of permanent gases (not quantified).

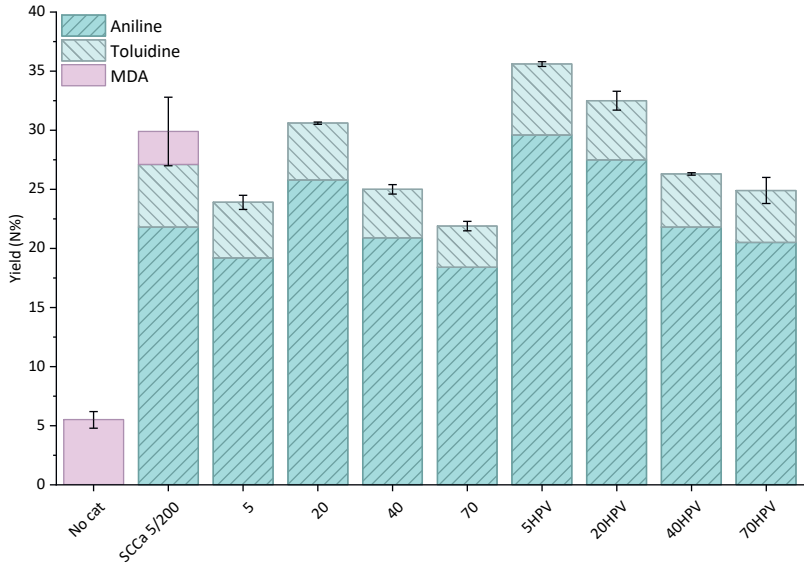

Figure 6.3. Overview of ASA catalyst performance for PUR pyrolysis in the tandem microreactor. Results for a thermal catalyst and a representative alumina catalyst are included as references. (550 °C, catalyst-to-feed ratio of 5 to 1)

Catalyst characterization

To establish catalyst structure-performance relations, the ASA catalysts were characterized in detail using various techniques, including X-ray fluorescence (ED-XRF), nitrogen physisorption (BET), solid-state ^{27}Al-NMR, ammonia TPD (NH_3-TPD), and pyridine-IR spectroscopy (Py-IR). The relevant catalyst features are summarized in Table 6.1.

Nitrogen adsorption measurements of the ASA catalysts showed significant differences in surface area (S_a), ranging from 143 to 436 m^2/g. This is in the range as reported in the literature (155-844 m^2/g).[16,23–25] The pore volumes (PV) were between 0.72 and 1.76 cm^3/g and pore widths (PW) varied between 9.0 and 18 nm, somewhat higher than reported by others (0.34 – 1.33 cm^3/g and 2 – 12 nm, respectively).[15,24,25] It is well known that both the synthesis protocol and the calcination temperature may affect morphology and lead to variations in surface area, pore width, and pore volume[24]. N_2 physisorption and pore size distribution plots are given in the supplementary information, Figures S6.5.1 and S6.5.2.

The total acidity (T_a) was determined by both Py-IR and NH_3-TPD. A comparison between the two techniques (see Parity plot in Section S6.5, Figure S6.5.3) showed a reasonably good fit (R-squared = 0.96). However, the NH_3-TPD values were systematically higher than those obtained by Py-IR, as evidenced by a slope of 0.87 rather than 1, which would indicate a perfect fit. This is a well-known feature of a wide range of heterogeneous catalysts.[26] Py-IR acidities were used for analyses, as they also provide information on the ratio of Brønsted to Lewis acid concentrations (BLR).[24]

Table 6.1. Yield data and relevant properties of the ASA catalyst family used in this study

Catalyst[b]	Aniline yield[a] (N%)	Toluidine yield[a] (N%)	Al content[c] (%)	Surface area[d] (m^2/g)	Pore volume[e] (cm^3/g)	Pore width[f] (nm)	Total acidity[g] (µmol/g)	Acid site density[h] (µmol/m^2)	Brønsted acidity[i] (µmol/g)	Lewis acidity[j] (µmol/g)	Brønsted /Lewis[k] Ratio
5SPV	19.2	4.7	94.5	163	0.74	18	268	1.9	4.76	263	0.02
20SPV	25.8	4.8	79.8	459	1.04	9.0	374	1.0	43.9	330	0.13
40SPV	20.9	4.1	58.5	330	0.98	12	383	1.3	42.0	341	0.12
70SPV	18.4	3.5	29.1	308	1.22	16	198	0.8	23.4	174	0.13
5HPV	29.6	6.0	94.3	304	0.72	9.5	300	1.2	6.56	294	0.02
20HPV	27.5	5.0	76.5	532	1.29	9.7	448	1.0	38.7	410	0.09
40HPV	21.8	4.5	57.2	484	1.48	12	390	1.0	37.3	353	0.11
70HPV	20.5	4.4	30.1	345	1.39	16	438	1.5	34.2	404	0.08

[a]Reaction conditions: 0.5 mg nPUR, catalyst-to-feed ratio of 5 to 1, 550 °C with a helium flow of 205 mL/min and a pyrolysis time of 10 s;[b]SPV is abbreviation for standard pore volume and HPV for high pore volume;[c]Values obtained with X-ray fluorescence; [d]Determined from N_2 adsorption data (BET); [e]Total pore volume from isotherm plot; [f]Average pore width calculated from N_2 adsorption data (BJH); [g]Determined by pyridine infrared adsorption measurements and calculated using Eq. 4; [h]Calculated using Eq. 5; [i]Determined using pyridine infrared adsorption experiments using Eq. 1; [j]Determined using pyridine infrared adsorption experiments and calculated using Eq. 2; [k]Determined using pyridine infrared adsorption experiments and calculated using Eq.3

Figure 6.4 shows a typical IR spectrum with characteristic pyridine adsorption bands. The spectra for all catalysts are provided in the supplementary information (Table S6.57, and Figures S6.5.4–S6.5.13). The blue lines represent Lewis acid sites (LAS), the orange lines Brønsted acid sites (BAS), and the green lines combined Brønsted and Lewis acid bands. LAS can be distinguished into weak (1622 cm^{-1}) and strong (1615 cm^{-1}) sites. In addition, strong LAS peaks are present in the range 1440-1460 cm^{-1} band. Here, the peak at 1455 cm^{-1} is associated with pyridine coordination to framework alumina (F-Al) and the one at 1444 cm^{-1} to non-framework alumina (NF-Al). BAS are present as strong (1639 and 1547 cm^{-1}) framework OH groups and weak (1596 cm^{-1}) terminal or geminal silanol OH groups. [27,28]

The total acidity, as determined by Py-IR, ranged from 198 to 448 µmol/g. The SPV catalyst series exhibits a volcano-shaped trend between Al content and total acidity, consistent with literature data.[24] Moreover, pore volume increases as alumina content decreases.

^{27}Al ss-NMR measurements were conducted on the HPV series to quantify the amounts of alumina IV, V, and VI species and use this information to correlate the acidity to the type and amount of alumina species (Figure 6.5). Relevant peaks are present at δ 72 ppm (Al_{IV}), δ 33 ppm (Al_V), and δ 12 ppm (Al_{VI}).[15] Most of the alumina species are 6-coordinated (Al_{VI}), and minor amounts of 4-coordinated (Al_{IV}) are present. 5-Coordinated Al species (Al_V) are absent in the 5HPV catalyst and increase with higher silica content, reaching 10% in 70HPV. Attempts to find a correlation between Lewis/Brønsted acidity determined by Py-IR and the amounts of different alumina species determined by NMR were unsuccessful.

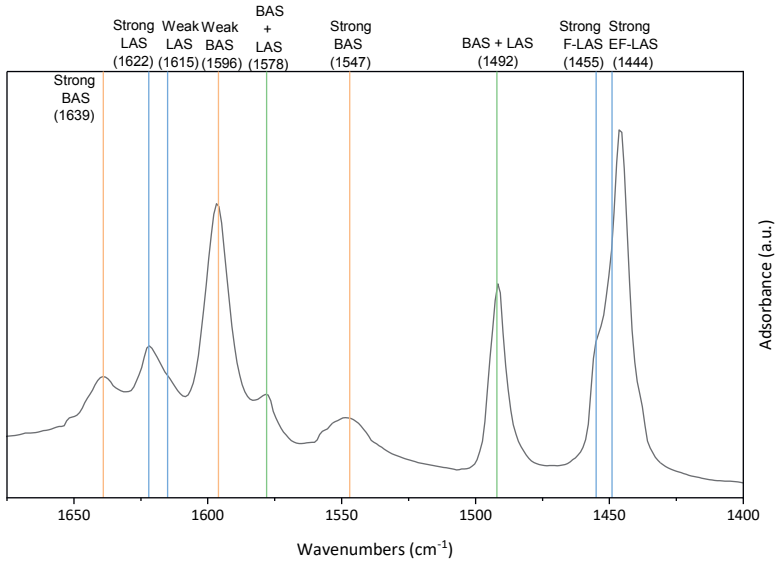

Figure 6.4. Pyridine adsorption at room temperature for catalyst 70HPV, including peak identification. Peak identifications obtained from:[13,15,16,29,30] Blue lines: Lewis acid sites; Orange lines: Brønsted acid sites; green lines: combined Lewis and Brønsted acid sites

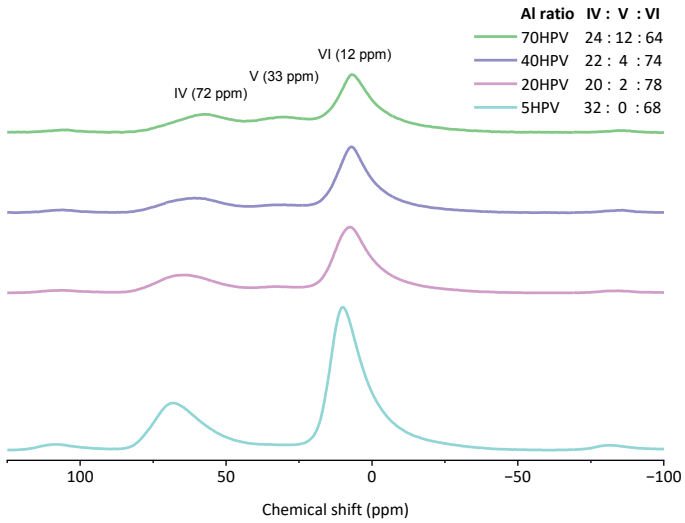

Figure 6.5. 27Al ss-NMR spectra of the HPV catalyst series and the relative amounts of alumina IV, V, and IV species

Catalyst structure- performance relations

Catalyst properties (Si/Al ratio, surface area, pore volume, pore width, total acidity, Brønsted acidity, Lewis acidity, acid site density, Brønsted/Lewis ratio) and performance in terms of combined aniline and toluidine yield were modeled with linear models with 2 (equation 6.9) and 3 independent variables (equation 6.10).

$$Yield = A + B\,X_1 + C\,X_2 \tag{6.9}$$

$$Yield = A + B\,X_1 + C\,X_2 + D\,X_3 \tag{6.10}$$

Extended models with, among others, more independent variables and interaction terms between independent variables were not addressed due to the limited dataset (8 catalysts in duplicate, see Table 6.1 and Section S6.5 Table S6.5.8). Model quality was assessed using R^2, adjusted R^2, AIC (Akaike Information Criterion), and a corrected AIC for small datasets (AICc). Initially, we used the average of the duplicates, given 8 independent datasets (n=8).

In the first modeling phase, all 36 possible combinations of 2 independent variables were tested, and the results are given in Table S6.5.9. The best model uses pore width (PW) and the Brønsted/Lewis acid (B/L) ratio as independent variables (equation 6.11), with R^2 = 0.9465 and R^2adj = 0.9251.

$$\mathrm{Y} = 48.92 - 1.300 \cdot \mathrm{PW} - 54.70 \cdot (\mathrm{B/L}) \tag{6.11}$$

Both independent variables and the model are significant, with p-values of 0.0007 for PW, 0.0044 for the B/L ratio, and 0.0044 for the model. This means that these 2 independent variables explain about

95% of the variation in yield. Other relevant data, including confidence intervals of the model parameters, are given in Table 6.2.

Table 6.2. Relevant data for the model parameters

Parameter	Value	95% confidence interval	p-value
A – intercept	48.92	42.99 – 54.86	<0.001
B – pore width	−1.300	−1.672 – −0.927	<0.001
C – B/L ratio	−54.70	−83.16 – −26.25	0.004

The second-best model also includes PW as the independent variable and Brønsted acidity instead of the B/L acid ratio. However, the R-squared values of this model are significantly lower. To better assess model quality, we evaluated AIC (equation 6.12) and AICc for the 10 best 2-variable models.

$$\mathrm{AIC} = -2\ln(\mathrm{L}) + 2\mathrm{k} \tag{6.12}$$

Here L is the model likelihood and k is the number of parameters (3 in this case). These model indicators are typically used for model discrimination, and the models with the lowest values are preferred. AICc is an adjusted indicator for relatively small datasets, as in this case with 8 experiments. Table S6.5.9 (Supporting Information) reports the results for the 10 best 2-variable models. The difference in AICc between the first-ranked model (PW and B/L ratio) and the second-best model (PW and Bronsted acidity) is 6.82, indicating a strong preference for the first one.

The models were also evaluated using the 16 independent experiments (n=16) instead of averaging the duplicate yields (n=8). No significant differences were obtained, with the model with PW and B/L as the best (e.g. R^2 = 0.946 for n = 16 versus 0.9475 for n= 8), and model parameters equal to those obtained when fitting the average yields.

In a subsequent stage, 3 independent variable models (equation 9) were evaluated, though, given the small sample size, overfitting should be avoided. The results are given in Table S6.5.10 and show that a linear model with PW, B/L ratio, and Bronsted acidity is the best when considering R-squared values (R^2 = 0.9465, R^2adj = 0.9251). Interestingly, the R-squared values for the best 2-variable model with PW and B/L are as good as for this 3-variable model (R^2 = 0.9461, R^2adj = 0.9378). As such, the additional term in the 3-variable model (Bronsted acidity) does not improve the model. In addition, the AICc value for the best 3-variable model is 54.63 versus 35.2 for the 2-variable model, indicating that the 2-variable model better describes the experimental data.

Thus, we conclude that linear 2-variable models are preferred over 3-variable models and that among all 36 2-variable linear models evaluated, the combination of pore width and Brønsted/Lewis acid ratio provided the best description of the experimental yield (R^2 = 0.947, adjusted R^2 = 0.926, AIC = 29.10), with an AICc difference of 6.82 relative to the second-ranked model. A parity plot (Figure 6.6) illustrates that agreement between the linear 2-variable model with PW and B/L ratio and experimental data is very good. The actual dependence of the combined aniline and toluidine yield on the PW and B/L acid ratio is shown in the 3D response surface plot (Figure 6.7).

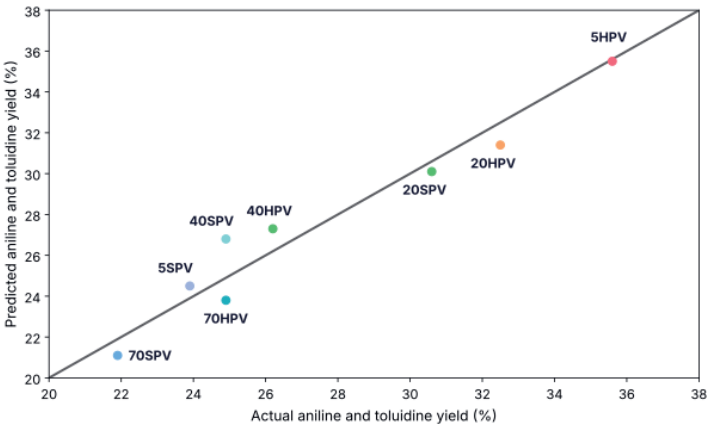

Figure 6.6. Predicted vs modeled combined aniline and toluidine yields using the best linear 2-variable model

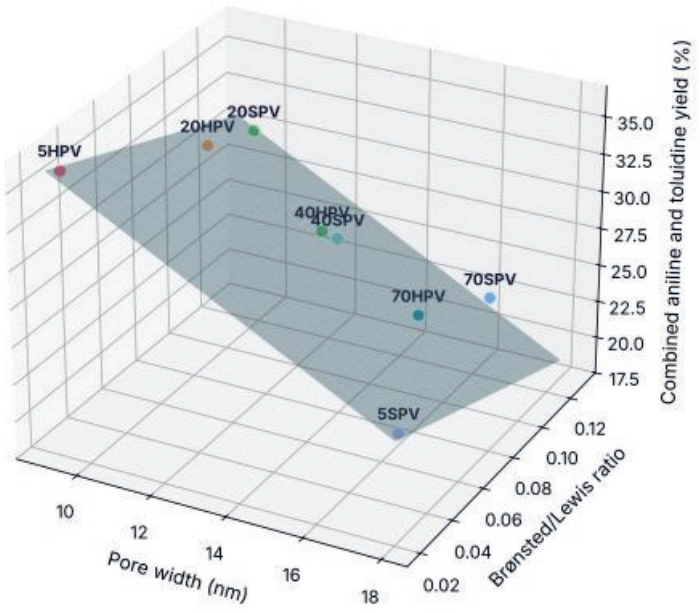

Figure 6.7. 3D-plot showing the combined aniline and toluidine yield versus pore width and Brønsted/Lewis ratio

The model implies that higher Lewis acidity positively affects aniline and toluidine yields (*vide infra*). Regarding pore width, smaller pores are preferred, the first indication that a more confined space is optimal for aniline and toluidine formation. Possibly, smaller pores prevent large fragments from entering, which may be advantageous because these fragments can facilitate coking, block active sites,

and reduce MDA cleavage and thus the formation of aniline and toluidine. However, additional experiments are needed to verify the hypothesis. The model suggests that narrowing the pore width will improve combined yields of aniline and toluidine, providing a guideline for tailored catalyst design.

Reaction network

Based on the observed results, a reaction network is proposed and is given Figure 6.8. Proposed mechanism for the depolymerization of PUR into aniline and toluidine via the ASA's Brønsted and Lewis acid sites. It is assumed that PUR depolymerization mainly occurs on the outside catalyst surface, yielding (oligomeric) MDA and polyol fragments. This carbamate and polyol cracking may occur via interactions between the lone pairs of the oxygen and nitrogen atoms in PUR and the Lewis acid sites on the catalyst surface (**1**). Brønsted acid sites are unlikely to be involved, as shown previously, because an Al catalyst with very limited Brønsted acidity was also shown to be active for the depolymerization of PUR mainly to MDA.[10] However, this needs to be confirmed by additional mechanistic investigations e.g. involving model components in combination with pure Al_2O_3 catalysts and ASAs. The large polyol fragments are subsequently converted to smaller C1-C4 components and permanent gases.[31] (**2**). The MDA fragments are broken down to aniline and toluidine by cleavage of the CH_2 groups by the action of Lewis acid sites, with a significant enhancement of some Brønsted acid sites in the catalyst's pore (**3**). The origin of the hydrogen atoms required for cleaving MDA into aniline and toluidine has been studied in detail using labeling studies involving deuterium- and ^{13}C-labeled model components.[22] It was shown that the hydrogen atoms required for aniline and toluidine formation from MDA are from the polyol segment, and particularly from α-hydrogens of substituents."

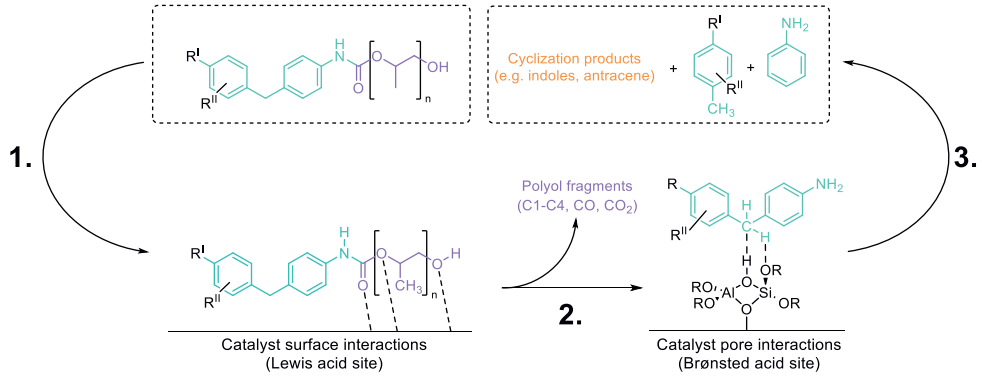

Figure 6.8. Proposed mechanism for the depolymerization of PUR into aniline and toluidine via the ASA's Brønsted and Lewis acid sites

6.4. Conclusions

In this work, we have performed experimental studies on the catalytic depolymerization of PUR to small nitrogen-containing molecules (aniline and toluidine) using a range of ASA catalysts. The highest combined aniline and toluidine (36 N%) was achieved with an alumina-to-silica ratio of 95 to 5, combined with a high-pore-volume catalyst variant. This value is higher than that found for an alumina-only catalyst, as shown in previous work, and shows the potential of this catalytic family for

PUR recycling. Catalyst-structure-performance relations were established, and it was shown that the highest combined aniline/toluidine yields are achievable with a catalyst that has an intermediate Brønsted/Lewis acid ratio and low pore width. These findings were used to establish a reaction network for PUR depolymerization catalyzed by ASA. Polyurethane is depolymerized into polyol and carbamate fragments via coordination of nitrogen and oxygen lone pairs in PUR to Lewis acid sites on the catalyst. The carbamate moiety is subsequently cleaved to MDA by either Brønsted or Lewis acid sites. Finally, Brønsted acid sites crack the methylene bridge of MDA via hydrogen donation from the polyol segment, yielding aniline and toluidine.

References

1. Kemona, A. & Piotrowska, M. Polyurethane recycling and disposal: Methods and prospects. *Polymers (Basel).* **12**, 1752 (2020).
2. Banik, J., Chakraborty, D., Rizwan, M., Shaik, A. H. & Chandan, M. R. Review on disposal, recycling and management of waste polyurethane foams: A way ahead. *Waste Management and Research* **41**, 1063–1080 (2023).
3. Zia, K. M., Bhatti, H. N. & Ahmad Bhatti, I. Methods for polyurethane and polyurethane composites, recycling and recovery: A review. *React. Funct. Polym.* **67**, 675–692 (2007).
4. Deng, Y. *et al.* Reviewing the thermo-chemical recycling of waste polyurethane foam. *J. Environ. Manage.* **278**, 111527 (2021).
5. Datta, J., Kopczyńska, P., Simón, D. & Rodríguez, J. F. Thermo-Chemical Decomposition Study of Polyurethane Elastomer Through Glycerolysis Route with Using Crude and Refined Glycerine as a Transesterification Agent. *J. Polym. Environ.* **26**, 166–174 (2018).
6. Liu, B. *et al.* Opportunities in Closed-Loop Molecular Recycling of End-of-Life Polyurethane. *ACS Sustain. Chem. Eng.* **11**, 6114–6128 (2023).
7. Shin, S. R., Kim, H. N., Liang, J. Y., Lee, S. H. & Lee, D. S. Sustainable rigid polyurethane foams based on recycled polyols from chemical recycling of waste polyurethane foams. *J. Appl. Polym. Sci.* **136**, 47916 (2019).
8. Van Belleghem, L. *et al.* Recovery of Polyol and Aromatic Amines from Rigid Polyurethane Foams via Ammonolysis. *JACS Au* **5**, 3444–3452 (2025).
9. Bulan, A. *et al.* Process for producing isocyanates. (2012) doi:US8,153,838B2.
10. Engels, T. G. W. *et al.* Chemical recycling of rigid polyurethane foam via thermocatalytic conversion to aniline. *ChemRxiv* (2026).
11. Bozi, J. & Blazsó, M. Catalytic thermal decomposition of polyamides and polyurethanes mixed with acidic zeolites. *J. Anal. Appl. Pyrolysis* **97**, 189–197 (2012).
12. Hensen, E. J. M., Poduval, D. G., Magusin, P. C. M. M., Coumans, A. E. & Veen, J. A. R. van. Formation of acid sites in amorphous silica-alumina. *J. Catal.* **269**, 201–218 (2010).
13. Crépeau, G. *et al.* Nature, structure and strength of the acidic sites of amorphous silica alumina: An IR and NMR study. *Journal of Physical Chemistry B* **110**, 15172–15185 (2006).
14. Ali, M. A., Tatsumi, T. & Masuda, T. Development of heavy oil hydrocracking catalysts using amorphous silica-alumina and zeolites as catalyst supports. *Appl. Catal. A Gen.* **233**, 77–90 (2002).
15. Bao, J. *et al.* Synthesis of amorphous silica-alumina with enhanced specific surface area and acidity by pH-swing method and its catalytic activity in cumene cracking. *Microporous and Mesoporous Materials* **337**, 111897 (2022).

16. Rivera-Barrera, D., Guzman, A., Ramirez, I. & Molina V, D. Effect of Si/Al ratio, calcination temperature and post-synthesis phosphorus modification on the textural, structural, acidic, and catalytic properties of amorphous silica-alumina prepared by deposition methods. *Journal of Physics and Chemistry of Solids* **209**, 112403 (2026).
17. Groen, J. C., Peffer, L. A. A. & Pérez-Ramírez, J. Pore size determination in modified micro- and mesoporous materials. Pitfalls and limitations in gas adsorption data analysis. *Microporous and Mesoporous Materials* **60**, 1–17 (2003).
18. Emeis, C. A. Determination of Integrated Molar Extinction Coefficients for Infrared Absorption Bands of Pyridine Adsorbed on Solid Acid Catalysts. *J. Catal.* **141**, 347–54 (1993).
19. Horaguchi, T., Oyanagi, T., Creencia, E. C., Tanemura, K. & Suzuki, T. Synthesis of carbazole, acridine, phenazine, 4H-benzo[def]carbazole and their derivatives by thermal cyclization reaction of aromatic amines. *J. Heterocycl. Chem.* **41**, 1–6 (2004).
20. Creencia, E. C., Taguchi, K. & Horaguchi, T. Thermal reactions of N-alkyl-2-benzylaniline and N-alkyl-N'-phenyl-o-phenylenediamine: An unusual route to 2-phenylindole and 2-phenylbenzimidazole. *J. Heterocycl. Chem.* **45**, 837–843 (2008).
21. Brosius, R. *et al.* Vapour-phase synthesis of 2-methyl- and 4-methylquinoline over BEA* zeolites. *J. Catal.* **239**, 362–368 (2006).
22. Engels, T. G. W. *et al.* Catalytic pyrolysis of rigid polyurethane to aniline: Mechanistic insights using 13C and deuterium model compounds. (2026).
23. Serrano, D. P., Aguado, J. & Escola, J. M. Catalytic conversion of polystyrene over HMCM-41, HZSM-5 and amorphous SiO2-Al2O3 : comparison with thermal cracking. *Appl. Catal. B* **25**, 181–189 (2000).
24. Xu, B. *et al.* Synthesis and characterization of mesoporous Si-modified alumina with high thermal stability. *Microporous and Mesoporous Materials* **238**, 84–89 (2017).
25. Ishihara, A. Preparation of Amorphous Silica-Alumina Using the Sol-Gel Method and its Reactivity for a Matrix in Catalytic Cracking. *Catalysis Surveys from Asia* **16**, 36–47 (2012).
26. Liu, L., Zhao, L. & Sun, H. Simulation of NH3 temperature-programmed desorption curves using an ab initio force field. *Journal of Physical Chemistry C* **113**, 16051–16057 (2009).
27. Coster, D., Blumenfeld, A. L. & Fripiat, J. J. Lewis Acid Sites and Surface Aluminum in Aluminas and Zeolites: A High-Resolution NMR Study. *J. Phys. Chem.* **24**, 6201–6211 (1994).
28. Blumenfeld, A. & Fripiat, J. J. Acid sites topology in aluminas and zeolites from high-resolution solid-state NMR. *Top. Catal.* **1**, 119–129 (1997).
29. Hensen, E. J. M. *et al.* Acidity characterization of amorphous silica-alumina. *Journal of Physical Chemistry C* **116**, 21416–21429 (2012).
30. Rivera-Barrera, D. & Poveda-Jaramillo, J. C. Thermal desorption of trimethylphosphine (TMP) on the HY zeolite followed by FT-IR and 31P MAS NMR. *J. Solid State Chem.* **294**, 121862 (2021).
31. Klaimy, S. *et al.* Flash Catalytic Pyrolysis of Polyethylene over (Alumino)silicate Materials. *ChemCatChem* **12**, 1109–1116 (2020).

Table 6.5.1. Relevant examples on the use of ASA-based catalysts

Group [year]	Catalyst	Feed (Bio, plastic, other)	Temperature (°C)	Target
Tamele [1950][1]	Not specified	Isopropyl-benzene, propylene	500, 200	Cracking, polymerization
Trombetta [1998][2]	SA8, SA13, AS	Butene	430 - 480	Isomerization
Ali [2002][3]	Mix: SIRAL-40, USY, beta-zeolite	desulfurized vacuum gas oil (DS-VGO)	380 – 410	Hydrocracking
Klerk [2006][4]	ASA, not specified	C_3-C_6, C_7-C_{10}	370	Olefin oligomerization
Triantafyllidis [2007][5]	MSU-S_{bea}	Beech wood	500	Polycyclic aromatic HC
Xu [2007][6]	ASA 3,7,15	Propane	400 - 600	Mechanistic study
Hensen [2010][7]	ASA with various Si/Al loading and synthesis methods (cogel, fumed, comm)	n-Heptane	233 - 800	Dehydrogenation, isomerization, cracking
Zabeti [2012][8]	ASA (Na, K, Cs, Mg, Ca)	Canadian pinewood	450	Oxygen reduction
Ishihara [2012][9]	MA0.22-5, MA1.22-0, MA1.22-5	n-Dodecane	500	Hydrocarbons
Klaimy [2020][10]	Si-Al, Si-MFI, Si/Al-MFI	Polyethylene	450	Liquid/gas/char ratios
Wang [2020][11]	Al^{v}-enriched ASAs	phenylglyoxal, Glucose, Propylene glycol	160 – 195	C-H bond activation
Li [2020][12]	SA0.5, 1.0, 1.5, 2.0	n-hexadecane	338	Isomerization
Bao [2022][13]	ASA-1,2,3,4	Cumene	300	Cracking
Karami [2023][14]	A0 – A4	Propane	*40 - 800*	Dehydrogenation
Reif [2023][15]	Siralox 30, HY-5	Alkyl methyl ketones	200 - 300	Aromatization

*Values in italic are performed via thermogravimetric analysis and do not represent a specific pyrolysis temperature

Materials

New rigid polyurethane refrigerator foam obtained from Covestro Germany was used as the feedstock for all experiments. The feed was cryo-milled to powder prior to use using an IKA Tube Mill 100 control. Elemental analysis and metal content of the PUR were analyzed using a CHNS analyzer and XRF, respectively. The metal content was calculated based on the polyurethane ash content (0.8%). Results are shown in Table S6.5.2. For XRF data, it was assumed that each impurity was in the oxygenated state.

Table S6.5.2. Chemical composition of nPUR refrigerator foam obtained from Covestro Germany

C[a] (%)	H[a] (%)	N[a] (%)	O[b] (%)
65.7	6.69	7.52	19.5

Sillicon[c,d] (%)	CaO[c,d] (%)	K_2O[c,d] (%)	Fe_2O_3[c,d] (%)	MgO[c,d] (%)	TiO_2[c,d] (%)
0.206	0.144	0.144	0.0037	0.035	0.003

[a]Average of 2 measurements; [b]By difference; [c]Percentage calculated using absolute ash values in combination with XRF data; [d]Impurity values below 25 ppm have been left out for brevity

Table S6.5.3. Chemical composition of ASA catalysts as determined via ED-XRF

Catalyst[b]	Al_2O_3[a] (%)	SiO_2[a] (%)	MgO[a] (%)	CaO[a] (%)	Si/Al Ratio
5SPV	94.5	4.94	0.324	0.151	5/95
20SPV	79.8	20.0	0.000	0.159	20/80
40SPV	58.5	41.3	0.000	0.162	41/59
70SPV	29.1	70.7	0.00	0.159	71/29
5HPV	94.3	4.73	0.648	0.167	5/95
20HPV	76.5	23.3	0.003	0.170	23/77
40HPV	57.2	42.6	0.000	0.161	43/57
70HPV	30.1	69.6	0.000	0.151	70/30

[a]ppm amounts of impurities have been left out for brevity; [b]SPV is standard pore volume and HPV is Higher pore volume catalysts

Pyrolysis results

The results shown below originate from the thermal decomposition of nPUR, coupled with mass spectroscopy, catalyzed by 5HPV. Reaction conditions: 0.5 mg nPUR, catalyst-to-feed ratio of 5 to 1, 550 °C with a helium flow of 205 mL/min and a pyrolysis time of 10 seconds. The yields calculated on input, and N-base are shown in Tables Table S6.5.4 and Table S6.5.5.

Table S6.5.4. Catalyst screening pyrolysis results, calculated on input according to calculation 6.6

Catalyst[a,b]	Aniline[c,d] (wt%)	Toluidine[c,d] (wt%)	MDA[c,d,e] (wt%)	Total[c,d] (wt%)	Error[f] (%)	An/Tol Ratio[g]
No cat	0.0	0.0	3.5	3.5	0.5	0.0
SCCa 5/200	11.0	3.1	1.8	15.8	1.6	3.6
5SPV	9.6	2.7	0.0	12.3	0.3	3.5
20SPV	13.0	2.8	0.0	15.8	0.1	4.6
40SPV	10.5	2.4	0.0	12.8	0.2	4.4
70SPV	9.2	2.0	0.0	11.2	0.2	4.6
5HPV	14.8	3.5	0.0	18.3	0.1	4.3
20HPV	13.8	2.9	0.0	16.7	0.4	4.8
40HPV	10.9	2.6	0.0	13.5	0.0	4.2
70HPV	10.3	2.6	0.0	12.8	0.6	4.0

[a]Reaction conditions: 0.5 mg nPUR, catalyst-to-feed ratio of 5 to 1, 550 °C with a helium flow of 205 mL/min and a pyrolysis time of 10 seconds; [b] SPV is standard pore volume and HPV is Higher pore volume catalysts; [c]Determined via calibration curve of according compound; [d]Average of 2 measurements; [e]4,4-MDA and 4,2-MDA isomers were observed during pyrolysis, grouped, and their yields were corrected for nitrogen content; [f]Calculated yield percentage error; [g]Calculated via $\frac{Aniline\ Yield\ (\%)}{Toluidine\ Yield\ (\%)}$

Table S6.5.5. Catalyst screening pyrolysis results, calculated on N-based content according to calculation 6.7

Catalyst[a,b]	Aniline[c,d] (N%)	Toluidine[c,d] (N%)	MDA[c,d,e] (N%)	Total[c,d] (N%)	Error[f] (%)	An/Tol Ratio[g]
No cat	0.0	0.0	5.5	5.5	0.7	0.0
SCCa 5/200	21.8	5.3	2.8	29.9	2.9	4.1
5SPV	19.2	4.7	0.0	23.9	0.6	4.1
20SPV	25.8	4.8	0.0	30.6	0.1	5.4
40SPV	20.9	4.1	0.0	25.0	0.4	5.1
70SPV	18.4	3.5	0.0	21.9	0.4	5.3
5HPV	29.6	6.0	0.0	35.6	0.2	4.9
20HPV	27.5	5.0	0.0	32.5	0.8	5.5
40HPV	21.8	4.5	0.0	26.2	0.1	4.9
70HPV	20.5	4.4	0.0	24.9	1.1	4.7

[a]Reaction conditions: 0.5 mg nPUR, catalyst-to-feed ratio of 5 to 1, 550 °C with a helium flow of 205 mL/min and a pyrolysis time of 10 seconds; [b] SPV is standard pore volume and HPV is Higher pore volume catalysts; [c]Determined via calibration curve of according compound; [d]Average of 2 measurements; [e]4,4-MDA and 4,2-MDA isomers were observed during pyrolysis, grouped, and their yields were corrected for nitrogen content; [f]Calculated yield percentage error ; [g]Calculated via $\frac{Aniline\ Yield\ (\%)}{Toluidine\ Yield\ (\%)}$

Pyridine infrared characterization

The total acidities determined via ammonia TPD and pyridine IR are shown in Table S6.5.6. The parity plot (Figure 6.5.1) shows a slope of 0.86, indicating that the TPD acidities are, on average, higher than

the IR acidities. The integrated areas with calculated Brønsted and Lewis concentrations are shown Table S6.5.7. The IR measurements with desorption at 150, 250, and 350 °C for each catalyst are shown in Figures S6.5.2 – S6.5.11.

Table S6.5.6. Total acidities determined via NH_3-TPD and Py-IR

Catalyst	Total acidity NH_3-TPD[a] (µmol/g)	Total acidity Py-IR[b] (µmol/g)
5SPV	254	268
20SPV	458	374
40SPV	339	383
70SPV	211	198
5HPV	377	300
20HPV	600	448
40HPV	514	390
70HPV	363	438

[a]Determined via ammonia-TPD, calculated by total peak integration; [b]Determined via pyridine-IR, calculated using Eq 6.7.

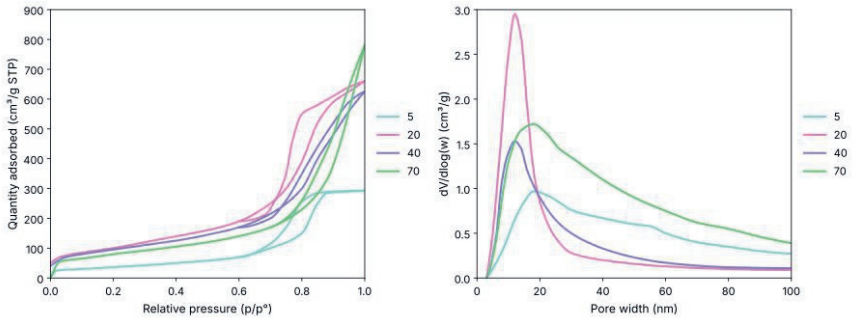

Figure 6.5.1.N_2 physisorption isotherms (top) and pore width distributions (bottom) of the SPV catalysts

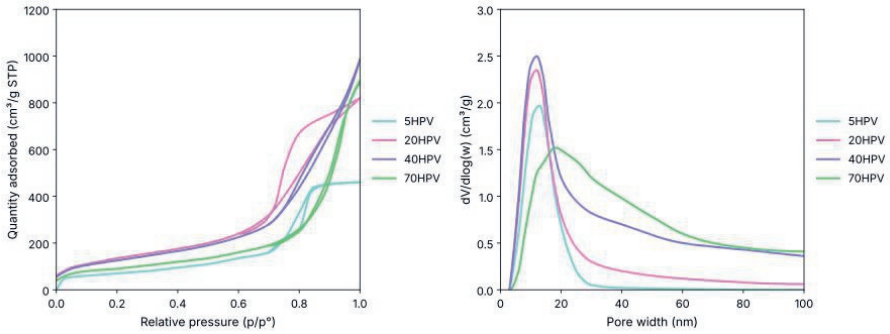

Figure S6.5.2. N_2 physisorption isotherms (top) and pore width distributions (bottom) of the HPV catalysts

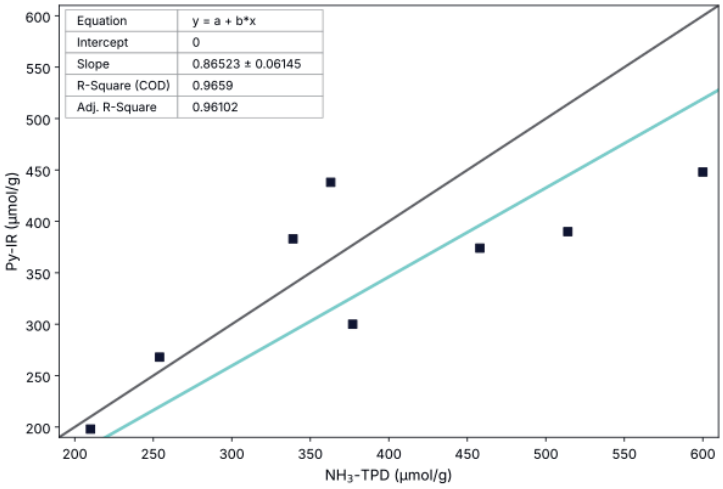

Figure S6.5.3. Parity plot of ammonia TPD vs pyridine IR data (black: parity line: blue: linear regression line

Table S6.5.7. Pyridine IR data for the ASA catalysts

	Brønsted (1535 – 1565 cm^{-1}) [area integration]				Lewis (1429 – 1465 cm^{-1}) [area integration]			
Sample	**Rt**	**150 °C**	**250°C**	**350°C**	**Rt**	**150 °C**	**250°C**	**350°C**
5SPV	0.37	0.13	0.03	0.01	15.6	4.99	1.58	0.99
20SPV	1.31	0.83	0.32	0.02	7.45	5.40	4.08	2.55
40SPV	1.22	0.52	0.22	0.02	7.47	2.00	1.37	0.71
70SPV	0.66	0.34	0.14	0.02	3.71	0.63	0.41	0.12
5HPV	0.27	0.22	0.10	0.02	9.06	9.05	7.59	4.25
20HPV	1.41	1.08	0.07	0.01	11.2	5.71	2.31	1.57
40HPV	1.87	1.64	0.37	0.30	13.4	8.21	3.25	2.64
70HPV	1.23	0.89	0.52	0.28	11.0	2.56	1.92	1.89

	Brønsted (1535 – 1565 cm^{-1})[a] [µmol/g]				Lewis (1429 – 1465 cm^{-1})[b] [µmol/g]			
Sample	**Rt**	**150 °C**	**250°C**	**350°C**	**Rt**	**150 °C**	**250°C**	**350°C**
5SPV	4.76	1.65	0.40	0.07	263	84.4	26.6	16.7
20SPV	43.9	27.9	10.9	0.70	330	91.3	69.0	43.1
40SPV	42.0	17.8	7.49	0.73	341	33.8	23.2	12.0
70SPV	23.4	11.9	4.92	0.76	174	10.7	6.96	2.03
5HPV	6.56	5.41	2.38	0.37	294	153	128	71.9
20HPV	38.7	29.8	2.06	0.32	410	96.5	39.0	26.5
40HPV	37.3	32.7	7.41	6.08	353	139	55.0	44.6
70HPV	34.2	24.8	14.3	7.66	404	43.3	32.4	31.9

[a]Determined using pyridine infrared adsorption experiments using Eq. 6.1; [b]Determined using pyridine infrared adsorption experiments and calculated using Eq. 6.2

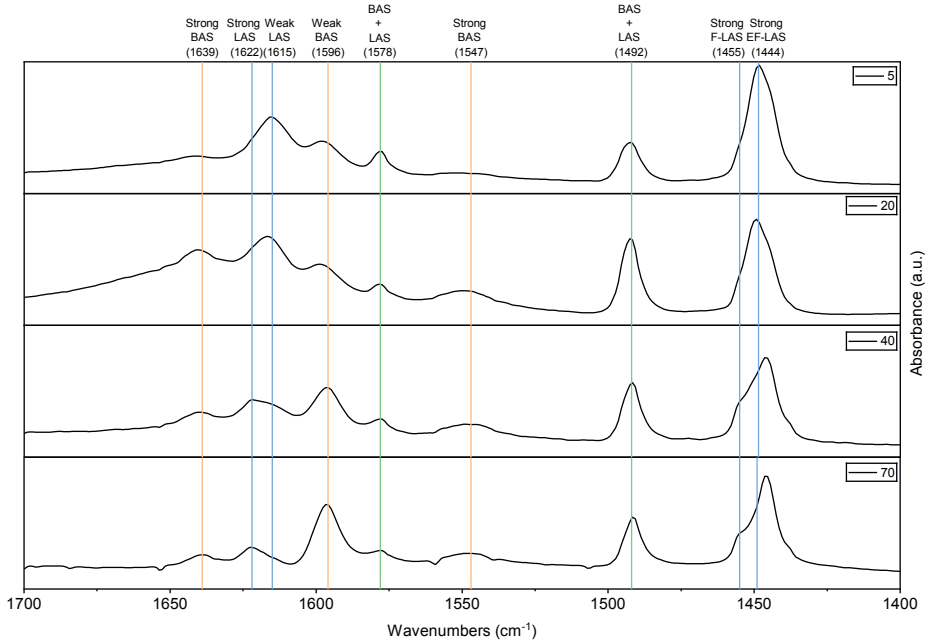

Figure S6.5.4 Pyridine adsorption of the normal pore volume set at room temperature, including peak identification for catalysts: 5SPV, 20SPV, 40SPV, 70SPV. Peak identifications obtained from:[16–20]

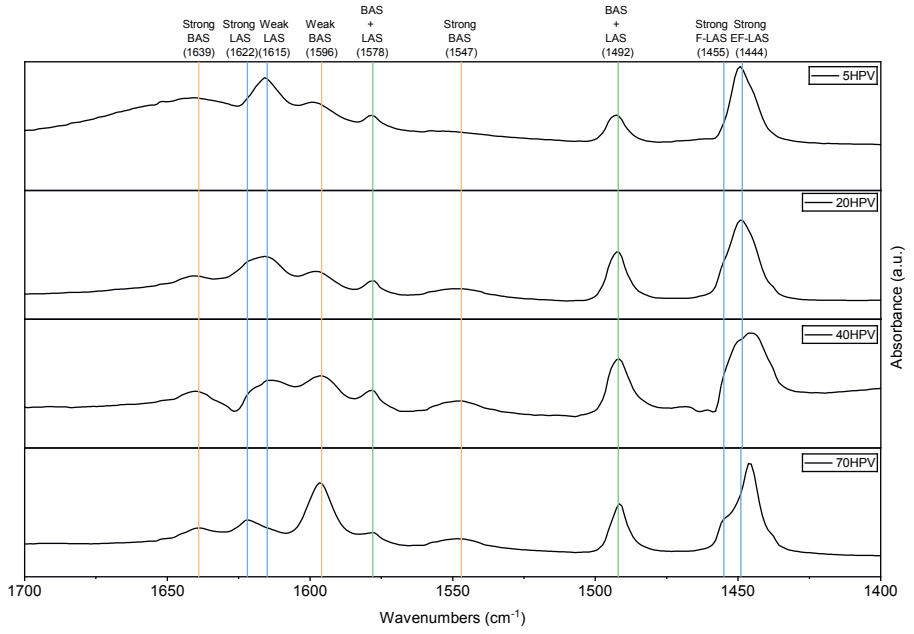

Figure S6.5.5. Pyridine adsorption of the high pore volume set at room temperature, including peak identification for catalysts: 5HPV, 20HPV, 40HPV, 70HPV. Peak identifications obtained from:[16–20]

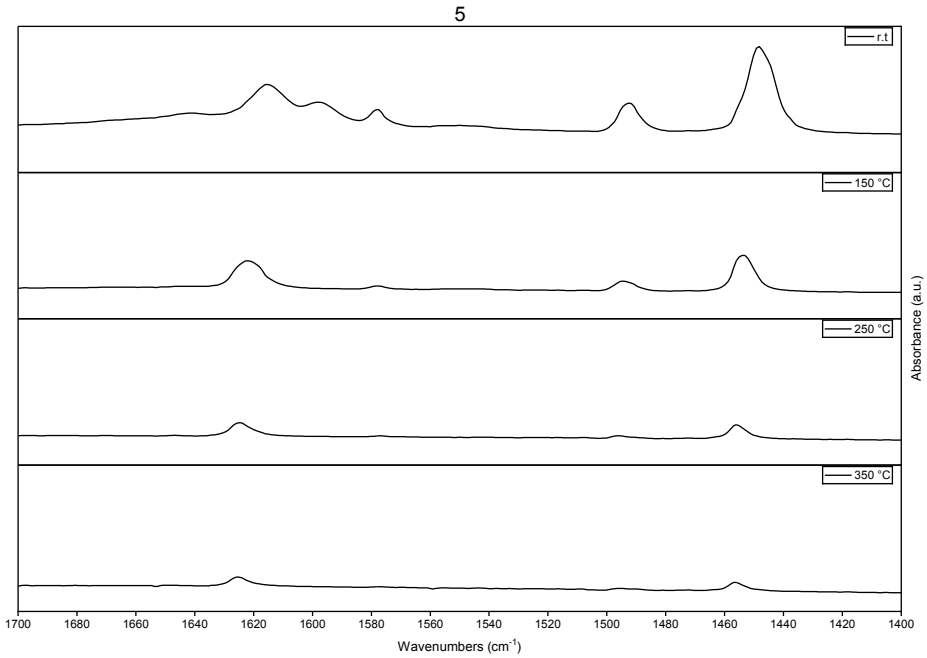

Figure S6.5.6. Pyridine infrared results of Siralox 5SPV. From top to bottom: room temperature, 150 °C, 250 °C, and 350 °C

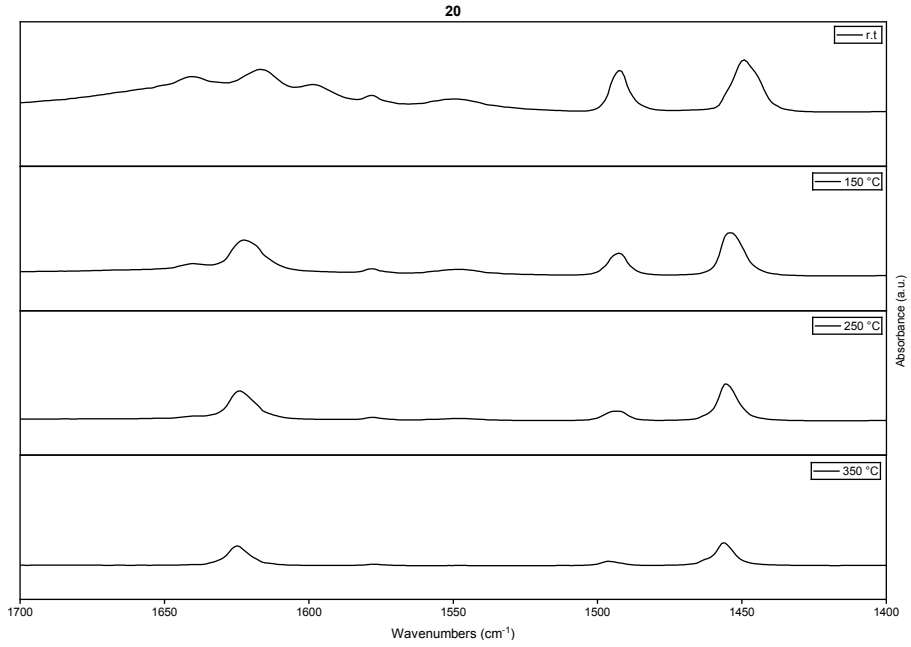

Figure S6.5.7. Pyridine infrared results of Siralox 20SPV. From top to bottom: room temperature, 150 °C, 250 °C, and 350 °C

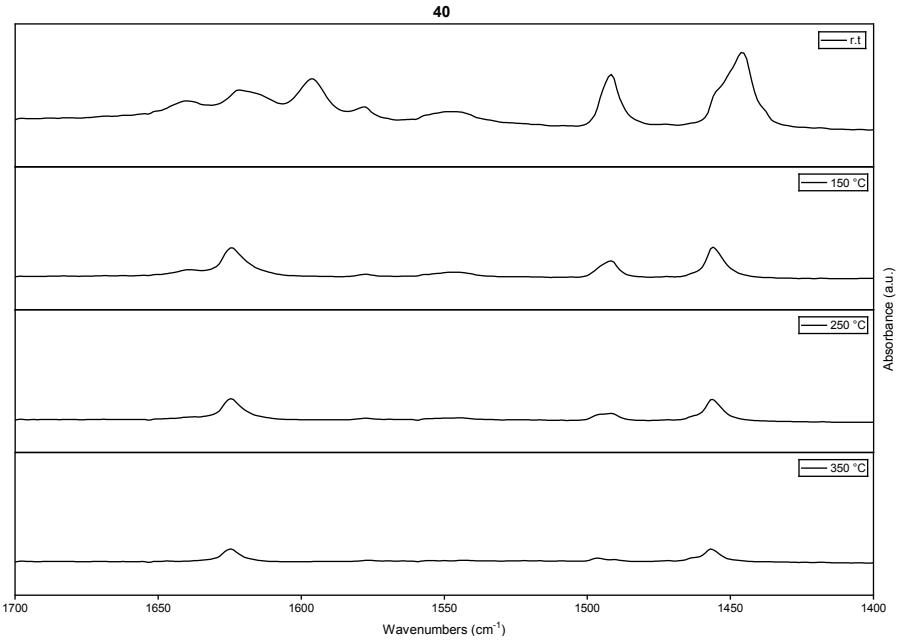

Figure S6.5.8. Pyridine infrared results of Siralox 40SPV. From top to bottom: room temperature, 150 °C, 250 °C, and 350 °C

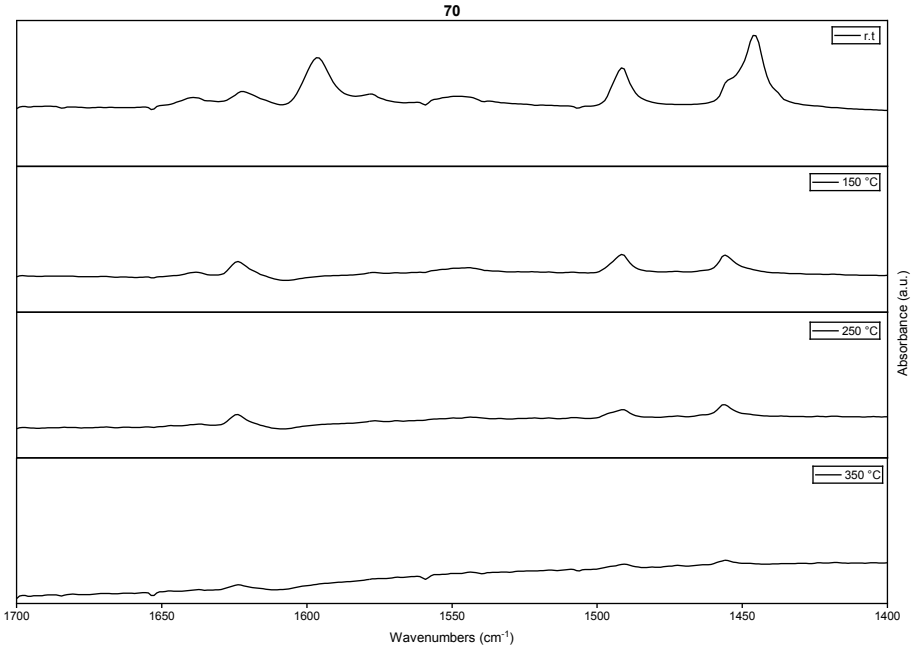

Figure S6.5.9. Pyridine infrared results of Siralox 70SPV. From top to bottom: room temperature, 150 °C, 250 °C, and 350 °C

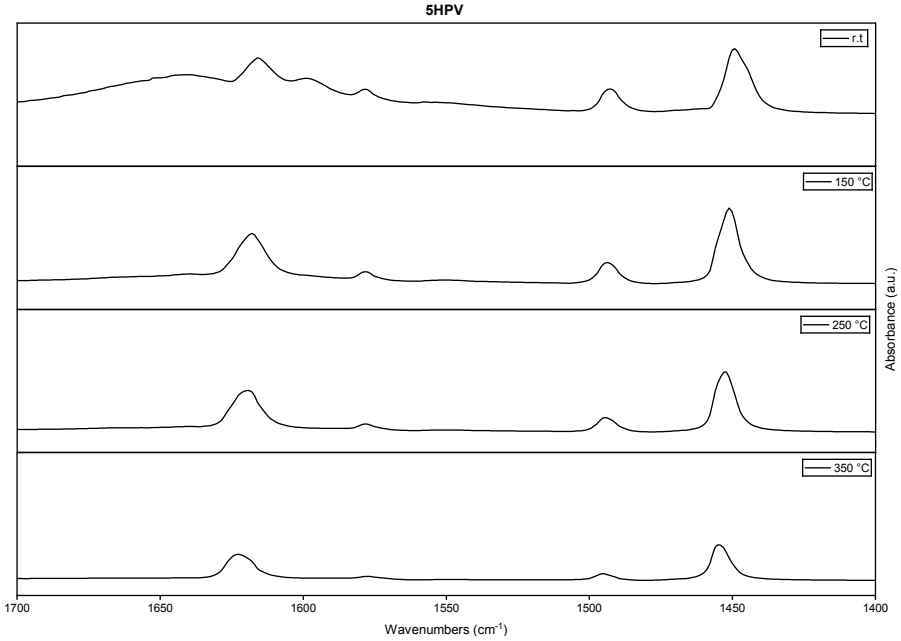

Figure S6.5.10.Pyridine infrared results of Siralox 5HPV. From top to bottom: room temperature, 150 °C, 250 °C, and 350 °C

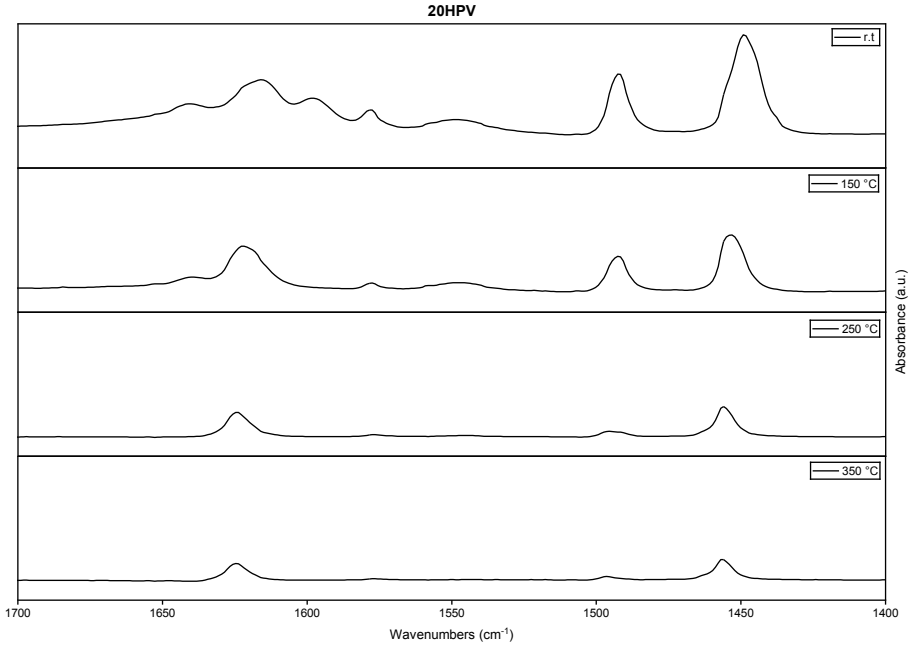

Figure S6.5.11. Pyridine infrared results of Siralox 20HPV. From top to bottom: room temperature, 150 °C, 250 °C, and 350 °C

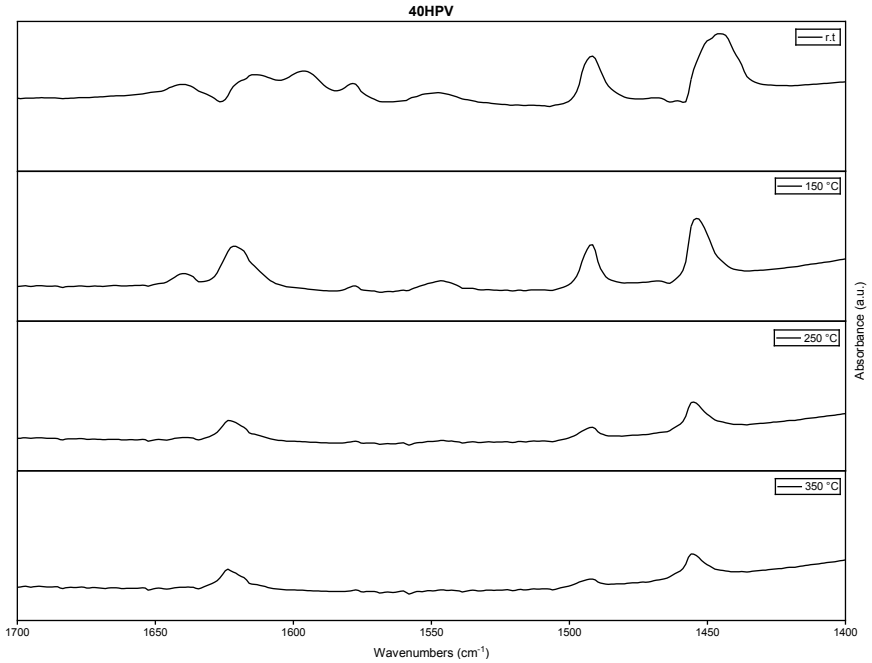

Figure S6.5.12. Pyridine infrared results of Siralox 40HPV From top to bottom: room temperature, 150 °C, 250 °C, and 350 °C

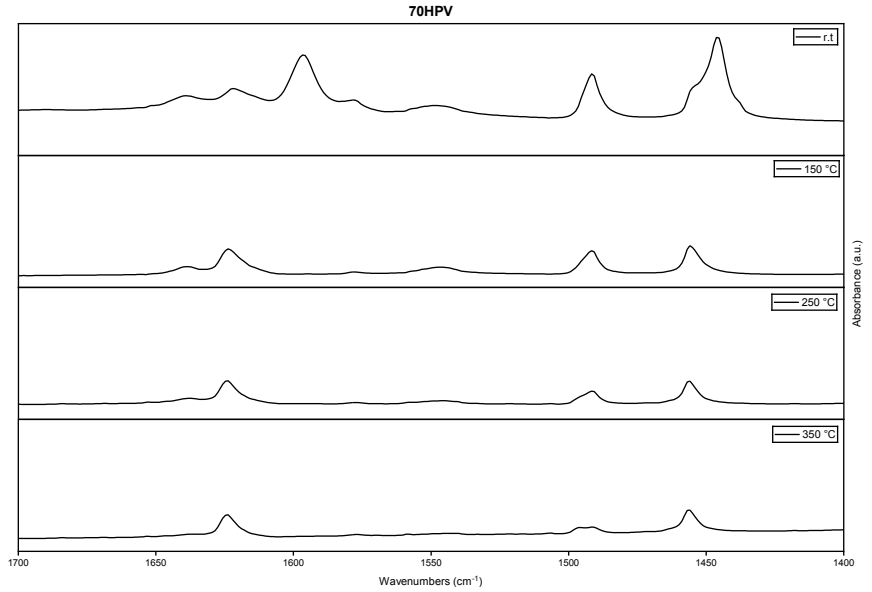

Figure S6.5.13. Pyridine infrared results of Siralox 70HPV. From top to bottom: room temperature, 150 °C, 250 °C, and 350 °C

Table 6.5.8. Input parameters for statistical analysis

Catalyst[a]	Response (%)	Al loading (%)	Surface area (m^2/g)	Pore volume (cm^3/g)	Pore width (nm)	Total Acidity (µmol/g)	Acid site density (µmol/m^2)	Bronsted acidity (µmol/g)	Lewis acidity (µmol/g)	Brønsted /Lewis Ratio
5SPV	23.7	94.5	143	0.74	18	268	1.9	4.76	263	0.02
5SPVDuplicate	24	94.5	143	0.74	18	268	1.9	4.76	263	0.02
20SPV	30.5	79.8	359	1.04	9.0	374	1	43.9	330	0.13
20SPVDuplicate	30.7	79.8	359	1.04	9.0	374	1	43.9	330	0.13
40SPV	24.7	58.5	288	0.98	12	383	1.3	42	341	0.12
40SPVDuplicate	25.1	58.5	288	0.98	12	383	1.3	42	341	0.12
70SPV	22.2	29.1	259	1.22	16	198	0.76	23.4	174	0.13
70SPVDuplicate	21.5	29.1	259	1.22	16	198	0.76	23.4	174	0.13
5HPV	35.7	94.3	242	0.72	9.5	300	1.2	6.56	294	0.02
5HPVDuplicate	35.4	94.3	242	0.72	9.5	300	1.2	6.56	294	0.02
20HPV	32.5	76.5	436	1.29	9.7	448	1	38.7	410	0.09
20Duplicate	32.5	76.5	436	1.29	9.7	448	1	38.7	410	0.09
40HPV	26.1	57.2	383	1.48	12	390	1	37.3	353	0.11
40Duplicate	26.3	57.2	383	1.48	12	390	1	37.3	353	0.11
70HPV	24.8	30.1	292	1.39	16	438	1.5	34.2	404	0.08
70Duplicate	24.9	30.1	292	1.39	16	438	1.5	34.2	404	0.08

Table 6.5.9. Model ranking and model indicators for the models with 2 independent variables

Rank	Independent variables	R^2	Adj. R^2	AIC	AICc	ΔAICc
1	Pore width + B/L ratio	0.947	0.926	29.10	42.43	0.00
2	Pore width + Brønsted acidity	0.877	0.827	35.92	49.26	6.82
3	Al loading + Pore width	0.803	0.725	39.66	53.00	10.56
4	Pore width + Acid site density	0.771	0.679	40.90	54.23	11.80
5	Pore volume + Pore width	0.758	0.661	41.34	54.67	12.23
6	Surface area + Pore width	0.752	0.652	41.53	54.86	12.43
7	Pore width + Lewis acidity	0.693	0.570	43.23	56.56	14.13
8	Pore width + Total acidity	0.693	0.570	43.23	56.57	14.13
9	Surface area + Pore volume	0.680	0.552	43.56	56.89	14.46
10	Al loading + Surface area	0.643	0.500	44.43	57.77	15.33

Table 6.5.10. Model discrimination using linear models with 3 independent variables

Rank	Variables	R^2	Adjusted R^2	AIC	Highest p-value
1	Pore width + Acid site density + B/L	0.958	0.926	29.39	0.384
2	Pore width + Total acidity + Brønsted acidity	0.956	0.924	29.61	0.054
3	Pore width + Brønsted acidity + Lewis acidity	0.956	0.924	29.62	0.054
4	Pore width + Total acidity + Lewis acidity	0.956	0.923	29.67	0.008
5	Surface area + Pore width + B/L	0.955	0.921	29.87	0.461
6	Al loading + Pore width + B/L	0.955	0.920	29.95	0.475
7	Pore volume + Pore width + B/L	0.954	0.919	30.09	0.503

References

1. Tamele, M. W. Chemistry of the surface and the activity of alumina-silica cracking catalyst. *Discuss. Faraday Soc.* **8**, 270–279 (1950).
2. Trombetta, M. *et al.* FT-IR Studies on Light Olefin Skeletal Isomerization Catalysis III. Surface Acidity and Activity of Amorphous and Crystalline Catalysts Belonging to the SiO2-Al2O3 System. *J. Catal.* **179**, 581–596 (1998).
3. Ali, M. A., Tatsumi, T. & Masuda, T. Development of heavy oil hydrocracking catalysts using amorphous silica-alumina and zeolites as catalyst supports. *Appl. Catal. A Gen.* **233**, 77–90 (2002).
4. de Klerk, A. Oligomerization of Fischer-Tropsch olefins to distillates over amorphous silica-alumina. *Energy and Fuels* **20**, 1799–1805 (2006).
5. Triantafyllidis, K. S. *et al.* Hydrothermally stable mesoporous aluminosilicates (MSU-S) assembled from zeolite seeds as catalysts for biomass pyrolysis. *Microporous and Mesoporous Materials* **99**, 132–139 (2007).
6. Xu, B. *et al.* Strong Brønsted acidity in amorphous silica - Aluminas. *Journal of Physical Chemistry C* **111**, 12075–12079 (2007).
7. Hensen, E. J. M., Poduval, D. G., Magusin, P. C. M. M., Coumans, A. E. & Veen, J. A. R. van. Formation of acid sites in amorphous silica-alumina. *J. Catal.* **269**, 201–218 (2010).

8. Zabeti, M., Nguyen, T. S., Lefferts, L., Heeres, H. J. & Seshan, K. In situ catalytic pyrolysis of lignocellulose using alkali-modified amorphous silica alumina. *Bioresour. Technol.* **118**, 374–381 (2012).
9. Ishihara, A. Preparation of Amorphous Silica-Alumina Using the Sol-Gel Method and its Reactivity for a Matrix in Catalytic Cracking. *Catalysis Surveys from Asia* **16**, 36–47 (2012).
10. Klaimy, S. *et al.* Flash Catalytic Pyrolysis of Polyethylene over (Alumino)silicate Materials. *ChemCatChem* **12**, 1109–1116 (2020).
11. Wang, Z., Jiang, Y., Baiker, A. & Huang, J. Pentacoordinated Aluminum Species: New Frontier for Tailoring Acidity-Enhanced Silica-Alumina Catalysts. *Acc. Chem. Res.* **53**, 2648–2658 (2020).
12. Li, T. *et al.* Synthesis and characterization of amorphous silica-alumina with enhanced acidity and its application in hydro-isomerization/cracking. *Fuel* **279**, 118487 (2020).
13. Bao, J. *et al.* Synthesis of amorphous silica-alumina with enhanced specific surface area and acidity by pH-swing method and its catalytic activity in cumene cracking. *Microporous and Mesoporous Materials* **337**, 111897 (2022).
14. Karami, H. *et al.* Amorphous silica-alumina as robust support for catalytic dehydrogenation of propane: Effect of Si/Al ratio on nature and dispersion of Cr active sites. *Appl. Catal. A Gen.* **658**, 119167 (2023).
15. Reif, P., Gupta, N. K. & Rose, M. Highly stable amorphous silica-alumina catalysts for continuous bio-derived mesitylene production under solvent-free conditions. *Green Chemistry* **25**, 1588–1596 (2023).
16. Crépeau, G. *et al.* Nature, structure and strength of the acidic sites of amorphous silica alumina: An IR and NMR study. *Journal of Physical Chemistry B* **110**, 15172–15185 (2006).
17. Hensen, E. J. M. *et al.* Acidity characterization of amorphous silica-alumina. *Journal of Physical Chemistry C* **116**, 21416–21429 (2012).
18. Rivera-Barrera, D. & Poveda-Jaramillo, J. C. Thermal desorption of trimethylphosphine (TMP) on the HY zeolite followed by FT-IR and 31P MAS NMR. *J. Solid State Chem.* **294**, 121862 (2021).
19. Rivera-Barrera, D., Guzman, A., Ramirez, I. & Molina V, D. Effect of Si/Al ratio, calcination temperature and post-synthesis phosphorus modification on the textural, structural, acidic, and catalytic properties of amorphous silica-alumina prepared by deposition methods. *Journal of Physics and Chemistry of Solids* **209**, 112403 (2026).
20. Bao, J. *et al.* Synthesis of amorphous silica-alumina with enhanced specific surface area and acidity by pH-swing method and its catalytic activity in cumene cracking. *Microporous and Mesoporous Materials* **337**, 111897 (2022).



Summary, perspective, and final remarks



7

7.1. Context and objectives

The growing demand for plastics is reflected in a vast increase in global plastic production, which reached 430.9 million metric tons in 2024.[1] This has led to a significant increase in plastic waste, which is currently mainly landfilled or incinerated. In the context of material transition, developing efficient recycling methods for plastic waste is essential. The growing environmental impact of plastics and the limited recycling options have prompted substantial regulatory and research initiatives within the European Union. Several collaborative programs were launched to accelerate the transition toward a circular plastics economy within the framework of the European Green Deal[2] and the Circular Economy Action Plan.[2–5]

Polyurethanes, an important class of plastics with many applications, are notoriously difficult to recycle.[6] Consequently, only approximately 25% of polyurethane waste is currently mechanically recycled, with the remaining 75% disposed of by incineration or landfilling. [7] State-of-the-art work on polyurethane recycling demonstrated successful closed-loop strategies for recovering polyols at TRL level 3-5. [8]However, an efficient recycling strategy for the isocyanate segment is yet to be discovered. In particular, MDI-based foams remain difficult to recycle, with only one chemical recycling pathway reported to recover 87% pMDA via ammonolysis. [9] However, minor impurities and/or shifts in oligomer distribution hinder their conversion into high-quality pMDI. Consequently, there is considerable interest in developing a method for recovering aniline, as it can be easily purified and reused in the pMDI-based production chain.

The Circular Foam project[10] a Horizon 2020 project[11] aimed to develop an integrated value chain for polyurethane recycling encompassing improved waste collection, chemical recycling technologies for polyol and isocyanate recovery, and the introduction of recycled materials in new polyurethane products. Through coordinated industrial, academic, and regional collaboration, the project aimed to develop a scalable and economically viable solution for the circular management of rigid polyurethane foam waste. The research described in this dissertation was conducted within work package 4 of the Circular Foam project, with the goal of developing an improved catalytic process for aniline recovery from PUR waste.

Catalytic pyrolysis has emerged as a promising route to recycle rigid polyurethane foams into valuable low-molecular-weight chemicals, including nitrogen-containing compounds.[12] Heterogeneous catalysts are typically used in catalytic pyrolysis due to their robustness under harsh conditions, ease of separation, and potential for scalability in industrial polyurethane recycling.

The research presented in this thesis builds on prior patented work[13], which described the pyrolysis of PUR in a fixed bed reactor at 500 °C using an alumina-magnesium catalyst. To advance this process and to increase the TRL from 2 to 4, the aim of this PhD project was to I) screen a wide range of potentially attractive catalysts, II) set up a catalyst property performance relationship to identify the most important catalyst properties and use this information to design improved catalysts, and III) gain insights in catalyst stability and when stability is insufficient for scale up, identify potential solutions to improve stability, IV) develop a mechanistic understanding of the reactions taking place at molecular level and V) scale up the process to TRL 5.

7.2. Summary

The prelude (Chapter 1) introduces the Circular Foam project and places it within the broader context of Europe's ambitions to transition to a circular plastics economy. Each work package is briefly presented, with an emphasis on work package 4, which focuses on developing a recycling pathway for rigid polyurethane foams and is the topic of this PhD thesis.

The Introduction (Chapter 2) presents the issue of plastic waste, with particular emphasis on polyurethanes. State-of-the-art work on recycling rigid pMDI-based polyurethanes is outlined, with particular attention to the literature on recovering nitrogen- containing chemicals from the isocyanate segments. In this context, catalytic pyrolysis emerged as an attractive recycling strategy. Key considerations for catalytic pyrolysis are discussed to provide the reader with sufficient conceptual and practical understanding of the research described in the subsequent chapters. The chapter concludes with specific strategies to address these issues, presented in the following sections.

Chapter 3 describes a catalytic strategy for recovering aniline from end-of-life rigid polyurethane (PUR) foam waste. Initial catalyst screening at a batch milligram scale showed that an alumina-based catalyst gave the highest aniline yield. An extended catalyst screening study with a wide range of alumina catalysts identified catalyst SCCa 5/200 as the best option, with surface area and acidity as the most relevant parameters for aniline formation. Up to 50% aniline yield, based on the nitrogen content in the feed (N%), was obtained using a tandem microreactor at 550 °C, with an additional 15 N% as toluidine. Upscaling was conducted in multiple stages, from mg-scale to continuous operation at >100 $g_{\text{feedstock}}\ h^{-1}$ and 5 $kg_{\text{feedstock}}\ h^{-1,}$ achieving a combined aniline and toluidine yield of 25 N%. Techno-economic evaluations were performed based on a preliminary process design, indicating that catalyst use is a significant cost driver. The environmental impact was assessed which revealed a CO_2 reduction of 0.6 $ton \cdot ton_{PUR}^{-1}$ under non-optimized conditions.

The long-term stability and deactivation mechanisms of the alumina-based SCCa 5/200 catalyst were evaluated, and the results are provided in Chapter 4. Distinct changes in catalyst performance were observed during multiple catalytic pyrolysis cycles using post-production polyurethane (nPUR) without intermediate reactivation. Results revealed significant catalyst deactivation, accompanied by a shift in chemoselectivity from aniline and toluidine to predominantly MDA formation. Analysis showed that hard coke formation was the primary cause of deactivation. The catalyst could be regenerated via oxidative reactivation at 550 °C, with the main changes in catalyst properties being the surface area and acidity. Multiple regeneration-recycle cycles were performed at batch milligram scale using nPUR and end-of-life rigid polyurethane foam (EOL PUR) to determine the limits of catalyst lifetime and the main cause of deactivation. Catalyst activity for nPUR was reduced in the first 4 reaction-regeneration cycles, stabilized at half of the original activity for 28 cycles, and decreased in the remaining cycles to a value close to thermal pyrolysis. For EOL, catalyst stability was significantly worse, and the catalytic reaction performance was equal to thermal pyrolysis after 18 reaction-regeneration cycles. The spent catalysts for both PUR feeds were characterized using GC-MS/FID, TEM-EDX, indicating that coking was the main cause of deactivation for nPUR and metal contamination (primarily iron) for EOL PUR.

Chapter 5 describes a study focused on identifying molecular pathways involved in the thermal and catalytic pyrolysis (using SCCa 5/200) of PUR by using deuterated and ^{13}C-labeled model compounds. Changes in isotopic distribution and label positions were identified through careful analysis of the

products' fragmentation patterns. These changes provided key insights into the depolymerization of rigid MDI-based polyurethane foams into low-molecular-weight N-containing compounds. Results showed that catalytic pyrolysis leads to the cracking of the isocyanate methylene bridge, thereby promoting the formation of the desired target molecules (aniline and toluidine). Product fragmentation pattern analysis of deuterated model compounds revealed a unidirectional flow of hydrogen atoms from the alcohol to the isocyanate segment, suggesting that the α-hydrogen (with a calculated low bond energy) of an isopropanoyl moiety is most mobile and therefore contributes primarily to the decomposition of MDA into aniline and toluidine. Pyrolysis of ^{13}C-enriched model compound confirmed that side product formation (acridine and methylacridine) arises only from a cross-reaction between two isocyanate fragments, possibly via an intermolecular mechanism. To explain the observations, a 3-step mechanism was proposed that begins with a retropolymerization, assisted by Lewis acid site coordination on the catalyst, forming MDA, CO, CO_2, propene, and acetone. The methylene bridge of the MDA fragment is cleaved by hydrogen donation (most likely from the α-H of polyol), resulting in aniline and toluidine. N-containing side products form via **I**) cross reaction between polyol- and isocyanate fragments (ethylaniline and ethyltoluidine) or **II**) homocoupling between isocyanate fragments (aniline and toluidine) to form acridine and methylacridine.

Experimental studies aimed at identifying catalyst performance structure relations are described in Chapter 6. Studies involved catalytic pyrolysis of nPUR at the batch-milligram scale using a range of amorphous silica-alumina (ASA) catalysts. Statistical modeling revealed a maximum yield of aniline and toluidine of 36.6 N%, at a Brønsted-to-Lewis ratio of 0.05 and a pore width of 9.1 nm. Additionally, the absence of MDA suggested that Brønsted acidity promotes cracking of MDA into aniline and toluidine.

The research described in this dissertation has provided valuable insights into the catalytic pyrolysis of waste rigid polyurethane foam to produce aniline and toluidine. On a molecular level, catalyst screening studies revealed that alumina and ASA catalysts are promising for further scale-up. Relevant knowledge has been gained on the mechanism of catalytic pyrolysis, which will aid in developing tailored catalyst formulations. In addition, catalyst stability has been assessed in detail, and relevant deactivation pathways have been identified. This knowledge will aid in developing efficient strategies for catalyst reuse and recycling, thereby reducing catalyst costs. At the process level, the catalytic pyrolysis concept was scaled up to pilot scale (5 $kg_{feedstock}$ h^{-1}), yielding a combined aniline yield of 25 N%. The findings will aid the further scale-up of the process and, more broadly, contribute to the development of efficient recycling strategies for waste plastics.

7.3. Perspective

Beyond Circular Foam

The Circular Foam project successfully demonstrated the feasibility of recovering aniline from waste polyurethane foam by catalytic pyrolysis. The process was validated at a 5 kg h^{-1} scale, and the aniline from these tests was used to produce a PUR-based isolation foam. The chemical and physical properties of this foam from recycled aniline were shown to be equal to those of a virgin PUR-based foam. The project reached Technology Readiness Level (TRL) 6, corresponding to a validated prototype system. Progression to TRL 9, representing full commercial deployment, requires the construction and continuous operation of a demonstration plant to verify long-term technical and economic viability.

To this end, the industrial partner Covestro aims to advance the technology toward commercialization by constructing a 2-kiloton-per-year pilot plant, which is expected to be operational in 2028.[14]

Waste product utilization

The catalytic pyrolysis process produces, next to the desired aniline, significant amounts of gases and solids. To reduce the environmental impact and to increase the economic viability of the process, outlets for these byproducts need to be identified. Typical pyrolysis gases contain a mixture of C1–C4 hydrocarbons, CO, and CO_2. Possible valorization routes for these gases include the conversion to higher hydrocarbons e.g. via the Fischer-Tropsch process (FTS)[15] or by producing advanced carbon materials such as nanotubes (CNT)[16]. The solid has fuel value or may alternatively be used as biochar.

Catalyst recycling

Techno-economic analysis identified the catalyst as a dominant cost driver, forming the basis for the catalyst lifetime study presented in Chapter 4. The results showed rapid deactivation in the presence of metal contaminants, specifically iron species, whereas a cleaner feed (post-production PUR) showed a significantly longer catalyst lifetime. For this reason, it is essential to identify the most detrimental impurities and implement pre-separation technologies or in-process purification steps to preserve catalytic activity. End-of-life spent catalyst may be used as an absorbent [17,18] or in the conductor industry.[19]

Aniline yield improvement

The mechanistic investigations presented in Chapter 5 offered valuable insights into the various reactions occurring during the catalytic pyrolysis of polyurethanes. Based on these insights, it was shown that MDA conversion to aniline and toluidine requires a hydrogen donor, and that one option is the polyol segment in the PUR. This was further evaluated by conducting model experiments with MDA derivatives bearing different terminal alcohol groups (OMe, OEt, O^iPr, O^nHex). Details can be found in the supporting section of this chapter. It was shown that the presence of an O^iPr group increases the yields of aniline and toluidine, while the amounts of MDA and other byproducts are significantly reduced. This implies that structural changes in the polyol segment, the hydrogen donor for MDA cleavage to the desired aniline and toluidine, may lead to higher yields of these products. Thus, changes in the polyol formulation may increase the aniline yield and thus the economic viability of the catalytic pyrolysis approach.

A possible alternative hydrogen source to cleave the MDA bridge to aniline and toluidine is H_2 gas. Preliminary experiments with H_2 were conducted in the TMR with an alumina-based catalyst (SCCa 5/200). Mian products in this case were aromatics, mainly BTX, indicative of overcracking and undesired deamination reactions, most likely due to the presence of acid sites on the catalyst. As such, an additional experiment was performed with a basic catalyst (Y_2O_3) first in the absence of hydrogen, which was shown to produce high amounts of MDA (Chapter 3). Combining Y_2O_3 with pure H_2 gas, intended to assist the cleavage of MDA, unfortunately resulted only in volatile formation, and neither aniline/toluidine nor BTX was detected. Details on these experiments are provided in the supporting section of this chapter

Long-term challenges

The Circular Foam project successfully demonstrated that, in addition to aniline recovery via catalytic pyrolysis, polyol recovery via chemolysis is also possible. However, as the project progressed, technical and non-technical challenges stemming from current regulations emerged, posing significant barriers to the use of recycled plastics.

The technology-oriented work packages (2–7) revealed substantial constraints in developing a universal recycling method for polyurethane foam, as many different types of foams are on the market, each tailored to a specific application. As a result, each polyurethane end-of-life stream yields different amounts of aniline. Moreover, this complicates downstream processing of the liquids due to the varying types and levels of contaminants in the stream. Industrial stakeholders and policy actors who focused on the non-technical work packages (1, 7, and 8) concluded that governmental engagement is critical, since regulatory frameworks and policy incentives play a decisive role in enabling large-scale adoption of recycling technologies. In particular, consumers should also be convinced that recycled products produced by chemical recycling methods have properties comparable to those of virgin feedstocks and should not be considered inferior. In addition, it was shown that, in addition to general actions, region-specific strategies are required to address the challenges associated with polyurethane recycling.

Final remarks

The research described in this dissertation has shown that catalytic pyrolysis is a potential waste-valorization option for end-of-life polyurethanes. Over the 4-year period, the technology was scaled up and validated at TRL 4-5. In addition, product development showed promising results, and a polyurethane foam was successfully produced from aniline derived from waste PUR using catalytic pyrolysis technology. The announcement that further scale-up is foreseen by one of the industrial partners (as discussed in 3.1) shows the promise of the technology for further commercialization.

So what are the remaining hurdles for implementation?

I) Successful implementation of a circular system requires alignment between technology and supportive legislative actions. It is evident that a circular transition is not merely a technological challenge but also a transformation of societal mindsets, requiring coordinated efforts across multiple sectors.

II) The manufacturing price of recycled polyurethane foam has to be in the same ball game compared to the current, fossil-based virgin products. This needs to be established in future scale-up activities, but is currently considered a significant hurdle. Targeted governmental interventions may facilitate this, for instance, through regulations that promote the incorporation of circular feedstocks into polymer production and/or penalties for the use of virgin fossil-based feeds.

References

1. Plastics Europe AISBL. Plastics the Fast Facts 2025. (2025).
2. Akindoyo, J. O. et al. Polyurethane types, synthesis and applications-a review. RSC Adv. **6**, 114453–114482 (2016).
3. Pillich, M., Schilling, J., Bosetti, L. & Bardow, A. What to do with polyurethane waste? The environmental potential of chemically recycling polyurethane rigid foam. Green Chemistry **26**, 10893–10906 (2024).
4. Liu, B. et al. Opportunities in Closed-Loop Molecular Recycling of End-of-Life Polyurethane. ACS Sustain. Chem. Eng. **11**, 6114–6128 (2023).
5. Van Belleghem, L. et al. Recovery of Polyol and Aromatic Amines from Rigid Polyurethane Foams via Ammonolysis. JACS Au **5**, 3444–3452 (2025).
6. van Akker, M. et al. Full Utilization of Hard-to-Recycle Mixed Plastic Waste by Conversion toward Pyrolysis Oil and BTX Aromatics on a Pilot Scale. Energy and Fuels **39**, 6438–6451 (2025).
7. von der Leyen, U. The European green deal. (2019).
8. European Commission Directorate-General for Communication. The European Green Deal. https://commission.europa.eu/strategy-and-policy/priorities-2019-2024/european-green-deal_en.
9. European Parliament and the Council of the European Union. Directive (EU) 2025/1892 of the European Parliament and of the Council of 10 September 2025 Amending Directive 2008/98/EC on Waste. http://data.europa.eu/eli/dir/2009/ (2025).
10. European Parliament and the Council of the European Union. Regulation (EU) 2025/40 of the European Parliament and of the Council of 19 December 2024 on Packaging and Packaging Waste, Amending Regulation (EU) 2019/1020 and Directive (EU) 2019/904, and Repealing Directive 94/62/EC. http://data.europa.eu/eli/reg/2024/1781/oj (2025).
11. DECHEMA Gesellschaft für Chemische Technik und Biotechnologie e.V. CIRCULAR FOAM – Systemic expansion of territorial CIRCULAR Ecosystems for end-of-life FOAM. https://circular-foam.eu.
12. ICONS Italy. The LOOP Cluster. https://circular-foam.eu/About+us/Related+Initiatives/_/FRONT1SHIP_Loop_Factsheet__20240404.pdf.
13. Eiden, S. et al. Pyrolysis of polyurethane compound-containing material in order to recover raw materials. (2024).
14. Bart Pals. Covestro en Fraunhofer bouwen pilotinstallatie voor pyrolyse-recycling van PUR-schuim. https://www.industrielinqs.nl/chemie/2026/03/covestro-en-fraunhofer-bouwen-pilotinstallatie-voor-pyrolyse-recycling-van-pur-schuim/?gdpr=accept&gdpr=accept (2026).
15. de Jong, B. C. A. et al. Sustainable Fuels from CO2-Rich Synthesis Gas via Fischer-Tropsch Technology. ACS Catal. **15**, 10946–10956 (2025).
16. Kumar Singh, R., Ruj, B., Kumar Sadhukhan, A. & Gupta, P. Conventional pyrolysis of Plastic waste for Product recovery and utilization of pyrolytic gases for carbon nanotubes production. Environ Sci Pollut Res **29**, 20007–20016 (2020).
17. Al-Gaashani, R., Almasri, D., Shomar, B. & Kochkodan, V. Preparation and properties of novel activated carbon doped with aluminum oxide and silver for water treatment. J. Alloys Compd. **858**, (2021).

18. Abussaud, B. et al. Sorption of phenol from waters on activated carbon impregnated with iron oxide, aluminum oxide and titanium oxide. J. Mol. Liq. **213**, 351–359 (2016).
19. Jaouadi, M., Andolsi, A. & Ghodbane, O. Activated Carbon–Aluminum Oxide Composite Material on Nickel Foam as Supercapacitor Electrode in KOH Electrolyte. Energy Technology **13**, 2500123 (2025).
20. European Parliament and the Council of the European Union. Regulation (EC) No 1907/2006 of the european parliament and of the council of 18 December 2006 concerning the Registration, Evaluation, Authorisation and Restriction of Chemicals (REACH), establishing a European Chemicals Agency, amending Directive 1999/45/EC and repealing Council Regulation (EEC) No 793/93 and Commission Regulation (EC) No 1488/94 as well as Council Directive 76/769/EEC and Commission Directives 91/155/EEC, 93/67/EEC, 93/105/EC and 2000/21/EC. (2006).
21. European Parliament and the Council of the European Union. Directive (EU) 2019/904 of the European parliament and of the council of 5 June 2019 n the reduction of the impact of certain plastic products on the environment. (2019).
22. Wegener, J. et al. Stakeholder map and regional readiness for a systemic territorial solution D1.1. https://doi.org/10.48812/uew.wir/bnyn7844 (2023) doi:10.48812/uew.wir/bnyn7844.
23. Volpi, M. P. C., Silva, J. C. G., Hornung, A. & Ouadi, M. Review of the Current State of Pyrolysis and Biochar Utilization in Europe: A Scientific Perspective. Clean Technologies **6**, 152–175 (2024).
24. Zhao, Y. et al. Is pyrolysis technology an advisable choice for municipal solid waste treatment from a low carbon perspective? Chemical Engineering Journal **449**, 137785 (2022).
25. European Commission. Questions and answers on the circularity plastics package. https://ec.europa.eu/commission/presscorner/detail/en/qanda_25_3152 (2025).

7.4. Supporting information

Upstream modifications

Materials

Unless otherwise indicated, reagents and substrates were used as received. Standard chemicals were purchased from Sigma Aldrich, the labelled compounds were obtained from Cambridge Isotopes, and technical-grade solvents were purchased from Boom B.V. Meppel. Dry solvents were collected from a dry solvent purification system. Inert-atmosphere experiments were performed using standard Schlenk techniques with dry P_2O_5-nitrogen gas or in the glovebox.

The catalyst used in this study is an alumina-based catalyst (Puralox SCCa 5/200) obtained from Sasol Germany. It is a semi-crystalline, mesoporous catalyst with 99% purity and a pore volume of 0.59 cm^3/g. Other elements present include 0.6% magnesium oxide and 0.2% calcium oxide. The catalyst has an average agglomerate size of 84 µm, composed of 15 nm particles. The catalyst has a surface area of 218 m^2/g with an acidity of 406 µmol/g. See chapter 3 for more details on the catalyst.

1. Dimethyl (methylenebis(4,1-phenylene))dicarbamate

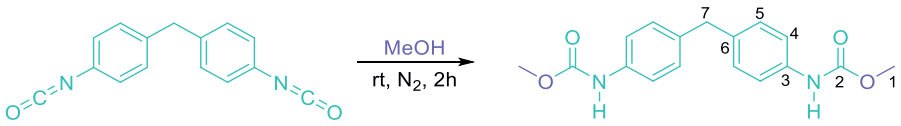

0.45 mmol **99%**

4,4'-methylenediphenyl diisocyanate (0.45 mmol, 113 mg) was dissolved in 3 mL Methanol at room temperature. The reaction progress was monitored by TLC using n-hexane/ethyl acetate 80:20 ratio. TLC analysis indicated the formation of a single product after 2 hours. Upon completion, the reaction mixture was concentrated under vacuo, affording a white solid in 99 % yield.

^{1}H-NMR (400 MHz, CD_3COCD_3): δ 8.53 (s, 2H, N-H), 7.47 (d, *J* = 8.73 Hz, 4H, C4-H), 7.14 (d, *J* = 7.50 Hz, 4H, C5-H), 4.09 (t, *J* = 6.41, 4H, C7-H), 3.67 (s, 6H, C1-H)

^{13}C-NMR (400MHz, CD_3COCD_3): δ 154.00 (C2), 137.41, 135.62 (C3), 128.82, 118.21 (C4), 51.05 (C1), 40.15 (C5)

^{1}H and ^{13}C NMR data is shown in Figure S7.4.1 and Figure S7.4.2

2. Diethyl-(methylenebis(4,1-phenylene))dicarbamate

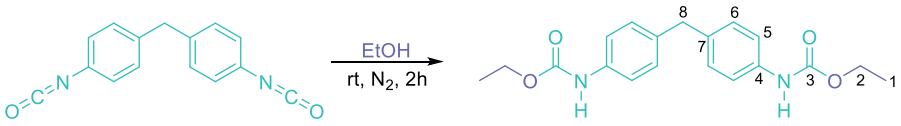

0.47 mmol **99%**

4,4'-methylenediphenyl diisocyanate (0.47 mmol, 118 mg) was dissolved in 1 mL ethanol at room temperature, and the reaction progress was monitored by TLC using n-hexane/ethyl acetate 80:20 ratio. TLC analysis indicated the formation of a single product after 2 h. Upon completion, the reaction mixture was concentrated *in vacuo*, affording a white solid in 99% yield.

^{1}H-NMR (400 MHz, CD_3COCD_3): δ 9.46 (bs, 2H, N-H), 7.46 (d, *J* = 8.75 Hz, 4H, C5-H), 7.07 (d, *J* = 9.11 Hz, 4H, C6-H), 4.07 (q, *J* = 7.17 Hz, 4H, C2-H), 3.76 (s, 2H, C8-H), 1.21 (t, *J* = 6.81 Hz, 6H, C1-H)

^{13}C-NMR (400MHz, CD_3COCD_3): δ 153.01 (C3), 137.56 (C4 or 7), 135.76 (C4 or 7), 129.23 (C6), 118.28 (C5), 60.38 (C2), 40.24 (C8), 14.83 (C1)

^{1}H and ^{13}C NMR data is shown in Figure S7.4.3 and Figure S7.4.4

3. Diisopropyl (methylenebis(3,1-phenylene))dicarbamate

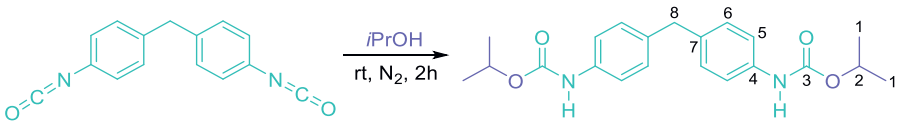

4,4'-methylenediphenyl diisocyanate (4.0 mmol, 1.0 g) was dissolved in 25 mL isopropanol under nitrogen at room temperature, and the reaction progress was monitored by TLC using n-hexane/ethyl acetate 70:30 ratio. TLC analysis indicated the formation of a single product after 2 h. Upon completion, the reaction mixture was concentrated *in vacuo*, affording a white solid in 99% yield.

^{1}H-NMR (400 MHz, $CDCl_3$): δ 7.27 (d, *J* = 7.24 Hz, 4H, C5-H), 7.09 (d, *J* = 8.45 Hz, 4H, C6-H), 6.46 (bs, 2H, N-H), 5.00 (m, 2H, C2-H), 3.88 (s, 2H, C8-H), 1.28 (d, *J* = 7.25 Hz, 12H, C1-H)

^{13}C-NMR (400MHz, $CDCl_3$): δ 153.01 (C3), 136.31 (C4 or 7), 136.26 (C4 or 7), 129.35 (C6), 118.97 (C5), 68.66 (C2), 40.38 (C8), 21.88 (C1)

HRMS (ESI) m/z: $[M+H]^+$ calcd for $C_{21}H_{27}N_2O_4$ 371.1965; found 371.1959

^{1}H, ^{13}C, COSY, and HSQC NMR data is shown in Figure S7.4.5 and Figure S7.4.8

4. Di-tert-butyl (methylenebis(4,1-phenylene))dicarbamate

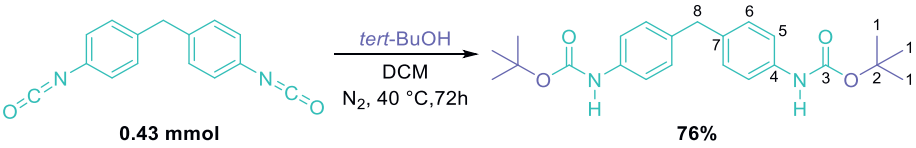

4,4'-methylenediphenyl diisocyanate (0.43 mmol, 108.6 mg) and *tert*-Butanol (15 mmol, 1.17 g) were dissolved in 3 mL DCM and heated to 40 °C. The reaction progress was monitored by TLC using n-hexane/ethyl acetate 70:30 ratio. TLC analysis indicated the formation of a single product after 3 days. Upon completion, the reaction mixture was concentrated under vacuo, affording a white solid in 76 % yield.

^{1}H-NMR (400 MHz, C_4D_8O): δ 10.42 (s, 2H, N-H), 9.21 (d, *J* = 8.56 Hz, 4H, C5 or C6-H), 8.89 (d, *J* = 8.56 Hz, 4H, C5 or C6-H), 5.68 (s, 2H, C8-H), 5.50 (s, 6H, C1-H)

^{13}C-NMR (400MHz, C_4D_8O): δ 153.60 (C3), 137.55, 135.39 (C4 and C7), 128.63, 117.90 (C5 and C6), 50.84 (C1), 40.22 (C8), 24.38 (C1)

^{1}H and ^{13}C NMR data is shown in Figure S7.4.9 and Figure S7.4.10

5. Dihexyl (methylenebis(4,1-phenylene))dicarbamate

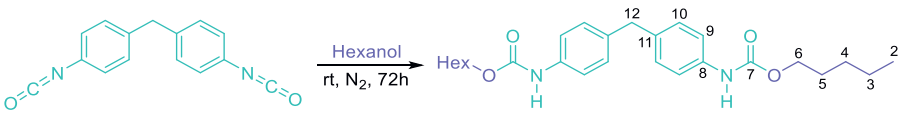

0.47 mmol **99%**

4,4'-methylenediphenyl diisocyanate (0.47 mmol, 116.3 mg) heated to dissolve in 6 mL n-hexanol. The reaction was proceeded at room temperature. The reaction progress was monitored by TLC using hexane/ethyl acetate 70:30 ratio. TLC analysis indicated the formation of a single product after 3 days. Upon completion, the reaction mixture was concentrated under vacuo, affording a white solid in 99 //% yield.

^{1}H-NMR (400 MHz, CD_3COCD_3): δ 8.51 (s, 2H, N-H), 7.47 (d, *J* = 8.73 Hz, 4H, C9-H), 7.14 (d, *J* = 9.38 Hz, 4H, C10-H), 4.08 (t, *J* = 6.76 Hz, 4H, C6-H) 3.87 (s, 2H, C12-H), 1.63 (m, 4H, C2-H), 1.35 (m, 12H, C3, 4, 5-H), 0.89 (t, *J* = 6.93, 6H, C1-H)

^{13}C-NMR (400MHz, CD_3COCD_3): δ 153.71, 153.64 (C7), 137.46, 137.36, 135.82, 135.80 (C8), 128.99, 118.36, 118.30 (C9 and C10), 64.40, 59.81 (C6), 40.17 (C12), 31.43 (C5), 25.37, 22.28 (C2, C3, and C4), 13.31 (C1)

^{1}H and ^{13}C NMR data is shown in Figure S7.4.11 and Figure S7.4.12

NMR Spectra of synthesized compounds

A complete interpretation (^{1}H, ^{13}C, COSY, and HSQC NMR) of model compound **1** (Diisopropyl (methylenebis(3,1-phenylene))dicarbamate) is shown as example in Figure S7.4.5 and Figure S7.4.8 respectively. Note that all synthesized model compounds in this manuscript have been confirmed in similar fashion.

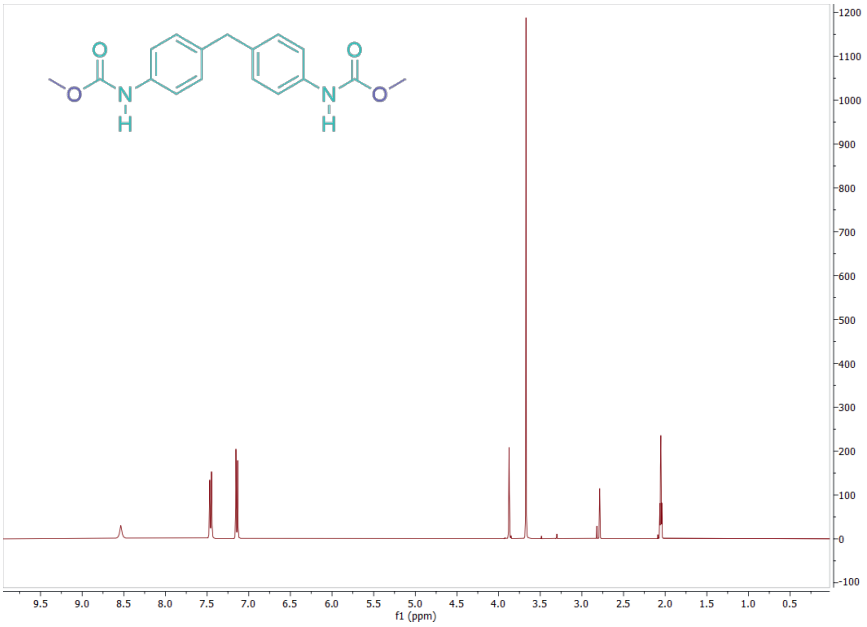

Figure S7.4.1 ^{1}H NMR spectra of model compound 1 Dimethyl (methylenebis(4,1-phenylene))dicarbamate

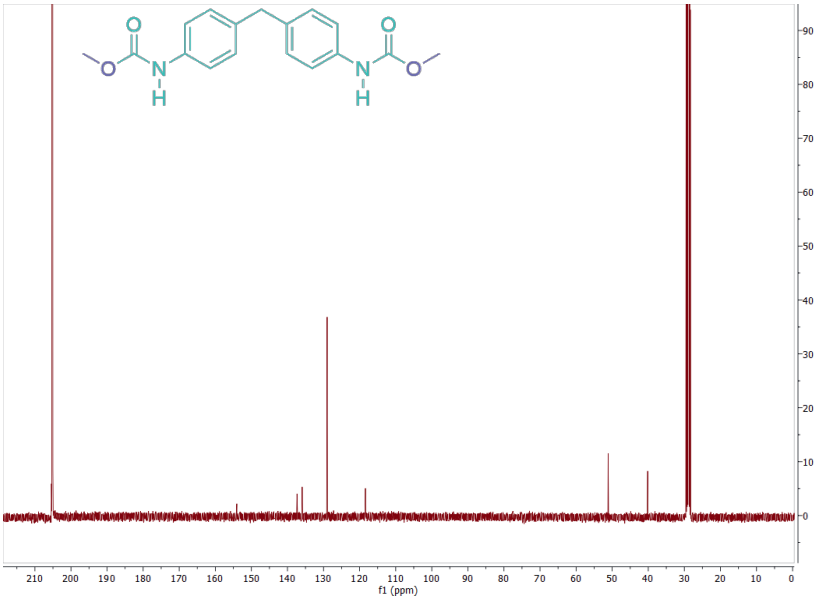

Figure S7.4.2. ^{13}C NMR spectra of model compound **1** Dimethyl (methylenebis(4,1-phenylene))dicarbamate

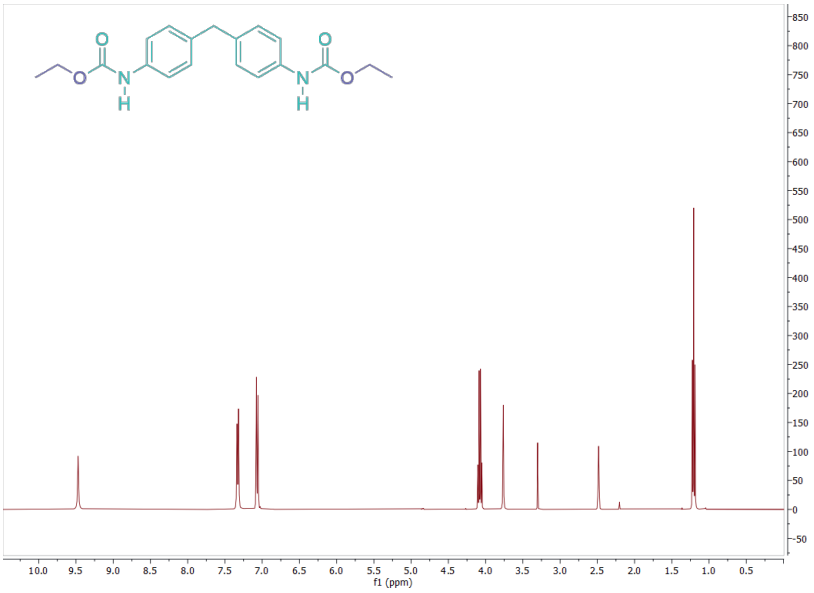

Figure S7.4.3. ^{1}H NMR spectra of model compound **2** Diethyl-(methylenebis(4,1-phenylene))dicarbamate)

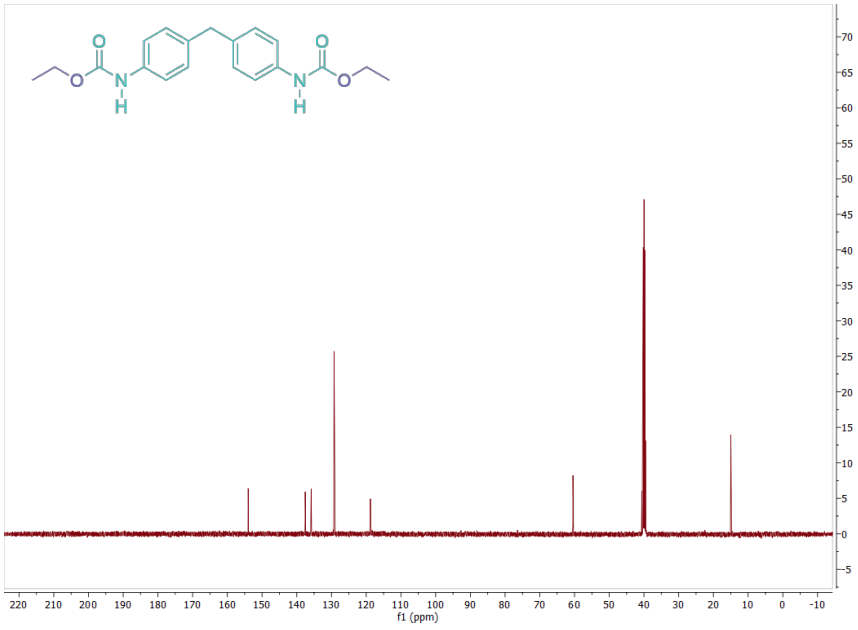

Figure S7.4.4. ^{13}C NMR spectra of model compound **2** Diethyl-(methylenebis(4,1-phenylene))dicarbamate)

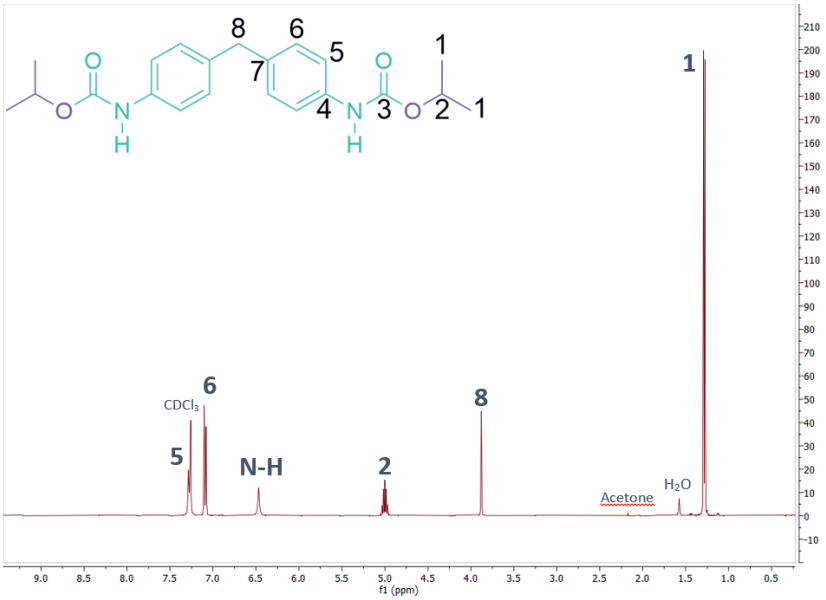

Figure S7.4.5. ^{1}H NMR spectra of model compound **3** Diisopropyl (methylenebis(3,1-phenylene))dicarbamate

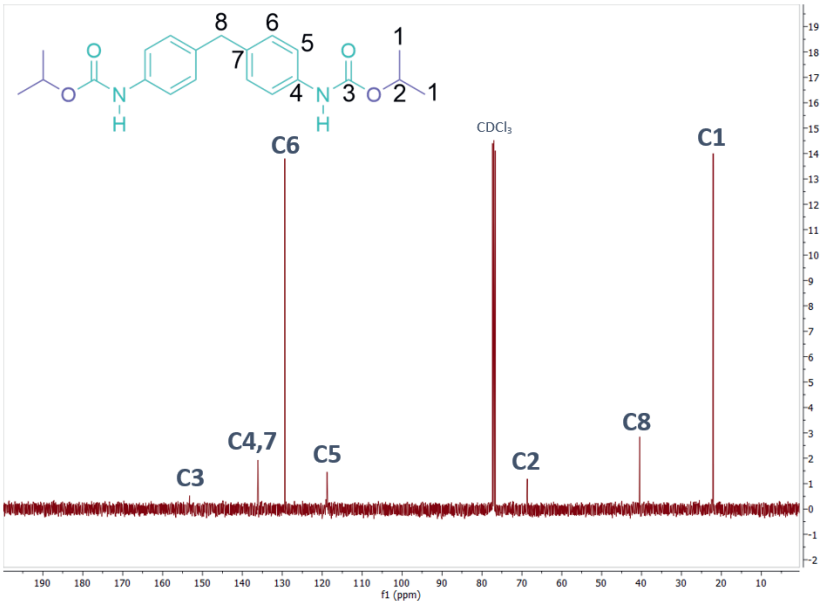

Figure S7.4.6. ^{13}C NMR spectra of model compound **3** Diisopropyl (methylenebis(3,1-phenylene))dicarbamate

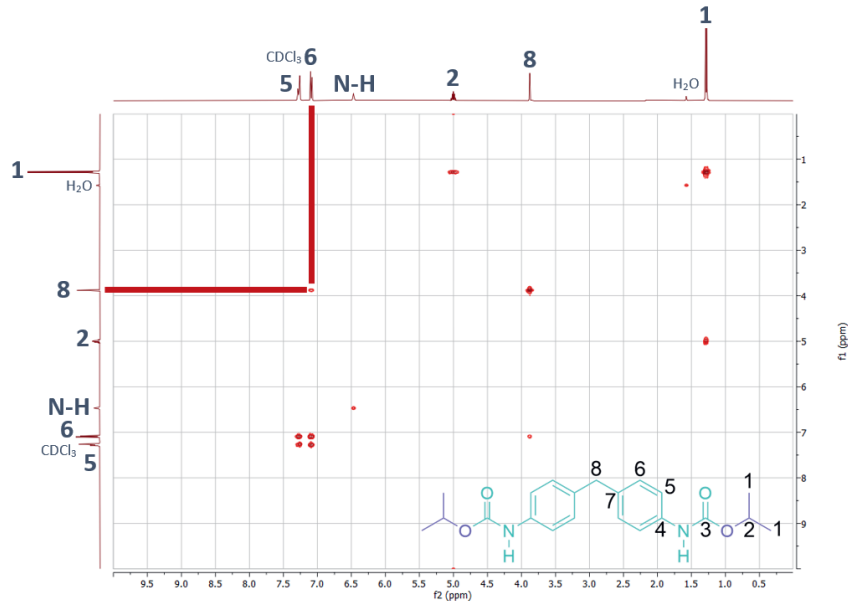

Figure S7.4.7. COSY NMR spectra of model compound **3** Diisopropyl (methylenebis(3,1-phenylene))dicarbamate

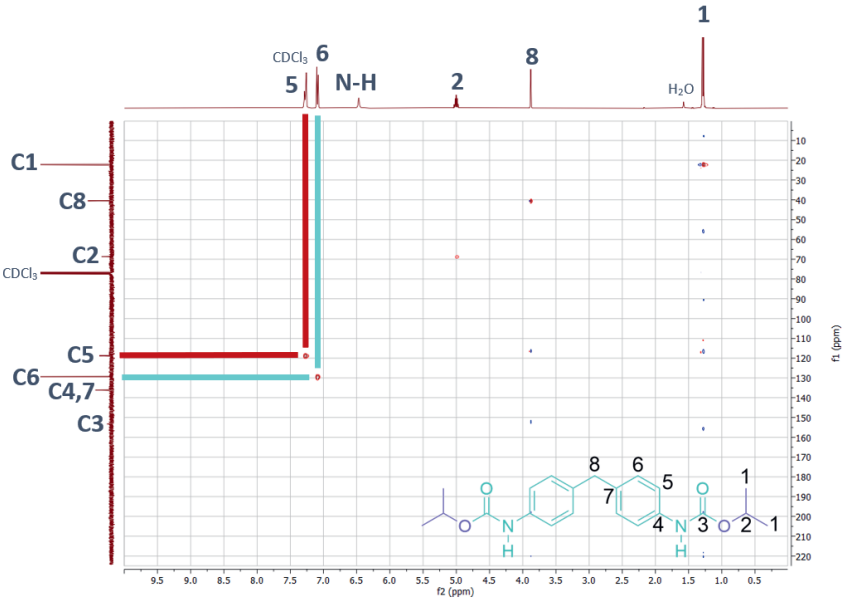

Figure S7.4.8. HSQC NMR spectra of model compound **3** Diisopropyl (methylenebis(3,1-phenylene))dicarbamate

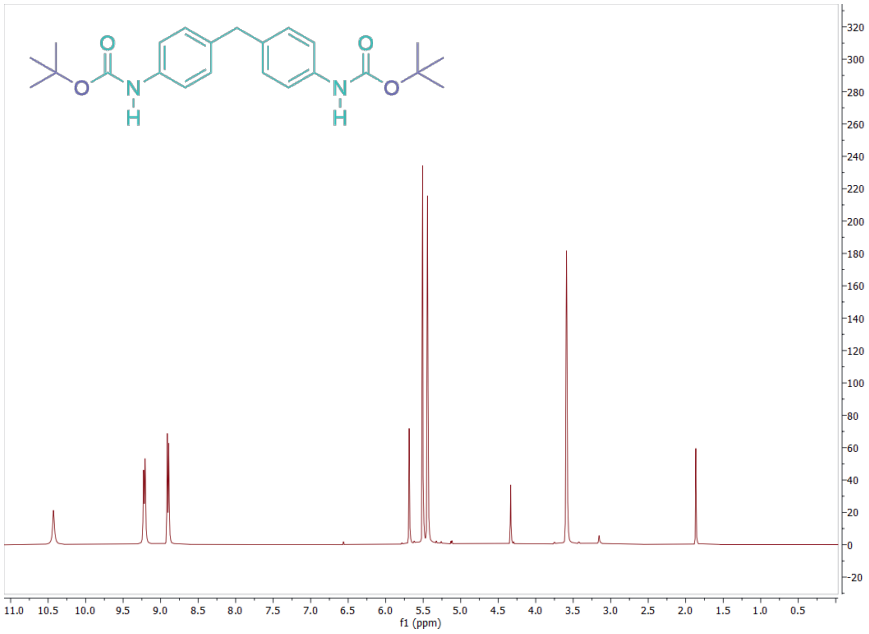

Figure S7.4.9. ^{1}H NMR spectra of model compound **4** Di-tert-butyl (methylenebis(4,1-phenylene))dicarbamate

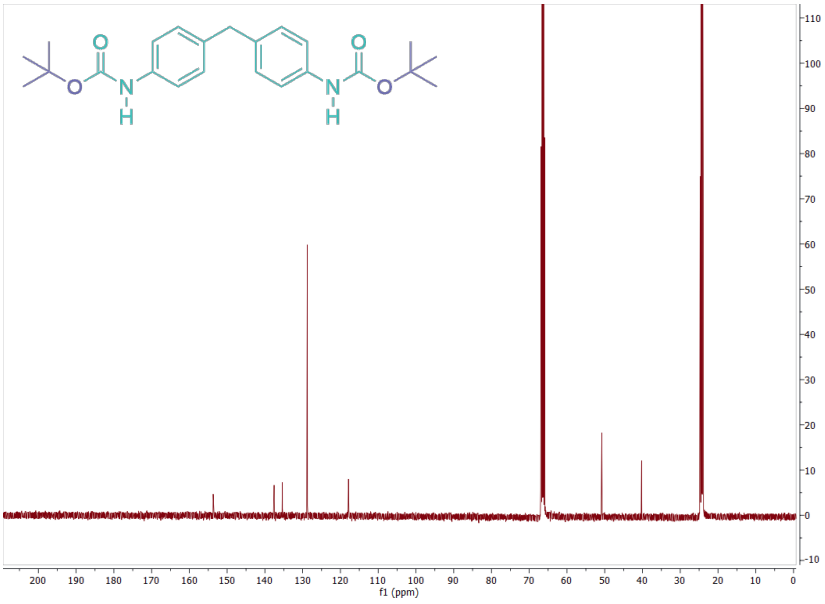

Figure S7.4.10. ^{13}C NMR spectra of model compound **4** Di-tert-butyl (methylenebis(4,1-phenylene))dicarbamate

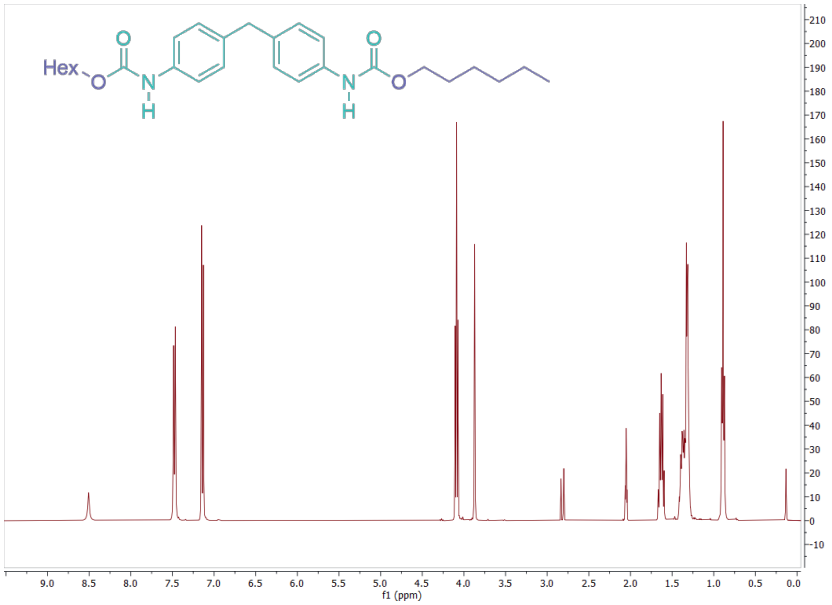

Figure S7.4.11. ^{1}H NMR spectra of model compound **5** Dihexyl (methylenebis(4,1-phenylene))dicarbamate

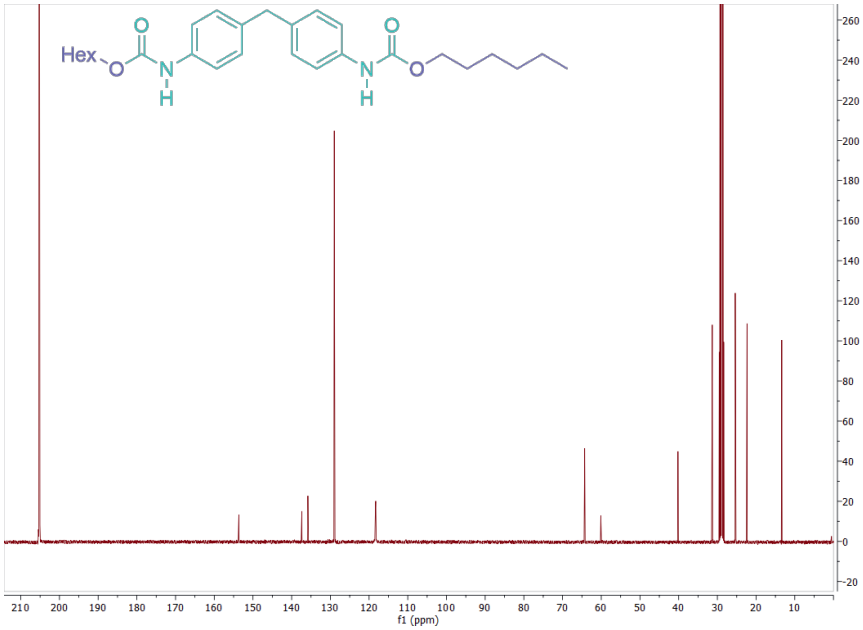

Figure S7.4.12. ^{13}C spectra of model compound 5 Dihexyl (methylenebis(4,1-phenylene))dicarbamate

Structural characterization techniques

NMR spectra were recorded on an Agilent 400-MR (^{1}H at 400 MHz; ^{13}C at 101 MHz) equipped with an Agilent OneNMR probe. Chemical shifts are reported in parts per million (ppm) relative to the corresponding residual solvent peak. Coupling constants are reported in Hertz (Hz). Multiplicity is noted with the usual abbreviations (s: singlet, br s: broad singlet, d: doublet, dd: doublet of doublets, t: triplet, q: quartet, m: multiplet).

The exact mass of the synthesized model compounds was determined via high-resolution mass spectrometry (HRMS) on a Thermo Vanquish core HPLC coupled to a Thermo Exploris 480. 1 µL of sample was injected without a column. The Mobile phase was acetonitrile with 0.1% formic acid

All pyrolysis experiments in this study were performed using a commercial Frontier Lab Tandem Microreactor (TMR, Rx 3050TR). A 0.5 mg sample and 2.5 mg catalyst (1:5 ratio) were brought together in a Frontier Lab Eco Cup (LF PY1-EC80F) and loaded into the reactor using a single-shot sampler (PY1-1040). A pyrolysis time of 10 seconds was assumed to ensure that all material had been transferred from the reactor to the online gas chromatograph coupled to mass spectrometry (GC-MS). Please note that, in reality, the pyrolysis process occurs faster due to heating rates of 1000 °C/s. The resulting oil was analyzed using an online gas chromatograph (Agilent Technologies 8890) coupled to a 5977B MSD and an FID detector at 300 °C. The gas chromatograph was equipped with a 30 m × 0.25 mm capillary column (HP-5 MS) coated with a 0.25 µm film of 5 % phenylmethyl polysiloxane. Helium was used as the carrier gas at a constant flow rate of 1 mL/min. A Frontier Lab Microjet Cryo-Trap was connected to the column to separate all volatile gases. The initial oven temperature was set at 40 °C, with a ramp rate of 10 °C/min (maintained for 1 min) to reach a final column temperature of 300 °C, which was held for 5 min. The injector and detector temperatures were maintained at 300 °C. Data were collected in full-scan mode with mass-to-charge (m/z) ratios ranging from 35 to 500. Chromatographic peaks were identified using the NIST mass spectral data library. Quantification of the desired products was performed using the external calibration curve method.

Calculations

2 different yield calculations have been used in this paper to allow a fair comparison between the model compounds.

(**S7.5.1**) Yield based on area% integration. This yield is calculated by integrating all peaks identified via GC/MS FID. Please note that the quantitative data from the FID are used for calculations; the MS data are used only for product identification. The total integration has been used as 100% yield. From here, the yield of the target molecule is calculated by taking the area integration of the target molecule divided by the summed peak integration of all identified compounds. This yield is expressed in the paper as "*Yield on peak integration*" with % as the unit. It should be noted that no GC calibration has been performed to obtain this yield. The calculation of this yield is shown in equation S7.5.1.

$$Yield\ on\ peak\ integration\ (\%) = \frac{\#prod\ peak}{\#total\ peak} * 100 \qquad \text{(S7.5.1)}$$

In which:
#prod peak is the peak integration of the target molecule
#total peak is the summed peak integration of all integrated compounds

(**S7.5.2**) Yield based on mol %. This yield is calculated by dividing the amount of target molecules produced by the amount of input molecules. The yield is expressed in the paper as "Mol % yield" with % as the unit. The Calculation is shown in equation S7.5.2.

$$Mol\ \%\ yield = \frac{\#\text{prod} * \#\text{molm}}{2\ (\#\text{molp} * \#\text{model})} \quad \text{(S7.5.2)}$$

In which:
#prod is the amount of product produced
#model is the amount of model feed input
#molm is the molecular weight of the model compound
#molp is the molecular weight of the product:
Aniline: 93 g/mol
Toluidine: 107 g/mol
Acridine: 149 g/mol
MDA 198 g/mol

The 2 represents the 2 aromatic rings in the model compound that can be converted in 2 aniline molecules.

Results on polyol modification experiments

The structural architecture of the polyol segment has been shown to affect product formation in Chapter 5, as an ethanol-based model yielded different products and product distributions than isopropanol. For this reason, 3 additional model compounds have been synthesized by using methanol, hexanol, and *tert*-butanol. An overview is shown Figure S7.4.13.

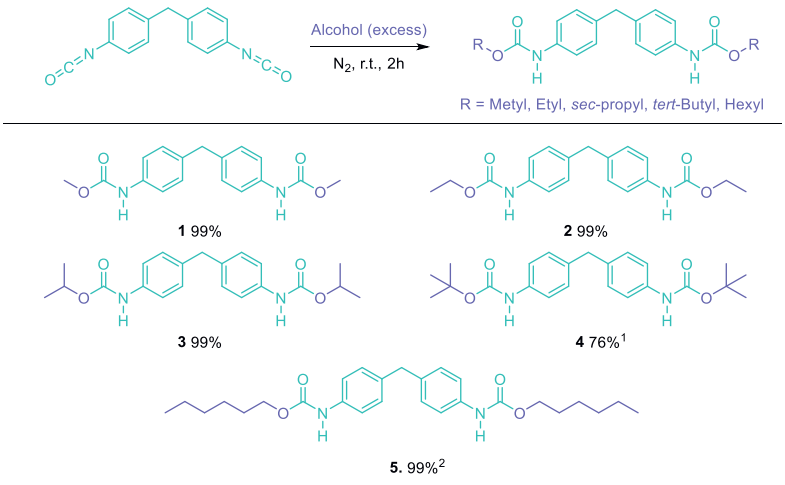

1:Reactions conditions: 40 °C, 72 h, in DCM
2: Reaction time 72h

Figure S7.4.13. Synthesized alcohol modified model compounds. General reaction conditions: MDI (0.43 – 4.0 mmol), 1 – 25 mL alcohol (MeOH, EtOH, *i*PrOH, *tert*-BuOH, or Hexanol), at 20 - 40 °C under N_2 for 2 - 72 hours. For specific reaction conditions, see materials section.

All Models (1 – 5) were subjected to catalytic (1:5 model:puralox SCCa 5/200) pyrolysis at 550 °C in a microreactor coupled to an online GC-MS/FID to investigate the effect of alcohol modification on the product formation and distribution. The quantified yields of the target molecules were calculated on mol% input to allow a fair comparison between the two models. Yield calculations are described in the calculations section. Products formed with each model compound is shown in Table S7.4.1 and Table S7.4.5 with the yield on area% shown in Figure S7.4.15 and on mol% in Figure S7.4.14.

The yields on mol% input (Figure S7.4.14) show that isopropanol (*i*PrOH), *tert*-butanol *t*-BuOH), and hexanol based models resulted in nearly equal amounts of aniline and toluidine yields. Methanol (MeOH) and ethanol (EtOH) based models resulted in lower amount of aniline and toluidine, indicating that the amount of alpha hydrogens is not a determining factor for aniline formation.

The product ratios (Figure S7.4.15) showed significant amount of alkylated products (including various di- and trimethyl benzamines) for MeOH and EtOH models whereas more volatile products for *i*PrOH, *t*-BuOH, and Hexanol based models. This observation indicates that short chains (MeOH and EtOH) are more susceptible to alkylation due to a higher mobility, contrarily to more bulky groups (*i*PrOH, *t*-BuOH, and hexanol). The increase in alkylated products on MeOH and EtOH is most likely the main reason for the lower observed aniline and toluidine yields.

Additionally, it is indicative from Figure S7.4.15 that the *t*-BuOH model is lacking sufficient cracking of MDA into aniline and toluidine since a significant amount of MDA is observed. A possible reason would be the absence of an alpha positioned hydrogen, leading to less MDA being cracked into aniline and toluidine.

Table S7.4.1. Identified products from the thermal decomposition of model **1** catalyzed by Puralox SCCa 5/200

#	Area integration[a] (%)	Match (%)	ID
1	7.66	47	Dimethyl ether
2	0.14	9	Acetamide, 2,2,2-trifluoro-
3	34.7	97	Aniline
4	11.7	97	Aniline, N-methyl-
5	14.9	94	o-Toluidine
6	7.21	93	Benzenamine, N,N-dimethyl-
7	1.08	59	Pyridine, 3-methyl-6-(1-methylethenyl)-
8	3.99	95	Benzenamine, N,4-dimethyl-
9	3.30	97	Benzenamine, 3,4-dimethyl-
10	2.97	87	Benzenamine, N,N,3-trimethyl-
11	0.88	95	Benzenamine, 2,4,5-trimethyl-
12	1.65	97	Acridine
13	4.16	90	Acridine, 9-methyl-
14	2.24	90	1H-Indole, 1-methyl-2-phenyl-
15	0.81	86	Benzo[h]quinoline, 2,3,4-trimethyl-
16	2.22	98	Benzenamine, 4,4'-methylenebis-

17	0.38	46	2,5-Dimethyl-4-(3-amino-4-methylphenyl)pyridine
18	0.03	42	Pyrrolo[2,3-f]quinolin-7-one, 2,3,5,9-tetramethyl-1,6-dihydro-

[a]Reaction conditions: 0.5 mg model, catalyst-to-feed ratio of 5 to 1, 550 °C with a helium flow of 205 mL/min and a pyrolysis time of 10 seconds

Table S7.4.2. Identified products from the thermal decomposition of model **2** catalyzed by Puralox SCCa 5/200

#	Area integration[a] (%)	Match (%)	ID
1	4.96	80	Acetaldehyde
2	5.01	87	Ethanol
3	2.76	90	Ethyl ether
4	0.072	38	Tetrahydro-4H-pyran-4-ol
5	0.10	64	Benzene
6	42.3	95	Aniline
7	0.25	91	Aniline
8	16.5	95	p-Aminotoluene
9	5.57	97	Benzenamine, N-ethyl-
10	0.76	81	Pyridine, 3-ethyl-5-methyl-
11	1.40	96	Benzenamine, 3,4-dimethyl-
12	0.44	70	1H-Indole, 2,3-dihydro-1,2-dimethyl-
13	2.42	96	N-Ethyl-p-toluidine
14	0.22	70	Benzenamine, N-ethyl-3-methyl-
15	0.30	94	Quinoline
16	0.33	83	Isoquinoline
17	0.10	83	Benzenamine, N,N-diethyl-4-methyl-
18	0.46	70	Quinoline, 2-methyl-
19	0.10	95	Quinoline, 8-methyl-
20	0.066	38	Quinoline, 3-methyl-
21	0.089	41	Formamide, N-(2-acetylphenyl)-
22	0.21	96	Quinoline, 2,7-dimethyl-
23	0.024	30	Quinoline, 5,8-dimethyl-
24	0.022	64	Quinoline, 3-ethyl-
25	0.100	43	Quinoline, 2,7-dimethyl-
26	0.062	49	3,5-Dimethyl-4-phenylpyridine
27	1.14	97	Acridine
28	2.24	83	Acridine, 9-methyl-
29	0.14	78	1H-Indole, 1-methyl-2-phenyl-
30	0.15	38	2,2-Diphenylpropionitrile
31	0.046	78	1H-Indole, 1-methyl-2-phenyl-
32	10.9	99	Benzenamine, 4,4'-methylenebis-
33	0.71	72	1-Ethyl-4-methoxy-9H-pyrido[3,4-b]indole
34	0.092	78	Benzenamine, 4,4'-methylenebis[N,N-dimethyl-

[a]Reaction conditions: 0.5 mg model, catalyst-to-feed ratio of 5 to 1, 550 °C with a helium flow of 205 mL/min and a pyrolysis time of 10 seconds

Table S7.4.3.Identified products from the thermal decomposition of model **3** catalyzed by Puralox SCCa 5/200

#	Area integration[a] (%)	Match (%)	ID
1	32.0	90	Propene
2	8.39	64	Acetone
3	0.30	64	Diisopropyl ether
4	45.7	97	Aniline
5	8.56	94	o-Toluidine
6	1.76	97	Acridine
7	2.82	86	Acridine, 9-methyl-
8	0.03	70	2-(4-Methylphenyl)-1H-indole
9	0.44	90	1H-Indole, 1-methyl-2-phenyl-

[a]Reaction conditions: 0.5 mg model, catalyst-to-feed ratio of 5 to 1, 550 °C with a helium flow of 205 mL/min and a pyrolysis time of 10 seconds

Table S7.4.4.Identified products from the thermal decomposition of model **4** catalyzed by Puralox SCCa 5/20

#	Area integration[a] (%)	Match (%)	ID
1	39.4	93	1-Propene, 2-methyl-
2	0.74	79	2-Propanol, 2-methyl-
3	35.9	95	Aniline
4	6.25	94	p-Aminotoluene
5	0.39	96	Naphthalene, 1,2,3,4-tetrahydro-
6	1.79	97	Acridine
7	2.75	74	Acridine, 9-methyl-
8	1.24	70	1H-Indole, 1-methyl-2-phenyl-
9	11.6	97	Benzenamine, 4,4'-methylenebis-

[a]Reaction conditions: 0.5 mg model, catalyst-to-feed ratio of 5 to 1, 550 °C with a helium flow of 205 mL/min and a pyrolysis time of 10 seconds

Table S7.4.5.Identified products from the thermal decomposition of model **5** catalyzed by Puralox SCCa 5/200

#	Area integration[a] (%)	Match (%)	ID
1	0.98	67	2-Hexyn-1-ol
2	0.71	72	2-Pentene, 3-methyl-, (E)-
3	38.0	91	1-Hexene
5	0.29	62	3-Heptyn-1-ol
6	0.28	75	1-Hexene, 2-methyl-
7	0.34	72	3-Heptene
8	3.81	96	Hexanal
9	2.92	91	1-Hexanol
10	31.2	92	Aniline
11	10.4	89	p-Aminotoluene
12	0.27	47	4-Undecene, 5-methyl-, (Z)-
13	0.59	95	Benzenamine, 3,4-dimethyl-
14	0.08	81	Benzenamine, 2,4-dimethyl-
15	0.05	35	2-Pyridineethanol
16	0.10	25	Aniline, N-methyl-
17	0.40	78	Hexane, 1,1'-oxybis-
18	0.01	27	Silacyclobutane
19	0.01	38	1-Octanamine, N-methyl-
20	0.25	35	Succinic acid, 2-fluorophenyl 1-phenylpropyl ester
21	0.08	46	Quinoline, 2-propyl-
22	2.17	80	4-N-Hexylaniline
23	0.86	49	2-Aminoindane
24	0.41	64	4-Methyl-1,2,3,4-tetrahydroquinoline, N-acetyl-
25	0.89	72	3-Ethyl-3,4-dihydro-2H-1,3-benzoxazine-2,4-dione
26	0.32	70	Quinoline, 6-butyl-
27	0.07	55	Quinoline, 2,7-dimethyl-
28	0.09	64	4-Biphenylamine, 3-methoxy-
29	0.09	62	4-Piperidylmethanol, O,N-diacetyl-
30	0.88	97	Acridine
33	0.14	47	Naphthalene, 2,3-dimethoxy-
34	0.22	25	Acridine, 9-methyl-
35	1.26	81	2-Phenylindolizine
36	0.31	78	Iminostilbene
37	0.08	68	7-Hydroxyquetiapine
38	0.11	90	1H-Indole, 1-methyl-2-phenyl-
39	0.02	90	Quinoline, 2-butyl-3-methyl-
40	0.54	70	1H-Indole, 1-methyl-2-phenyl-
41	0.10	93	Benz[j]isoquinoline, 3,6,8-trimethyl-
42	0.21	86	Benzenamine, 4,4'-methylenebis-

[a]Reaction conditions: 0.5 mg model, catalyst-to-feed ratio of 5 to 1, 550 °C with a helium flow of 205 mL/min and a pyrolysis time of 10 seconds

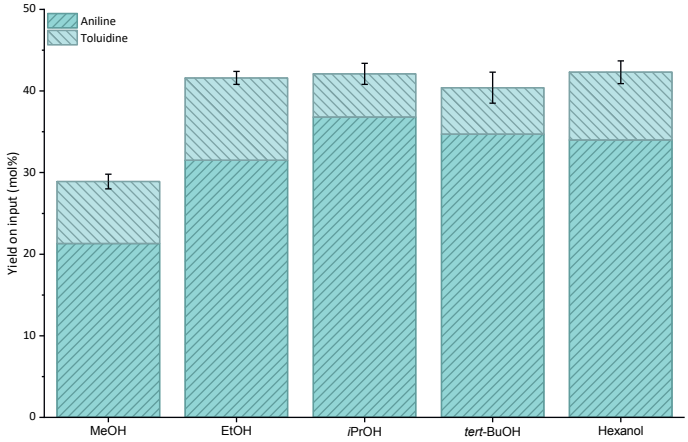

Figure S7.4.14.Overview of model compound pyrolysis in the tandem microreactor catalyzed by alumina based catalyst SCCa 5/200. Reaction conditions: 0.5 mg model compound, catalyst-to-feed ratio of 5 to 1, 550 °C with a helium flow of 205 mL/min and a pyrolysis time of 10 seconds. Product ratios are determined on weight input corrected for mol% according to equation 7.5.2 in the calculations section

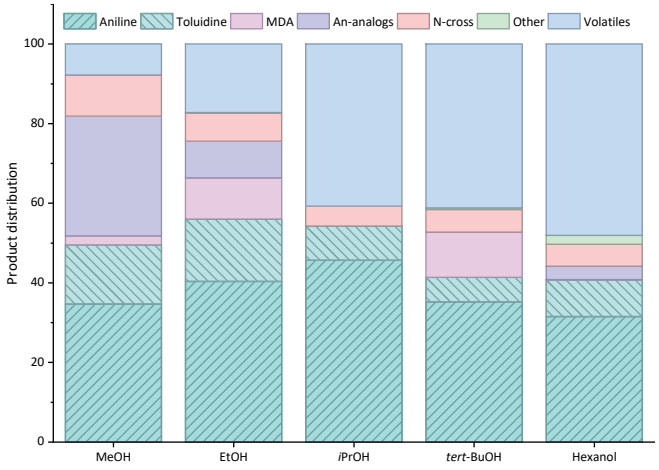

Figure S7.4.15. Overview of model compound pyrolysis in the tandem microreactor catalyzed by alumina based catalyst SCCa 5/200. Reaction conditions: 0.5 mg model compound, catalyst-to-feed ratio of 5 to 1, 550 °C with a helium flow of 205 mL/min and a pyrolysis time of 10 seconds. Product ratios are determined on area integrations of Table S7.4.1Table S7.4.5

Results on H_2 gas experiments

The critical role of hydrogen has been investigated by using H_2 as carrier gas which would react as proton donor. It was expected that PUR would crack into polyol and isocyanate in the initial phase followed by cracking of the methylene bridge of MDA trough a hydrogen donation fashion, thereby forming aniline and toluidine. Results are shown in TablesTable S7.4.6 and Table S7.4.7. The presence

of an acidic catalyst (SCCa 5/200) resulted in an unwanted deamination reaction, forming BTX. The presence of an basic catalyst resulted in mainly formation of volatiles.

Table S7.4.6. Identified products from the thermal decomposition of post-production polyurethane foam catalyzed by Puralox SCCa 5/200 under H_2 gas

#	Area integration[a] (%)	Match (%)	ID
1	34.3	5	Ethylamine
2	4.74	86	Cyclopentane
3	1.87	52	1-Pentene, 2-methyl-
4	8.63	70	Furan, 2,3-dihydro-3-methyl-
5	32.4	94	Benzene
6	14.0	95	Toluene
7	0.27	94	Ethylbenzene
8	0.98	97	p-Xylene
9	0.21	97	p-Xylene
11	0.09	76	Benzene, propyl-
15	0.19	93	Naphthalene
16	0.05	89	Tetradecane
17	2.32	96	Diphenylmethane

[a]Reaction conditions: 0.5 mg model, catalyst-to-feed ratio of 5 to 1, 550 °C with a helium flow of 205 mL/min and a pyrolysis time of 10 seconds

Table S7.4.7. Identified products from the thermal decomposition of post-production polyurethane foam catalyzed by Puralox Y_2O_3 under H_2 gas

#	Area integration[a] (%)	Match (%)	ID
1	16.708	4	Acetonitrile
2	55.583	52	Propene
3	9.414	38	Ethylenimine
4	6.269	40	Cyclopropene
5	6.751	2	Cyclopropene
6	0.449	64	Cyclopentene, 1-ethenyl-3-methylene-
7	4.826	96	Diphenylmethane

[a]Reaction conditions: 0.5 mg model, catalyst-to-feed ratio of 5 to 1, 550 °C with a helium flow of 205 mL/min and a pyrolysis time of 10 seconds



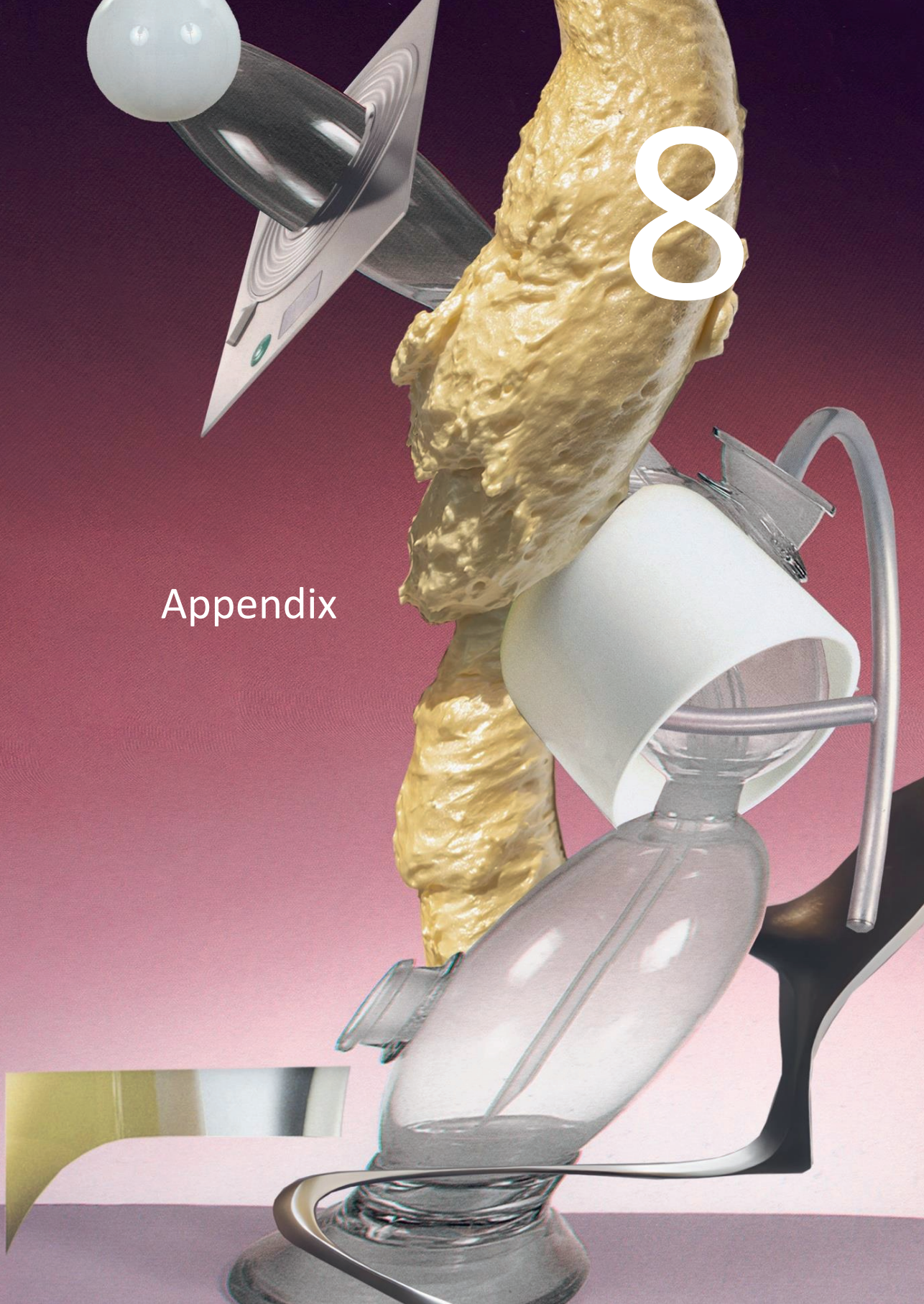

8

Appendix

Summary

The prelude (Chapter 1) introduces the Circular Foam project and places it within the broader context of Europe's ambitions to transition to a circular plastics economy. Each work package is briefly presented, with an emphasis on work package 4, which focuses on developing a recycling pathway for rigid polyurethane foams and is the topic of this PhD thesis.

The Introduction (Chapter 2) presents the issue of plastic waste, with particular emphasis on polyurethanes. State-of-the-art work on recycling rigid pMDI-based polyurethanes is outlined, with particular attention to the literature on recovering nitrogen- containing chemicals from the isocyanate segments. In this context, catalytic pyrolysis emerged as an attractive recycling strategy. Key considerations for catalytic pyrolysis are discussed to provide the reader with sufficient conceptual and practical understanding of the research described in the subsequent chapters. The chapter concludes with specific strategies to address these issues, presented in the following sections.

Chapter 3 describes a catalytic strategy for recovering aniline from end-of-life rigid polyurethane (PUR) foam waste. Initial catalyst screening at a batch milligram scale showed that an alumina-based catalyst gave the highest aniline yield. An extended catalyst screening study with a wide range of alumina catalysts identified catalyst SCCa 5/200 as the best option, with surface area and acidity as the most relevant parameters for aniline formation. Up to 50% aniline yield, based on the nitrogen content in the feed (N%), was obtained using a tandem microreactor at 550 °C, with an additional 15 N% as toluidine. Upscaling was conducted in multiple stages, from mg-scale to continuous operation at >100 g $_{feedstock}$ h^{-1} and 5 kg $_{feedstock}$ $h^{-1,}$ achieving a combined aniline and toluidine yield of 25 N%. Techno-economic evaluations were performed based on a preliminary process design, indicating that catalyst use is a significant cost driver. The environmental impact was assessed, which revealed a CO_2 reduction of 0.6 ton·ton$_{PUR}^{-1}$ under non-optimized conditions.

The long-term stability and deactivation mechanisms of the alumina-based SCCa 5/200 catalyst were evaluated, and the results are provided in Chapter 4. Distinct changes in catalyst performance were observed during multiple catalytic pyrolysis cycles using post-production polyurethane (nPUR) without intermediate reactivation. Results revealed significant catalyst deactivation, accompanied by a shift in chemoselectivity from aniline and toluidine to predominantly MDA formation. Analysis showed that hard coke formation was the primary cause of deactivation. The catalyst could be regenerated via oxidative reactivation at 550 °C, with the main changes in catalyst properties being the surface area and acidity. Multiple regeneration-recycle cycles were performed at batch milligram scale using nPUR and end-of-life rigid polyurethane foam (EOL PUR) to determine the limits of catalyst lifetime and the main cause of deactivation. Catalyst activity for nPUR was reduced in the first 4 reaction-regeneration cycles, stabilized at half of the original activity for 28 cycles, and decreased in the remaining cycles to a value close to thermal pyrolysis. For EOL, catalyst stability was significantly worse, and the catalytic reaction performance was equal to thermal pyrolysis after 18 reaction-regeneration cycles. The spent catalysts for both PUR feeds were characterized using GC-MS/FID, TEM-EDX, indicating that coking was the main cause of deactivation for nPUR and metal contamination (primarily iron) for EOL PUR.

Chapter 5 describes a study focused on identifying molecular pathways involved in the thermal and catalytic pyrolysis (using SCCa 5/200) of PUR by using deuterated and ^{13}C-labeled model compounds. Changes in isotopic distribution and label positions were identified through careful analysis of the products' fragmentation patterns. These changes provided key insights into the depolymerization of rigid MDI-based polyurethane foams into low-molecular-weight N-containing compounds. Results

showed that catalytic pyrolysis leads to the cracking of the isocyanate methylene bridge, thereby promoting the formation of the desired target molecules (aniline and toluidine). Product fragmentation pattern analysis of deuterated model compounds revealed a unidirectional flow of hydrogen atoms from the alcohol to the isocyanate segment, suggesting that the α-hydrogen (with a calculated low bond energy) of an isopropanoyl moiety is most mobile and therefore contributes primarily to the decomposition of MDA into aniline and toluidine. Pyrolysis of ^{13}C-enriched model compound confirmed that side product formation (acridine and methylacridine) arises only from a cross-reaction between two isocyanate fragments, possibly via an intermolecular mechanism. To explain the observations, a 3-step mechanism was proposed that begins with a retropolymerization, assisted by Lewis acid site coordination on the catalyst, forming MDA, CO, CO_2, propene, and acetone. The methylene bridge of the MDA fragment is cleaved by hydrogen donation (most likely from the α-H of polyol), resulting in aniline and toluidine. N-containing side products form via **I**) cross reaction between polyol- and isocyanate fragments (ethylaniline and ethyltoluidine) or **II**) homocoupling between isocyanate fragments (aniline and toluidine) to form acridine and methylacridine.

Experimental studies aimed at identifying catalyst performance structure relations are described in Chapter 6. Studies involved catalytic pyrolysis of nPUR at the batch-milligram scale using a range of amorphous silica-alumina (ASA) catalysts. Statistical modeling revealed a maximum yield of aniline and toluidine of 36.6 N%, at a Brønsted-to-Lewis ratio of 0.05 and a pore width of 9.1 nm. Additionally, the absence of MDA suggested that Brønsted acidity promotes cracking of MDA into aniline and toluidine.

The research described in this dissertation has provided valuable insights into the catalytic pyrolysis of waste rigid polyurethane foam to produce aniline and toluidine. On a molecular level, catalyst screening studies revealed that alumina and ASA catalysts are promising for further scale-up. Relevant knowledge has been gained on the mechanism of catalytic pyrolysis, which will aid in developing tailored catalyst formulations. In addition, catalyst stability has been assessed in detail, and relevant deactivation pathways have been identified. This knowledge will aid in developing efficient strategies for catalyst reuse and recycling, thereby reducing catalyst costs. At the process level, the catalytic pyrolysis concept was scaled up to pilot scale (5 $kg_{feedstock}$ h^{-1}), yielding a combined aniline yield of 25 N%. The findings will aid the further scale-up of the process and, more broadly, contribute to the development of efficient recycling strategies for waste plastics

Samenvatting

De positie van het Circular Foam project binnen het kader van de Europese transitie naar een circulaire economie is in de inleiding (Hoofdstuk 1) uitgelegd. Hierbij zijn ook alle andere relevante initiatieven toegelicht. Een overzicht van elk werkpakket is weergegeven met speciale aandacht voor werkpakket 4 waar de focus ligt op de ontwikkeling van een recyclingtechnologie voor op MDA-gebaseerde polyurethaanschuimen. Dit hoofdstuk biedt een perspectief op het grotere geheel van het Europese project. Het algemene plastic afvalprobleem met een focus op polyurethaanschuim is uiteengezet in de introductie (Hoofdstuk 2). Hierin wordt de huidige stand van zaken omtrent de beschikbaarheid van recycling technologieën voor pMDI-gebasseerde foams besproken waarbij de minimale aanwezigheid aan literatuur voor het terugwinnen van startmaterialen uit de polyol of de isocyanaat segmenten wordt uitgelicht. Met dit doel in het oog komt katalytische pyrolyse via thermische degradatieroutes naar voren als een voorkeursstrategie voor het terugwinnen van startmaterialen. Het gebruik van katalysatoren in pyrolyse, met bijbehorende aandachtspunten, wordt behandeld om voldoende conceptueel en praktisch inzicht te bieden voor de komende hoofdstukken. Het hoofdstuk sluit af met een beknopte samenvatting van de centrale probleemstellingen en de specifieke strategieën die in elk van de volgende secties aan bod komen. Hoofdstuk 3 beschrijft een thermokatalytische strategie voor de terugwinning van startmateriaal aniline uit end-of-life pMDI-gebaseerd polyurethaanschuim (PUR). Via een initiële katalysatorscreening op milligramschaal in batchmodus was aangetoond dat de hoogste aniline opbrengst met een aluminium katalysator behaald kon worden. Een uitgebreide screening van aluminium gebaseerde katalysatoren identificeerde SCCa 5/200 als de meest geschikte optie, waarbij de oppervlakte en de zuurgraad werden vastgesteld als de parameters met de grootste invloed op de vorming van aniline. Een tandem-microreactor bij 550 °C onder geoptimaliseerde omstandigheden resulteerde in de terugwinning van meer dan 50% aniline in de PUR, met een aanvullende opbrengst van 15% toluidine. Opschaling werd uitgevoerd van batch milligramschaal naar continue reactorwerking bij >100 $g_{feedstock}\ h^{-1}$ and 5 $kg_{feedstock}\ h^{-1}$, waarbij een totale terugwinning van meer dan 25% aniline en toluidine werd bereikt. De reductie in klimaatimpact van de ontwikkelde technologie werden berekend om inzage te krijgen tot de mate van integreerbaarheid in de maatschappij. De resultaten toonde een CO_2-reductie van 0.6 ton · ton_{PUR}^{-1} onder niet-geoptimaliseerde omstandigheden. De stabiliteit en het deactiveringsmechanisme van de beste katalysator (SCCa 5/200) zijn in Hoofdstuk 4 in detail geanalyseerd. De katalytische reversibele en irreversibele veranderingen in activiteit en chemoselectiviteit werden onderzocht door de katalysator meerdere malen in het PUR pyrolyseproces te gebruiken zonder tussentijdse regeneratie. Hierbij werd een snelle deactivatie geobserveerd met een verschuiving in chemoselectiviteit van de vorming van aniline en toluidine naar voornamelijk MDA. Uitgebreidde analyse op de gebruikte katalysator toonde aan dat harde coke vorming de de primaire oorzaak van de deactivatie was. De katalysator kon worden geregenereerd via oxidatieve thermische reactivatie bij 550 °C, waarbij de belangrijkste veranderingen in de katalysatoreigenschappen betrekking hadden op de oppervlak en de zuurgraad. Verschillende regeneratie–cycli werden uitgevoerd op milligramschaal met post-productie PUR (nPUR) en end-of-life PUR (EOL PUR) om de katalysatorlevensduur en de belangrijkste deactivatie oorzaken te identificeren. Voor nPUR nam de katalytische activiteit in de eerste vier runs af, stabiliseerde vervolgens op ongeveer de helft van de initiële activiteit gedurende de 28 opvolgende runs en daalde uiteindelijk tot een niveau dat vergelijkbaar is met thermische pyrolyse. Voor EOL PUR was de katalysatorstabiliteit aanzienlijk lager aangezien de aniline opbrengst na 18 runs gelijk was aan

thermische pyrolyse. De gebruikte katalysatoren werden voor beide PUR-feedstocks gekarakteriseerd met GC-MS/FID en TEM-EDX, waaruit bleek dat coking de dominante deactivatieoorzaak was voor nPUR, terwijl contaminatie (voornamelijk ijzer) de hoofdoorzaak was voor EOL PUR. Hoofdstuk 5 beschrijft een studie gericht op het thermische en katalytische pyrolyse degradatiemechanisme van polyurethaan waarbij SCCa 5/200 als katalysator is gebruikt. Voor deze studie zijn verschillende D en ^{13}C modelstoffen gesynthetiseerd waarbij de fragmentatiepatronen van de gevormde producten zijn geanalyseerd om zo het degradatieproces in kaart te brengen. Een vergelijking tussen niet-katalytische en katalytische pyrolyse toonde aan dat katalytische pyrolyse leidde tot het kraken van de isocyanaat-methyleenbrug, waardoor aniline en toluidine werden gevormd. Fragmentatiepatroon analyse van de D-modelverbindingen wees op een unidirectionele waterstof migratie van het alcoholgedeelte naar het isocyanaatsegment, dit suggereerde dat het α-waterstofatoom (met een berekende lage bindingsenergie) van een isopropanoyl-segment het meest mobiel was en dus primair bijdraagt aan de afbraak van MDA tot aniline en toluidine. Pyrolyse van de ^{13}C-modelverbindingen bevestigde dat de vorming van bijproducten (acridine en methylacridine) voortkomt uit twee isocyanaatfragmenten, mogelijk via een intermoleculair mechanisme. Het enkelvoudig gelabelde acridine duidde op vorming via een reactie tussen aniline en toluidine, terwijl het dubbel gelabelde methylacridine op productvorming uit twee toluidinefragmenten wees. Door middel van de observaties kon er een drie staps mechanisme voorgesteld worden waarbij eerst een retropolymerisatie plaatsvindt via coördinatie tussen de katalysator Lewis-zuren en de vrije elektronenparen van PUR, resulterend in de vorming van MDA, CO, CO_2, propeen en aceton. Het MDA-fragment blijft vermoedelijk gecoördineerd aan de katalysator, waarna kraking van de methyleenbrug optreedt via waterstofoverdracht (waarschijnlijk afkomstig van het α-waterstof van de polyol), wat leidt tot de vorming van aniline en toluidine. Stikstofhoudende bijproducten ontstaan via een kruisreactie tussen polyol- en isocyanaatfragmenten (ethylaniline en ethyltoluidine) of via homokoppeling tussen isocyanaatfragmenten (aniline en toluidine), wat resulteert in de vorming van acridine en methylacridine. Experimentele studies gericht op het vaststellen van relaties tussen katalysator prestatie en structuur, met name de rol van Brønsted- en Lewis-zuren, is beschreven in Hoofdstuk 6. Hierbij was nPUR op batch-milligramschaal gepyrolyseerd in de aanwezigheid van verschillende amorfe silica-alumina (ASA) katalysatoren. Statistische modellering resulteerde in een berekende maximale opbrengst aan aniline en toluidine van 36.6 N% (op stikstof basis) bij een Brønsted/Lewis-verhouding van 0.052 en een poriënbreedte van 9.09 nm. Daarnaast suggereerde de afwezigheid van MDA dat Brønsted-zuren sites de kraking van MDA tot aniline en toluidine bevorderen.

Het onderzoek dat in dit proefschrift is beschreven heeft waardevolle inzichten opgeleverd in de katalytische pyrolyse van end-of-life polyurethaanschuim, met als doel de productie van aniline en toluidine. Op moleculair niveau is aangetoond dat alumina- en ASA-katalysatoren veelbelovend zijn voor verdere opschaling. Daarnaast is de katalysatorstabiliteit in detail geëvalueerd en zijn relevante deactivatie mechanismen geïdentificeerd. Deze kennis zal bijdragen aan de ontwikkeling van efficiënte strategieën voor hergebruik en recycling van katalysatoren, wat kan leiden tot een verlaging van de katalysatorkosten. Op procesniveau is het concept van katalytische pyrolyse opgeschaald naar pilotschaal (5 $kg_{feedstock}$ h^{-1}), waarbij een gecombineerde aniline-opbrengst van 25 N% werd bereikt. Op basis van deze bevindingen lijkt katalytische pyrolyse een veelbelovende strategie voor de recycling van polyurethaanafval, en draagt deze bij aan de ontwikkeling van een closed loop PUR-productieproces.

Academic output

Within this dissertation

[1] Engels, T. G. W., Stevelink, R., Vaze S., van der Zijpp, M., Pillich, M., Eiden, S., Schenk, N., Bardow, A., Heeres, H. J. & Deuss, P. J. Chemical recycling of rigid polyurethane foam via thermocatalytic conversion to aniline. (2026)

[2] Engels, T. G. W., van der Zijpp, M., Eiden, S., Heeres, H. J. & Deuss, P. J. Polyurethane recycling using catalytic pyrolysis: insights into catalyst stability. (2026)

[3] Engels, T. G. W., Talkami, L., Heeres, A., Heeres, H. J. & Deuss, P. J. Catalytic pyrolysis of rigid polyurethane to aniline: Mechanistic insights using ^{13}C and deuterium model compounds. (2026)

[4] Engels, T. G. W., P., Heeres, H. J. & Deuss, P. J. Catalyst-structure-performance relations for the depolymerization of polyurethanes to aniline using amorphous silica alumina (ASA) catalysts. (2026).

Other publications

[5] Jayasundera, K. P., Engels, T. G., Lun, D. J., Mungalpara, M. N., Plieger, P. G., & Rowlands, G. J. (2017). The synthesis of planar chiral pseudo-gem aminophosphine pre-ligands based on [2.2] paracyclophane. *Organic & Biomolecular Chemistry*, *15*(42), 8975-8984. DOI: 10.1039/C7OB02393F

[6] de Freitas, A. L. S., Engels, T. G., Llorens, S. B., Lasorsa, A., van der Wel, P. C., Heeres, H. J., & Deuss, P. J. (2026). In-depth characterization of tertiary cellulose from wastewater treatment facilities. *Biomass and Bioenergy*, *210*, 109012. DOI:10.1016/j.biombioe.2026.109012

[7] Jiang, C., Zhang, Z., Amponsah, A. P., Engels, T. G. W., Wasseem, M., Grubišić-Čabo, A., Zhang, X., Deuss, P. J., & Morales, D. CoO x /Ni foam as catalyst for the electrochemical reforming of a complex ethanosolv-derived carbohydrate waste stream.

[8] Wang, T., Ruan, C., Post, C., Zhang, W., Engels, T. G. W., van de Bovenkamp, H. H., Yang, Y., Gerlach, D., Voet, V. S. D., Folkersma, R., Loos, K., Pei, Y., Yue, J., Rudolf, P., Tromp, M., Heeres, H. J., & Deuss, P. J., Oxidation-State-Modulated Cobalt Catalysts for Ambient Selective Hydrogenation of Bio-Derived Aldehydes: Toward Bio-BasedPolyesters, ACS catal. (2026)

[9] Witte, J., Engels, T. G. W., Genuino, H., van Eijk, M. C. P., Keller, E., Gebben, B., Heeres, A., & Heeres, H. J. Valorisation of PET-rich mixed plastic waste using a cascading concept involving selective ammonolysis and catalytic pyrolysis. (2026)

Conference contributions

Title: Recycling of polyurethane via pyrolysis: a catalyst screening study

Poster Europacat 2023, 27 Aug - 1 Sept, CZ international

Title: Recycling of polyurethanes via smart pyrolysis: a study into catalyst structure-performance relations

Poster NCCC 2024, 4 - 7 March, NL national

Title: Recycling of polyurethanes via smart pyrolysis: a study into catalyst stability

Poster ENTEG day 2024, 3 Oct, NL National

Title: Catalytic pyrolysis: paving the way for circulair polyurethanes

Oral NCCC 2025, 10 - 12 March, NL national

Title: Towards circular polyurethane via catalytic pyrolysis

Oral Pyroliq III 2025 15 - 19 Sept, IT international, Winner best Oral presentation

Title: Catalytic pyrolysis of rigid polyurethane foams

Poster Pyroliq III 2025 15 - 19 Sept, IT international

Title: Catalytic pyrolysis of rigid polyurethane foams

Poster ENTEG day 2025, 30 Oct, NL National

Acknowledgements

After 8 years, my time here in Groningen has come to an end and it was truly amazing, as reflected in the endless list of people I have met. Each of you made it truly memorable for me. For this reason, I have awarded a title to every individual. The sentence relates to a memory we shared or to how I see you as a person. Of course, I know some of you better than others, so one award will be more personal than the other. The same holds for close friends, of course I can't describe you in one sentence, but I still wanted to give you a word of appreciation. Please take it with a grain of salt, as I don't want to offend anyone 😊. Go ahead, find your name on the next page, and write your title on the award! Please accept my apologies if I have forgotten anyone with my head, you are most definitely in my heart. For this reason, you also deserve an award since you are an exceptional and amazing person. So treat yourself and write the best title you can think of on the trophy!



First and foremost, I would like to express my gratitude to **Peter** and **Erik**. 4 jaar geleden heb ik de keuze gemaakt om van Chemie naar Chemical Engineering te switchen door een PhD bij jullie te gaan doen. Ik moet zeggen dat dit een van de beste keuzes in mijn carrière is geweest, want ik ben van begin tot eind met veel goede zin naar de uni gegaan waarbij alle taken voelden alsof ze geen energie kostten. Ze zeggen dat een goede supervisor je PhD maakt of breekt, en dat heb ik zeker gemerkt. Jullie hebben mijn PhD 100% gemaakt en ik zou er zo blind weer een bij jullie doen. De relaxte en positieve sfeer die jullie bij ENTEG hebben is echt uniek. De toegankelijkheid die jullie bieden als supervisor met precies de juiste balans tussen het formele en het persoonlijke aspect heeft ervoor gezorgd dat ik het gevoel heb gehad dat ik de ruimte kreeg om te groeien zonder druk om te presteren. Ik ben van mening dat dit aspect iemand tot een goede supervisor maakt. Bedankt voor de ontzettend leuke tijd, relaxte meetings en vooral het vertrouwen dat jullie in mij hadden om dit project tot een goed einde te brengen. Hopelijk kijken jullie er net zo positief op terug als ik.

Reading committee **Prof. F. Picchioni**, **Prof. J. Xie**, **and Prof. M. Carrier.** Thank you for taking the time to go through my work and provide valuable suggestions.

BioBTX team: **Ruben, Niels, Shruti, Matthijs, Mart, Kimon, Diana, Tijmen**, thank you for the positive work environment and for all the nice Christmas presents. I couldn't have wished for better people to have collaborated with over the past 4 years.

Bachelor and Master students **Kath**, **Marlies**, **Stijn**, **Thomas**, **Tobias**, thank you for the hard work and for the good times in the lab with me.

Marcel, Wout, Rick, Léon, Marjan, Henk, Xander, Gert-Jan, bedankt voor alle gezelligheid de afgelopen 4 jaar, jullie zijn stuk voor stuk toppertjes en ik ga jullie missen!

Ting, thanks for the amazing 2 years together, the nice conversations we had, and most of all, the great collaborations about shrimps. Sad that I couldn't be at your promotion, but nevertheless, it was great meeting you! **Loes Talkami,** bedankt voor het maken van de modelstoffen, hopelijk zien we elkaar op mijn promotie weer! **Esther**, bedankt voor je hulp door aan Peter te laten zien dat het de moeite waard was om aan deuterium labeling te beginnen. Mijn hype trein en jouw glovebox skills hebben 100% het idee aan Peter verkocht! **Chongyang**, thank you so much for doing the bond energy calculations for my paper. It was the cherry on the cake! **Alessia**, thank you so much for taking the time to do the solid-state NMR runs with me. It provided all the remaining questions that were left

unanswered! **Jarno**, bedankt voor de fijne samenwerking over de PET trays, het is een mooi manuscript geworden. **Gert**, **Marc**, **Jacob**, **Pieter**, **Folkert** Bedankt voor alle hulp tijdens de metingen om mijn thesis tot een goed einde te brengen.

Jesse and **Giulia**, two amazing people that I am glad I have met here in Groningen. Thank you for filling the ow so hard task as paranymph, but most of all, thank you for being one of my dearest friends. We definitely stay in touch to party in Den Bosch or Groningen!

Bedankt **Fenna** voor het maken van mijn cover. Toen ik je draaimolenposter in 2022 zag, was ik meteen verkocht. Ik had niet verwacht dat het echt zou lukken, maar het is echt precies geworden waar ik op had gehoopt. Jouw artwork hangt nu ook in ons appartement als aandenken aan mijn PhD en mijn geweldige tijd in Groningen. Het gaat je goed en hopelijk treffen we elkaar ooit nog op een festival zodat ik je persoonlijk kan bedanken.

Bedankt **Sylke** voor het maken van de fotos!

Awards

Appiah	Most relaxed person of the building with the best handshake
Angelo	Best NCCC, bringing drunk girl back to her room, roombuddy
Angela	Best tips on how to make a better nasi
Andries	Best visje buddy
Agus	Hardest weight lifting person that I have ever seen
Arne	Best Den Haag travel buddy
Ali	Best history lesson on Iran
Adrivit	Best aura. Doesn't need any more explanation right?
Amanda	Best extroverted entrance at a meeting
Aravid	Best out of the box idea with butter rum
Ana Luiza N.d.A	Best dancer on my Brazilian music during Christmas borrel
Ana luiza S.F.	Best person to gossip with
Bart	Best Slavic coca cola imitator
Bi	Best random ACLO appearance
Bianca	Most icon okayyye i ever heard
Chengcong	Hardest ACLO sporter
Chongyang	The most beautiful curly hairs I have ever seen
Corniek	Best microgoals buddy
Corwin	Best shared interest on NASA rockets that explode
Di	The beast from the east doesn't need any more introduction
Eleonora C	Best conversation on recycling vs downcycling hahahah
Eleonora M	Best swimming buddy (that never happened)
Elia	Became most buffed by looking at the mirror
Fadhli	Best hidden gem conversations on unexpected topics
Floris	best person to be in front with at mall grab
Frederique	Best random appearance at Paradigm
Folkert	Best astrophotography buddy (als je eindelijk je 585 terug krijgt hihi)
Firman	Best dutch speaker (het gaat je goed!)
Federico F	Best stadspark bbq organiser
Federico P	Best massa town guide
Friso	Best Indonesia room buddy
Ge	The happiest person in the department
Giovanni	Best bicep picture buddy
Gertjan	Best tips on good wines

Geraldine	Best candy snack collector
Giulia	Best unexpected poster stealer
Hani	Best sneeze
Henk	Best unexpected appearance at JX borrel at Baxbier
Javier	most sophisticated handshake giver
Jesse	Best music taste buddy
Julian	By far the best group meeting questions
Jing	Best daily conversation meeting buddy
Jos	Best person to go to when i wanted a nice compliment on my tie
Jorge	Most invested in my astronomy hobby
JZ	Best overall outfit of the whole building
Kath	Best first time skier
Kim	Best gift wrapping buddy
Kevin	Best tip on caramelized unions
Khairul	Extraordinary dedicated 24/7 working person
Kathryn	Best conversation on how the weekend was
Luize	Without a doubt the best handshakes
Lorenzo	Best teacher on how to make a fast pasta that takes 4 hours to make
Léon	Best person to impersonate Henk from Agilent
Matteo	Best pesto teacher (still making your pesto almost every month)
Marjan	Best compliments received about my mullet
Martijn	Best random conversation on how your clothes smelled like fish
Marcel	Best side project buddy
Marianne	Best plant keeper
Mimi	The best friendly smile of the whole building
Memoona	Best conversation on the dark side of Pakistan hahahaha
Nicoleta	Best tip on which museum I should visit when I live in Den Bosch
Nannan	Best hotpot organizer
Oualid	Best conversation on my poop project, or was it PUR?
Paul	Best vibe on Brabantse comedians
Phiciato	Best shared interest in microscopes
Putu	Most attempt to get Dutch working hours in his system
Reza	Most interesting conversation on the Arabic text on my t-shirt
Roelf	Most contagious laugh
Sarah	Best conversation on wearing contacts vs glasses hahaha
Salvador	Best whirlwind impersonator
Stijn	Best swimming buddy
Siti	Best GCRE question about microreactors
Sietse	Best coffee buddy
Yiwei	Most friendly way of saying Hi to me on the hallway
Yumi	Best conversations on Dutch and Japanese culture Arigato gozaimasu!
Wout	Best advice on getuigeschrift vragen na ontslag nemen
Weixin	Most beautiful PhD promotion outfit II have ever seen
Xiyan	Best conversation on Chinese etiquette while drinking sake in a bar in Japan
Xander	Best NMR prepper

Thank you all Indonesian Bernoullians: **Amanda , Bart, Corniek, Dani, Frederique, Friso, Gabriela, Hidde, Jelle, Julian, Jesse, Mark, Maria, Nicoleta, Paul, Reinier, Roelf, Simon, Stefanie** and Japan Bernoullians: **Alessia, Amanda, Ana, Ana Luiza, Aravind, Bart, Bianca, Corniek, Dani, Floris, Giulia,**

Jesse, Julian, Léon, Marianna, Mark, Roelf, Shreya, Marc, Xiyan, Arne for the amazing time during these holidays… oh I mean "studytrips"

A special thanks to the Hive and Shitted crew: **Faku**, **Jakob**, **Lucas**, **Maria**, **Melina**, **Milena**, **Muriel**, **Sven**, **Victor**. Every festival has been a blessing with you guys and see you next year at Shifted! Thank you Faku and Muriel for coming all the way to Groningen for my defense as well!

Alle mensen buiten de uni, **De hele familie Engels**, **Rick**, **Roy**, **Annelies**, **Yannick**, **Pim**, **Süreyya**, **Geert**, **Laura**, **Jan**, **Anne**, **Samme**, **Niels**, **Lotte**, **Bartje keer zes Mulder**, **Noor**, **Jasper**, **Sarah**, **Mark**, **Esmeralda**, **Robert Jan**, **Selwyn, Vera**, **Max, Sylke, David, Stefan, Hanna, René**. Bedankt voor alle gezelligheid de afgelopen jaren, jullie hebben stuk voor stuk mijn leven ingekleurd en ik weet zeker dat er nog veel leuke herinneringen gaan komen.

5 jaar geleden heb ik er een superleuke schoonmoeder bij gekregen. Bedankt **Truus** dat je altijd interesse in mijn vakgebied hebt getoond en voor alle leuke tripjes die we hebben gemaakt. Dat je nog vaak door het gluurijzer komt kijken in Den Bosch!

Pap, mam, Saira, Davey, Jesse, en Chloë, zonder dat we het allemaal doorhadden, hebben jullie van mij een wetenschapsgekkie gemaakt. Een telescoop, microscoop, zo zit dat tijdschrift, robot lieveheersbeestje in elkaar zetten met papa, zien jullie nu ook waar het vandaan komt? Ik had me geen betere zus kunnen wensen om mee op te groeien dan jou Saira. Ik weet zeker dat jij een stukje van je creativiteit aan mij hebt meegegeven want wat jij vroeger allemaal in elkaar draaide moet haast wel een voorbeeld zijn geweest. Mam, jij hebt me altijd bij de gekste ideeën gesteund waardoor ik altijd in mezelf geloofde. Dat jij altijd tegen mij hebt gezegd: "als jij dat leuk vindt, dan moet je dat gewoon doen, maakt niet uit wat anderen ervan vinden" is sowieso de reden waarom ik zo zelfverzekerd ben geworden. Pap, als jij niet had gezegd "ga anders een NT studie op HBO doen" had ik hier niet gestaan. Dan was ik nu waarschijnlijk een doodongelukkige gymleraar geweest. Ondanks dat het voor jullie sinds HBO een mysterie is wat ik iedere dag met mijn leven loop te doen zijn jullie alsnog mijn grootste fan. Bedankt voor alles.

Bedank **Poes** voor al je brommerij dat mijn stresslevels omlaag heeft gebracht. Had je niet hoeven te doen, maar zo ben je dan weer wel.

Mijn laatste VO is voor **Roos**, Egyptisch naanbrood, Alberts. Ons Kokolino kan zichzelf nu ook ervaringsdeskundige noemen na 4 jaar PhD meej men. Vanaf het moment dat jij met je bordeelsluipertjes de drempel van de viaduct bent overgelopen, is mijn leven een grote kleurrijke muzikale fruitmand geworden. Iedere dag is met jou een feestje en ik hoop dat daar nooit een einde aan komt. Op naar eindeloos veel worstenbroodjes naar binnen trappen in Den Bosch. Handjes en spekjes!

Tim



